A Materials Chemistry Investigation of Archaeological Lead Glazes

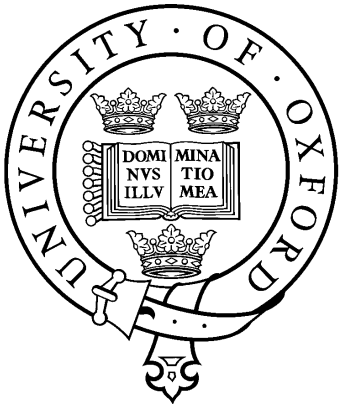

Marc Sebastian Walton

Linacre College

University of Oxford

A thesis submitted for the degree of

Doctor of Philosophy

Michaelmas 2004

To Sherine, my amazing wife, for supporting me emotionally, financially, and lovingly.

Acknowledgements

Working on this thesis was made stimulating and enjoyable under the supervision of Professor Michael Tite. I thank him for taking me on as his student at the Research Laboratory for Archaeology and the History of Art and for his continuing guidance into the first years of my career. The fruitful discussions with the members of the Materials Group – over tea, and otherwise – on all matters of archaeology and the physical sciences were always appreciated. Particularly, I am grateful to Chris Doherty for sharing his passion for geology and computers with me. I will always value the friendship of Gareth Hatton, my fellow basement troglodyte. Dr. Andrew Shortland provided me with astute guidance and afforded me the unforgettable opportunity to see the Egyptian deserts. Finally, I would like to express my gratitude to Dr. Trinitat Pradell who shared her profound knowledge of materials science and, in particular, ceramic technology. Many ideas in this thesis were inspired by conversations with her.

Outside RLAHA, I thank Dr. Norman Charnley of the Department of Earth Sciences for selflessly sharing his time and expertise in electron microprobe analyses. Also, the advice of Dr. Eberhard Sauer (Keble College) on the Roman archaeology portions of this thesis were much appreciated. For providing the majority of samples used in this work, I especially thank Dr. Robin Symonds of the Museum of London Archaeological Services Unit.

At the Los Angeles County Museum of Art, I owe a great debt of thanks to Victoria Blyth-Hill who allowed me to set aside time to complete this study. Dr. Terry Schaeffer kept me on track when my attention occasionally wandered from the task at hand.

This research was made possible by the Samuel H. Kress Foundation, New York. I thank them for supporting my career and for nurturing the fields of archaeological and conservation science.

Finally, I thank my daughter, Lara Nour, whose precious existence reminded me daily – and nightly – that there is more to life than my work.

Abstract

In this thesis, the fabrication technology of Roman lead glazes were examined using a number of materials science techniques: namely, electron probe microanalysis, X-ray diffraction, and inductively coupled plasma atomic emission spectroscopy. The overall aim of this work was to discern particular technological styles for a wide group of lead glazes by quantifying the chemical and microstructural features of glaze production. Using experimental replication, it was found that two basic methods of glazing could be identified chemically. When applying PbO alone to an earthenware ceramic, the resulting glaze was in equilibrium with the ceramic as indicated by flat compositional profiles obtained along the glaze cross-section. However, when applying $PbO{\cdot}SiO_2$ mixtures to earthenware ceramics, gradient profiles indicative of diffusive mass transfer were obtained from the glaze cross-section. On the basis of these chemical criteria, these two methods of glazing were identified in archaeological material. It has been determined that the earliest lead glazes from Anatolia and Italy (approximately 1^{st} century B.C.) were made using $PbO{\cdot}SiO_2$ mixtures applied to calcareous clays with Fe and Cu oxides added as colourants. Later production (post 2^{nd} century A.D.), seems to have employed PbO alone applied to non-calcareous clays with no intentionally added colourants. The Roman production of lead glazes was compared to both those of Late Antiquity (4^{th} – 10^{th} centuries A.D.) which continued to use PbO applied to non-calcareous clays, and to those of Byzantine and Islamic contexts (8^{th} – 14^{th} centuries A.D.) which seem to have used $PbO{\cdot}SiO_2$ mixtures applied to both calcareous and non-calcareous clays. It is also argued that the technological features of the Byzantine and Islamic glaze production shared more in common with the contemporary Chinese lead glazing tradition (the Sancai wares of the 7^{th} century A.D.) which also used $PbO{\cdot}SiO_2$ mixtures applied to non-calcareous clays, than with the Late Antique glazing tradition.

Contents

List of Figures

List of Tables

Chapter 1

Introduction: Rhosica Vasa

In 50 BC this relatively obscure correspondence was exchanged between Cicero and Atticus: "*Rhosica vasa mandavi. Sed heus tu! quid cogitas? in felicatis lancibus et splendidissimis canistris holusculis nos soles pascere; quid te in vasis fictilibus appositurum putem?*"[1] This passage, which so impressed Francis Follin Jones (1945), the first archaeologist to seriously study lead glazed wares, also sets the stage for this thesis for reasons that will be addressed shortly.

As correctly pointed out by Jones, the mere mention of using an earthenware ceramic is strikingly uncharacteristic of the Roman taste-makers of the 1^{st} century BC who had more splendid tablewares at their disposal: silver and gold services replete with mythological scenes intended to inspire dinnertime oration and debate. Therefore, Cicero's interests in the Rhosian ware were likely peaked by the novelty of these vessels which were not yet available to those in Italy, but were certainly desired by them. Although it is a matter of debate whether Jones was correct in attributing lead glazed wares to the *Rhosica vasa*, it is noteworthy that these ceramics first appear in the archaeological record at this same time not far from ancient Rhosus in the Hellenistic/Parthian East.

[1] Cicero, Ad Atticum VI, 1, 13: *I have ordered [for you] a service of Rhosian ware. But, alas! what are you thinking (speaking to self)? You are accustomed to feed us vegetables on plates engraved with a pattern of fern leaves, and in very splendid baskets; why should I think you will put them in earthenware vessels?*

Figure 1.1: Examples of early lead glazed wares. A skyphos shown on the left belongs to the British Museum (GR.1935.5-14.1). The kanthros, signed by Likinnios, on the right is housed at the J. Paul Getty Museum (83.AE.40). Both are "high status" wares thought to date to the 1^{st} century BC with a provenance of Asia Minor.

If indeed *Rhosica vasa* may be equated with lead glazed wares, this letter from Cicero may elucidate the expansion of this craft from small-scale localized production into a larger "world" market. It may be posited that the diffusion of lead glazed vessels was motivated by the taste and the desire of the elite. This hypothesis is based on the tendency in ancient Rome to adapt the technology of foreign cultures and, especially, to consume all things Greek which is often cited as the catalyst for all of Roman art and technology (Elsner 1998).

Lead glazed wares seem to follow this model of expansion. Soon after they emerge from the Hellenistic centres of the East in the 1^{st} century BC, lead glazed vessels appear in Italy where workshops produced similar wares to their Eastern predecessors (Hochuli-Gysel 1977). Moreover, given their virtuosity in execution, it is easy to understand the Roman desire for early lead glazed wares which were surely more affordable versions of popular forms in metal (see Figure 1.1). However, the question of how the technology of this craft ended up in the Western Mediterranean still remains.

Were craftsmen who had the "know-how" brought from the East to specifically satisfy the need for these wares? Or, could the technology have been simply re-invented by local skilled potters who fashioned lead glazed wares in the likeness of these newly imported ceramics? These questions are central to this study. Of equal interest is how this technology was sustained over the duration of the Roman Empire into late antiquity. To answer these questions adequately is a daunting and multifaceted task which relies ultimately on the composite story told by social history, archaeology, and, crucially, materials science. It is to this latter story that this thesis aims to make a contribution.

1.1 A Materials Science Approach

Materials scientists working in archaeology are uniquely positioned to address the mechanisms of craft transmission by establishing what is known as a 'technological style' for a particular class of object (Lechtman 1977). Although 'technological style' has been an ever evolving framework within which technological historians (otherwise known as archeometrists, archaeological chemists, *etc.*) have been plying their trade over the last twenty-five years, the term essentially implies the close study of an object's physical properties to understand how it was made. It is also a term that incorporates the traditional art historical sense of 'style' as it is used to describe, classify, and group similar objects. What 'technological style' specifically addresses, which 'style' in its traditional meaning does not, is the process by which objects first come to life. Known as the *chaîne opératoire*, this concept follows the chain of technological choices made during the fabrication of an object which link up to produce its final properties and performance characteristics (Sillar and Tite 2000; Tite 2001). This approach has been championed by Lemonnier (1993) who views technological choices as social strategies which directly relate to the identity and world-view of the artisans involved in the production of the object. The *chaîne*

opératoire therefore provides an opportunity to trace the cultural fingerprint of an object through its technology.

1.2 The Larger Picture: Silicate Glass

Lead glazes are part of a long cultural tradition of vitreous material production in and around the Mediterranean basin. From at least the 4^{th} millennium BC, it was recognised that plant ash could either be applied to or mixed with silica (in the form of quartz pebbles or sand) and heated to produce a liquid melt which, on cooling, formed a vitreous glaze or glass. These glassy substances were particularly unique. Although they were man-made, they possessed properties, such as hardness, clarity, and, sometimes, vibrant color, that were associated with precious stones and gems. This transformation from prosaic raw materials into something useful, and even valuable, must have been a magical and likely ritualized experience (Budd and Taylor 1995). As a result of these properties, silicate glazes and glasses have been amongst the most commonly exploited man-made materials – along with metals – making them prototypical.

The beginnings of vitreous material production can be traced to Mesopotamia and Predynastic Egypt (circa 4000 BC). These earliest examples were comprised of quartz and steatite pebbles glazed with alkaline plant ash. Although often cited as a slightly later invention, faience was also produced in Predynastic period Egypt (Vandiver 1983). Faience was a type of ceramic made of crushed quartz and encapsulated by a glaze created from plant ash. It is the general consensus that the first glasses (defined by their lack of stone or ceramic substrate) emerged from this tradition of glazed material production in the 16^{th}–15^{th} centuries BC (Barag 1962; Barag 1970; Bimson and Freestone 1987). These first glasses were made from plant ash, lime, and silica which resulted in (Na_2O, K_2O)–CaO–SiO_2 compositions (Moorey 1994; Brill 1999). Also during the 2^{nd} millennium, frit (crushed glass) with compositions comparable

to those of alkali glasses were being applied to earthenware ceramic surfaces to form glazes (Freestone 1991; Tite et al. 1998; Paynter 2001). With few exceptions, this use of alkali frits remained the prevalent ceramic glazing material in the Near East through the Islamic period. A prominent exception to this rule, however, was when glazes composed of PbO–Al_2O_3–SiO_2 first appeared on fine wares around the 2^{nd} century BC (Caley 1947). These lead glazed wares constituted an unprecedented experiment in glaze production. Although these wares were produced only on a minor scale, the glazes were remarkable for the amounts of lead incorporated into their composition (50-70% by weight). The wares themselves were a novel class of ceramic that was similar in form and decoration to silver flagons and cups typical of Hellenistic Anatolia (Cvjetićanin 2000b).

1.3 Scope of Thesis

This thesis intends to examine the various methods of lead glazing from its Hellenistic beginnings to the early Christian and Islamic periods. Particular emphasis will be placed on tracing technological change in lead glazes during the Augustan period through the 4^{th} century AD, which represents the apogee of Roman lead glaze production. Although some archaeometric work on Roman lead glazes had already been conducted prior to this thesis (Paynter 2001; Tite et al. 1998; Pérez-Arantegui et al. 1995; Hatcher et al. 1994; Caley 1947), these studies were limited by the number of samples that they reported. For instance, Caley (1947) contained a single average for a handful of glaze analyses from the site of Tarsus in Anatolia. Likewise, Pérez-Arantegui et al. (1995) presented only a few analyses from the Tarraconensis region in the Northwest of Spain. Although the study by Tite et al. (1998) provided an excellent discussion on the technological advantages of lead glazes over alkaline glazes, this work did not focus on Roman glaze technology in specific. The most comprehensive set of Roman lead glaze analyses came from Hatcher et al. (1994),

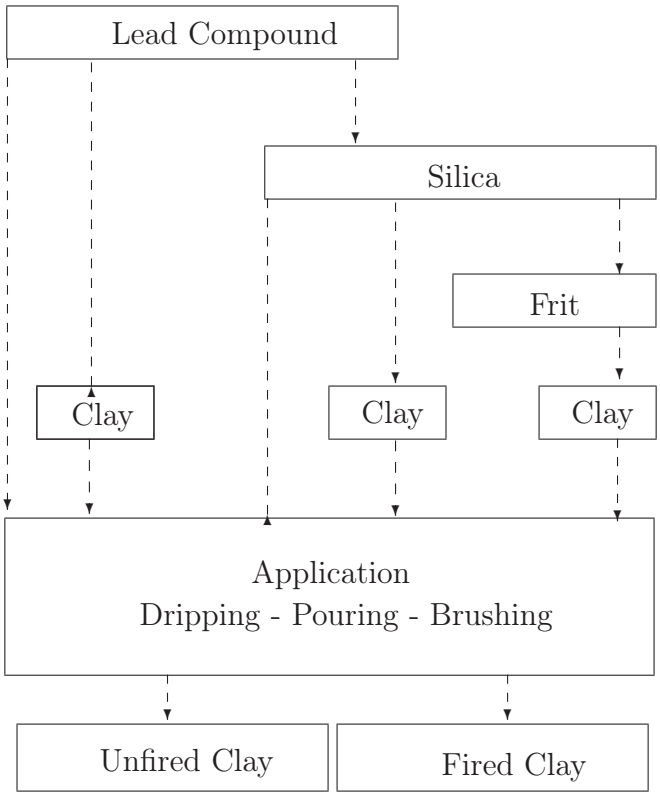

Figure 1.2: The possible technological choices that may be made when producing a lead glaze (recreated from Tite et al. (1998)).

but these analyses were of questionable value considering they were obtained with an open air X-ray fluorescence spectrometer (XRF) on the weathered outside surfaces of the glazed sherds. However, the qualitative interpretation of the data of Hatcher by Paynter (2001) is useful and informs some of the work presented in this thesis (see section 5.1.3 in Chapter 5).

These deficiencies in the literature are hopefully redressed by the data presented in Chapters 4 and 5 of this thesis. However, before considering the analyses of the archaeological material, the technological and material choices available to the artisan when producing a lead glaze need to be clarified. Such choices made by an artisan will cause the diagnostic microstructural features of a glaze to vary systematically according to both the body fabric and raw glaze materials used, as well as by the firing conditions employed. These choices therefore manifest themselves as unique fingerprints of the fabrication technique (Tite et al. 1998). This theoretical/experimental exercise is critical to the current study as it is the means by which the *chaîne opératoire* is reconstructed for a particular archaeological glaze.

The basic outline of the choices available to a potter creating a lead glaze are presented in Figure 1.2. As illustrated in this figure, the simplest technique would be to apply a ground lead oxide powder directly to a ceramic surface. If heated above 700 ℃, a glaze would be produced on the ceramic through the dissolution and mass transfer of glass-forming components (silica and alumina) from the body into the lead oxide melt. One of the problems with this glazing technique is that the artisan is required to choose a clay substrate which has enough silica available to form a glaze. A second, alternative, method would be to mix the lead with the necessary amounts of SiO_2 prior to its application to a ceramic. In this way the artisans could select their starting materials to better control the wetting characteristics and viscosity of a glaze. Third, it is also possible, following the tradition of producing alkali glazes, to use frits which would introduce yet another measure of control. These material

options, together with replication experiments demonstrating their microstructural appearance, are examined in further detail in Chapter 3.

To begin, Chapter 2 will briefly place the subject of lead glazed wares into its historical and archaeological context.

Chapter 2

Archaeological Context

The purpose of this chapter is to bring together the disparate pieces of archaeological and art historical evidence for the production, spread, and use of lead glazes. This brief survey of the literature presents an outline rather than a fully rendered historical study of lead glazed ceramics since this topic has already been covered extensively by others (Cvjetićanin 2000b; Parlasca 1990; Casas i Genover and Merino i Serra 1990; Desbat 1987; Arthur 1978; Hochuli-Gysel 1977; Pinkwart 1972).

Naturally, this discussion must begin with the excavations on the mound of Gözlü Kule at Tarsus in present day Turkey, where the earliest known examples of lead glazing were discovered (Goldman 1950). The dating for these glazed wares is imperfect. Although their iconographic and stylistic features led the archaeologists to believe the vessels were produced earlier than the Augustan period (27 BC–14 AD), the *ante quem* date for the first stratigraphic occurrence is between 14–54 AD. It is certain, however, that these wares were produced at Tarsus given that the assemblage found at the site consisted of patterned moulds, and their corresponding completed vessels together with kiln stilts intended to separate vessels during glaze firing, biscuit fired but unglazed vessels, and vessels with only the underglaze[1] painted.

As pointed out by Jones (1945) and substantiated by others (Cvjetićanin 2000b;

[1]Underglaze is a term used by Goldman (1950). It refers to drawing that was applied to a ceramic prior to a final overall glaze application. No ceramics with this type of decoration were examined in this thesis.

Hayes 1997; Rotroff 1982; Lane 1948), the forms and decorations of Tarsian lead glazed wares bear their closest resemblance to Greek metal forms dating back to the 4^{th} century BC which were typically decorated with raised vegetal motifs. In fact, it is probable that these ceramics are skewmorphically related to metal forms. For instance, according to Michael Vicker's theory, the type of skyphos shown in Figure 1 was intended to look like a bronze (Vickers 1995; Vickers 1986; Vickers et al. 1986). The green exterior would have been designed to mimic the typically patinated surface of a copper-alloy vessel, while the yellow interior echoed the polished inner surface created by regularly wiping away the residues of drink. A lead glaze was thus a surface treatment intended to produce the effect of metal. From an economic standpoint, this treatment would have elevated the appearance of these earthenwares by creating a cheap facsimile of an item that would have otherwise been made of the more expensive alloys.

What is surprising about these lead glazed ceramics is that they emerge from the archaeological record without precedent. As of yet, no examples of mistakes or what may be recognized as transition pieces have been identified, though perhaps new excavations[2] at the Gözlü Kule mound will shed light on this gap in our knowledge. Alternatively, this could mean that the already established technology was introduced to Tarsus from another locale.

So if not at Tarsus, then where did the lead glazed vessels originate? Unfortunately, much of the evidence for other occurrences of lead glazes in Anatolia – as well as further East – is indirect and unscientifically dated. In her early survey of lead glazed wares in private and museum collections, Jones (1945) speculates that the objects originated from the Cilician region ranging from Georgia to Northern Iraq. Although the slightly more recent study of Hochuli-Gysel (1977) does not recognize a specific grouping as coming from here, several of the vessels that she assigned to

[2]A joint American-Turkish effort organized through Bryn Mawr College (Pennsylvania, USA) has recently re-opened the excavations.

the supposed Tarsus workshop were actually found through chemical analysis not to belong to this group (Hatcher et al. 1994). Instead, these vessels from Ain Tab (Gaziantep, Turkey) and Dura Europas (Syria), seem to be comprised of fabrics native to the regions in which they were found.

Glazing was not an uncommon practice in the Near East where the technology extends back to at least 1500 BC (Paynter 2001; Freestone and Gorin-Rosen 1999; McCarthy 1996). Instead of using lead, however, glazed wares employed alkaline fluxes of plant ash. It is interesting to note that the 2^{nd} century BC Parthian ceramics, to which these alkaline glazes were applied, displayed Hellenized forms and vegetal motifs similar to those rendered on the Tarsian lead glazed wares (Eiland 1995). It is possible that the skewmorphic commonalities between alkali and lead glazed vessels best explain the potential origins of lead glazing. In a region with a lengthy tradition of producing glazed wares, one can easily envision either a cross-over to lead oxide fluxes or some type of experimentation with this material at one of the Eastern Hellenistic centres. Although some of these hypotheses are tested using the chemical evidence presented in this thesis (see the discussion in Chapters 5 and 6), many more critical questions on the subject remain unanswered. It is certain that more archaeological work in the region focusing on the Hellenistic/Parthian period would help clarify the transmission of lead glazes into the Mediterranean world.

2.1 The Spread of Technology

2.1.1 From the Earliest Lead Glazes: Western Anatolia into Italy and Gaul

Fortunately, the evidence for lead glazes in Western Anatolia during the Augustan period is much more thoroughly documented than the Eastern material. The most comprehensive study on the subject is that of Hochuli-Gysel (1977), who accurately and painstakingly developed stylistic classifications for lead glazes in the region, and

suggested several workshops in Anatolia, other than Tarsus, with one particularly notable atelier located at Smyrna producing a large number of these wares. More recent excavations have also revealed an extensive workshop area at the site of Perge in Pamphylia where kilns dedicated to lead glazing together with saggars and other pieces of kiln equipment have been found *in situ* (Atik 1995). It should be emphasized that very few locations in the Eastern Mediterranean, outside Anatolia, either possessed or manufactured lead glazed wares.

Anne Hochuli-Gysel (1977) suggested that lead glazed wares started to diffuse from Anatolia into Italy from around 50 BC. However, the arrival of these wares in Italy actually predates their first documented occurrence at Tarsus. In addition, it is thought that workshops producing lead glazes in the north of Italy were established at this same time though hard evidence indicating this production is lacking (Maccabruni 1987). Even more surprising, scant evidence from Saint-Romain-en-Gal and Lyon (both in central Gaul) demonstrates possible lead glaze ware fabrication began there by 40–30 BC (Desbat 1985; Génin et al. 1996). Despite these early examples of production in the Western Mediterranean, there is still little doubt that glazed vessels originated in the east.

The Lyon vessels are particularly interesting as they bear the stamp of the potter *ACO* (Desbat 1987; Iliffe 1936). *ACO* was known to have produced wares in the north of Italy prior to arriving in central Gaul. Although Desbat (1987) only cites eleven fragments found in a spoil heap as accounting for *ACO*'s Lyonasse production, it nevertheless appears that he, or one of his followers, brought the technology of lead glazes to central Gaul with him. *ACO*'s stamp is therefore a particularly useful piece of evidence which demonstrates the exact mechanism of technological transfer in this case: the movement of a knowledgable craftsman. Other Lyon workshops, in addition to the one described by Desbat (1987), were established at slightly later dates. At La Muette (another sector of Lyon) a probable branch factory of *ACO* was

Oxford No.	*Findspot*	*Hochuli-Gysel's Attribution*	*Hatcher et al. (1994)'s Location Assignment*
RG5	?	Tarsus, group 3	Italy
RG6	Alexandria, Egypt	Tarsus, group 3	Italy
RG11	Paphos, Cyprus	Tarsus, group 2	Italy
RG12	?	Tarsus, group 3	Italy
RG22	?	Tarsus, group 3	Italy
RG9	Asia Minor	West Asia Minor	Smyrna
RG8	Xanthos, Lycia	West Asia Minor	Smyrna
RG19	?	Smyrna, group 3	Smyrna
RG49	?	Smyrna, group 3	Italy or Smyrna
RG50	Asia Minor	Smyrna, group 3	Smyrna
RG54	Troad or Smyrna	Smyrna, group 4	Smyrna

Table 2.1: Probable origins of some of the objects studied by both Hatcher et al. (1994) and Hochuli-Gysel (1977). The complement between body analysis groupings of Hatcher et al. (1994) and the stylistic analysis of Hochuli-Gysel (1977) shows how an artist from one workshop may have moved to another. It should be noted that the assignments of Hatcher et al. (1994) are based on reference fabrics that are not necessarily lead glazed.

established around 10 BC and was ostensibly dedicated to the production of glazed wine services (Génin et al. 1996; Green 1979). Again this workshop is known by the potters who worked there (Chrysippus, Hilarus, Philarcurus, *etc.*) all of whom were migrants from workshops located in the north of Italy. This information further substantiates the theory that lead glaze technology arrived in central Gaul with these craftsmen. As a cautionary note, however, Desbat (1987) points out that the early lead glazes were exceedingly rare. They are found in a proportion of 1 of every 1000 ceramic vessels excavated in central Gaul. These numbers certainly beg the question of what purpose these wares served, especially when terra sigillata was produced in high volume and was readily available. In addition, why was production of these wares necessary when imports of lead glazed ware from Italy would have certainly sufficed for such a small market? Ultimately these question must remain unanswered without additional archaeological evidence for lead glazes in these regions.

The transfer of lead glaze technology from Anatolia to Italy also seems to have occurred through the movement of artisans. Although not explicitly recognized by

Hatcher et al. (1994), the most compelling data showing this diffusion is from this study. This evidence is presented in an abridged form in Table 2.1. Hochuli-Gysel (1977) bases her groupings on the various artistic styles, and assigns the vessels according to the particular artistic hand of a craftsman, or a school. The designations made by Hatcher et al. (1994) are based on the chemical composition of the body fabric, which provides a specific geographic location for the vessel. When these two pieces of information are viewed together, it becomes clear that a style, previously attached to one workshop, could have migrated to another atelier located in a different geological setting as suggested by a change in raw materials. Using this logic, Table 2.1 shows that craftsmen with a "Tarsian hand" mostly produced vessels of Italian clays thereby suggesting this westwardly movement of an artisan, or artisans.

From these data on early lead glazes in the Western Mediterranean, a date and mechanism of arrival can be extrapolated. It is suggested that Anatolian craftsmen brought this technology to the north of Italy around 50 BC at the latest. This was followed by the introduction of the technology to Lyon by 40–30 BC. It should be noted that, like the Eastern wares and those of northern Italy, these early vessels were two-toned and clearly mimicked metal forms. Although these workshops in Lyon seem to have been abandoned by the start of the new millennium, Green (1979) argues that potters, likely inspired by *ACO*, continued the tradition of lead glazing into the Tiberian period (14–37 AD) with their centre of production changing to the Allier valley.

2.1.2 The Height of Roman Lead Glaze Production: Workshops in the Allier River Valley and Central Italy

The heritage of *ACO* is certainly recognized in the vessel forms produced in the Allier valley (skyphoi and goblets, such as Déchellete's number 57, continued to be produced), but these newer vessels did not possess the two-toned colouring schemes of previous lead glazed wares. Instead, these glazes were routinely of uniform yellow or

olive colours. Also, new forms were developed by these workshops to serve the tastes of a wider Roman market (Green 1979). Therefore these lead glazed wares represented a stylistic departure from the Eastern tradition as it was filtered through the north of Italy. Starting around 20 AD, the most prominent Allier workshop seems to have been at Saint-Rémy-en-Rollat (again, specific evidence demonstrating the production of lead glazes at this workshop site is missing). Although this workshop was short-lived and was only active during the Tiberian period, other workshops in the area must have addressed the need for lead glazes since relatively large quantities of these wares continued to be produced into the 2^{nd} century AD (Vertet 1986).

It is from these central Gaul workshops that extensive long-distance trade of lead glazes becomes apparent. Central Gaul lead glazed wares were certainly being exported to Great Britain between 70–140 AD as proved by the analysis of available evidence from this country by Kevin Green (1979) and Paul Arthur (1978), and later substantiated by Symonds and Hatcher (1989) upon excavation at Colchester outside London. Also, as is shown in this thesis (see Chapter 4), during the same time in the 2^{nd} century similar wares appeared in the Danubian provinces of Upper Moesia (at sites such as Diana and Singidunum) and Dacia Repensis (at sites such as Apulum Partos) as well as in the Tarraconensis region of North Eastern Spain (Cvjetićanin 2000a; Cvjetićanin 2000b; Cvjetićanin 1997; Pérez-Arantegui et al. 1996). As discussed in Chapter 4 of this thesis, workshops producing these glazed wares may have been long-lived with continued production into the 4^{th} century AD.

Martin (1995) documented a transition similar to that seen in the central Gaul material for the lead glazes of Italy starting in the 2^{nd} half of the first century AD. The glazed wares recovered from the excavations of Terme del Nuotatore at Ostia indicated that their production shifted from the north of Italy to central Italy with probable fabrication at Latium or Campania. Unlike the north Italian wares, these glazes were plainly decorated and were clearly intended for functional use such as cooking.

As shown by Martin (1995) these glazed wares in no way mimicked metal forms – unlike their fore-runners – as they were being made into less decorated utilitarian forms such as bowls, jars, lamps, and plates. These Ostian wares probably marked a shift in glazed ware production that provides a stylistic liaison between the early, and supposedly luxurious, metal inspired forms and the prosaic forms found around the 5^{th} century at such sites as Carlino in the north of Italy (Brogiolo and Gelichi 1997; Martin 1992; Mannoni 1992).

The reason for the decline in the prestige of glazed wares beginning mid 2^{nd} century and later is not known. It is interesting to note that glass wares undergo a devaluation in terms of decoration and prestige at this same point in time (Martin 1995; Isings 1957). In addition, the scale of production and distribution over the Roman world constituted a major growth in terms of the number of lead glazed ceramics and glass vessels made (though the proportion glazed ceramics remains a small proportion of the total amount of pottery produced). Perhaps, then, these processes represented, for both industries, the age old economic problem wherein to keep the price of production low, quality often suffered to meet increased demand.

2.1.3 Late Antique Lead Glazes: North Italy, The Limes, and Byzantine Constantinople

Following the 4^{th} century AD, the production of lead glazes in Gaul wanes. So too, the production in Ostia and in North Italy at Carlino began to drop away by the 5^{th} century (Martin 1995; Martin 1992). However, Cvjetićanin (1997) has shown evidence for continued use of lead glazes in another region, that of the Limes of Moesia and Dacia Ripensis (present day Serbia and Romania), through the late 5^{th} century. These later occurrences of lead glazes certainly show continuity with the earlier Roman lead glazing traditions. However, after this period there is a general gap in our knowledge about lead glazed production until the early 7^{th} century when there was an explosion in production coming from the site of Saraçhane in present day Istanbul. These early

Byzantine lead glazes were produced exclusively in Constantinople, and were thus probably intended to meet local demands that had once been fulfilled by Roman wares (Hayes 1992). For the most part, the colour palette of the glazes remained similar to those found in Roman contexts (yellow, green, and brown) but the clay was a coarse white clay native to Saraçhane.

Whether this Byzantine production of lead glazes belongs to the technological lineage of lead glazing that began in the Hellenistic period is difficult to assess. Certainly, the gap in time between the last known production in the Yugoslav regions and the onset of Byzantine production is not insurmountable and it may only represent the passing of two generations of craftsmen. However, although the subject is only briefly discussed in this thesis (see section 5.2.4 in Chapter 5), it is equally possible that the technology arrived in Constantinople via the silk routes from China where lead glazing had certainly shown continued production from the 2^{nd} century BC (Scott et al. 1995; Rawson et al. 1988).

Chapter 3

Experimental Replication: Reactions of Earthenware Ceramics with Lead Oxide and Lead Silicate Compounds.

Despite their common use in modern industry, the chemistry of lead silicate glasses have been studied surprisingly little. A review of the literature on this material reveals that only a handful of researchers have attempted to address the molecular structure of these glasses, and even fewer studies have examined the reactivity of lead oxide and lead silicate with refractory materials.

The attempts to characterize the molecular structure of lead silicate glass constitute the most active research on this material. However, the subject has proven to be contentious especially when lead content exceeds 70% by weight causing the silicate structural network to become discontinuous (Rybicki et al. 2001; Mylyanych et al. 1999; Fayon et al. 1999). Furthermore, none of this current research has adequately addressed the glass structures that can form with lead oxides that have oxidation states other than Pb^{2+}. As is most pertinent to this present work, only four studies were located that examined the reactions of PbO and $PbO{\cdot}SiO_2$ frits with refractory materials such as crucibles and ceramic substrates (Molera et al. 2001; Bersani et al. 1997; Hurst and Freestone 1996; Hilger et al. 1981). Only a scattering of further studies, which are primarily concerned with the optimization of metallurgical slag chemistry, have measured diffusion coefficients in lead silicate glasses together

with their corresponding melt viscosities (Ouchi and Kato 1983; Schmalzried et al. 1981; Petusky 1980; Petusky and Schmalzried 1980; Matousek 1975; Langanke and Schmalzried 1979). The most comprehensive work on lead silicate and lead aluminosilicate glasses are the early studies of Geller and Bunting (1943) and the more recent phase equilibria study of Chen et al. (2001). Geller and Bunting's PbO-SiO_2-Al_2O_3 phase diagram, however, is incomplete and unhelpful when examining lead silicate glasses that contain less than 80% PbO, a region in compositional space where the majority of the glazes in this study fall. Chen et al.'s work significantly expands on Geller and Bunting, but it remains inadequate when attempting to explain the non-equilibrium behaviours associated with ceramic glazes.

Although this thesis was undertaken specifically to characterize the chemistry of Roman lead glazes, the shortcomings in the literature necessitated further work to elucidate some of the critical temperature and time transformations of lead silicate glasses and glazes. Besides being interesting in its own right, a rudimentary understanding of the reactions that take place between a lead glass melt and a ceramic is required to characterize the chemistry of this type of archaeological glaze. Therefore, in this chapter, an attempt is made to bring together the disparate pieces of knowledge regarding lead silicate glasses and glazes. This review of the relevant literature is presented in section 3.1. Discussion of the literature is supplemented with experimental work which has focused on the reactions of PbO alone (section 3.4.1), and PbO + SiO_2 mixtures (section 3.4.2) with earthenware ceramics. Before describing the experimental work, a general introduction is presented on two key concepts that will serve as touchstones for the remainder of the thesis: 1) a general definition of silicate glasses with some details on their reaction mechanisms (section 3.1.1), and 2) a generic description of the mineralogical composition of ceramic substrates(section 3.2).

3.1 Introduction to Silicate Glasses

3.1.1 SiO_2 and SiO_2 Glass: A General Description

Silicon atoms have 14 electrons of which 4 are in the valence state and are available for chemical bonding. In solids, either crystalline or amorphous, these electrons form covalent sp^3 hybrid orbitals in a tetrahedral formation. In a perfect SiO_2 crystal, these bonds have an angle of 109.5°, and when cooled with sufficient time they fall into a regular diamond-like crystal lattice. In a glass system, many silicon atoms are brought together without the necessary time and kinetic energy to achieve a ground state configuration and, as a result, they arrange in a meta-stable amorphous state. These amorphous glass structures have the same bond lengths as in their crystalline state, and each atom still creates four bonds in an approximate tetrahedral configuration. However, there are slight deviations in bond angles which are compounded over short distances creating significant distortions in the position and orientation of the atom. As modelled by the random network theory of Zachariasen, any individual Si atom in an amorphous structure looks almost exactly like its crystalline counterpart, but the extended structure possesses none of the translational and rotational symmetry (Zachariasen 1932). Accordingly, there are only very slight differences between the ground state energy of the crystal and that of the amorphous material.

3.1.2 Acid-base Solvent Systems

The covalent description of SiO_2 is a key concept in the formation of lead glasses and glazes. As a covalent material, silica breaks and forms bonds with other glass components following common acid-base rules. The most general approach to acid-base behaviors is Lewis's theory which has been quantitatively adapted by Duffy and Ingram to describe oxide compounds (Duffy and Ingram 1971; Duffy and Ingram 1976; Duffy 1993). Duffy and Ingram have called their theory "optical basicity" since their experimental basicity values are derived by examining optical wavelength shifts

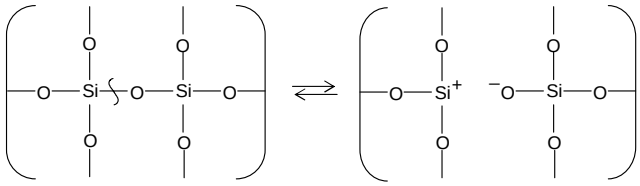

Figure 3.1: Bond structure diagram of equation 3.2 where each oxygen is bonded to a silicon atom to form a branched chain silicate.

relative to a probe ion (usually Pb^{2+}). This solvent independent theory suggests that the oxygen atoms in an branched silicate polymer $[\text{-Si-O-}]_n$ behave as bases transferring electrons to more electropositive (in other words, more acidic) metal oxides to form covalent bonds (Stoch 1999). The ability of a metal oxide flux to stabilize a silicate chain may be quantified using an optical basicity scale which is based on the measurement of oxygen electronegativity when it is bonded to a metal (Duffy 1993). From this scale, the rule of thumb to assess the capacity of an oxide to act as a flux in a silicate system is determined by increasing optical basicity (see Table 3.1 for optical basicity values of common metal oxides).

	K_2O	Na_2O	SrO	CaO	MgO	ZnO	FeO	PbO	Al_2O_3	SiO_2
Optical Basicity (λ)	1.40	1.15	1.10	1.00	0.78	0.95	1.00	1.01	0.60	0.48
Electronegativity (χ)	0.80	0.90	1.00	1.00	1.20	1.60	1.70	1.80	1.50	1.80

Table 3.1: Optical basicity scale and cation electronegativity

Although Lewis's acid-base theory provides a general assessment of reactivity, a more specific explanation has been provided by Jander who described acid-base relationships in non-protonic solvents (Paul 1982). The Jander solvent system incorporates an auto-ionization mechanism wherein the non-protonic solvent species dissociates in a similar manner to water.

$$H_2O + H_2O \rightleftarrows H_3O^+ + OH^- \tag{3.1}$$

where the hydronium ion H_3O^+ is the acid and OH^- is the base. Analogously, a chain silicate, in its capacity as a solvent, can spontaneously form an ionic acid and

base.

$$Si_2(O)_7 \rightleftarrows Si(O)_3^+ + Si(O)_3O^- \tag{3.2}$$

where (O) represents a bridging oxygen covalently shared between two silicon atoms (see Figure 3.1 for the bond structure of $Si_2(O)_7$), $Si(O)_3^+$ is the acid, and $Si(O)_3O^-$ is the base. In this theory, silica has a strong solvent power in which an acid is defined by the tendency of a dissolved mono- or polyvalent metal oxide (M_2O or MO) to increase the cationic characteristic of the melt. This can be accomplished in a silicate solvent through the following mechanism with a monovalent metal oxide

$$Si(O)_3O^- + M_2O \rightleftarrows Si(O)_3OM + MO^- \tag{3.3}$$

and

$$MO^- + Si(O)_3OM \rightleftarrows MOSi(O)_2OM + O^- \tag{3.4}$$

where O^- is the anionic member of another extended $Si(O)_3O^-$ unit.

The mechanisms presented above involve a thermal rupture of the Si-O bonds which are subsequently stabilized by a reaction with a metal M. The kinetics of these reactions are determined by the ability of M (flux) to decrease the overall free energy of the silicate system. A flux meets this criterion through its capacity to delocalize excess electron charge around the silicate units. Thus, with a flux that is strongly polarizable, the rupture/re-polymerisation reactions (3.2 - 3.4) will proceed easily until either all Si-O bonds are severed, or all of the M_2O is depleted.

As a general rule, when melt temperatures are increased, the SiO_4 tetrahedra will become interlinked at their corners to form polyanions of decreasing size (Langanke and Schmalzried 1979). Q^n groups are usually used to describe the size of the polyanions and the corresponding viscosity of the melt, which is determined by the degree of polymerization of the extended silicate. In Q^n notation, n denotes the number of bridging oxygen atoms between silica tetrahedra. With increasing n, there is a rise in the melting temperature and the melt viscosity. Accordingly, an effective flux

species can be defined as one that reduces the number of bridging oxygens (read: decreases n) thereby breaking down the extensive network of Si-O linkages producing SiO_4 polyanions of increasingly smaller sizes.

3.1.3 Lead Aluminosilicate Glass Structures

Lead is an aggressive flux because it is effective in delocalizing the excess electron charge in a silicate polyanion. The high polarizability of the Pb^{2+} ion draws electrons away from the silicate oxygen thereby reducing the temperature of Si-O bond rupture. This property of lead also facilitates the formation of small silicate polyanions at relatively low temperatures. Even with increasing amounts of lead (up to 90%, above which the three-dimensional lead silicate structure is no longer viable), the solid state glass still remains stabilized by asymmetric oxygen coordination around the lead atom (Wang and Zhang 1996). As a result, significant amounts of lead can be dissolved into silica which reduces the melt temperatures of this binary mixture to below 700 ℃ yet maintains the extended structure of the glass once cooled. The introduction of Al_2O_3 acts to further stabilize the glass system (Mylyanych et al. 1999). In the liquid state, Al^{3+} is incorporated into the silicate structure as a tetrahedrally coordinated ion that can substitute for Si in the SiO_4 units. In the formation of aluminosilicate glasses, Si-O-Si also reacts with Al_2O_3 to form Si-O-Al linkages. The driving force behind this reaction is the lower energy of Si-O-Al bonds that renders them less susceptible to thermal bond rupture than the Si-O-Si bonds (Mungall et al. 1998). Also, Al linkages to silica tetrahedra cause further tetrahedral bond distortions that effect the orientation and position of the Si atoms. Such distortions reduce tendencies toward crystallization leading to a more stable glass. These high temperature properties of aluminosilicate melts produce a solid state glass that has an improved overall mechanical stability and hardness.

In a low-lead high-aluminosilicate glass, silica and alumina tetrahedra are struc-

tural units which branch out into a three dimensional network with 3 bridging oxygens (Q^3 units) and one bonded to Pb. Pb in this case is serving as a network modifier. However, as Pb is increased, the bridging bonds are broken and the three-dimensional network becomes increasingly linked by Pb-O-Pb linkages with PbO_3 or PbO_4 pyramids becoming major structural units in the solid state (Fayon et al. 1999). With melt temperatures readily attainable in antiquity, around 700 ℃, the greatest changes in lead silicate glass structure occur at compositions of 50% and 70% lead (Langanke and Schmalzried 1979). At 50% Pb, the major structural units are lead metasilicate ($PbSiO_3$), and likewise lead meta-aluminate ($PbAlO_3$). Above 70% the melt becomes composed of primarily orthosilicate and ortho-aluminate species (Pb_2SiO_4 and Pb_2AlO_4). The presence of the above units in archaeological glazes determines not only the possible temperatures reached during their formation, but also dictates the diffusive behaviour in the melt. At the interface between a silicate melt and a ceramic, the above silicate and aluminate units will form when the melt becomes saturated with the dissolved ceramic body. These units will then diffuse down a chemical gradient into the melt following a Stokes-like hopping mechanism which is caused by the tumble and rotation of the entire polyanion unit, and not an individual ion as is sometimes assumed to be the case (Lesher et al. 1996). As has been recently discussed by several researchers, the mean atomic "hop" distances (the radius of rotation of a diffusing species) as estimated by the Erying and Einstein-Stokes relations (see appendix B; equations B.5 and B.4) are often ten times larger than the corresponding ion (Lesher et al. 1996; Liang et al. 1996). The magnitude of these silicate and aluminate units are roughly the size of the $(SiO_4)_4^-$ polyanion (approximately 2.68 angstroms). Therefore, by correlating the rate of polyanion diffusion with the measurement of compositional profiles across the chemical gradient, it is possible to glean information on the chemistry of the glaze formation.

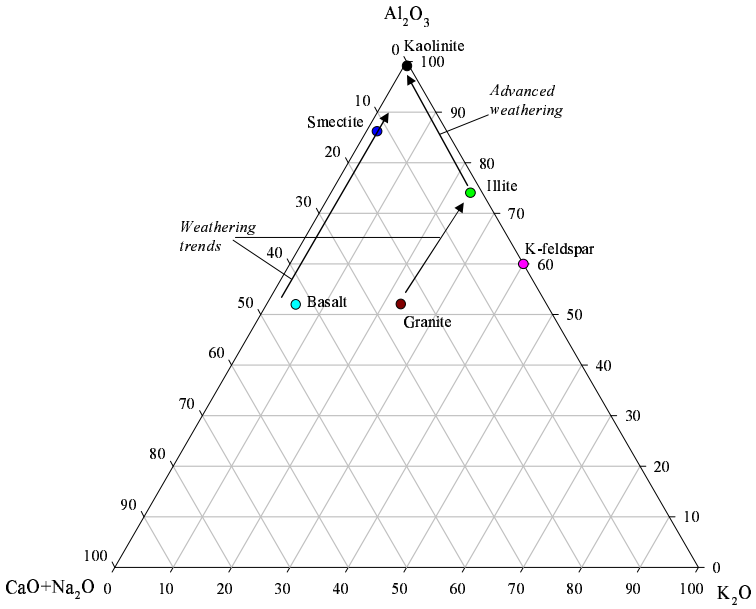

Figure 3.2: The (Na_2O + CaO)-Al_2O_3-K_2O diagram reproduced from Rollinson (1993) showing the weathering trends of an average granite (data from Deer et al. (1993)) and an average basalt from the Central Massif in France.

3.2 Ceramic Structure and the Effect of Heat

A ceramic substrate is the defining component which separates a glaze from a glass. Therefore, in any discussion of glazes, it is logical to include a description of the underlying ceramic. Specifically, the ceramic minerals that may react with an applied glass needs to be established. However, because archaeological and ethnographic ceramics have been discussed thoroughly elsewhere (for instance, the works by Rice (1987) and Velde and Druc (1998)), this rather complicated and extensive work need not be revisited, and only a brief sketch of clay chemistry and mineralogy will be presented here.

Modern ceramic materials are complex owing to the inexhaustible combinations of crystalline oxide compounds and interstitial glasses that can be mixed in different proportions and packed in variable arrangements (Kingery et al. 1976). In general, ceramics may be defined as an intimate assemblage of crystalline minerals with porosity. However, archaeological ceramics should be classified simply as fired clays due to

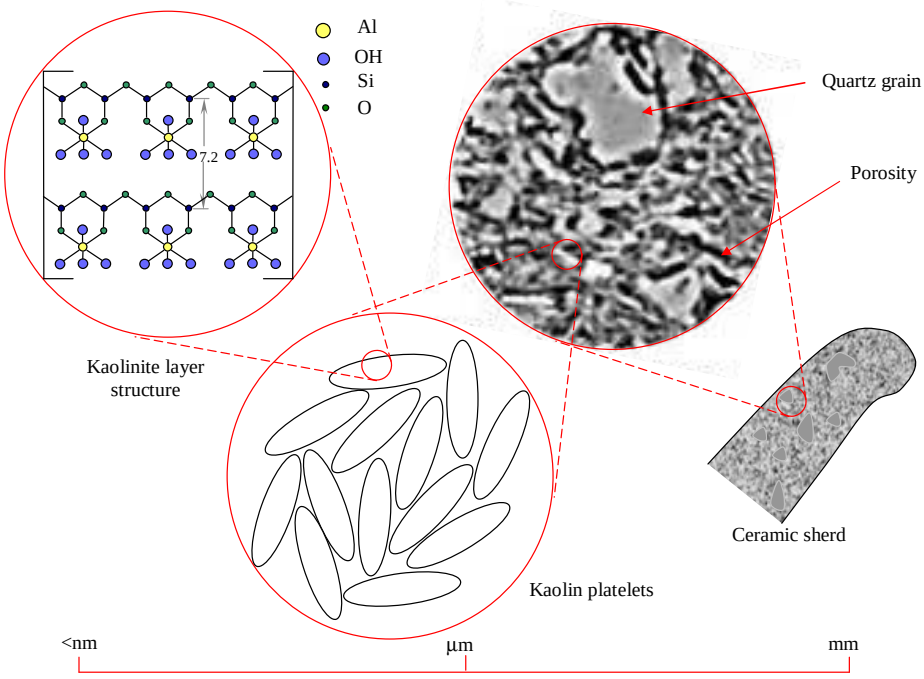

Figure 3.3: The structure of a simple kaolin based ceramic. Note that the kaolinite structure is represented in its unfired hydrated state (structure adapted from Brindley in Kingery (1958). Drawing reflects approximate scale.

the fact that only a small handful of man-made "synthetic" ceramics were fabricated in antiquity of which the most notable are Egyptian blue and Egyptian faience.

Clays are the end-products of the chemical weathering of rocks. Figure 3.2 is a (Na_2O+CaO)-Al_2O_3-K_2O ternary plot showing typical weathering trends of an average granite and an average basalt. This plot (which is redrawn after Nesbitt and Young (1984)) is designed to demonstrate the dissolution of alkalis and Ca from plagioclases and micas as the parent rocks are chemical degraded. In general, smectitic clays are derived from the weathering of basic rock, and illitic and kaolinitic clays are formed from acid rock (Rollinson 1993). In either case, the clay minerals that are formed have a layered structure composed of sheets (unit layers) of tetrahedrally coordinated Si^{4+} and octahedrally Al^{3+} which are covalently bonded by oxygen atoms (Velde and Druc 1998). Figure 3.3 shows such a chemical structure with two kaolinite unit layers.

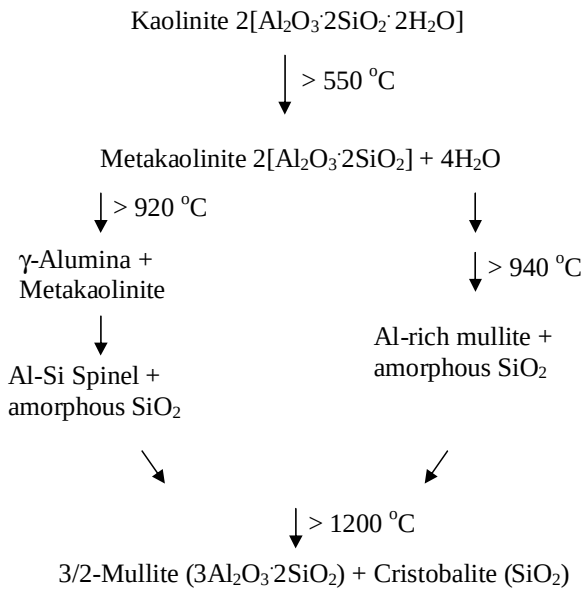

Figure 3.4: The phase transformation of kaolinite to mullite as proposed by Lee et al. (1999).

In addition to the clay minerals, other associated minerals, such as quartz, are usually present in a ceramic depending on the degree of weathering and processes of deposition (see Figure 3.3). Of course, the mineral suite present in a clay is representative of the parent rocks. The identification of these minerals, through chemical and petrographic means, can be used to identify possible geological origins of the clay and, hopefully, a geographic provenance (see chapter 4 for more on provenance). Of greatest importance here, the presence or absence of certain minerals in a ceramic fabric can alter the melting characteristics of a glaze. Furthermore, prior to the application of a glaze, the heat treatment of a clay (*i.e.*, biscuit firing) may alter the chemistry of the mineral suite thereby impeding chemical interaction between a glaze and ceramic as has been demonstrated by Molera et al. (2001).

To illustrate some of the changes that take place when a ceramic mineral is heated, kaolinite is used as an example. The transformations that kaolinite undergo are outlined in Figure 3.4. This diagram shows that above 550 ℃ kaolinite dehydroxylates to form metakaolinite (Lee et al. 1999). At the beginning of this reaction, the inner hydroxyl groups associated with the tetrahedral SiO_4 sheet remain intact whereas

the more reactive outer hydroxyl groups of the $Al(O,OH)_6$ sheet dissociate thereby collapsing this structure. Starting at 920 ℃, the collapsed alumina sheet transforms into γ-alumina concurrent with the formation of a spinel-type phase (Brindley and Nakahira 1959). Above 940 ℃, an alumina rich mullite phase has been recently elucidated by Lee et al. (1999). Both the spinel and mullite phases that occur simultaneously are accompanied by the further dehydration and thermal degradation of the SiO_4 sheet which transforms into an amorphous SiO_2 shell (Chakraborty and Ghosh 1978). The amorphous SiO_2 phase often appears in XRD traces as a broad peak centered between the region of 2.4-3 2Θ (for example see XRD traces shown in Figure 3.14).

Outlining the above kaolinite-mullite reaction series highlights a central issue in this thesis: how do PbO and $PbSiO_2$ react with clay minerals (sheet silicates) to form glazes. For instance, are different chemistries and microstructural features observed when using a fired ceramic as opposed to an unfired ceramic as a glaze substrate? Also, with a fired ceramic, is the first glass liquid formed out of the interaction between Pb^{2+} and the amorphous phases of metakaolinite, or is Pb^{2+} solely reacting with primary quartz inclusions in the ceramic matrix? The answers to these questions provide the chemical and microstructural criteria necessary to differentiate methods of glazing in the archaeological record. The next sections examine these questions in detail using the work of Molera (1996) as a starting point.

3.3 Interactions between Lead Glasses and Ceramics: Previous Experimental Work

The reactions of high-lead glasses with earthenware ceramics have been given their most thorough treatment by Molera (1996) during her thesis work at the University of Barcelona. As is widely known by contemporary potters, lead and lead glass

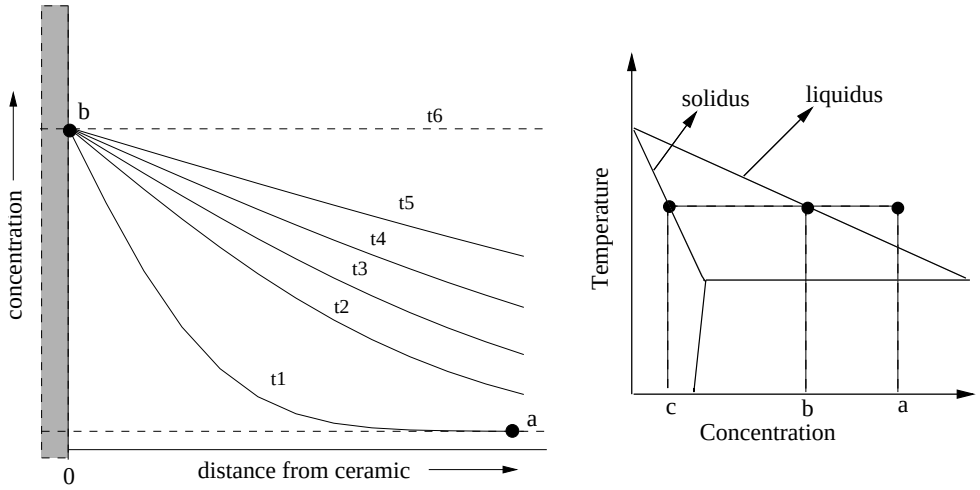

Figure 3.5: Isothermal one dimensional diffusion. When a silicate liquid (point a on the theoretical phase diagram, right hand image) comes into contact with a ceramic (point c) a liquidus, or melting composition, forms that is unique to that temperature. The dissolved component b then diffuses following the structure schematized in the diffusion curves above until the flat profile t6 is reached.

react with clay minerals causing the decomposition of the ceramic body. In turn, elements of the ceramic will diffuse through the glaze melt to different penetration depths. Archaeometric work before Molera, however, had never fully considered these reactions between the glazing mixtures and ceramic substrates.

In this section, the work of Molera, which comprised the first study to put these well-known glaze forming phenomena onto scientific footings, is considered. Also, a number of areas in Molera's study are identified as subjects upon which to draw and expand in a further experimental program. To begin with, however, Molera's work is placed in its proper context by providing a short introduction on diffusion.

3.3.1 Diffusion

The process of diffusion is illustrated by Figure 3.5 which shows the diffusion of a single element at stepped time intervals (t1, t2, *etc.*). The model presented in this figure is built on the case of one-dimensional diffusion in which the ceramic (represented in grey and with a composition denoted by point **c**) is considered to be a heterogenous crystalline slab which comes into contact with a multicomponent silicate melt at $t = 0$ (Crank 1975). Under isothermal and isobaric conditions, a liquidus

composition (point **b** in Figure 3.5) will quickly develop at the melt/ crystalline slab interface that is different from the bulk melt (point **a**). This new interface liquidus will allow the solid to dissolve until a condition of localized saturation is reached. The rate at which the slab can dissolve further depends on how quickly material is transferred away from the liquidus boundary into the bulk melt via diffusion. It has been found that this reaction can be described through a modified form of Fick's second law of diffusion (see equation B.1 in appendix 2; see this section in general for a more thorough and quantitative discussion of diffusion relevant to this thesis). The driving force of Fickian diffusion is a chemical gradient. In the case presented here, the gradient is equal to the difference between points **a** and **b**. When point **a** equals point **b** (curve t6 in Figure 3.5) equilibrium is achieved.

3.3.2 Reaction-Diffusion

Dissolution and diffusion of the ceramic body into a glaze melt is a critical issue in reconstructing glaze raw materials. Indeed, an assessment of the original glaze composition requires that the extent and nature of reaction between the ceramic and glaze is characterized. This fact provided the impetus for Molera's thesis which reconstructed the composition of lead glazes of Islamic and Mudejar ceramics excavated from the sites of San Nicolás and Paterna in Spain (Molera 1996). A sample of her more critical experimental results, namely those which illustrate the reaction-diffusion mechanism, may be seen in Figure 3.6 (Molera et al. 2001). These profiles show the progression of ceramic digestion with a sequence of temperatures (750℃, 850℃, and 950℃) followed by an immediate quench in water. For these diffusion experiments, a glaze powder made of 75 wt%[1] PbO and 25 wt% SiO_2 (70 wt% Pb, 12 wt% Si and 19 wt% O as shown in plots) was applied to green-bodied ("raw") kaolin-rich ceramics which also contained a significant amount of quartz. This glaze composition was selected since

[1] All percentages in this thesis are reported as the oxide weight unless otherwise noted.

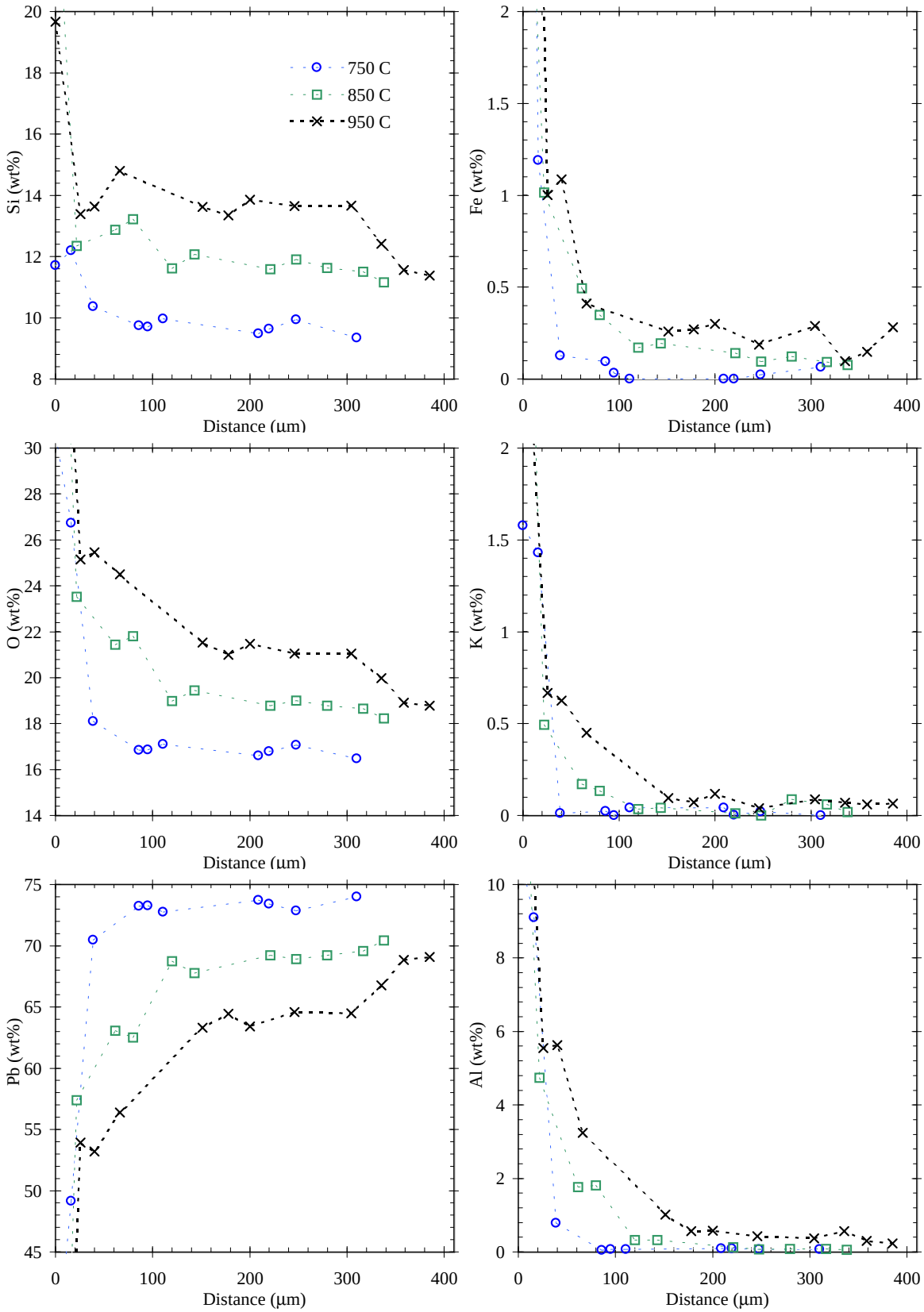

Figure 3.6: Compositional profiles produced from glaze powders with a 75/25 wt% PbO-SiO_2 composition applied over raw kaolinitic clay bodies. The firing ramps were 150°C/h with dwell times of 0 hours followed by a fast cooling by quenching in water (Molera et al. 2001).

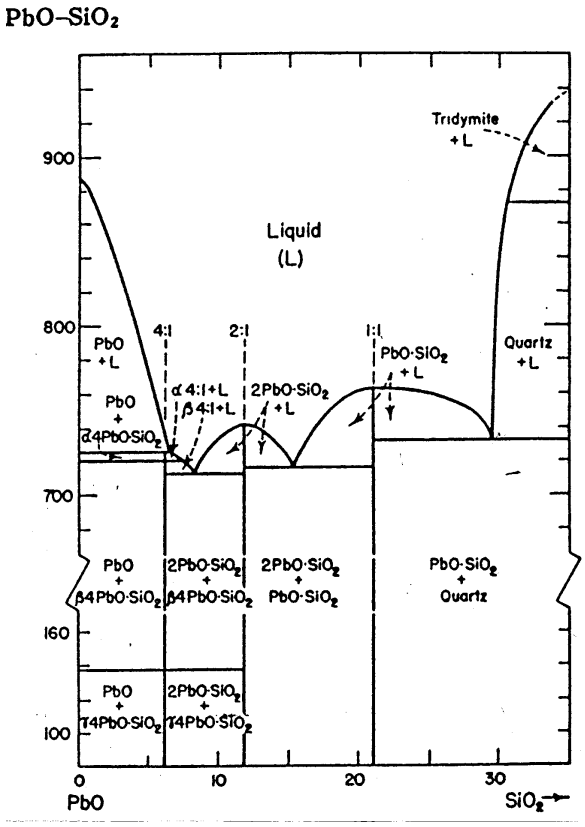

Figure 3.7: The system PbO-SiO_2 (Geller and Bunting 1943). The silica rich eutectic melt temperature is predicted to be 732°C.

it was hypoeutectic (to the left of the eutectic) with respect to the 30% SiO_2 eutectic seen in the PbO-SiO_2 phase diagram (see Figure 3.7). Since this glass composition was designed to be silica poor, it provided an opportunity to examine the temperature induced changes to the melt composition in the presence of a quartz rich ceramic. It was expected that the ceramic would act as a chemical buffer introducing SiO_2 into the melt until the eutectic composition was reached (70 wt% PbO and 30 wt% SiO_2).

Considering these ceramics were immediately quenched after reaching their maturing temperature, the profiles presented in Figure 3.6 represent conditions far from an equilibrium state. Therefore, this means that the diffusive processes and interfacial crystallization in these samples were suppressed allowing for an unobstructed examination of both the chemical gradients present, and the liquidus composition formed

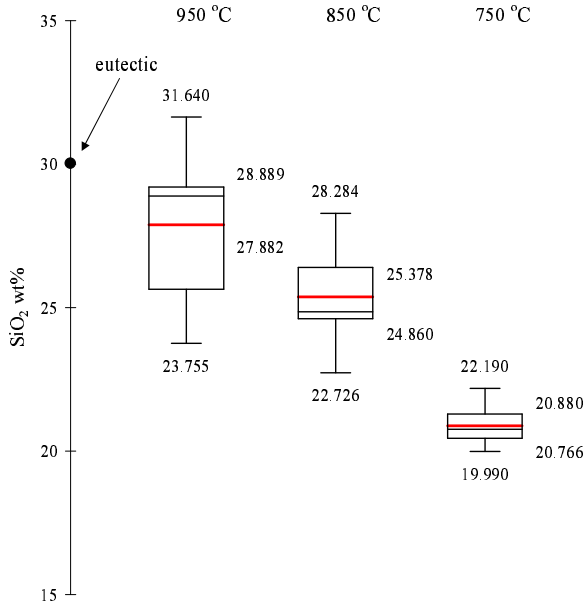

Figure 3.8: Univariate box plots showing change in SiO_2 glaze composition with respect to temperature as the glaze reacts with a kaolin rich ceramic. The red line is the arithmetic mean, the black line is the median, the box encompasses the 25th and 75th percentile confidence levels, and the error bars show the high and low values. The difference between the high and low values is equal to the chemical gradient in which the high values represent, to best approximation, the liquidus compositions at the ceramic interface.

at the ceramic/glaze interface (at distance = 0μm). The overall reaction between the glaze and ceramic is best summarized by a close examination of the Si compositional profiles. The data from these profiles are presented in a condensed form as univariate box plots in Figure 3.8.

At 750℃ the glaze remains incompletely reacted (see Figure 3.9, image A, with remaining quartz grains) causing the average Si composition to be 5% lower than designed. However, already at this low temperature, a small compositional gradient exists. By 850℃ the bulk of the glaze has melted (25 wt% SiO_2). Finally, once 950℃ has been reached, the bulk composition has become richer in SiO_2 (28 wt% SiO_2). What may be immediately gleaned from these data, and is especially clear in Figure 3.8, is that with temperature, the liquidus composition is driven toward the SiO_2-PbO eutectic. Therefore these plots confirm that the ceramic provides a SiO_2 buffer which drives the composition of the glaze toward the predicted eutectic point.

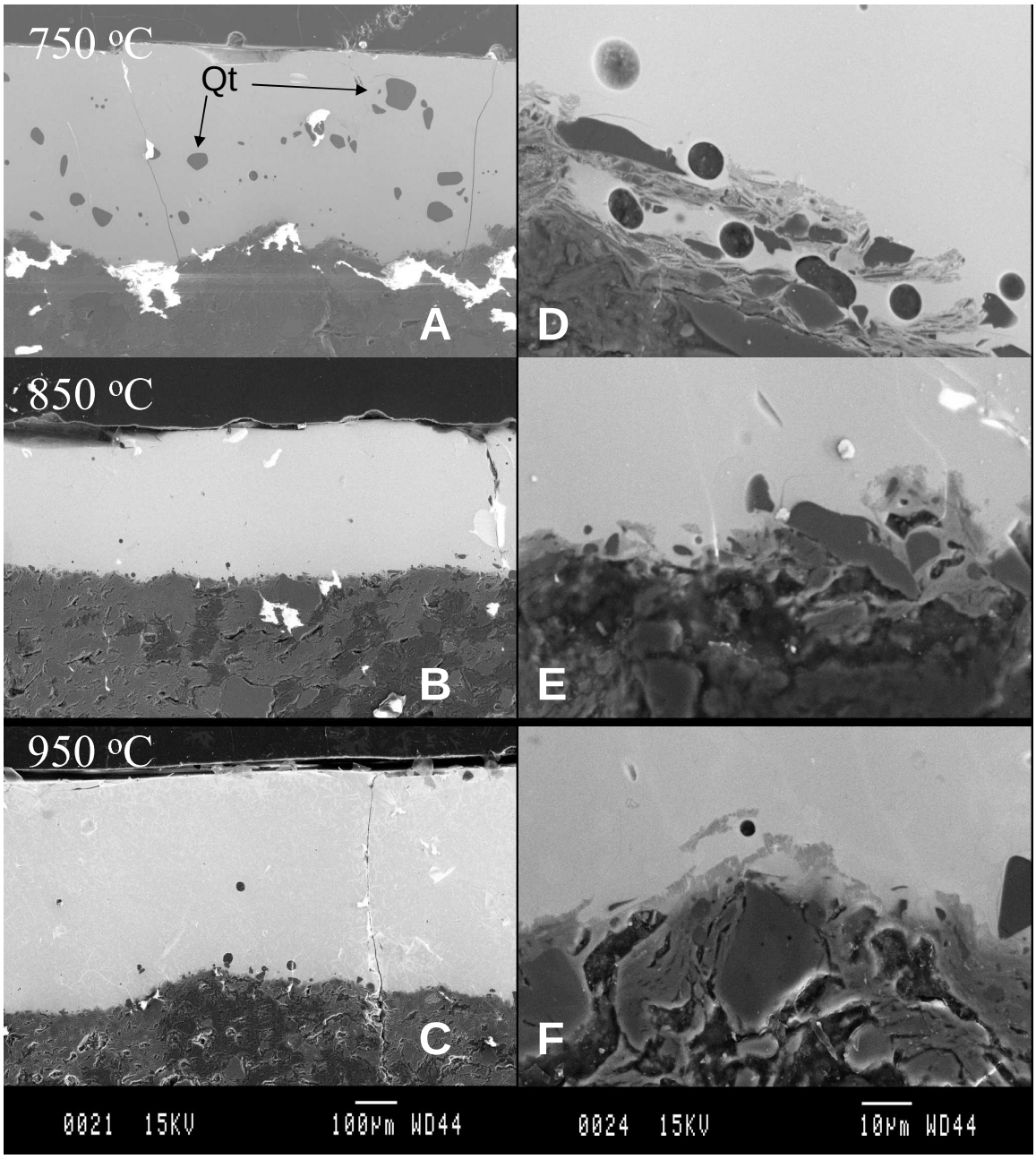

Figure 3.9: Backscatter electron images of the 75/25 wt% PbO-SiO_2 glaze compositions placed over raw kaolin rich clay bodies. The images correspond to the compositional profiles found in Figure 3.6. Images A-C are general views (100x magnification) of the glaze cross-sections heated at 750-950℃. Images D-F are close-up views (1200x magnification) of the glaze/ceramic interface. Note the unreacted quartz in image A marked by arrows. All images are reproduced from Molera et al. (2001).

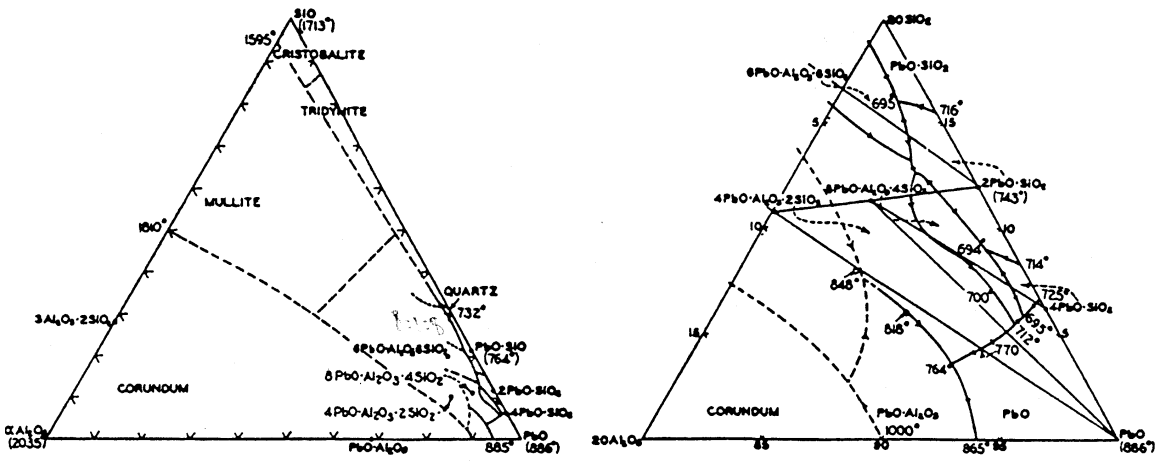

Figure 3.10: The System PbO-SiO_2-Al_2O_3 (Geller and Bunting 1943)

An equally notable feature of these curves is the rapidity of change in the liquidus composition. The diffusion of Si into the glaze accounts for the most significant alteration to the glaze chemistry with an approximate increase from 17 to 21 atomic wt%. The relative quickness of Si diffusion is testimony to the aggressive reactivity of Pb with Si. This reactivity is again predicted by the PbO-SiO_2 phase diagram. In the presence of excess quartz, the SiO_2 in a lead-silicate melt increases rapidly with temperature following a shallow liquidus. However, as may be seen in the remainder of the curves in Figure 3.6, the diffusion of other elements associated with the ceramic, such as Al, Fe, and K, is certainly more sluggish. It may be tempting to interpret this finding as a consequence of the slow diffusivity associated with these elements in a high viscosity melt, but it is more likely that the glaze was reacting preferentially with the quartz present in the ceramic body instead of with the clay minerals (see section 3.4.1.4 for experimental evidence and explanation).

Alternatively, the low Al, Fe, and K values could also be accounted for by the crystallization at the ceramic interface of sanidine-like feldspars that have a general structure of $KAlSi_3O_8$. In a lead silicate liquid, these crystals commonly form in equilibrium to the melt resulting in feldspars with a (K,Pb)$AlSi_3O_8$ structure, where K and Pb are end members of a solid solution (Molera et al. 1993; Scheel 1972;

Tribaudino et al. 1998). In addition to these main elements, Molera (1996) has also shown that small amounts of Fe and Ca can also be incorporated into empty spaces in the crystal structure. Furthermore, in the high Al conditions of lead silicate glasses in contact with mixed alumina zirconia silica (AZS) refractories, Hilger et al. (1981) found similar crystals near the composition of kaliophilite (38% SiO_2, 30% K_2O, and 32% Al_2O_3). The consensus in the literature is that these crystals form readily on cooling in lead silicate glasses as a mechanism to lower the free energy in the system. In terms of a phase diagram (see Figure 3.10 for some of the crystalline phases formed in PbO-SiO_2-Al_2O_3 compositional space), crystallization is necessary for maintaining the allowed liquidus composition. Since the crystals form by reverse diffusion (*i.e.*, in the opposite direction of the main chemical gradient), this significant gradient can rob Al, Fe, and K from the bulk melt composition. Although an examination of the backscatter electron images of the glaze/ceramic interface in Figure 3.9 (images D-F) does not show any significant crystallization, this is likely due to their rapid firing and quenching treatment. Therefore, crystallization does not play a role in the diffusive processes of these particular melts which underscores the suggestion that the low levels of Al, Fe, and K are caused by a lack of reaction between the glazing materials and the clay minerals.

Despite their absence in Figure 3.9, these lead feldspars are common features found in lead glazes. They are important for the purposes of microstructural characterization of glazes formed from PbO or PbO·SiO_2 mixtures that come into contact with refractory materials (see Figure 3.11 for a representative image of how they appear in an archaeological glaze). As both the temperature of the melt and dwell time increase, the fringe of crystals becomes thicker (as will be seen in Figure 3.16 of section 3.4.1.2, this series of images provides a good example of the development of the so-called "interaction zone"). As shown by Molera et al. (2001) this development of the fringe is also heavily influenced by the cooling rate and cooling duration. This is exemplified

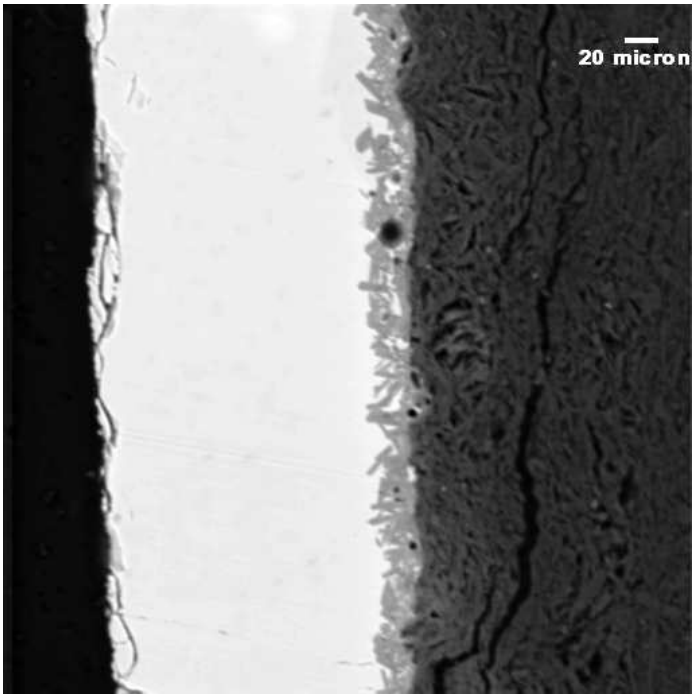

Figure 3.11: Backscatter electron image of a Roman archaeological glaze showing typical Pb-feldspar crystals forming the so-called "interaction zone" (shown by medium grey contrast tones) at the interface between the ceramic and the glaze. See sample D5571 in appendix 3 for additional information on this particular glaze.

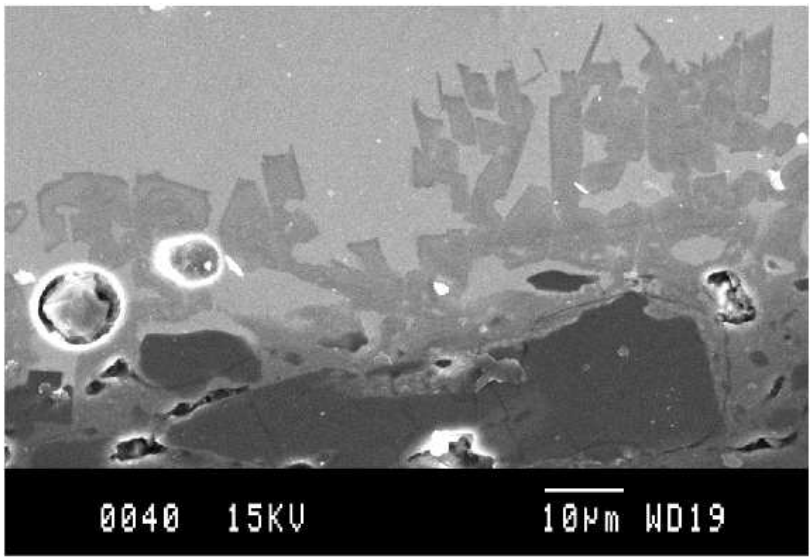

Figure 3.12: Backscatter electron image showing a Pb-feldspar fringe at 1200x at the interface between a kaolin rich ceramic and 75/25 lead silicate glaze. The glaze was fired to 1000 ℃ with a dwell of 0 hours and cooled at a rate 20 ℃/hr (Molera et al. 2001).

by the glaze shown in Figure 3.12. This fringe was produced using the same starting materials as the glazes shown in Figure 3.9, but under different firing conditions. Instead of being immediately quenched after being brought to temperature (1000 ℃ in this case), the glaze was cooled at a controlled rate of 20 ℃/hr.

3.3.3 Summary of Previous work

Molera's work was the first to characterize the reactions of lead silicate melts with earthenware ceramics. Specifically, it was found that silica from the ceramic body was readily incorporated into the melt via diffusion. Moreover, it was discovered that the chemical changes that took place in the melt obeyed the PbO-SiO_2 phase diagram and were not significantly influenced by dissolution of other elements associated with the ceramic substrate. Finally, on cooling, lead-potassium feldspars were seen to form at the interface between the ceramic body and the glaze. It was determined that the size and number of these crystals depended on the dwell time of melt and the cooling rate.

The studies summarized above have focused, predominately, on the reactions of lead silicate glasses in contact with unfired ceramic bodies. Molera choose to limit her research to these two variables for the reason that the study was designed to assess the particular technology of Medieval glazed ceramics from Northeast Spain. The archaeological evidence for these wares suggested that the glazing materials were pre-fritted lead glasses and that the ceramics were unfired prior to glazing. Both of these features of fabrication were confirmed by the analyses performed by Molera. The archaeology of Roman lead glazes, however, is quite unlike that of these Medieval wares. Most significantly, Roman lead glazes have bodies that seem to have been fired prior to glaze application (Atik 1995). Also, as will be explained later in Chapter 5, the majority of the Roman glazes used PbO (most likely in the form of litharge) as the sole glazing compound. For these reasons, the experimental program in the next

section was implemented.

3.4 Experimental Program

It is a common technique among contemporary potters to produce glazes by applying PbO alone to ceramic substrates. However, the chemistry behind this reaction has not, as of yet, been studied. In this section, the reactions between PbO and a commercially available kaolin-rich clay – prepared as both fired and unfired substrates – were studied to develop the criteria necessary to differentiate this technique from glazing with either a lead silicate mixture or frit. As secondary considerations, it was the aim to clarify 1) the temperature range in which a glaze will first occur with PbO, 2) the mechanism by which the first glaze liquid forms, 3) to understand the effects of crystallization on the melt composition, and 4) to determine the length of time required to obtain equilibrium in such melts. These experiments are presented in section 3.4.1.

Building upon the substantial experimental data provided by Molera et al. (2001), firing experiments were also conducted using $PbO{\cdot}SiO_2$ mixtures applied to a biscuit fired ceramics produced from a British Gault which was relatively poor in quartz (section 3.4.2). It was desirable to understand how these mixtures differed chemically and micro-structurally from using PbO alone. Also, by assessing these data, it was hoped that a mechanism of glaze formation using these materials could be elucidated.

3.4.1 Reactions between PbO and Ceramic

3.4.1.1 Experimental

To prepare the ceramic substrate, a commercially available "red" kaolin rich clay (clay #1137 supplied by Potclays Ltd., Stoke-on-Trent, UK) was pressed into disc shaped moulds with diameters of 3.5cm and 1cm thick. The clay discs were subsequently removed from the moulds and dried to a green body stage. Several of these green

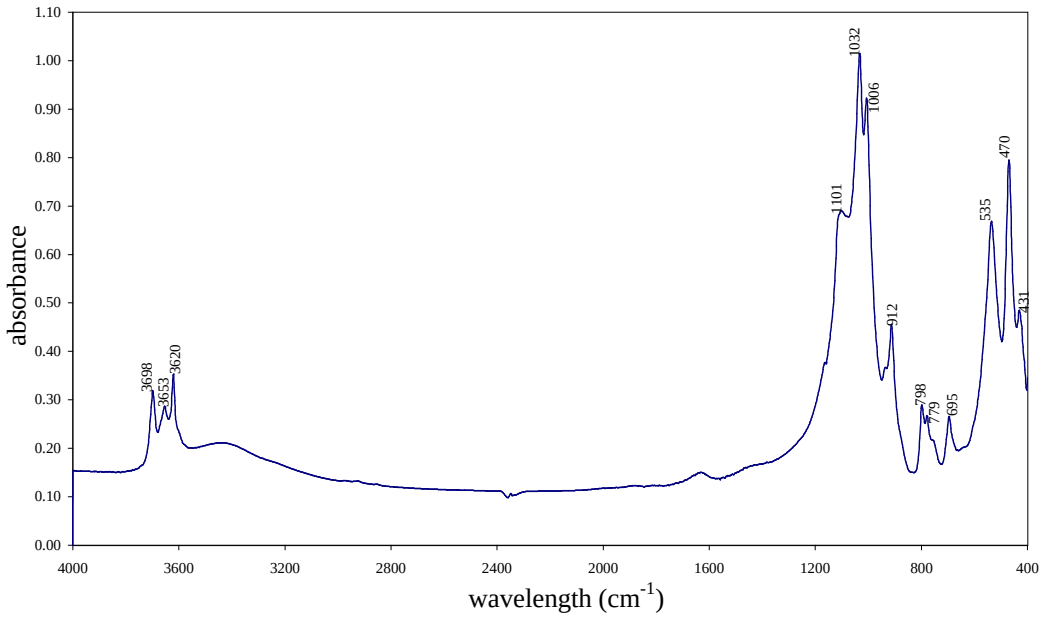

Figure 3.13: FTIR Spectra of Potclays Standard Red Clay #1137. Spectral bands show that the clay is composed almost entirely of kaolinite. The three sharp high frequency bands at 3698, 3653, and 3620 cm^{-1} are particularly diagnostic since these hydroxyl groups absorptions are specific to the hydrated interlayers of the dioctrahedral mineral.

body clay discs were set aside to serve as the "raw" clay substrates in subsequent experiments. The remainder of the disks were muffle fired to 900°C with dwell times of 2 hours at temperature.

Characterization of Clay Mineralogy and Chemistry. Basic characterization of Standard Red clay #1137 was performed previously by Paynter (2001). Paynter identified the chemistry of the clay and made simple morphological observations using reflected light microscopy which showed that it was fine grained and homogenous. A more thorough characterization was performed here using Fourier transform infrared microscopy (FTIR), x-ray diffraction (XRD), and inductively coupled plasma atomic emssion spectroscopy (ICP-AES). FTIR spectra were collected on a Nicolet Magna-IR 550 bench using a standard transmission technique with the sample dispersed in a KBr pellet formed under pressure. XRD traces were obtained on a Philips PW-1710 diffractometer in the Department of Materials Science. Spectra were collected with a Cu-Kα_1 radiation source operating in the Θ–2Θ mode. The

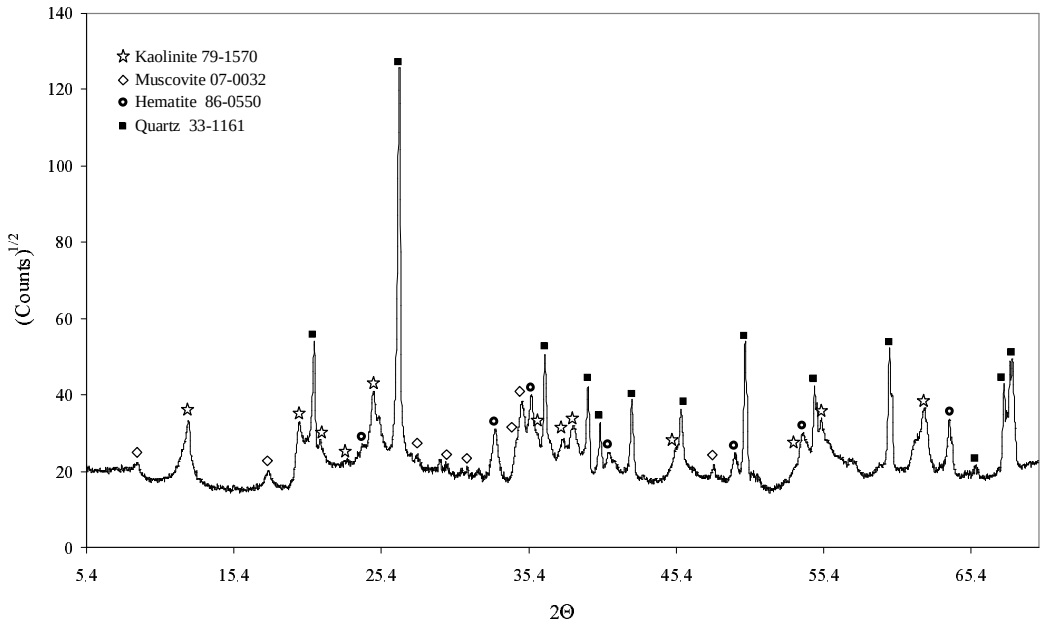

Figure 3.14: XRD trace of Potclays Standard Red Clay #1137. The major mineralogical phases were determined by fitting the spectra with JCPDF files. These phases, which are marked in the trace, are kaolinite, muscovite, hematite, and quartz.

data obtained from these scans was compared to know literature spectra found in the Powder Diffraction Data File (JCPDF). The oxide composition of the fired clay was determined by ICP-AES as outlined in appendix 1.

The FTIR spectra shown in Figure 3.13 demonstrates that the clay is composed predominantly of kaolinite. The diagnostic high frequency triplet of bands associated with the interlayer hydroxyl vibrations is clear in this spectra with positions centered at 3698, 3653, and 3620 cm^{-1} (Farmer 1974). The XRD trace shown in Figure 3.14 confirmed the identity of kaolinite as a main phase along with muscovite, hematite (intentionally added as a colourant), and quartz.

An XRD spectrum was also collected on clay fired to 900℃ (Figure 3.15) to identify the mineral phases formed after dehydroxylation (between approximately 550-800℃ depending on the mineral). As expected, the main clay mineral transformed into metakaolinite and a metakaolinite-like spinel phase where K is substituted into the structure ($KAl_3Si_3O_{11}$). Also, two new phases were revealed: diopside ($CaMg(SiO_3)_2$) and anatase (TiO_2).

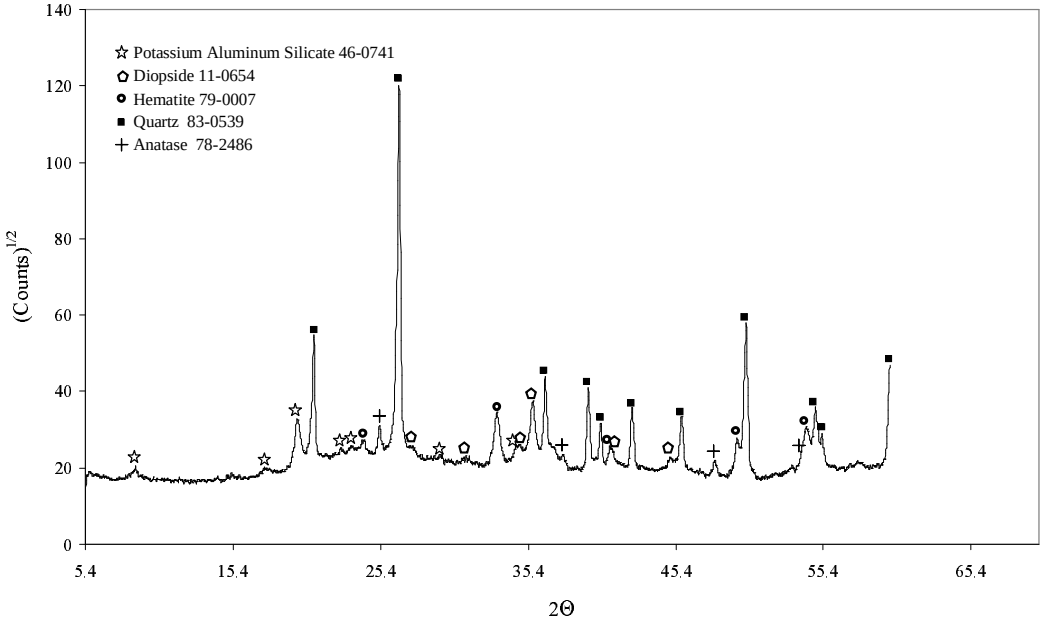

Figure 3.15: XRD trace of Potclays Standard Red Clay #1137 fired to 900 ℃. The major mineralogical phases marked in the trace are $KAl_3Si_3O_{11}$, $CaMg(SiO_3)_2$, hematite, and quartz. Minor amounts of anatase were also detected. Note that the scan was stopped prematurely at a position of 60° 2Θ.

	Na_2O	MgO	Al_2O_3	SiO_2	K_2O	CaO	Fe_2O_3	TiO_2	% of Phase
Red Clay	0.10	0.89	21.92	65.05	2.01	0.70	8.19	1.14	
$KAl_3Si_3O_{11}$			6.53	7.69	2.01				16.23
Metakaolinite			15.39	18.14					33.53
Hematite							8.19		8.19
Anatase								1.14	1.14
Diopside		0.50		1.50		0.70			2.70
Quartz				37.72					37.72
Total	0.00	0.50	21.92	65.05	2.01	0.70	8.19	1.14	99.51

Table 3.2: Chemical composition of a fired sample (900 ℃) of Potclays Standard Red clay #1137 as determined by ICP-AES. Together with the chemistry of the red clay, a budget of each mineral phase (as determined by XRD, see Figure 3.15) which contributes to the bulk clay total is also presented.

The chemical composition of the fired clay is presented in Table 3.2 along with the percentage of each mineral phase that contributes to the bulk oxide total. This mineralogical budget was produced by converting the individual mineral compositions to their constituent oxide parts. Once reduced to oxide compositions, these phases were then fitted to the bulk clay composition by adjusting each of the mineral totals by means of iterative least squaring. As may be seen in Table 3.2, the main phases in the clay are the metakaolinite species and quartz, which together account for over 87% of the composition.

Preparation of Ceramic Disks (*see Table 3.3*). One surface of each disk, both fired and unfired, was flattened by lapping with a medium grit silicon carbide paper. To the flattened surfaces of four of the "raw" ceramics (group 1) and eight of the fired ceramics (groups 2 + 5, each group containing four ceramics) a water suspension of AnalaR® grade PbO powder (a mixture of massicot and litharge supplied by BDH Laboratory Supplies, Poole, UK) was applied. To another four fired ceramics, a mixture of "raw" clay and PbO powder was applied to the flattened surface in a ratio of 1 part clay to 7 parts PbO (group 3). A final group of fired ceramics, was brushed with a 1 part clay to 3.5 parts PbO mixture (group 4).

Firing Procedures. To understand changes in glaze chemistry and microstructure that occur with an increase in temperature, ceramics from groups 1-4 were fired in a microprocessor controlled muffle furnace at temperatures of 730℃, 800℃, 900℃, and 1000℃ with ramps of 10℃/minute and dwell times of 3 hours. The ceramics in group 5 were fired at a single temperature of 900℃ at time intervals of 10 minutes, 30 minutes, 1 hour, 6 hours, and 24 hours.

Imaging and Analysis. Mounting and preparation of samples for analysis was performed as prescribed in appendix 1. All backscatter electron imaging was done on the in-house Cameca Su30 SEM. All quantitative analyses of this experimental material were made on the Jeol JXA 8800 Superprobe electron microprobe located

Group	*Clay Substrate*	*Glaze Mixture*	*Presented in Section*
1	"raw"	PbO	3.4.1.2
2	fired	PbO	3.4.1.2
3	fired	7:1 PbO:Clay	3.4.1.2
4	fired	3.5:1 PbO:Clay	3.4.1.2
5	fired	PbO	3.4.1.3

Table 3.3: Preparations of raw materials and section where firing conditions and analysis of the group is discussed. Each group contains four ceramics.

at Materials Science's Begbroke Facility. Each quoted analytical value is the average of, at least, six probe points. Analytical conditions of 15kV, 10nA, and 1 μm beam sizes were used. To ensure the accuracy and precision of the data, a secondary glass standard (DLH1) was analyzed before and after each session on the electron microprobe.

3.4.1.2 Thermally Induced Changes to Glaze Chemistry

The backscatter electron images of the glaze cross-sections corresponding to groups 1-4 can be be seen in Figure 3.16. The composition of these samples, measured at both the glaze-ceramic interface and the glaze edge are compiled in Table 3.4. As discussed later in this section, compositional profiles exhibiting the glaze chemistry across each cross-section in group 2 (PbO on a "fired" substrate) may be seen in Figure 3.19.

The lack of significant chemical and microstructural variation between groups 1-4 becomes apparent when examining the data in Table 3.4 and the backscatter electron images in Figure 3.16. At each temperature, only minor and seemingly random fluctuations in chemistry may be discerned between each group. In examination of the backscatter electron images it can be seen, at any given temperature, that each glaze preparation exhibits similar crystal morphologies and fringe thicknesses. These chemical similarities are presented graphically in Figure 3.17 which compares the temperature induced changes to the interface composition for PbO reacted with fired

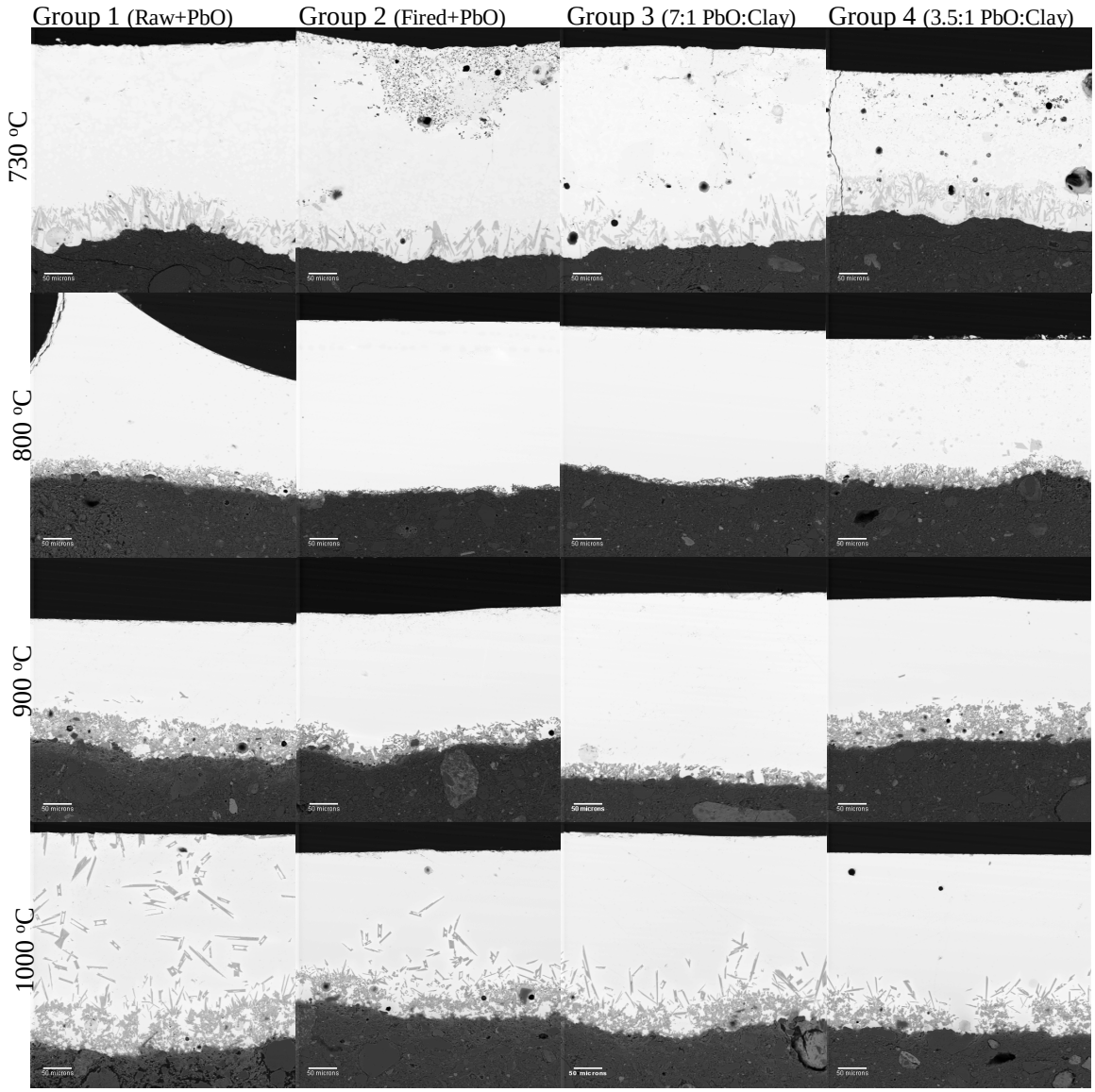

Figure 3.16: Backscatter electron images of glaze cross sections formed from PbO applied to "raw" bodies (Group 1) and to biscuit fired ceramics (900℃) made of Potclay's Standard Red clay #1137. In addition to PbO applied to the ceramic (Group 2), unfired clay was added to two of the preparations in ratios of 7:1 (Group 3) and 3.5:1 (Group 4) lead to clay. All preparations were fired with ramps of 10℃/minute and dwell times of 3 hours at 730℃, 800℃, 900℃, and 1000℃. Samples were fast cooled by quenching in water. The scale bar in the lower–left–hand corner of each image equals 50 μm.

		Interface Composition				**Edge Composition**			
	Groups:	1	2	3	4	1	2	3	4
730℃									
	Na_2O	0.05	0.08	0.04	0.10	0.03	0.04	0.03	0.00
	MgO	0.23	0.30	0.22	0.25	0.13	0.14	0.16	0.04
	Al_2O_3	5.02	3.36	4.71	4.25	5.44	4.65	3.70	4.77
	SiO_2	15.44	22.09	17.24	21.71	11.80	13.11	11.71	10.97
	PbO	76.20	73.20	74.38	71.93	80.94	80.26	82.51	82.47
	K_2O	0.24	0.32	0.22	0.37	0.09	0.15	0.11	0.05
	CaO	0.17	0.27	0.33	0.22	0.07	0.18	0.11	0.06
	FeO	1.83	1.38	1.93	1.35	1.37	1.48	1.31	1.43
	TiO_2	0.27	0.21	0.27	0.16	0.17	0.22	0.17	0.19
	Total	*99.45*	*101.20*	*99.32*	*100.35*	*100.03*	*100.23*	*99.82*	*99.98*
800℃									
	Na_2O	0.07	0.04	0.05	0.08	0.05	0.04	0.03	0.05
	MgO	0.29	0.21	0.23	0.32	0.20	0.21	0.21	0.21
	Al_2O_3	4.59	5.97	6.48	1.99	5.97	5.28	5.55	5.87
	SiO_2	20.45	16.22	17.16	26.28	16.55	14.56	14.64	16.14
	PbO	72.17	75.05	73.96	69.06	74.55	78.15	76.55	75.17
	K_2O	0.44	0.42	0.54	0.49	0.44	0.32	0.30	0.30
	CaO	0.41	0.24	0.20	0.21	0.17	0.16	0.19	0.14
	FeO	1.73	1.77	1.89	1.76	1.94	1.66	1.77	1.90
	TiO_2	0.35	0.28	0.30	0.21	0.33	0.29	0.28	0.37
	Total	*100.49*	*100.22*	*100.82*	*100.39*	*100.21*	*100.67*	*99.52*	*100.15*
900℃									
	Na_2O	0.04	0.05	0.06	0.07	0.03	0.04	0.06	0.06
	MgO	0.34	0.29	0.33	0.32	0.28	0.27	0.24	0.27
	Al_2O_3	6.18	6.05	3.67	5.60	7.29	6.97	6.75	7.25
	SiO_2	24.53	20.25	24.08	29.10	20.67	18.47	18.21	19.62
	PbO	66.74	70.42	69.97	62.38	69.88	70.56	71.81	69.16
	K_2O	0.40	0.38	0.45	0.55	0.47	0.49	0.46	0.38
	CaO	0.26	0.25	0.27	0.34	0.26	0.24	0.21	0.24
	FeO	2.05	2.34	1.84	1.91	2.32	2.21	1.98	2.44
	TiO_2	0.47	0.40	0.34	0.34	0.43	0.45	0.41	0.44
	Total	*101.02*	*100.43*	*101.01*	*100.62*	*101.64*	*99.69*	*100.12*	*99.86*
1000℃									
	Na_2O	0.05	0.11	0.10	0.07	0.04	0.07	0.03	0.06
	MgO	0.43	0.32	0.46	0.34	0.39	0.38	0.34	0.40
	Al_2O_3	7.91	7.66	7.89	7.96	7.66	8.70	8.70	8.91
	SiO_2	31.82	34.89	30.47	32.15	24.51	24.52	24.07	24.98
	PbO	56.71	53.19	58.39	55.54	64.13	63.09	63.16	59.61
	K_2O	0.55	0.87	0.74	0.58	0.33	0.43	0.56	0.46
	CaO	0.87	0.35	0.46	0.41	0.36	0.35	0.31	0.38
	FeO	2.64	2.17	2.01	2.58	2.86	2.83	2.58	3.00
	TiO_2	0.58	0.42	0.37	0.53	0.57	0.51	0.48	0.54
	Total	*101.57*	*99.96*	*100.89*	*100.17*	*100.85*	*100.88*	*100.23*	*98.34*

Table 3.4: Chemical compositions at the interfaces and edges of glazes from groups 1–4. Glazes were formed on Standard Red clay ceramics with PbO at temperatures of 730℃, 800℃, 900℃, and 1000℃. Each of the compositions quoted is an average of six analytical measurements.

and raw ceramic substrates. Furthermore, as is emphasized by the SiO_2-Al_2O_3 binary plot (plot A in Figure 3.18), it would be difficult, if not impossible, to differentiate between any of the original glazing compositions based on an assessment of this chemical data. Furthermore, if these data are linearly regressed (plot B in Figure 3.18), it may be seen that SiO_2 to Al_2O_3 ratio in the glaze (at all temperatures) is the same as this ratio in the body. This suggests that PbO is simply being diluted by body fabric as this digestion reaction proceeds. As will be shown in section 5.1.1 of Chapter 5, this linear relationship between temperature achieved and the amount of body dissolved may be used to calculate the firing temperatures of archaeological sherds.

From these results, it is certain that there is not enough chemical or microstructural resolution to distinguish between the methods of glazing either "raw" or "fired" ceramics with PbO and PbO + clay mixtures. The homogeneity resulting from these different methods of glazing limits the technological interpretation which may be applied to the archaeological material to be discussed in Chapter 5. It should also be noted that these present findings do not contradict those of Molera et al. (2001) who described an increased reactivity when firing a glazing mixture of 75% PbO and 25% SiO_2 with a raw kaolin rich substrate instead of a biscuit fired one. Although this issue will be discussed in depth later when an attempt is made to understand the mechanisms by which these glazes form, it seems as though glazing with PbO alone follows a different reaction path from glazing with $PbO{\cdot}SiO_2$ mixtures.

Despite the similarities described above, considerable information is still available from these glazes. For instance, at 730℃ the glazes are incompletely melted with masses of small crystals scattered throughout the glaze thickness (see Figure 3.16, image of 730℃ group 2 in particular). A sampling of the chemistry of these "edge" crystals/glass assemblages– named as such to differentiate them from the interface fringe– are presented in Table 3.5. The highest atomic number phase (lightest phase

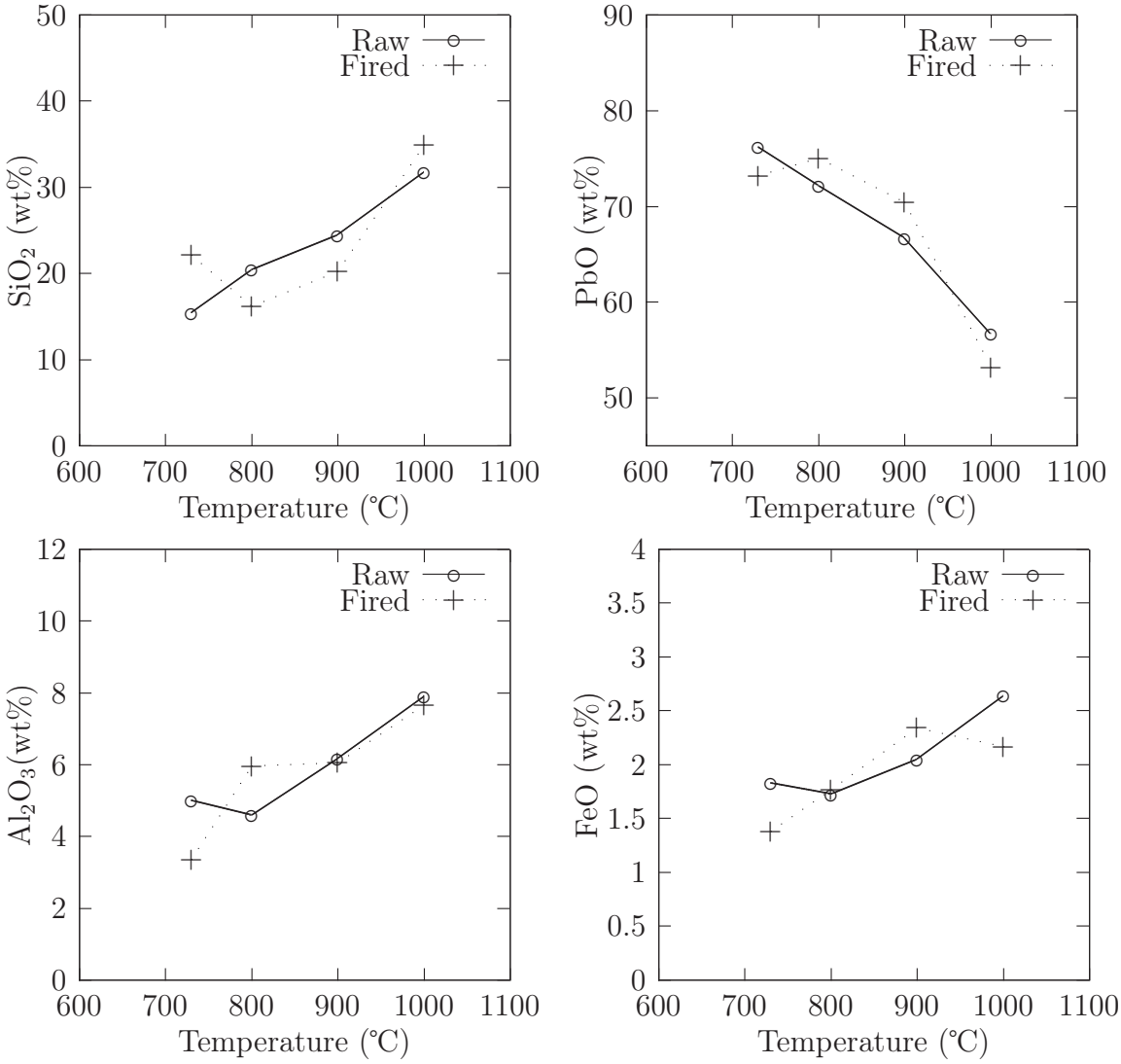

Figure 3.17: Comparison of the temperature induced changes to the interface glaze composition (only abundant oxides, > 1 %) of PbO applied to the surface of "raw" and "fired" ceramic substrates.

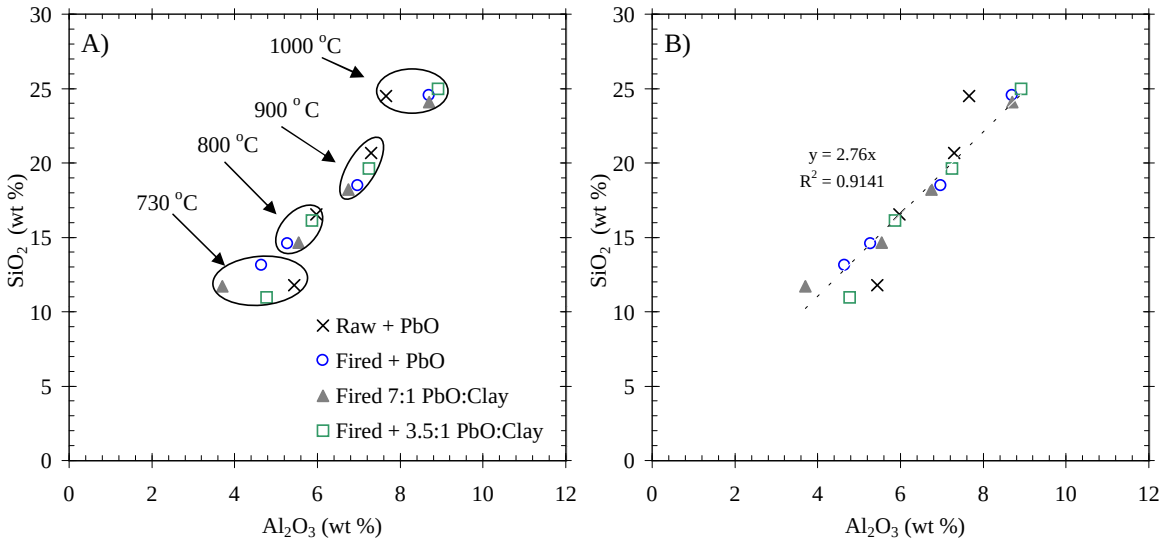

Figure 3.18: Temperature induced changes to glaze composition composed of either PbO or PbO + Clay mixtures on kaolinitic substrates. These data were collected at the glaze edges. Bivariate plots of SiO_2 vs. Al_2O_3 were chosen considering these oxides constitute the main elements of the body. Therefore, they may be used to assess the overall progression of body dissolution in the melt from 730–1000°C as seen in Plot A. Plot B shows a linear regression of the data points. This plot demonstrates that the approximate 1:3 ratio of Al_2O_3 to SiO_2 present in the ceramic is also expressed in the melt composition.

by contrast, labelled "light" in Table 3.5) as assessed by backscatter contrast, is an almost pure high-lead silicate glass with 90% PbO, 6% SiO_2 and the remainder of the composition made up of dissolved hematite and anatase. This high atomic number glass surrounds the darker crystalline phases which are composed of increasing amounts of Al_2O_3 and K_2O with compositions not far from the kaliophilite-like crystals identified by Hilger et al. (1981). This "light" glass phase, that is specifically associated with aggregations of crystals at the glaze edge, is not the same composition as the bulk glass phase at the glaze edge that is presented in Table 3.4.

These masses of crystals are interesting because they represent early melt formations and thereby provide clues on the preliminary stages of the glaze development. It is likely that the first liquid formed on melting is the "light" coloured glass phase. In fact, the PbO-SiO_2 phase diagram (Figure 3.7) predicts that this composition should form at 714°C. Since this glass surrounds the other crystalline phases, it is possible that these dark crystals form in equilibrium with the glass. Alternatively, a more

	Light	**Dark- 1**	**Dark- 2**	**Dark- 3**
Na_2O	0.01	0.02	0.08	0.13
MgO	0.07	0.04	0.08	0.08
Al_2O_3	0.68	8.64	7.15	18.96
SiO_2	6.15	10.92	15.25	25.19
PbO	90.17	80.41	74.05	31.93
K_2O	0.04	0.05	3.92	20.13
CaO	0.01	0.01	0.05	0.00
FeO	2.92	0.49	1.81	0.49
TiO_2	1.13	0.05	0.46	0.02
Total	*101.18*	*100.65*	*102.85*	*97.12*

Table 3.5: Analysis of "edge" crystals formed at 730℃. Points collected on group 2 (PbO applied to fired substrate).

reasonable assumption is that these crystals are non-equilibrium formations resulting from minor reactions between PbO with the metakaolinite species in the ceramic. However, it should be noted that neither the compositions of these phases, nor that of the bulk glaze, correspond to the often quoted 32%SiO_2–61%PbO–7%Al_2O_3 eutectic which would form if the metakaolinite were being digested by the PbO melt.

There are several significant implications of producing a high-lead silicate glass as a primary liquid. First, the presence of this glass phase suggests that PbO is not reacting, at first, with either the metakaolinite or spinel phases in the ceramic, and is instead preferentially reacting with the available quartz. Second, as will be discussed more in depth below, the viscosity of this melt liquid is extremely low which suggests that it is capable penetrating into and flowing through the ceramic pore structure. These observations certainly impact the interpretation placed on the most significant trend observed for these glazes, which is their overall compositional flatness (see Figure 3.19).

As is recognizable in Figure 3.19 there are no significant compositional gradients present in the major element profiles. These high resolution electron microprobe traverses (points taken every 5 μm) of major elements (defined here as abundances $>$1%) were taken across the glazes corresponding to the group 2 images in Figure 3.16 (PbO applied to a fired substrate). Similar to the profiles collected by Molera (shown

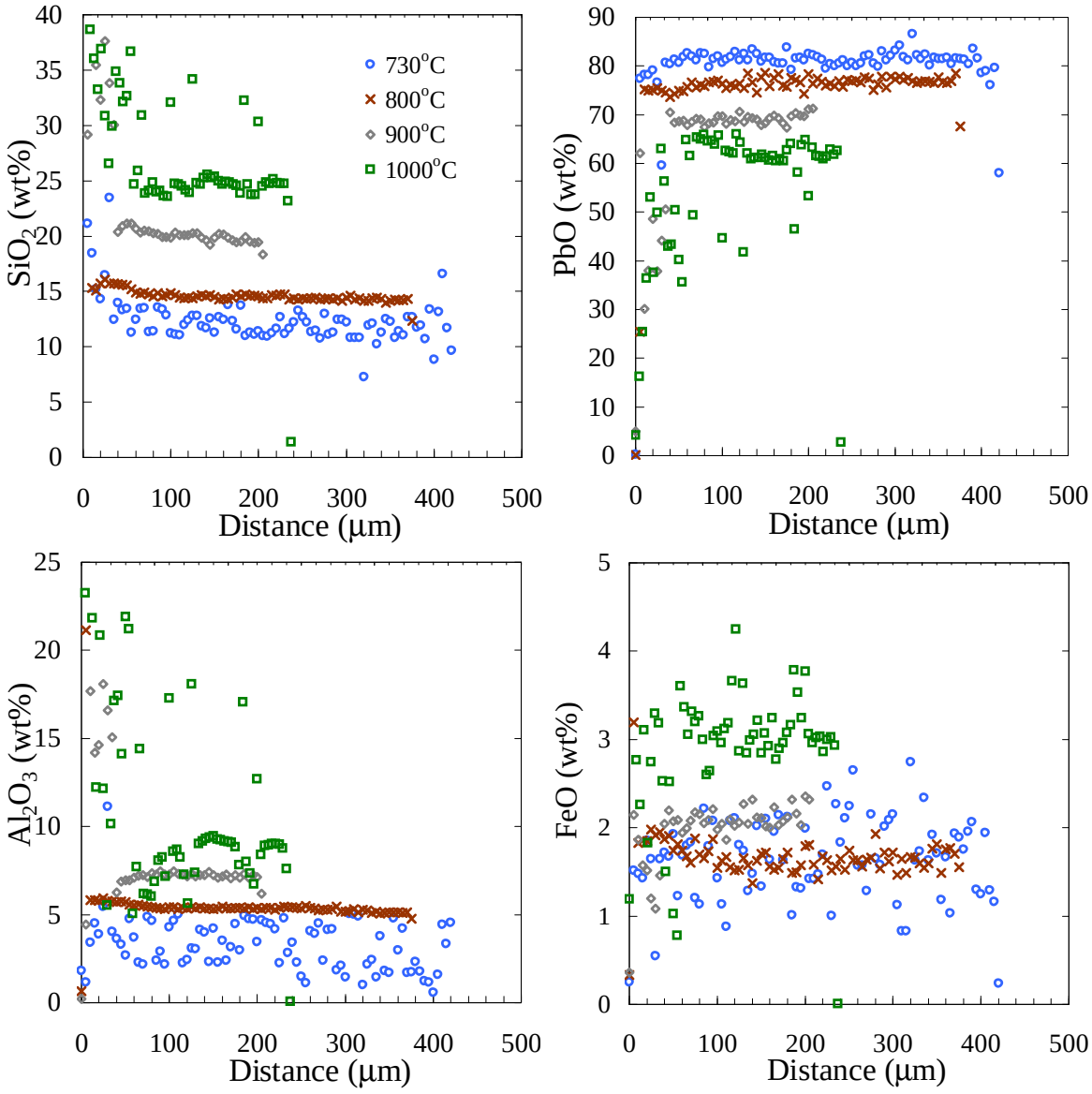

Figure 3.19: High resolution profiles across glazes cross sections formed from PbO applied to fired bodies.

in figure 3.6), 0μm marks the edge of the ceramic and the beginning of the glaze. The gap in contiguous data points between the edge of ceramic and the beginning of the profile, especially in the 900℃ and 1000℃ curves, marks the extent of interface fringe of lead feldspars developed at these temperatures. As may be seen near the ceramic interface, the feldspars crystal formation results in measurements where the weight percent of Al_2O_3 and SiO_2 is increased. In the 1000℃ images (refer to Figure 3.16), it may be seen that these crystals can detach from the interface, float toward the glaze surface and continue to form *in situ*. This process is implied by drops in the Al_2O_3 profile at this temperature, which are caused by diffusion of this element to the crystal from the bulk melt. Also it should be noted that this behaviour in Al_2O_3 results in corresponding spikes in concentration seen in the SiO_2, FeO, and PbO profiles.

As discussed in the introduction to this chapter, one-dimensional diffusion theory dictates that flat compositional profiles are associated with equilibrium conditions. In the profiles presented in Figure 3.19, it appears that these glazes are indeed in equilibrium with the ceramic substrate at each temperature, and, therefore, the average composition of the bulk melt represents a value near the liquidus composition. This is further corroborated by comparison of the interface and edge values presented in Table 3.4 (in particular, see Al_2O_3 values), which show that only shallow gradients are present, if they exist at all.

3.4.1.3 Changes that Occur with Time at a Fixed Temperature

To understand the flat profiles presented above, it was first necessary to find 1) how quickly equilibrium was achieved and 2) the processes by which these conditions were reached. This was accomplished by collecting compositional profiles at 900℃ with dwell times at temperature of 10 minutes, 30 minutes, and 1 hour. These experiments employed the samples from group 5 in Table 3.3 (PbO applied to a fired kaolinitic

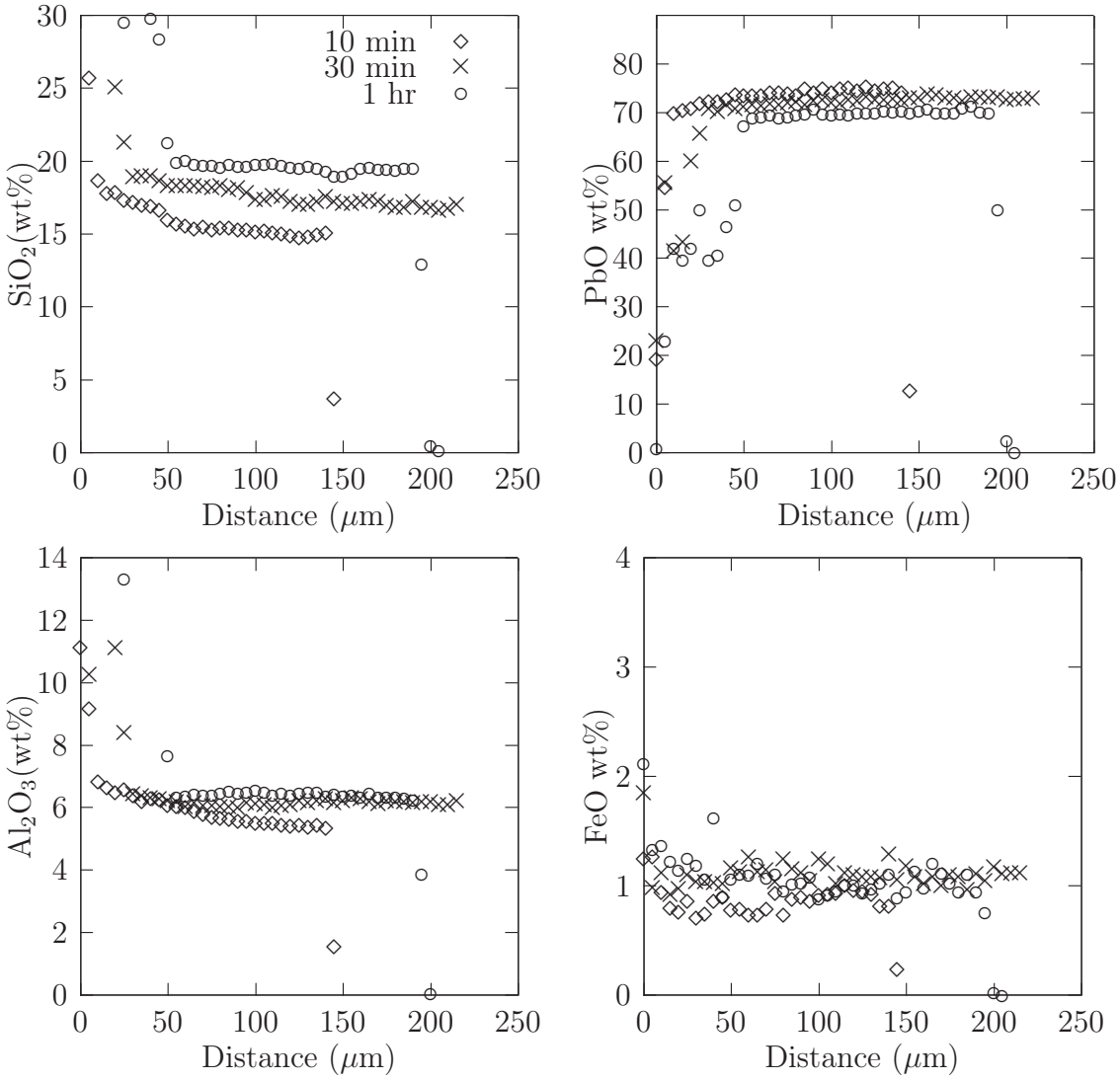

Figure 3.20: Compositional profiles showing the first hour of glaze development at 900℃ with dwell times of intervals of 10 minutes, 30 minutes, and 1 hour.

substrate). Shown in Figure 3.20, are the profiles associated with these three time intervals.

It may be seen in Figure 3.20 that migration of the major elements through the width of the glaze occur rapidly, and equilibrium conditions are achieved within 1 hour. What is most interesting, however, is that the shape of the profiles exhibited at 10 minute and 30 minutes is what one would expected when diffusion dictates mass transfer. To test whether it is at least plausible that the 10 minute and 30 minute profiles were indeed diffusion driven, a modelling approach was adapted. Theoreti-

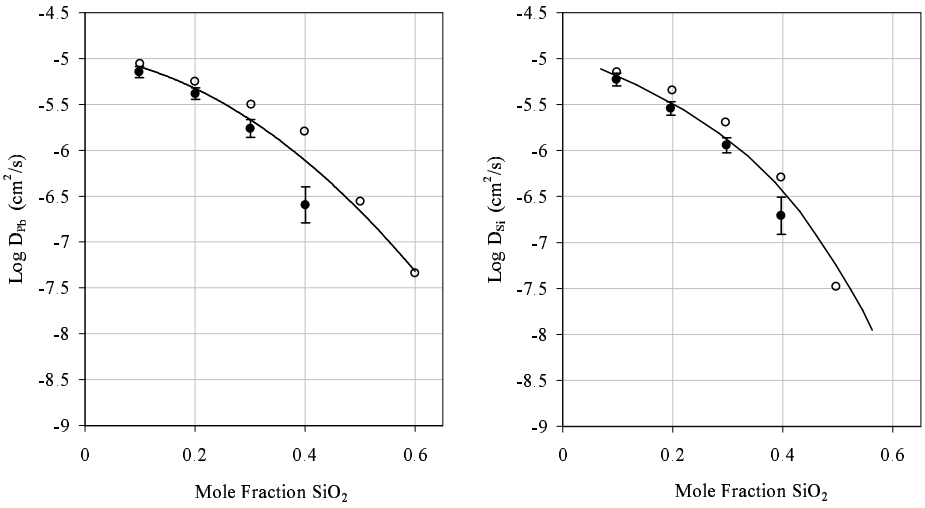

Figure 3.21: Tracer diffusion coefficients of Si and Pb in Pb-SiO_2 at 850°C. Open and closed circles show two separate experiments conducted by Schmalzried et al. (1981) to elucidate the diffusivity of Pb, Si, and O ions in PbO-SiO_2 melts. Line shows the 2^{nd} order polynomial fit to the data (y-intercepts for log D_{Pb}= -4.96 cm^2/s and for log D_{Si}= -5.16 cm^2/s).

cal SiO_2 profiles were modelled using the *EBDC* approach outlined in Appendix B (section B.1.1). As the starting point for this model, the substrate was taken to be a pure quartz slab which was brought into contact with a PbO melt at 850°C. The model was then stepped forward at time intervals of 1 minute, 10 minutes, 1 hour, and 6 hours. The tracer diffusion coefficients collected by Schmalzried et al. (1981) were used for these modelling experiments (see Figure 3.21).

As can be seen in Figure 3.22, SiO_2 can theoretically diffuse rapidly through a PbO melt. By 1 hour, equilibrium conditions are already nearly established. This model, consequently, fits nicely with the experimental observations presented above. Furthermore, if Figure 3.23 is examined, it may seen that the viscosity of PbO-SiO_2 melts is very low when Si values are low as well. For instance, at 850°C a 15% SiO_2 + 85% PbO melt (mole fraction SiO_2 = 0.15) has an approximate viscosity η of 0.039 (in Figure 3.23, this value corresponds to log η = -1.4) For comparison, water at room temperature has an approximate η of 1.0. It can easily be imagined then, as the first liquid is formed by reaction of PbO with SiO_2, it is of sufficiently low viscosity to be

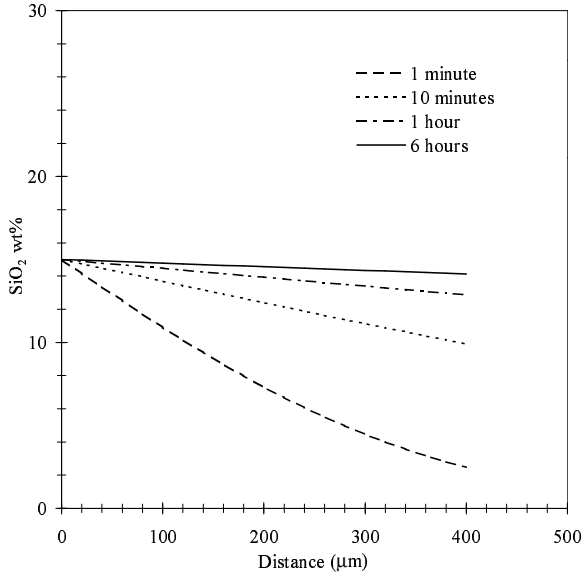

Figure 3.22: Theoretical diffusion of SiO_2 into Molten Pb at 850°C with time intervals of 1 minute, 10 minutes, 1 hour, and 6 hours. The diffusion coefficient for Si in PbO at this temperature ($6.9 \times 10^{-6} cm^2/s$) is from Schmalzried et al. (1981). The liquidus composition at this temperature was estimated to be 15% SiO_2 based on the experimental results presented in Figure 3.19.

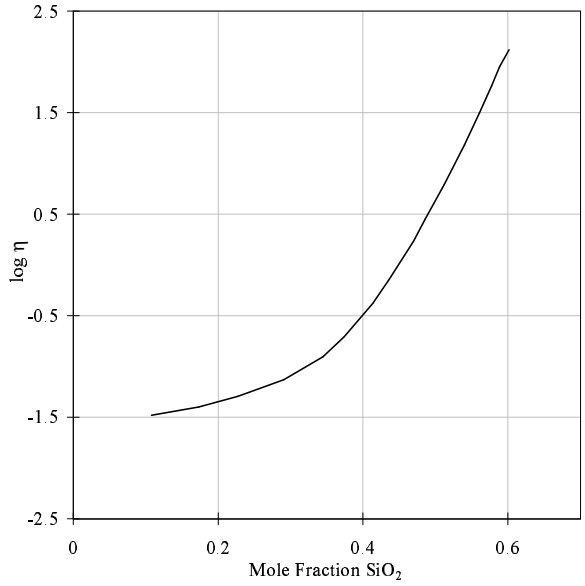

Figure 3.23: Viscosity of PbO-SiO_2 melts as a function of SiO_2 content at 850°C. Plot reproduced from Petusky (1980) from values originally collected by Rita (1976). The viscosity η is expressed as $\frac{N \cdot s}{m^2}$.

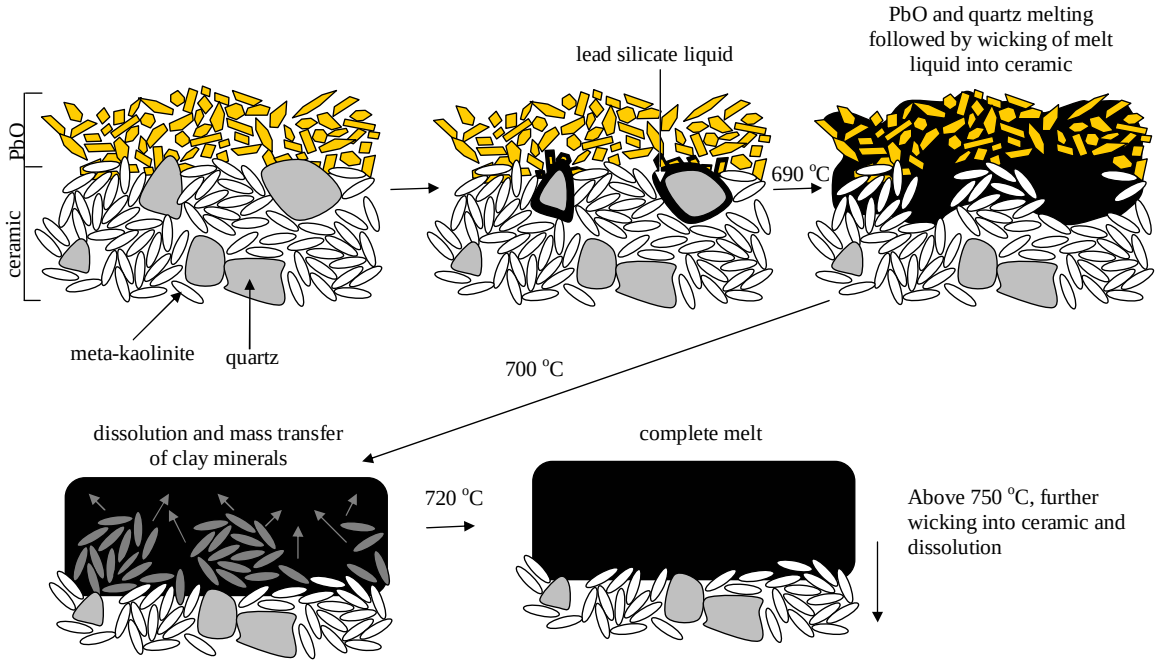

Figure 3.24: Mechanism of glaze formation when using PbO on a fired quartz bearing kaolinitic substrate. The initial liquid (formed by reaction with SiO_2) is wicked into the ceramic and around PbO crystals. The liquid is then absorbed into the body causing digestion of the remainder of the clay minerals.

wicked into the ceramic pore structure and around the remainder of the PbO crystals. The composition of the "light" glass phase shown in Table 3.5 certainly meets this low viscosity criteria having an η of 0.032. Due to processes of wetting, the low viscosity liquid may engulf the remainder of body minerals and, as is shown by the diffusion model, the transfer of the remaining elements into this surrounding liquid is rapid. This hypothesized mechanism of glaze formation is presented in Figure 3.24.

This mechanism of glaze formation requires that PbO reacts, at first, with only quartz grains embedded in the ceramic substrate in order to produce the low viscosity lead silicate liquid. Therefore to verify this hypothesized mechanism, the sequence of reactions leading to the formation of the glaze (*i.e.*, the preferential reaction of quartz with PbO followed by the remainder of the clay minerals) needs to be established. This aspect of the mechanism is explored in the next section 3.4.1.4 using high temperature X-ray diffraction.

3.4.1.4 High Temperature Synchrotron Radiation X-ray Diffraction

An in-situ X-ray diffraction experiment was designed to assess the sequence of reactions that take place between PbO and the kaolinite-based ceramic characterized in section 3.4.1.1. In particular, this work was carried out to elucidate further the mechanism by which a "flat" compositional profile is produced when PbO is applied to a ceramic surface. As discussed above, the role that quartz plays in the formation of the glaze seems to be critical in producing the first lead silicate liquid which is then wicked into the ceramic pore structure thereby incorporating the remainder of the clay minerals. To verify this proposed mechanism, a small furnace containing the ceramic powder and PbO was placed into a high brilliance X-ray beam (90 KeV) with an online image-plate detector located at the European Synchrotron Radiation Facility (ESRF) at Grenoble, France. The use of this setup allowed for high resolution and good signal-to-noise X-ray diffraction measurements to be collected at 1 minute intervals during a temperature ramp of 5℃/minute. This unique experiment allowed for a precise determination of the temperature at which the first ceramic liquid forms on reaction with PbO. Also it served as a check of the eutectic melt temperature originally established by Geller and Bunting (1943).

Experimental. The kaolinitic ceramic was pre-fired at 900℃ for two hours after which it was cooled and ground to a fine powder. The ceramic powder was mixed intimately with AnalaR® grade PbO in a ratio of 50:50 by weight. The resulting ceramic/PbO powder was packed into unsealed corundum tubes with an inner diameter of 0.5mm. The tube was placed into a cylindrical furnace located in the path of a 90 keV synchrotron beamline. Diffraction image patterns were collected on a MAR345 image-plate detector. Beam energy calibration and the beam centering was performed on a silicon standard using fit2D software. After collection of the 2-D image, it was integrated to produced the 2θ data which was fit with JCPDF files to identify the phases (Pradell 2003b). At first, the powder was ramped in the

furnace at 1℃/min until 110℃ to drive off residual water. After this, the ramp rate was increased to 5℃/min until a temperature of 870℃ was reached. X-ray measurements were taken every 14 minutes.

The data set produced from this experiment was large and unwieldy with 51 spectra each containing 2300 data points. To cope with this wealth of data, three approaches to data compression were attempted. First, a region of high spectral resolution, where all the main phases were represented, was chosen to qualitatively assess the temperature induced changes. This was followed by principal component analysis of the entire data set to give a precise temperature estimate of the major melting event. Finally, two dimensional correlation spectroscopy, a relatively new technique most often applied to vibrational spectra, was utilized to enhance spectral resolution and establish phase interactions in a specific region of the data set.

Data Treatment. The X-ray diffraction pattern of the pre-melt powder is presented in Figure 3.25. Most of this diffraction pattern is dominated by peaks from either massicot or the corundum tube. For this reason, after the identity of the main phases had been established, only one highly resolved region was chosen for examination of temperature induced changes. As can be seen in Figure 3.25 all the major phase information may be found in the low angle region of the spectra between 1-2.4 2θ. In this region, the main phases may be represented by peaks found at the following 2θ values: massicot at 1.36, litharge at 1.59, meta-kaolinite at 1.78, quartz at 1.88, a tertiary massicot peak at 1.99, the corundum tube at 2.30, and the main quartz peak at 2.39.

XRD spectra displayed at intervals of every 42℃ may be found in Figure 3.26. This plot of XRD spectra provides an overview of the changes that occur with temperature. From this presentation of data, several important features of the melt sequence may be discerned immediately. In qualitative terms, the litharge peak centered at 1.59 2θ gradually diminishes and disappears completely by 630℃. The massicot peak

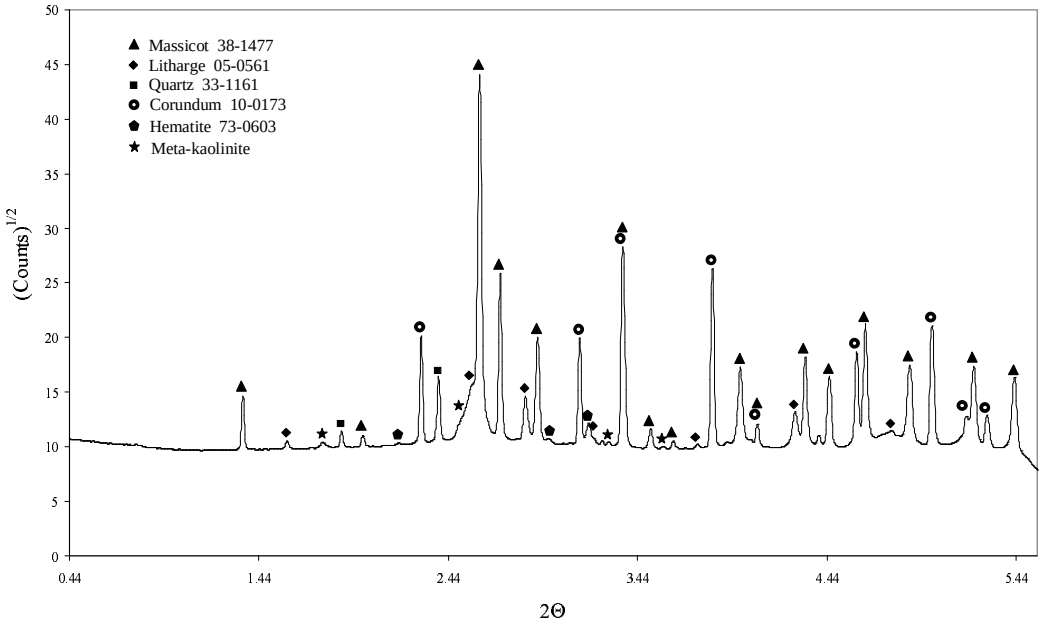

Figure 3.25: Room temperature SR-XRD spectra of pre-melt ceramic/PbO powder. Phases are identified in the spectra. Note that due to the high energy source, 2θ is not the same scale as seen in the conventional X-ray spectra of Figures 3.14 and 3.15.

at 1.36 persists in the melt until the surprisingly high temperature of around 757℃. These events are accompanied by the growth and expansion of disordered phases represented by the broad peak found in the region of 1.5 and 3.5 2θ. These disordered phases are also represented by the broad light coloured regions marked in Figure 3.27 which is an image of the entire X-ray diffraction data set.

To follow these changes in more detail, each of the peaks in the above mentioned region were fitted with gaussian curves using a non-linear least squares technique which was optimized by the solver function in Microsoft Excel (Howard and Cassidy 2000; Harris 1998). This allowed for the identification of the peak positions and intensities with respect to temperature. The recovered intensities were normalized by the peak intensity at 2.9 2θ associated with the corundum holder to produce a qualitative determination of the proportion of each phase present. The use of the corundum holder was chosen as an internal reference since it was an inert component which would not decompose or react with the analyte when brought through the tem-

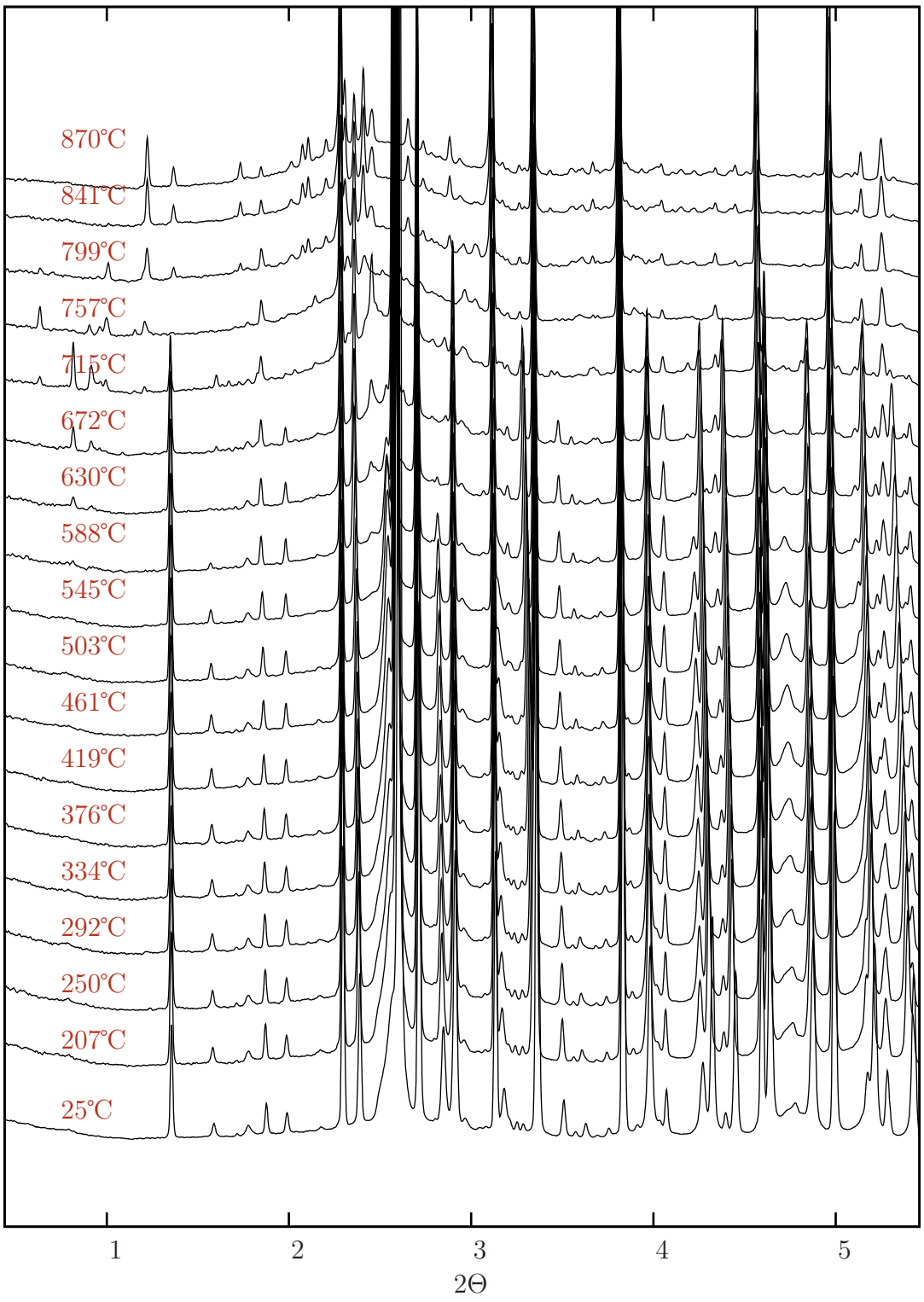

Figure 3.26: High temperature sequence of SR-XRD spectra of 50:50 wt% ratio of PbO and a pre-fired at 900°C "red clay" ceramic (see Table 3.2 for clay composition)

.

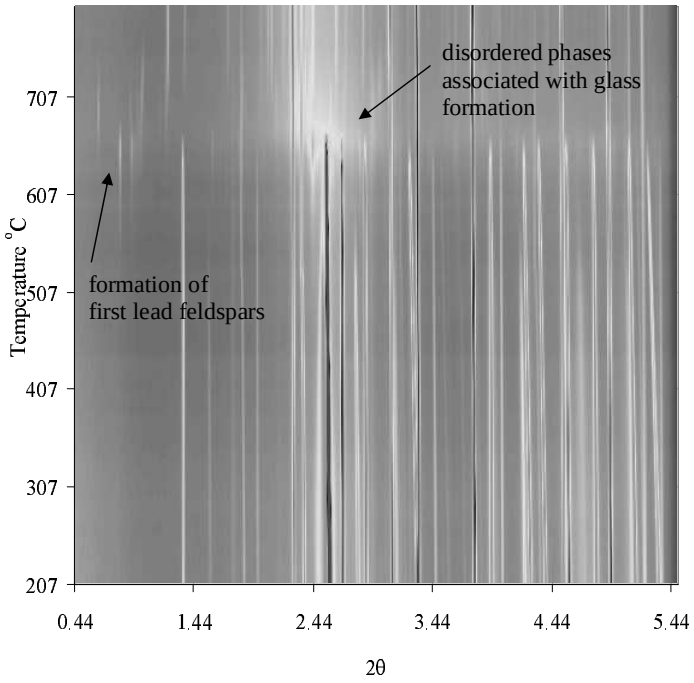

Figure 3.27: Image representing entire X-ray diffraction data set. The intensities of the peaks are give by their relative lightness. Illustrated in particular is the region of the disordered glass phases, the onset of melting, and the first formation of lead feldspars.

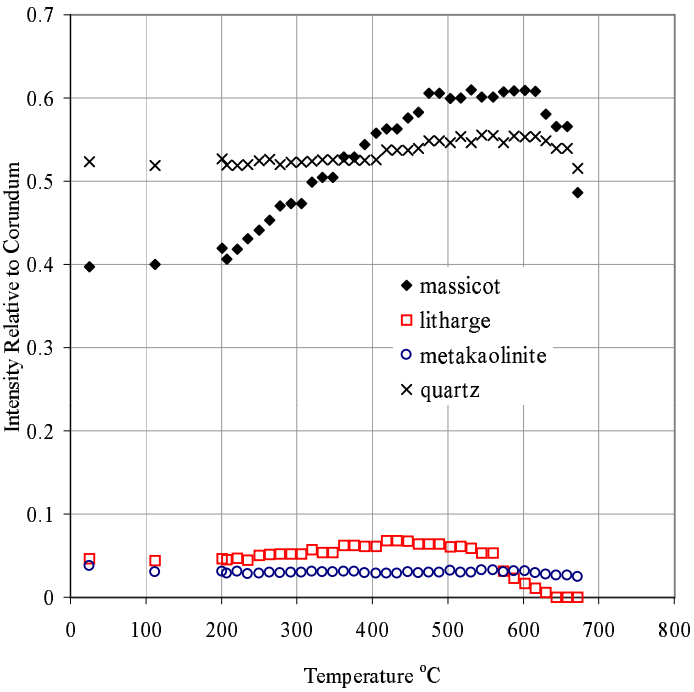

Figure 3.28: Phase intensities relative to corundum. The data, which was collected from the region of between 1-2.4 2θ, does not represent main intensity peaks. Also the data is not normalized to 100 % and therefore no inter-peak comparisons should be drawn from these data.

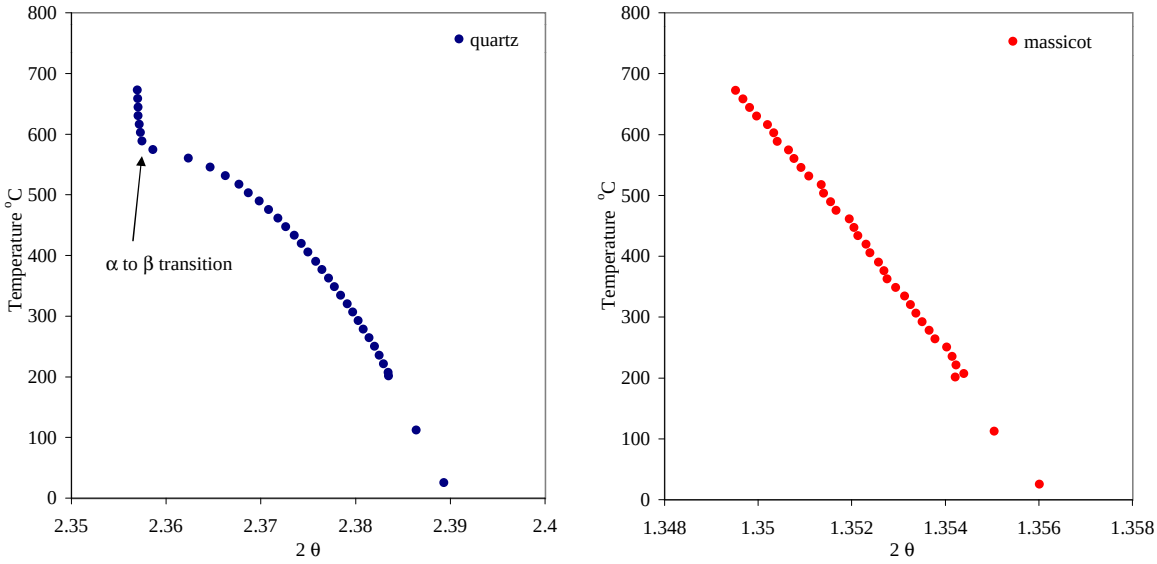

Figure 3.29: High temperature structural transformations to quartz and massicot as is shown by their change in peak position relative to temperature.

perature ramp. Of course, a rigorous treatment of the data to recover phase fractions may only be accomplished through a Rietvelt refinement which is not possible given the present experimental conditions.

The peak intensities relative to corundum are presented in Figure 3.28. This plot shows that the intensity of these peaks was influenced by temperature as well as by their interaction with other phases. The temperature dependence on peak intensity is most obvious with massicot which may be seen to rise steadily from 207 – 475°C before levelling into a plateau. It should be emphasized that this rise in peak intensity is not due to additional massicot entering the mixture, but rather it is caused by structural changes to the mineral itself. Other temperature induced structural changes may be seen in Figure 3.29 which shows the shifts in peak position of quartz and massicot due to dilatation of the minerals. Also seen in the quartz plot is the transformation of the mineral from its α to β form. Because of these mineralogical changes caused by heat, it is difficult to use the data shown in Figure 3.28 except in a very qualitative manner.

Bearing this in mind and returning to Figure 3.28, decomposition of the minerals

into disordered phases was found to occur at cooler temperatures than had been previously expected. Litharge was the first phase to begin decomposition starting at 560℃. Massicot and quartz seemed to start the process around same temperature of 616℃. Although only minor changes seem to have occurred to metakaolinite, a possible downward trend may be observed starting at 602℃.

Principal Component Analysis. PCA was used to establish an estimation of how the underlying factors of the XRD data set changed with temperature. The most important variable sought after was a point of inflection that marked an abrupt change to the underlying factors thereby signaling the onset of melting. PCA was performed using XLSTAT (Add-in Software, Inc, Paris, France), a second party statistical analysis add-in for Microsoft Excel. The data matrix consisted of all the 51 spectra each containing 2300 data points corresponding to the 2θ range of 0.44–5.5.

The loadings of the first three principal components may be seen in the left hand column of Figure 3.30. The right hand column of Figure 3.30 shows the first three principal components of an unpublished high temperature X-ray diffraction data set (same exact experiment as described here) of a 40 molar PbO and 60 molar SiO_2 mixture (Pradell 2003a). The first principal component accounts for 53% of the total variance of the data set. For this reason, the second and third components (which explain 28% and 12% of the variance respectively) were also displayed to confirm any observation drawn from the first component.

What may be seen in all of the loadings in the left hand column of Figure 3.30 is an abrupt change to the data structure at just below 700℃. This temperature corresponds to the approximate center of the region marked "disordered phases" in Figure 3.27. Also, it is very interesting that the loadings in the right hand column of Figure 3.30 also display the same melting temperature. Since both the clay/PbO powder mixture and pure SiO_2/PbO mixture have this melting temperature in common, this observation lends further support to the idea that PbO is solely reacting with

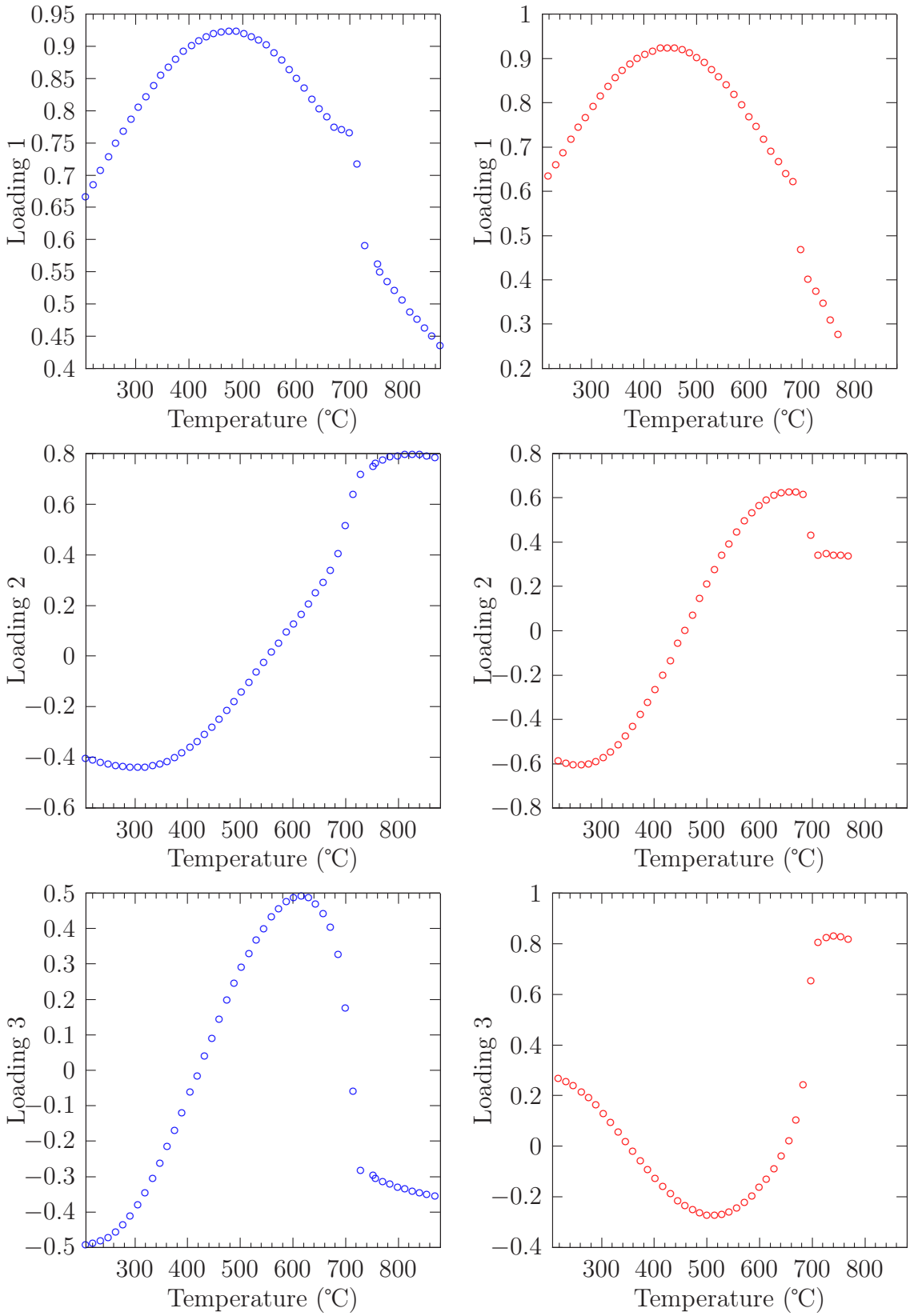

Figure 3.30: Loadings of first three principal components generated from high temperature XRD spectra sequences. Left hand column shows loadings of 50:50 wt% PbO:ceramic powder. Right hand column shows loadings for 40 molar PbO:60 molar SiO_2 powder

the quartz in the ceramic prior to incorporation of the remaining elements. Finally, the temperature of glaze formation (700℃) is slightly lower than had been expected (714℃) from the phase diagram of Geller and Bunting (1943).

2D Correlation Spectroscopy. 2D correlation spectroscopy was first developed by Noda for the treatment of perturbation-induced infrared spectral series (Noda 1986; Segtnan et al. 2001). The perturbation may be any number of applied chemical or physical conditions such as temperature, time, concentration, *etc.*. The usefulness of this technique derives from the increased spectral resolution that is achievable when the data is spread over a second dimension. Furthermore, similar to 2D nuclear magnetic resonance studies, detailed inter and intra-molecular interactions may be extracted when modulated data series are presented in a second statistically-derived dimension. Although no studies could be identified that have considered the use of 2D correlation methods on XRD spectra, the underlying concept of the technique should be theoretically applicable to any pertabated spectral series.

The statistical treatment of this technique has been described elsewhere (see Segtnan et al. (2001) for one of many articles on this subject) and, therefore, will not be repeated here. All 2D correlation calculations and plots were made in MATLAB (The Mathworks, Inc., Natick, MA., USA) using the algorithms written by the Ozaki group (downloaded from Kawasei Gakuin University Japan, http://science.kwansel.ac.jp/∼ozaki). All the terminology that is typically used in 2D correlation infrared studies will be adopted for the following discussion.

The synchronous and asynchronous 2d correlation maps are presented in Figure 3.31. The synchronous spectra map, which encompasses the region between 1.53 and 2.06 2θ, shows peaks that exhibit simultaneous changes in intensity at the same temperature. The peaks located on the diagonal, so-called autopeaks, represent the main spectral intensities which correspond, in this case, to litharge (1), meta-kaolinite (2), quartz (3), and massicot (4). The off-diagonal peaks, or cross peaks, are of

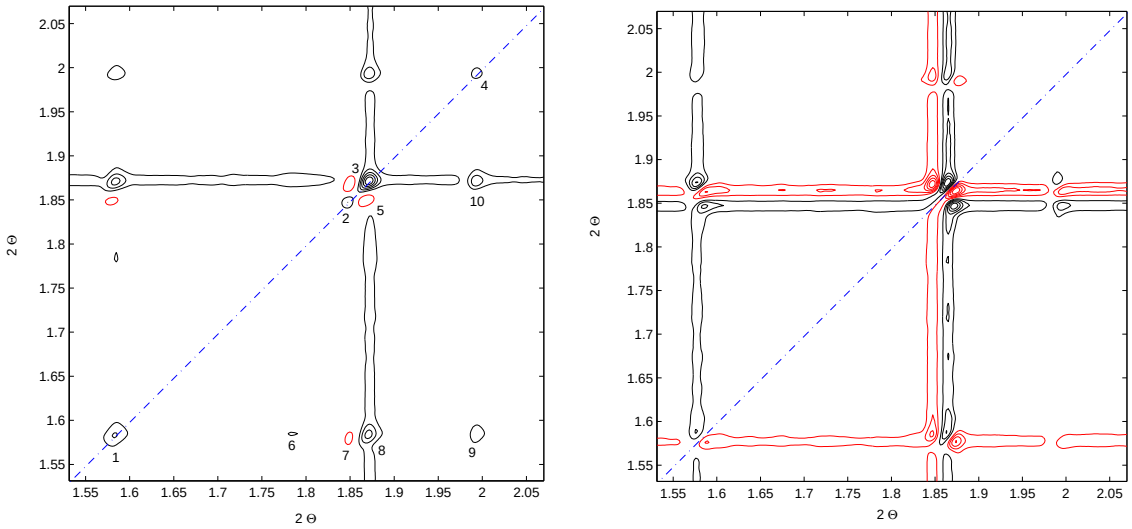

Figure 3.31: Synchronous (left) and asynchronous (right) 2D XRD correlation spectra from the temperature range 207 – 672°C. The 2θ interval between 1.53 and 2.06 was examined because it contains well separated and similar intensity characteristic peaks for litharge (1), meta-kaolinite (2), quartz (3), and massicot (4). These peaks (autopeaks) can be seen on the diagonal in the synchronous spectrum. Cross-peaks (5-10) show intermolecular correlations. The asynchronous spectra shows shifting peak positions and baselines.

main interest because they represent in-phase variation of two individual 2θ positions thus correlating these peaks in a mutual interaction. The sign of the cross peaks is also critical. A positive cross peak, denoted by black, represents a phase positively correlated to its respective autopeak (*i.e.*, the peak heights of the two correlated autopeaks rise at the same rate). A negative cross peak, denoted by red, represents a phase negatively correlated to its respective autopeak (*i.e.*, the peak heights change in opposite directions at the same rate). Asynchronous maps do not show autopeaks on the diagonal. Instead, they provide useful information on the sequence of events that take place, and provide an assessment of how the baselines may be shifting with temperature. Using the guidelines laid out by Noda, a negative peak in the asynchronous map, again denoted by red, suggests that the process occurring at the adjacent positive 2θ peak takes place first provided that corresponding peaks are present, and positive signed, in the synchronous map.

The temperature window of 207 – 672°C is shown in Figure 3.31. Already at these relatively low temperatures, the synchronous map shows a number of cross-

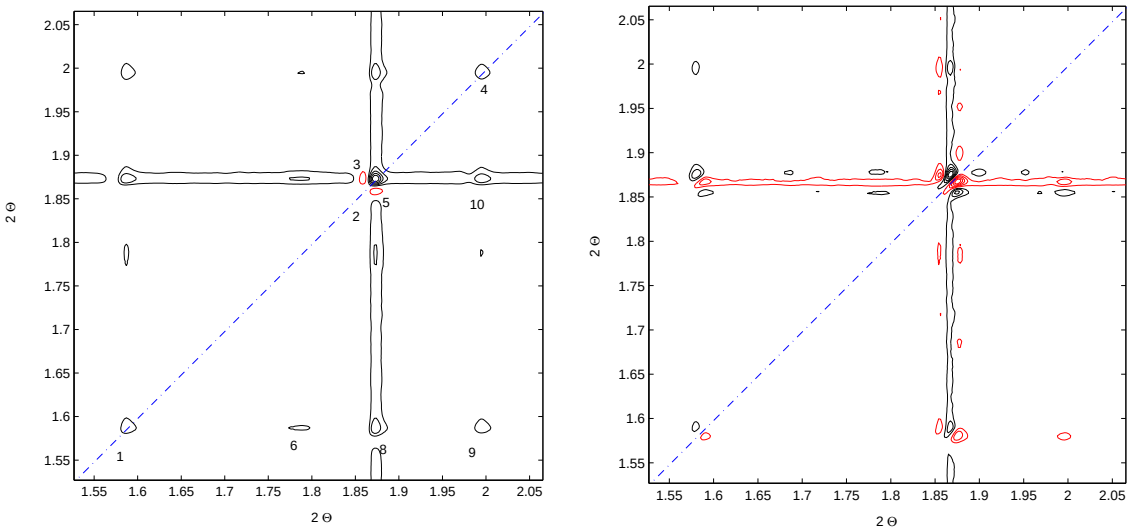

Figure 3.32: Synchronous and asynchronous spectra from the temperature range 650 – 870°C. Peak numbering is the same as in Figure 3.31.

peaks. Most interesting are the strong cross peaks, numbered 8 and 10, which show an in phase correlation between litharge and quartz, as well as massicot and quartz. Cross peak 9 also shows that massicot and litharge are changing at the same rate in this temperature range, and in the same direction. The negative peaks, 7 and 5, that are both associated with metakaolinite, exhibit a negative correlation with litharge and quartz. Because the spectral changes in this temperature window may be caused by structural dilatation of the minerals, it is possible that the correlations drawn between these peaks are spurious. Therefore, a high temperature window was also examined between 650-870°C (see Figure 3.32). In this region, it may again be seen that massicot and litharge are positively correlated to quartz. Also, the negative cross-peak between metakaolinite and quartz is confirmed.

The presence of a positive cross peak between quartz and both of the PbO species confirms that PbO reacts with quartz before any other phase. The negative cross peak with metakaolinite and quartz is likely to be a relative correlation caused by the rapid depletion of quartz from the ceramic matrix. These finding are also underpinned by the PCA treatment of the data which clearly shows that PbO and quartz mixtures melt at the same temperature as the PbO and clay mixture studied here.

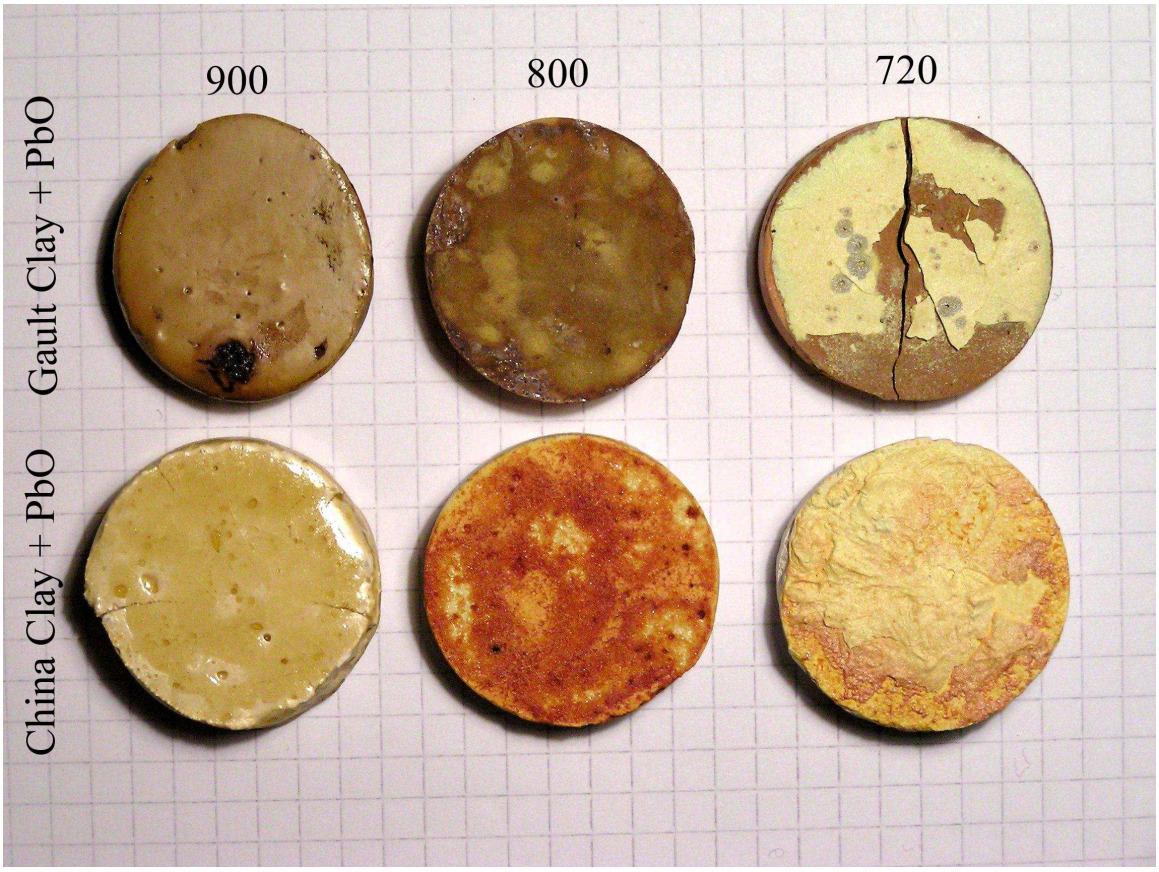

Figure 3.33: Gault and china clays glazed with PbO fired at 720, 800, and 900°C with dwell times of two hours. Note that each square of the above grid represents 1cm^2.

	Na_2O	MgO	Al_2O_3	SiO_2	K_2O	CaO	Fe_2O_3	TiO_2
Gault Clay	0.21	1.63	21.22	49.80	3.22	17.36	4.86	0.85
China Clay	0.30	0.25	38.30	46.60	0.68	0.33	0.03	0.07

Table 3.6: Chemical composition of fired samples (900 ℃) of Gault and China clays (supplied by Potclays, LTD.) used in this study as determined by ICP-AES. SiO_2 is calculated by difference.

	quartz	*calcite*	*kaolin*	*mica*	*montmorillonite*	*vermiculite*
Freeman, 1964	s	m	m	a	m	
Tite, 1975	s	a	m	a	m	t

Table 3.7: Mineralogical suite of British Gault clay as determined by Freeman (1964) and Tite-75 (need ref). The key to the table is as follows: a = abundant (>30%), s = subsidiary (15-30%), m = minor (5-15%), t = trace (<5%). Table reproduced from Paynter (2001).

The theory that the PbO starting material preferentially reacts with the available quartz in the ceramic was put to a further, and final, test in Figure 3.33 which shows a series of pre-fired (at 900℃) Gault clay and China clay (pure kaolin) disks glazed with PbO at temperatures of 720, 800, and 900℃ with dwell times of two hours. According to the ICP-AES analysis of these ceramics, neither of these bodies contained appreciable amounts of quartz (see Table 3.6 for composition and Table 3.7 for mineralogy of the Gualt clay. The Gault clay employed was on the low end of the quartz range with approx. 15% SiO_2. The China clay contained no quartz). Therefore, with these starting materials, a glaze should not be produced according to the proposed mechanism until high temperatures are reached. This is indeed the case considering that a glaze was not observed on either substrate in Figure 3.33 until a temperature of 900℃ was achieved.

3.4.1.5 Summary of Reaction of PbO with Earthenware Ceramics

The X-ray diffraction results presented above confirm that the mechanism proposed in Figure 3.24, in which PbO first reacts with quartz, is a plausible and likely route to producing a "flat" profile glaze. This result is based on several pieces of experimental evidence: 1) the low temperature glazes (730 ℃) shown in Figure 3.16 form incomplete melts with a low viscosity $PbO{\cdot}SiO_2$ glass phase that was shown to be capable

of wicking into the ceramic pore structure thereby surrounding and digesting the clay minerals; 2) The diffusion model and viscosity calculations from section 3.4.1.3 demonstrated that a low viscosity $PbO{\cdot}SiO_2$ phase could easily diffuse and wick into the ceramic pore structure thereby engulfing the ceramic minerals; 4) principal component analysis of the XRD data demonstrated that an intimate mixture of 50% PbO and 50% clay exhibited a main melting event at exactly the same temperature (700 ℃) as a pure PbO and SiO_2 mixture suggesting that the PbO is preferentially reacting with the available quartz in the clay; and 3) the positive and in-phase cross peaks, seen in the 2D X-ray map, between quartz and the PbO species suggest a simultaneous and mutual change in these compounds between the temperatures of 650 and 870℃. All of this evidence is underpinned by the experiment shown in Figure 3.33 which demonstrates that indeed a glaze does not form when using a ceramic body fabric poor in quartz.

To recap and conclude this section, the following points should be reiterated concerning glazing an earthenware ceramic with PbO alone:

1. There is not enough chemical or microstructural resolution to differentiate glazing a fired or unfired ceramic substrate. Also, one can not distinguish between glazing with PbO alone and PbO mixed with a clay of the same composition as the substrate.

2. When glazing with PbO, flat compositional profiles will result at all temperatures within one hour of firing indicating equilibrium with the ceramic.

3. The first liquid formed is from the interaction between PbO and quartz. Therefore to produce a glaze with PbO at a temperature between 700–900℃, a ceramic substrate that is quartz rich is required.

3.4.2 Reactions between PbO-SiO_2 Mixtures and Ceramic

This section builds of the work of Molera (1996) who found that diffusion dictated mass transfer of the ceramic substrate when glazing with $PbO{\cdot}SiO_2$ mixtures and frits. These diffusion driven processes resulted in glazes with steep compositional profiles along their cross-section. To re-affirm the observations of Molera (1996) here, $PbO{\cdot}SiO_2$ mixtures were used to glaze a fired British Gault clay (with a calcium carbonate rich and kaolin/illite/montmorillinite composition) which was intentionally chosen for its relatively poor quartz content (15% quartz as opposed to the 40% quartz rich ceramic used in the previous section), and its chemical similarity to the calcareous clays of the Italian peninsula (see Chapter 4 for the chemistry of these ceramic types). This work also expands on that of Molera (1996) with the development of a multicomponent diffusion model used to assess the progress of glaze development.

Experimental. Similar to the procedures outlined in section 3.4.1.1, Gault clay was pressed into disc shaped moulds and dried to a green body stage prior to biscuit firing at 900℃ for two hours. This clay, which was collected by Paynter (2001) during her thesis work, has a composition and mineralogy shown in Tables 3.6 and 3.7. To these fired ceramics, an intimately ground mixture of 75% PbO and 25% SiO_2 (both AnalaR® grade powders supplied by BDH Laboratory Supplies, Poole, UK) was applied as a water suspension by brush. The ceramics were then fired in a muffle furnace with ramps of 10℃/minute with dwell times of 2 hours at 750℃, 850℃, 950℃, and 1050℃. At the end of the firing sequence, the ceramics were quenched by placing them on a steel plate and allowing them to cool at ambient temperature.

As performed previously, cross sections were prepared by first sectioning the ceramic and then embedding the section into epoxy resin prior to polishing. Backscatter imaging as well as electron microprobe analyses were performed on the in-house Cameca Su30 SEM.

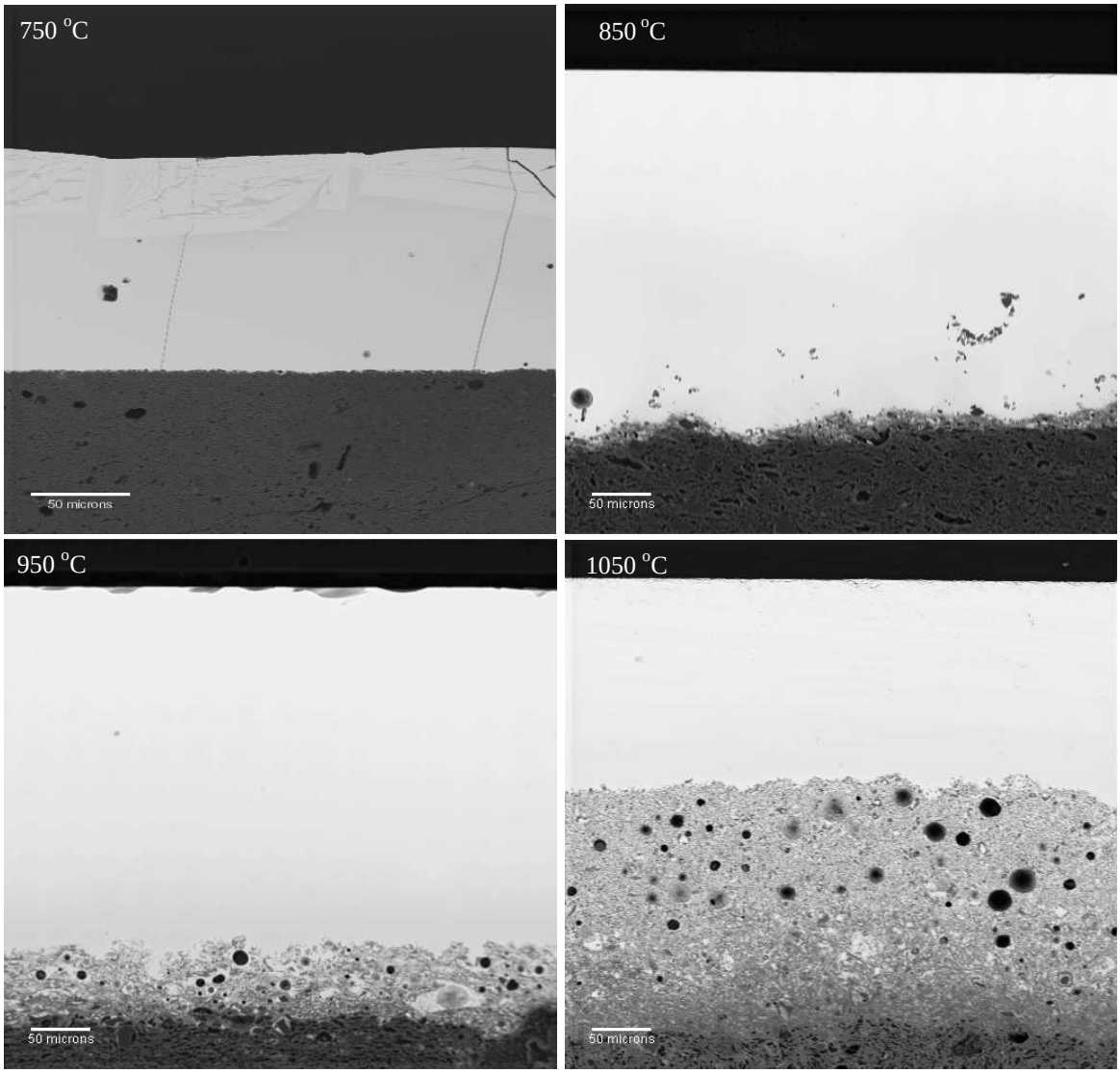

Figure 3.34: Backscatter images of glazes formed from 75-25 wt% mixture of PbO and SiO_2 applied to fired British Gault bodies.

3.4.2.1 Thermally Induced Changes to Ceramics Glazed with $PbO{\cdot}SiO_2$ Mixtures

The backscatter electron images associated with the firing sequence outlined in the experiment may be seen in Figure 3.34. The accompanying compositional profiles of major abundance oxides are presented in Figure 3.35.

The backscatter electron images show that the progression of firing is accompanied by an increase in the interaction zone thickness. Unlike the interaction zone observed in the samples when lead alone was used as a glazing compound, these interaction

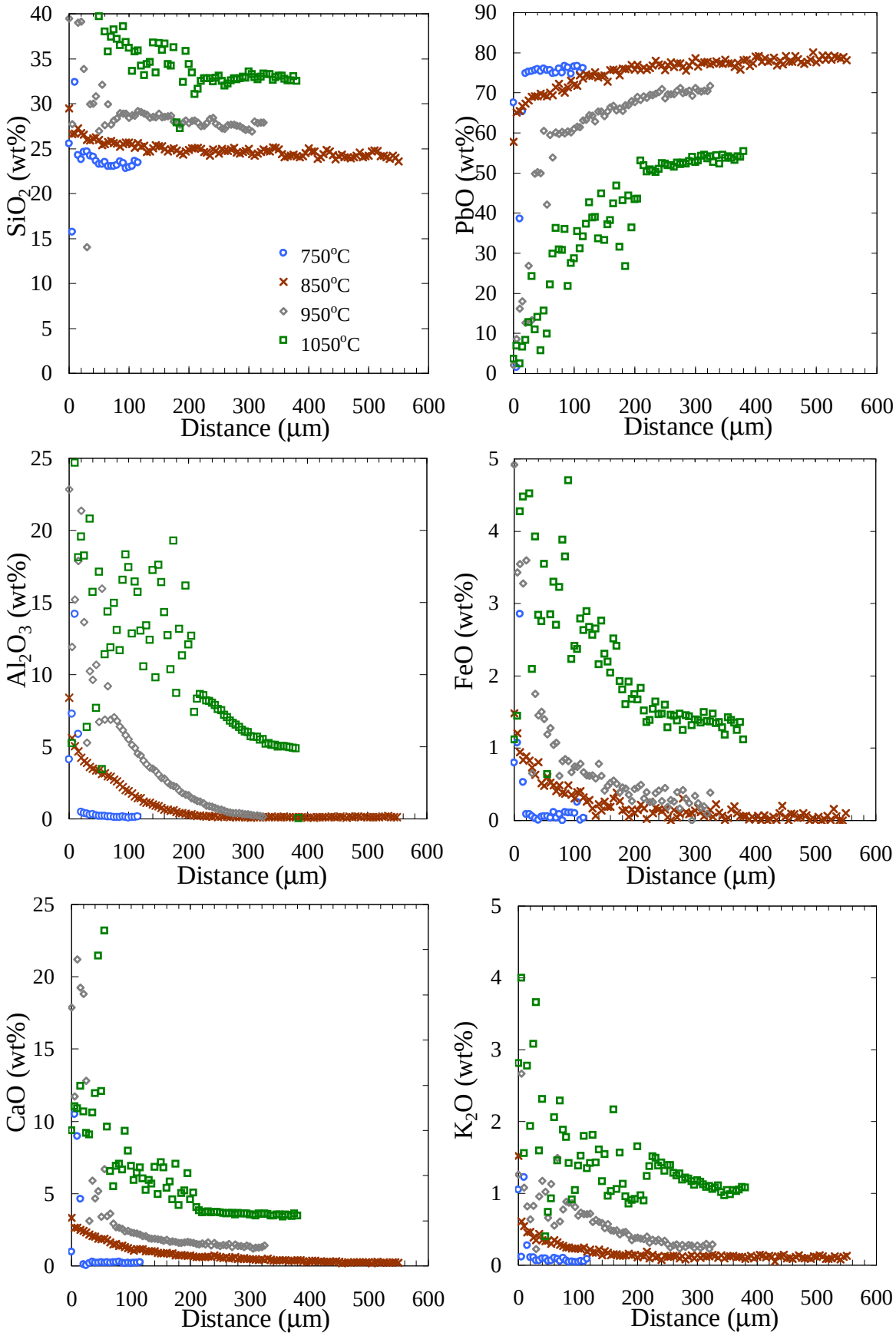

Figure 3.35: High resolution profiles across glaze cross sections formed from 75-25 wt% mixture of PbO and SiO_2 applied to fired bodies.

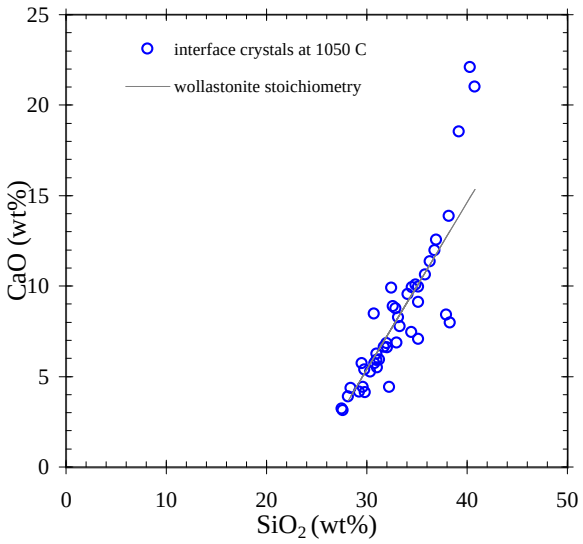

Figure 3.36: Binary plot showing correlation of CaO and SiO_2 in the interaction zone of the 1050 ℃ sample. The slope of the line shows the stoichiometry of wollastonite.

zones are formed of wollastonite. Evidence for this mineralogy may be observed in Figure 3.36, which shows a CaO–SiO_2 binary plot of data collected from the interaction zone of the 1050 ℃ sample. The fitted line represents the stoichiometry of wollastonite plus an offset of approximately 25% SiO_2 due to the contribution of the lead silicate glass phase which surrounds the crystals. It was necessary to calculate this offset considering that the interaction volume of the electron beam (at 1μm) was far larger than the wollastonite crystals themselves and, as a result, also excited the surrounding glass phase.

The wollastonite mineralogy is not surprising given the high calcium content of the ceramic substrate. However, in contrast to results of Molera (1996), the wollastonite composition of this interaction zone is quite unlike the lead feldspars (see Figure 3.12) described by Molera. This observed difference is certainly due to the composition of the ceramic substrate used in the experiment of Molera which possessed little CaO.

Of special note is the 750 ℃ sample which exhibits no interaction zone at the juncture between the ceramic and glass phase indicating little reaction between the $PbO{\cdot}SiO_2$ melt and the body fabric at this temperature. Also seen at the glaze edge

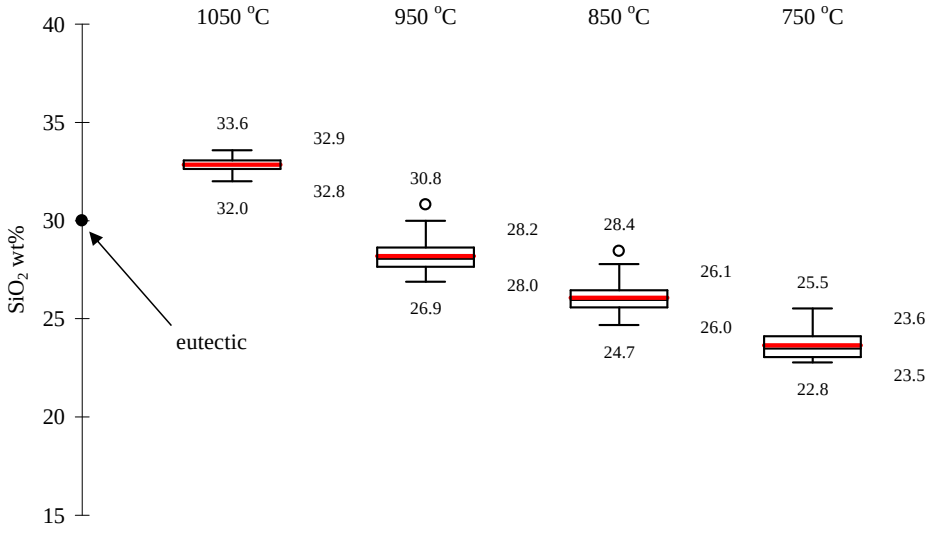

Figure 3.37: Univariate box plots showing changes in glaze composition with respect to temperature of the 75 % PbO and 25 % SiO_2 glaze mixtures on calcareous clay. For details on how to read this plot see Figure 3.8.

of this image are $PbO{\cdot}SiO_2$ crystals which form on freezing only under equilibrium conditions. Considering that minor amounts of dissolved ceramic can cause bond distortions in the melt sufficient to prevent such crystallization, the formation of these crystals provides further evidence demonstrating the lack of ceramic/glaze interaction. These observations are corroborated by the 750 ℃ compositional profiles (Figure 3.35) which are, for the most part, flat with only very small gradients observed for SiO_2, Al_2O_3, and PbO. Furthermore, the average amount of SiO_2 measured along the profile of this sample is below the designed 25% due to the crystallization of the $PbO{\cdot}SiO_2$ crystals which have robbed the melt of available SiO_2 during their formation.

Above 750 ℃, it becomes evident in both the backscatter images and the compositional profiles that substantial dissolution and diffusion of the body oxides into the melt is occurring. These processes are most clearly expressed by the compositional profiles which show, with increasing temperature, that both the liquidus composition (dissolution composition of the ceramic) and the total amount of each oxide increases in the melt following a diffusive gradient.

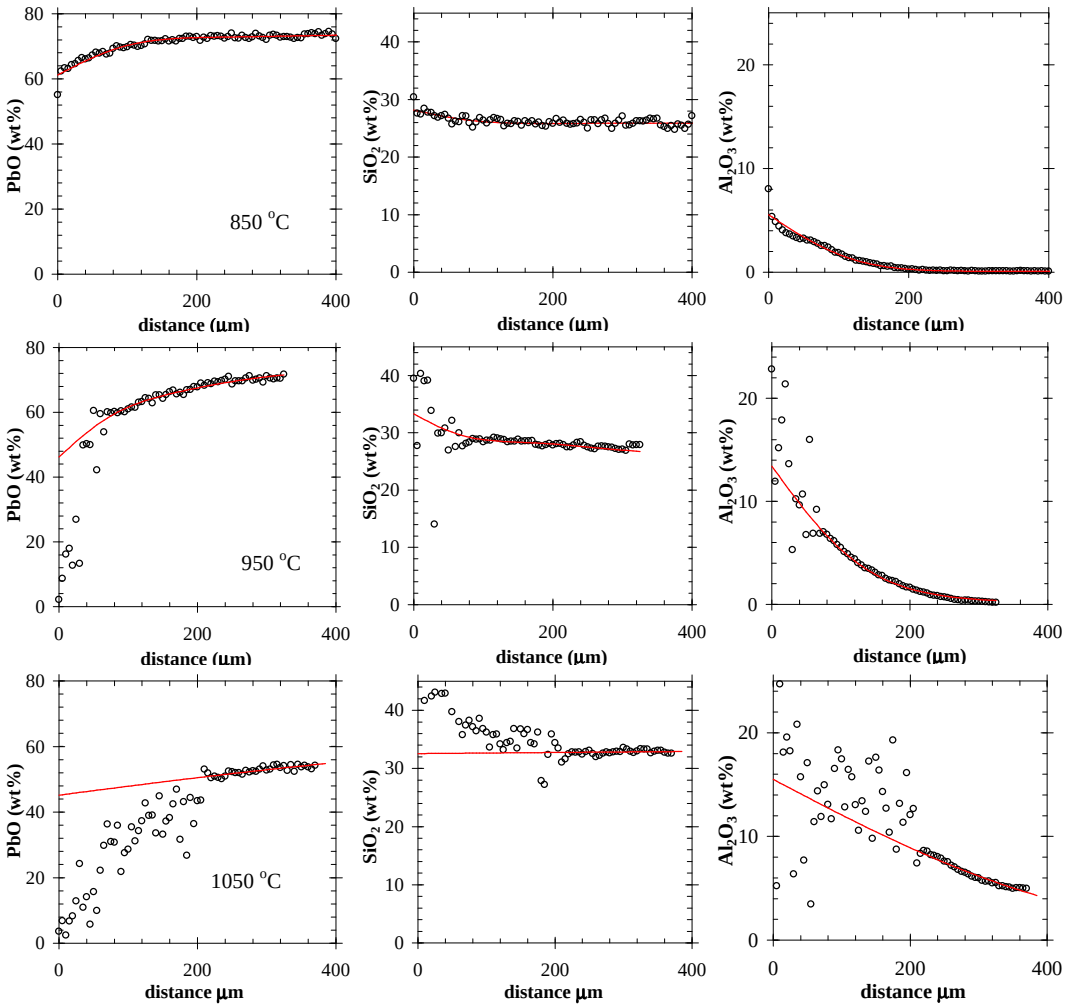

Figure 3.38: The diffusion-dissolution model fit (line in red) to the 850, 950, and 1050℃ experimental curves. Only the three most abundant oxides (PbO, SiO_2, and Al_2O_3) are shown.

To compare these data to the results of Molera (1996), who found that the ceramic provided a SiO_2 buffer which drives the composition of the glaze toward the eutectic, box plots of the SiO_2 profiles (Figure 3.37) were produced similar to those seen in Figure 3.8. These plots show that the glazes produced in this study behave similarly to those made by Molera (1996). The composition of the glaze is driven towards the eutectic composition until 1050 ℃ is reached whereupon the glaze becomes SiO_2 saturated and begins to slowly migrate up the steep liquidus line of ascent (see phase diagram in Figure 3.7).

To further examine the glaze formation processes, and specifically to assess the

	850℃	950℃	1050℃
Na_2O	1.5×10^{-5}	1.6×10^{-5}	3.1×10^{-5}
MgO	5.9×10^{-6}	6.7×10^{-6}	$2.4\times10^{+1}$
Al_2O_3	6.3×10^{-6}	7.5×10^{-6}	4.9×10^{-5}
SiO_2	$\mathbf{3.2\times10^{-6}}$	$\mathbf{3.9\times10^{-6}}$	$\mathbf{2.4\times10^{+1}}$
PbO	$\mathbf{5.5\times10^{-6}}$	$\mathbf{6.6\times10^{-6}}$	$\mathbf{2.1\times10^{-4}}$
K_2O	2.1×10^{-5}	1.9×10^{-5}	9.0×10^{-5}
CaO	2.3×10^{-5}	2.8×10^{-5}	2.5×10^{-3}
Fe_2O_3	1.2×10^{-5}	1.2×10^{-5}	5.4×10^{-4}
TiO_2	6.2×10^{-6}	5.7×10^{-6}	5.7×10^{-6}

Table 3.8: Diffusion coefficients (cm^2/s) calculated from the dissolution-diffusion model for each element in the 850℃, 950℃, and 1050℃ samples. Values that may be compared with the known tracer diffusion coefficient data of Schmalzried et al. (1981) (see Figure 3.21) are presented in bold.

mechanism of mass transfer in these glazes, a multicomponent diffusion model was fitted to the 850℃, 950℃, and 1050℃ curves. This diffusion model was designed to take into account common non-ideal behaviours such as chemically coupling and inverse chemical gradients (for further details on this model see Appendix B).

As shown in Table 3.8 (data derived from the model fits shown in Figure 3.38), the speeds of diffusion at 850 and 950℃ for SiO_2 and PbO are similar to the diffusion coefficients determined by Schmalzried et al. (1981) (data is presented in Figure 3.21). Furthermore the fits of the model to the data did not reveal substantial non-ideal behaviours. These results indicate that there are few, if any, elemental partitioning events or secondary reactions involved with the glaze forming reactions. In the 1050℃ melt, however, the measured speeds exceeded the predicted diffusion values (as extrapolated from data presented in Figure 3.21) by several orders of magnitude suggesting that convective forces were dominating the processes of mass transfer here. These convective forces could have been caused by a number of unknown factors including air currents, evolved gasses from the ceramic, and temperature differentials. Despite the 1050℃ melt, the results obtained from these ceramics were expected and they corroborate the original findings Molera (1996) on the nature of reactions of $PbO{\cdot}SiO_2$ compounds with ceramic substrates.

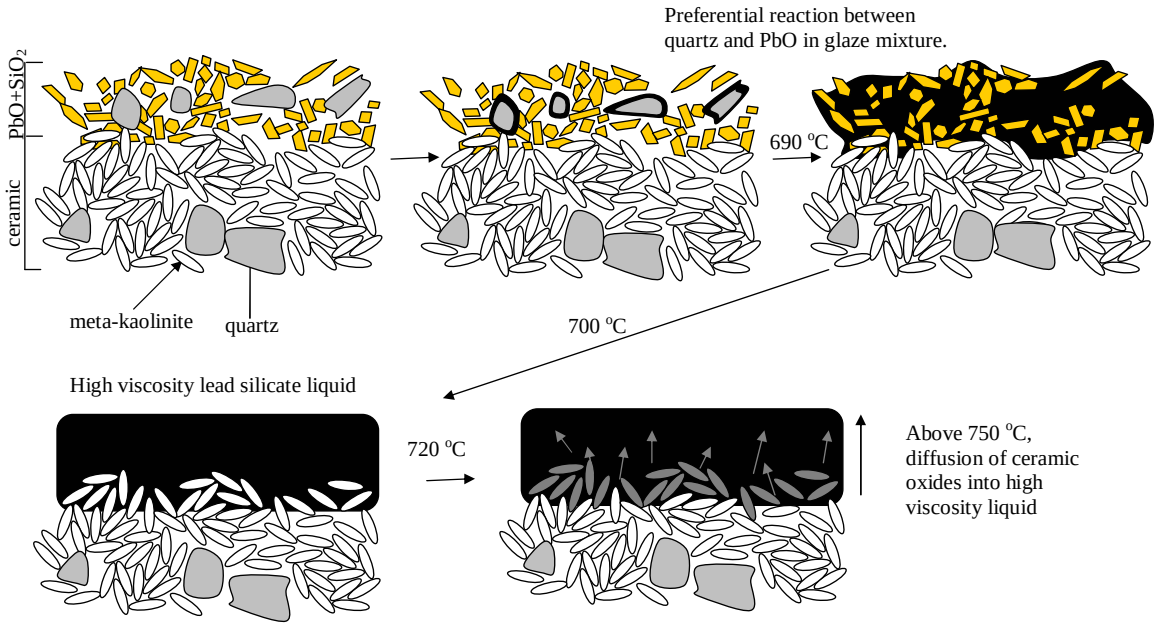

Figure 3.39: Mechanism of glaze formation when using $PbO{\cdot}SiO_2$ mixtures on a low quartz content clay.

3.4.2.2 Summary of Glazing with $PbO{\cdot}SiO_2$ Mixtures

As was originally shown by Molera (1996), the experiments here also demonstrate that ceramics glazed with $PbO{\cdot}SiO_2$ mixtures form under mechanisms of ceramic dissolution and diffusion. This mechanism of formation is presented diagrammatically in Figure 3.39. The PbO and SiO_2 first form a melt at around 700°C. Above 750°C, the lead silicate melt begins to react with and digest the ceramic substrate inducing diffusion of the ceramic into the melt.

3.5 Conclusions

In this chapter, two mechanisms of glaze formation were described. When glazing with PbO alone, the Pb reacts selectively with quartz available in the ceramic matrix forming a low viscosity liquid that flows into and engulfs the remaining clay minerals. Glazes formed form PbO alone may be characterized by flat compositional profiles. The second mechanism is associated with $PbO{\cdot}SiO_2$ mixtures wherein these compounds first react with themselves forming a relatively high viscosity liquid.

Subsequently, this liquid reacts with the underlying ceramic following a dissolution-diffusion mechanism. Glazes formed from $PbO{\cdot}SiO_2$ mixtures are characterized by steep compositional profiles associated with a diffusion driven gradient.

Chapter 4

The Provenance of Roman Lead Glazes

This chapter presents a preliminary provenance study. Inductively coupled atomic emission spectroscopy (ICP-AES) was used to identify groups of sherds with similar chemical profiles and to investigate fabric composition. In addition, thermal ionization mass spectrometry (TIMS) was used to measure Pb isotope ratios in the glazes. While the pin-pointing of an exact geographic provenance of a sherd was not the primary aim of this work, it was hoped that chemical fingerprints would specify distinct lines of production for lead glaze wares belonging to the primary period of study of this thesis– Imperial Rome during the 2^{nd}–4^{th} centuries AD. Based on previous archaeometric studies, most notably those of Pérez-Arantegui et al. (1996) and Hatcher et al. (1994), it has been suggested that production and distribution of lead glazes in the Western Mediterranean was limited to only a handful of centers in Italy and central Gaul (France) during this period.

The chapter begins with a discussion of previous studies which have examined the compositions of lead glazed fabrics (section 4.1). After reviewing the available chemical data from the literature, these results are compared with new analyses of sherds excavated from London, Upper Moesia (the Danubian regions in present-day Serbia), Apulum Partos (Dacia in present day Romania), the Lezoux region of central Gaul, and the Italian peninsula (section 4.2). This section is followed by a brief

pilot study using Pb isotope ratios to fingerprint the source of lead in these glazes. The discrete assemblages that result from these data is used mainly to assist the examination of fabrication technology to be presented in Chapter 5.

4.1 Previous Archaeometric Work: Introduction

The previous studies of Roman lead glazed wares focused almost exclusively on the elemental analysis of body fabrics in order to determine provenance and to suggest potential workshops from statistical groupings. A variety of elemental analysis techniques were used for this purpose: X-ray fluorescence (XRF), atomic absorption spectrometry (AAS), and inductively coupled plasma mass spectrometry (ICP-MS). The most significant of these studies examined lead-glazed body fabrics suspected to come from Italian and Gaul workshops (Pérez-Arantegui et al. 1996; Hatcher et al. 1994; Symonds and Hatcher 1989; Picon and Desbat 1986; Hatcher et al. 1980; Picon and Vichy 1974). Data from these studies form the main reference groups for this present study (see Figure 4.1).

The reference groups divide into two primary fields associated with either "non-calcareous" (at the bottom of the plot in Figure 4.1) or "calcareous" (at the top of the plot in Figure 4.1) fabrics. Based on archaeological considerations of fabric colour, vessel form, and decoration, Hatcher et al. (1994) suggested that the low calcium group, composed of sherds mostly from Colchester and Silchester (sites outside London), likely had an origin within the Loire or Allier valleys of central Gaul. Many archaeologists are even more specific about this provenance often calling the wares St. Remy or Vichy ware referring to the workshop site at Saint-Rémy-en-Rollat near Vichy (Green 1979). The high calcium group, which is composed mainly of sherds from the Northeast of Spain, have chemical signatures consistent with the weathering of dolomitic rocks. In the present context of the Western Mediterranean, the most

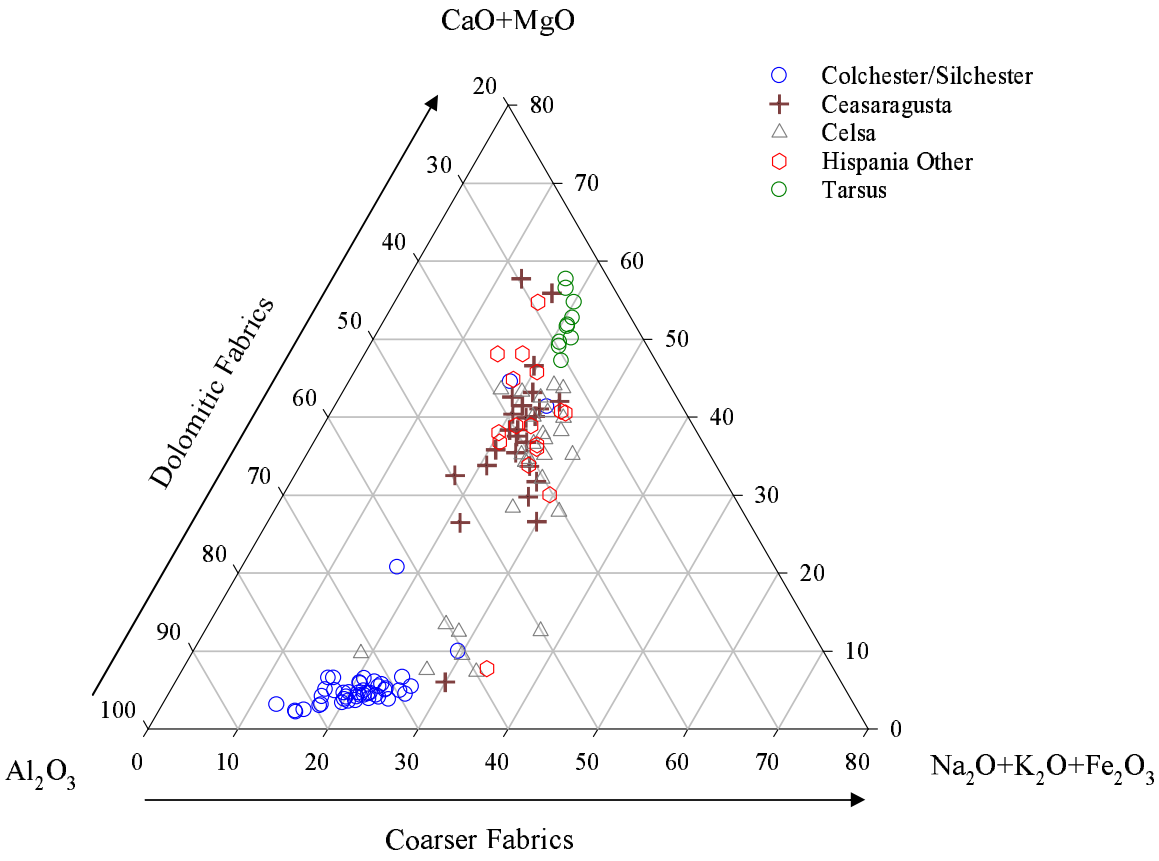

Figure 4.1: The normalized (Na_2O+K_2O+Fe_2O_3)-(CaO+MgO)-Al_2O_3 plot shows the gross division in clay chemistry of the reference groups. One primary field exhibits a dolomitic/calcareous character (high CaO+MgO). The other field is rich in Al_2O_3 but relatively poor in other constituent oxides associated with carbonates, feldspars, and iron bearing minerals. This "non-calcareous" group also shows an advanced weathering trend with pure kaolin (Al_2O_3) as its end-member.

likely source of these types of clays is along the length of the Italian peninsula as was presented by Pérez-Arantegui et al. (1996).

Although the tightly formed clusters presented in Figure 4.1 appear to be relatively straight-forward, it should be emphasized that none of the studies on Roman glazed wares have made attributions to specific workshops by chemical analysis alone. In the case of the "non-calcareous" group associated with central Gaul, a specific association to Saint-Rémy-en-Rollat has never been established, although the styles and outward appearance of the wares do substantiate this claim. The lack of chemical specificity of these arguments is due to the limitations imposed by the geology of the regions themselves as will be discussed briefly below. These limitations make a successful provenance study difficult at best. In an attempt to resolve some of these problems, it was deemed necessary to re-examine the data used in identifying the places of lead glaze fabrication prior to the examination of any new data.

4.1.1 Evidence for the Place of Origin of the Colchester/Silchester Group

Brief Description of the Geology of Central Gaul. The Central Massif forms the underlying geology of central Gaul. It is an expansive plateau composed of basanites, silica saturated lavas, and gneissic basement overlain with metamorphosed sedimentary deposits (Legendre et al. 2001). The whole of the region may be considered to be a "crumple-zone" where the geology has a number of overturned thrusted folds (known as nappes, see Figure 4.2) caused by the southward push of the Variscan continental collision between France and Spain (Van Den Dreissche and Brun 1991).

The formation processes of nappes, which induces a mixing of weathered country rock with overlying sedimentary deposits, leads to a significant amount of local variation in clay chemistry. However, this local variation tends to repeat over the geographic area with each fold in the geology. Therefore, there may be a variety of

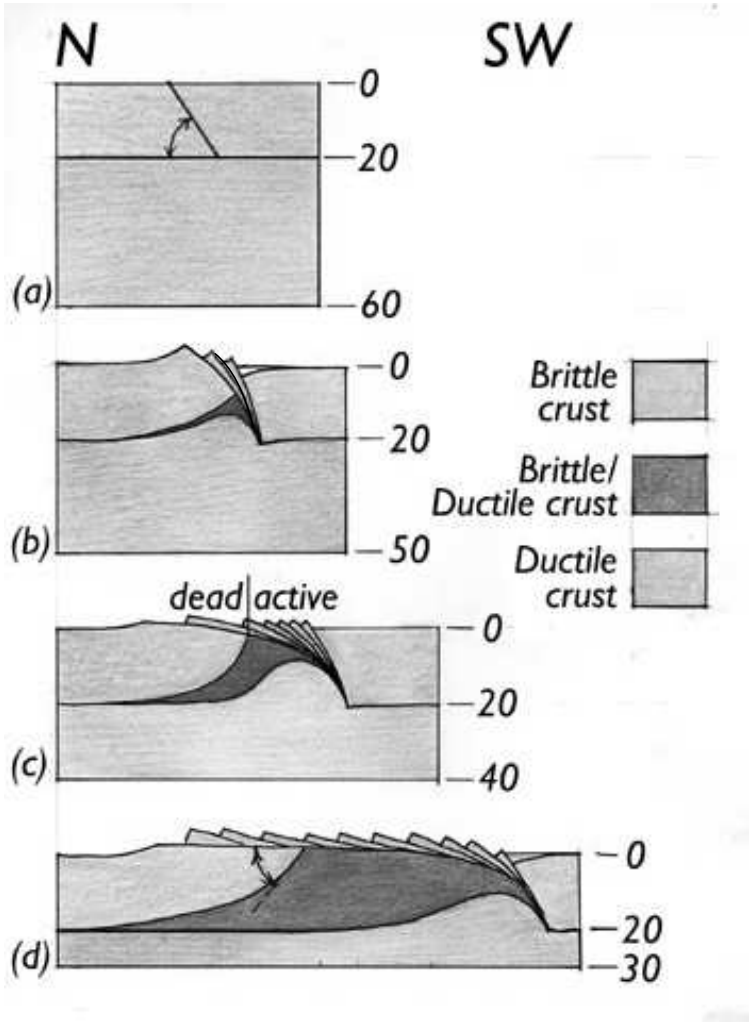

Figure 4.2: The formation of an uplifted dome which results from 'Variscan Origeny', the continental collision between France and Spain. A series of nappes are formed showing the "crumple zone" topography in cross-section which is typical of central Gaul. With such a model, it is easy to envision how clay chemistries are repeated over the geographic area resulting in non-specific and low resolution possibilities for ceramic provenance. The Figure is after Van Den Dreissche and Brun (1991) and drawn by Proudman on http://www.brookes.ac.uk/geology/8361/2003/paul/a_geology_page.htm.

chemically distinct clays available to a potter in the vicinity of any given workshop, but these same clay varieties tend to reoccur over the whole of central Gaul.

This geology leads to a situation where choices in clay type could vary according to the period of fabrication or to the personal choice of the potter leading to wares that look dissimilar chemically but are produced at a single workshop site. As a relevant example, terra sigillata (also called samian ware) produced in ateliers in the central Gaul region of Lezoux utilized low lime kaolinitic clays in the 1^{st} century AD followed by higher calcareous clays during the 2^{nd}–4^{th} centuries (Argyropoulos 1995; Schneider 1978; Picon 1973). This shift from the kaolinitic clays found in the Oligocene troughs near the Allier river to nearby marly clay deposits reflects a possible change in location of only several kilometers. This emphasizes the point that the location of the ateliers and tradition of fabrication remained unaltered, however the chemistry of the clay differed significantly. The alternative possibility, which must also be borne in mind, suggests that independent workshops separated by significant distances may have exploited chemically similar clay deposits. Therefore, ceramic groups from this region may express similar major element signatures, but be produced at separate workshops.

Re-analysis of the Colchester/Silchester data. Although Hatcher et al. (1994) found through canonical discriminant analysis that the most comparable material to the monochrome yellow sherds of Colchester/Silchester (Col/Sil henceforth) were so-called 'Rhenish' wares from central Gaul, they rightly acknowledged that the Col/Sil cluster was extended and partly fragmented which argued in favor of more than one atelier contributing to the group. The 'Rhenish' reference clusters of Hatcher et al. (1994), however, possess compositions that warrant a comparison and contrast with the Col/Sil group, and serve as a starting point to discriminate the origins of the Col/Sil group.

Rhenish wares were fine drinking vessels which had wide production across Gaul. They were studied extensively by Pollard et al. (1982) who discovered chemical

	Na_2O	MgO	Al_2O_3	K_2O	CaO	Fe_2O_3	TiO_2
Colchester/Silchester	*0.57*	*0.82*	*25.70*	*3.34*	*0.78*	*3.30*	*1.29*
σ (n=40)	2.67	0.80	0.23	0.44	0.37	0.71	0.36
Jaulge-Villiers-Vineux	*0.27*	*0.81*	*19.81*	*2.26*	*0.49*	*4.67*	*1.17*
σ (n=20)	0.02	0.21	2.36	0.34	0.14	0.74	0.11
Alésia	*0.5*	*1.1*	*17.92*	*2.66*	*0.72*	*5.21*	*1.08*
σ (n=19)	0.14	0.30	1.35	0.30	0.44	0.50	0.07

Table 4.1: Data sets of 'Rhenish' wares from Jaulge-Villiers-Vineux and Alésia compared to Colchester/Silchester Data. These data sets differ most significantly by there alumina content with a spread between 18-26%.

similarities between these wares from Britain and terra sigillata produced in Trier and Lezoux (Pollard et al. 1980). In this present study, comparison of the 'Rhenish' ware suite of analyses to the Col/Sil group (see Figure 4.4), demonstrated that their chemistries were quite different with the exception of two groups of sherds from north central Gaul (called mid Gaul in Pollard et al. (1982)) with find spots at Jaulge-Villiers-Vineux (henceforth JVV) and Alésia (Table 4.1 and Figure 4.3). It should be noted that these matches made by Ward's method of Euclidian distance clustering, are different from those originally identified by Hatcher et al. (1994).

The compositions of the Col/Sil, JVV, and Alésia groups are consistent with a basaltic chemistry given their low calcium content (CaO$<$ 0.78%) and high $Fe_2O_3/(Fe_2O_3+MgO)$ ratios between $0.80 - 0.85$ (in a typical basalt $Fe_2O_3/(Fe_2O_3+MgO) \cong 0.68$). Also, when the high Al_2O_3 content of the sherds is considered together with the chemical alteration index (CIA[1]) of Nesbitt and Young (1982), which shows ratios of between 0.82-0.87 for the considered groups, these data suggest that all of these clays have undergone advanced weathering leaving an illite/kaolinitic clay matrix devoid of most alkalis and Ca bearing minerals. Furthermore, the presence of a possible ilmenite assemblage– seen by the positive correlations in the Col/Sil data of TiO_2–MgO in plot A and of Fe_2O_3–MgO in plot B of Figure 4.4– is a common feature of basanite rock.

[1]where CIA= $Al_2O_3/Al_2O_3+Na_2O+K_2O+CaO$. As the ratio approaches unity, the more weathered the clay.

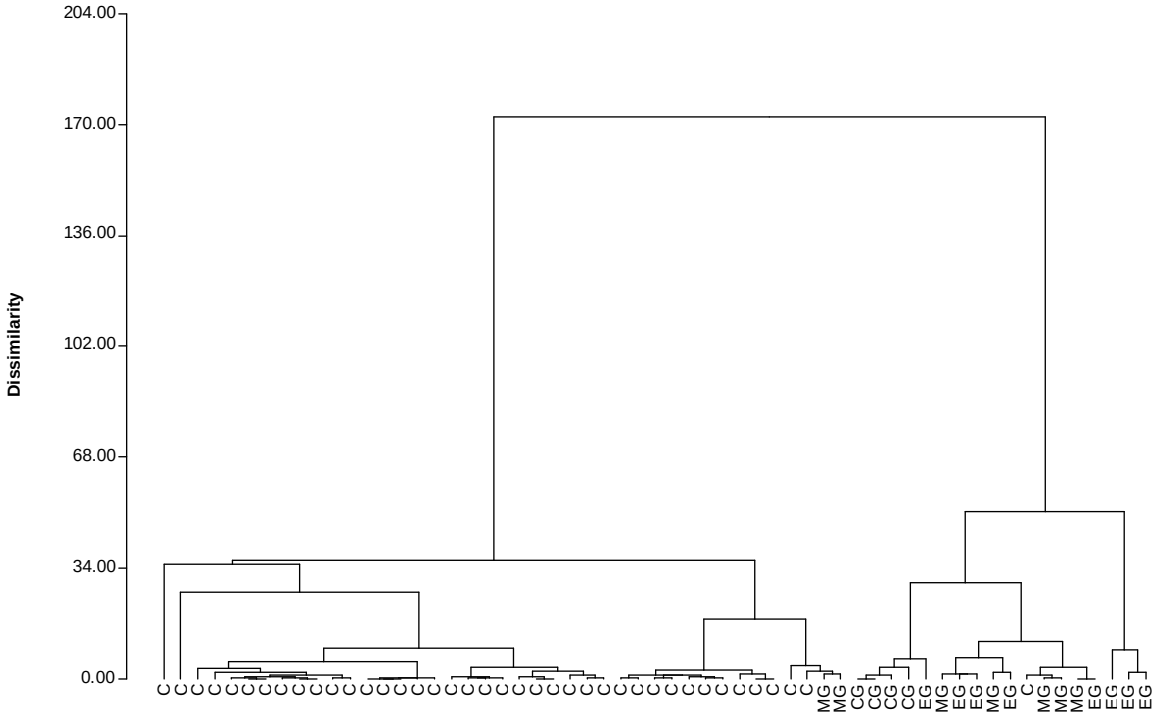

Figure 4.3: Agglomerative hierarchical clustering of lead glazed sherds from Colchester/Silchester (C) and 'Rhenish' wares from eastern Gaul (EG), mid Gaul (MG), and central Gaul (CG). The following elements were used in the clustering algorithm: Na_2O, MgO, Al_2O_3, K_2O, CaO, Fe_2O_3 TiO_2. The dendogram shows that the mean values of two groups of sherds from Jaulge-Villiers-Vineux and Alésia in mid Gaul (shown respectively in the dendogram) are consistent with the chemistry of the Colchester/Silchester group. These reference groups are composed of 20 and 19 sherds respectively. Also note that the C points refer to individual sherds.

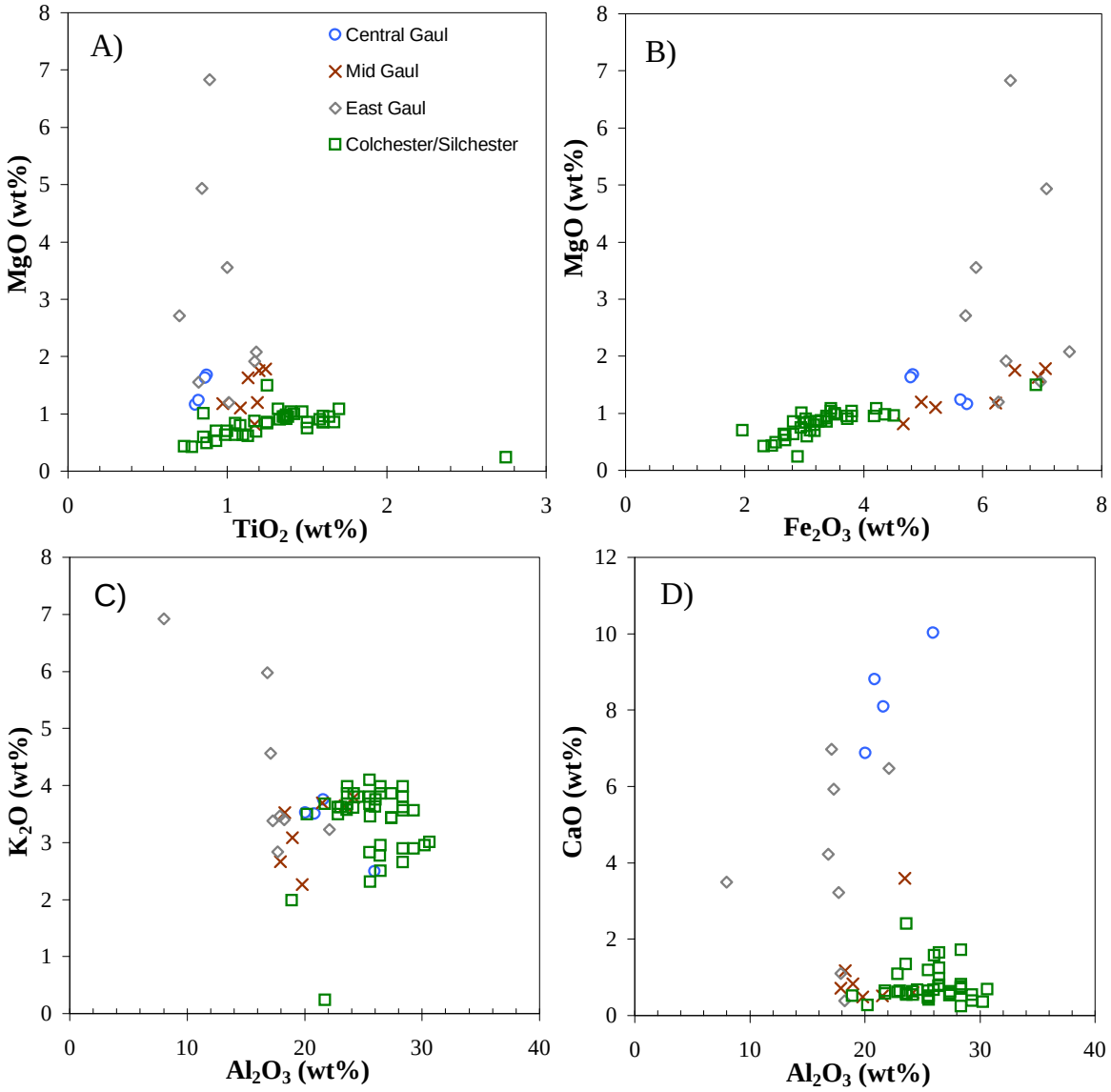

Figure 4.4: Bivariate plots showing chemical similarities and differences between the Colchester/Silchester group and 'Rhenish' ware reference groups. The Colchester/Silchester group exhibits strong positive correlations in plots A and B demonstrating the possible presence of ilmenite-geikielite solid solution (Fe,Mg)TiO_3 in these fabrics. None of the reference groups can be found to exhibit this behaviour nor do they consistently match in Al_2O_3 or CaO content as may be seen in plots C and D.

While it is tempting to draw conclusions about the place of origin of the Col/Sil material from these results, caution should be exercised considering there is no evidence to suggest that Jaulge-Villiers-Vineux and Alésia were the centres of production for these 'Rhenish' reference groups. The inability to identify the source of these high quality fine wares vexed Pollard et al. (1982) as well. Also, although all three of the groups discussed have compositional similarities allowing them to be classified together as having been likely made of clays derived from basaltic rock weathering, they actually can be seen to have quite different compositional fields (see Figure 4.5) in comparison to the Col/Sil group. Most significantly, the Al_2O_3–K_2O discriminant field (see Plot C in Figure 4.5) shows that the JVV and Alésia reference groups fall well outside the 90% confidence limits of the Col/Sil Group.

In addition to this 'Rhenish' reference data, the Col/Sil data was compared to coarse pottery excavated from known terra sigillata ateliers in Lezoux (Picon et al. 1971). As may be seen in Figure 4.5, the Lezoux fabrics form compositional fields that match the Col/Sil group much more closely than those of JVV and Alésia. However, the Lezoux field of data is fragmented showing some high calcium data (see Plot D of Figure 4.5). Also, the Col/Sil group shows a distinct cluster of data with a lower K_2O content than the majority of the field (Plot C of Figure 4.5).

To see whether these fragments of data actually formed separate compositional groups, Ward's clustering was again employed (see the dendogram in Figure 4.6). After clustering, three compositional groups (named Groups A, B, C) emerged with chemistries that are shown in Figure 4.7 and enumerated in Table 4.2. Group A is characterized by a relatively high CaO content ($\sim 3\%$) and is composed entirely of Lezoux sherds. Group B, which contains the majority of the data (57 sherds out of a total of 99) has high $Al_2O_3(\sim 26\%)$ and $Fe_2O_3(\sim 4\%)$ content. Group C has low potash and iron content and is formed entirely of sherds from the Col/Sil group.

In terms of provenance, the amount of overlap between the Lezoux and the Col/Sil

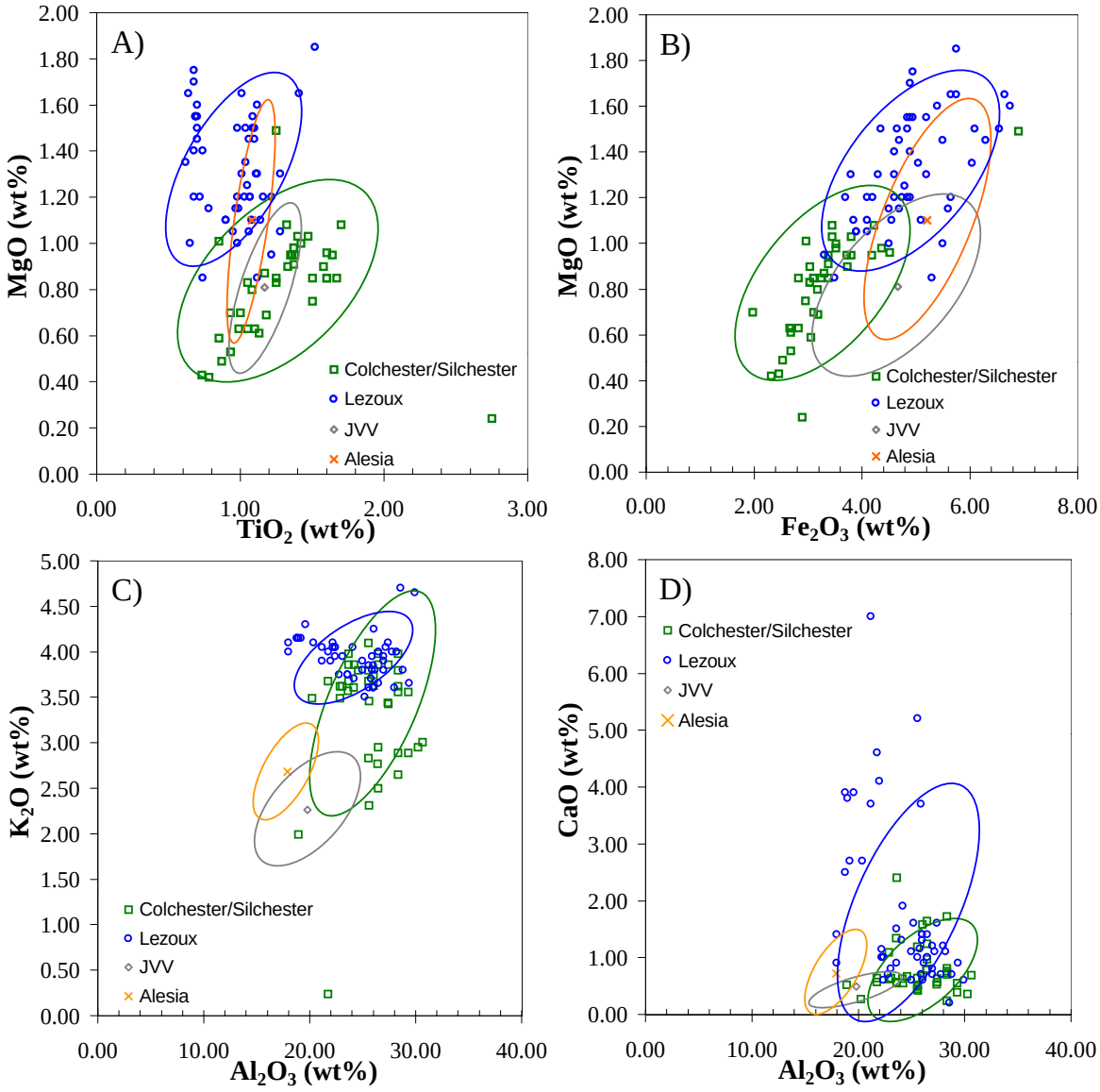

Figure 4.5: Bivariate plots showing comparable fields of low calcareous sherds from central Gaul. Ellipses are 90% confidence intervals calculated from the entirety of each of the sherd groups. The JVV and Alésia fields are represented only by their mean value.

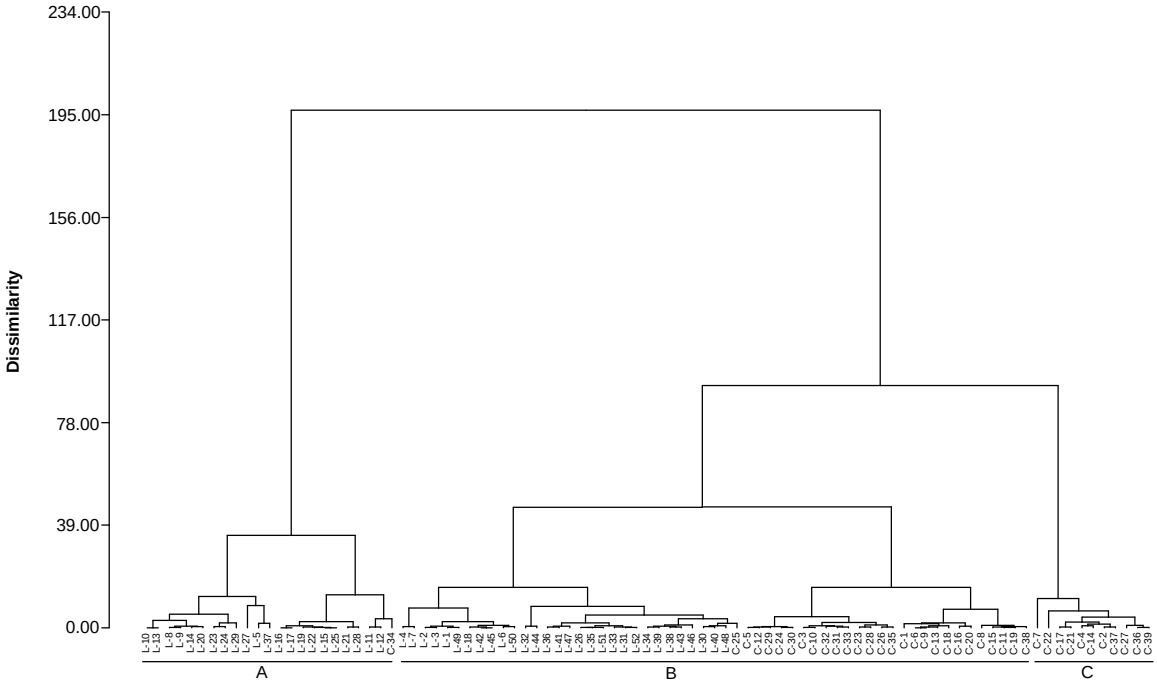

Figure 4.6: Ward's agglomerative hierarchical clustering dendogram of Colchester/Silchester Lead Glazes and Lezoux Samian ware. The following elements were used in the clustering algorithm: MgO, Al_2O_3, K_2O, CaO, Fe_2O_3 TiO_2. The data divides into three main compositional branches labelled A, B, and C.

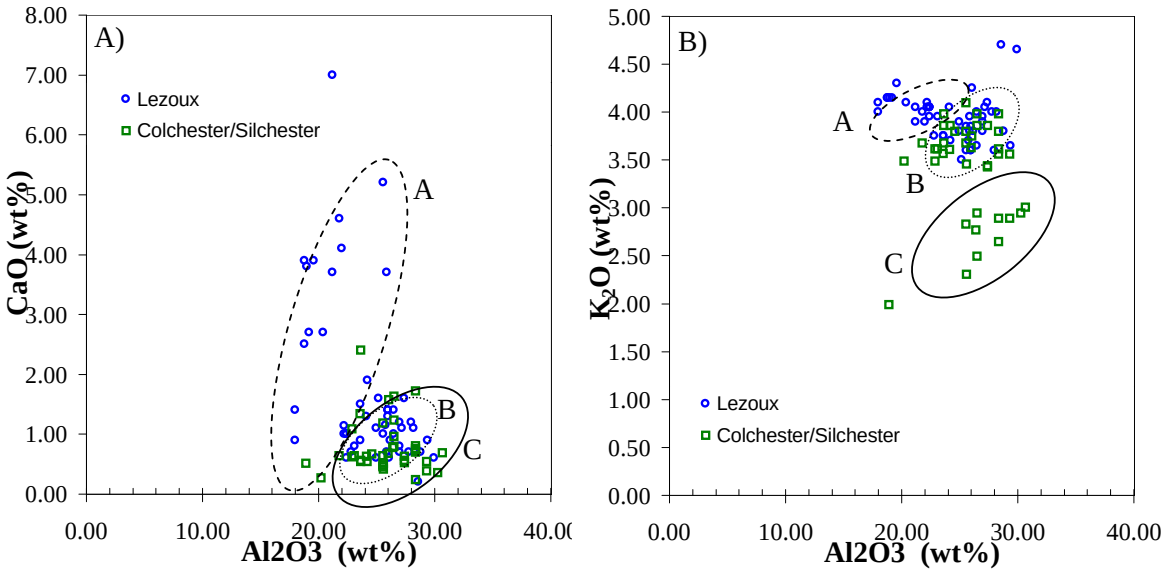

Figure 4.7: Bivariate Plots showing groups defined by Ward's agglomerative hierarchical clustering of pottery from Colchester/Silchester and Lezoux. Ellipses encompase the 90% confidence intervals for each data set.

	MgO	Al_2O_3	K_2O	CaO	Fe_2O_3	TiO_2
Group A	*1.42*	*21.58*	*4.03*	*2.62*	*5.50*	*0.80*
σ (n=23)	0.23	2.39	0.14	1.72	0.74	0.18
Group B	*1.08*	*25.84*	*3.80*	*0.90*	*4.01*	*1.22*
σ (n=57)	0.25	2.11	0.25	0.37	0.78	0.22
Group C	*0.61*	*26.93*	*2.70*	*0.73*	*2.66*	*1.00*
σ (n=11)	0.13	3.07	0.30	0.48	0.32	0.22

Table 4.2: Groups defined by Ward's agglomerative hierarchical clustering of pottery from Colchester/Silchester and Lezoux.

data in group B is significant. To compare these data and further assess this overlap, a semi-quantitative comparison index, modified from Porat (1989), was employed. For this index, the averages and 90% confidence intervals were compared for each element using the following equation:

$$S = \frac{No.\ of\ elements\ within\ M\ \pm\ 90\%\ confidence * 100}{No.\ of\ elements\ measured} \tag{4.1}$$

where S represents the similarity index and M is the mean of the group. This index is based on the percentage of test samples that fall within the 90% confidence intervals of a reference group. A match between two compositional groups is considered reasonable when the overall similarity S is above 66%. In multidimensional compositional space, this means that at least 66% of the test data points must fall within the 90% confidence volume of the reference group for there to be a passing match.

	MgO	Al_2O_3	K_2O	CaO	Fe_2O_3	TiO_2	S
Col/Sil	55.6	85.2	100.0	96.3	44.4	33.3	69.1

Table 4.3: Similarity indices calculated for each element when comparing the Colchester/Silchester group B sherds to the Lezoux group B sherds. S represents the overall similarity between the compositional fields.

The results from equation 4.1, in which the Col/Sil data was compared to the Lezoux field, may be seen in Table 4.3. The overall similarity (69.1%) suggests that the group B data from Col/Sil and Lezoux share many major element compositional characteristics suggesting similar geological origins. This is particularly true for the major element data of Al_2O_3, K_2O, and CaO where the Col/Sil data falls

	MgO	Al_2O_3	K_2O	CaO	Fe_2O_3	TiO_2
MgO	1	0.204	-0.007	0.053	**0.642**	**0.400**
Al_2O_3		1	0.160	0.242	-0.125	0.261
K_2O			1	**0.348**	-0.201	0.209
CaO				1	-0.064	0.249
Fe_2O_3					1	**0.354**
TiO_2						1

Table 4.4: Geometric mean centered log-ratio covariance matrix of Colchester/Silchester Group B. Significant values are in bold.

directly within the 90% confidence ellipses of the Lezoux data. Furthermore, if the Fe_2O_3/(Fe_2O_3+MgO) ratio is examined, it may be seen that it is essentially identical for both groups (Col/Sil = 0.79 ± 0.02, Lezoux = 0.78 ± 0.02). Despite this ratio, however, just over 50% of the Col/Sil sherds fall within the Lezoux space in MgO compositional space according to the similarity index. Also, for both Fe_2O_3 and TiO_2, less than 50% of the Col/Sil data falls within the 90% confidence interval of Lezoux.

Since the Lezoux and Col/Sil data sets were not analytically calibrated against one another, there is a distinct possibility that some of the variational differences seen in Table 4.3 may be accounted for by the varying degree of precision inherent in the measurement of each element. Therefore, a final statistical check was performed to compare the overall structure of the Lezoux and Col/Sil group B data sets using covariance matrices. Employing the recommendation of Aitchison (1986), the data was transformed by taking the log of each element point normalized by the geometric mean in order to mitigate any problems from closure in the data. The covariance matrix was calculated by the XLSTAT ® statistical add-in for Microsoft Excel. The resulting so-called centered log-ratio covariance matrices identify element pairs that exhibit the greatest variability in the data set. In addition, strong associations in this matrix show elements that coexist in the same mineral.

The covariance matrices for the Col/Sil group B data and the Lezoux group B data may be seen in Tables 4.4 and 4.5 respectively. The Col/Sil group shows strong correlations between MgO–Fe_2O_3, MgO–TiO_2, and Fe_2O_3–TiO_2. These correlations

	MgO	Al_2O_3	K_2O	CaO	Fe_2O_3	TiO_2
MgO	1	**0.341**	-0.172	0.136	**0.710**	**0.371**
Al_2O_3		1	**0.356**	-0.232	-0.177	**0.717**
K_2O			1	**-0.641**	**-0.445**	-0.033
CaO				1	0.237	0.096
Fe_2O_3					1	-0.002
TiO_2						1

Table 4.5: Geometric mean centered log-ratio covariance matrix of Lezoux Group B. Significant values are in bold.

underpin many of the observations previously made when examining the bivariate plots of these data in Figure 4.4. In specific, these sherds have a limited mineral assemblage composed of clay (likely illite/kaolinite) and possibly ilmenite as shown by the high values for MgO–TiO_2 and Fe_2O_3–TiO_2. The covariance matrix for Lezoux differs from the Col/Sil group. The Lezoux data set again exhibits a strong correlation between MgO–Fe_2O_3, and a relatively high correlation for MgO–TiO_2, but no correlation may be seen between Fe_2O_3–TiO_2. Also, the Lezoux set shows a strong correlation between Al_2O_3–K_2O demonstrating the possible presence of alkali feldspars in these sherds. Finally, a very strong correlation between Al_2O_3–TiO_2 shows that rutile is likely coming into the assemblage with the primary clay mineral.

These data demonstrate that although the Col/Sil group shares major compositional characteristics with the Lezoux data set, which again suggests similar geological origins, they do not possess sufficient enough similarities to warrant a common provenance. Without having further trace element data and/or petrographic information, one may not preclude considering numerous other potential sources of this Col/Sil clay type. However, as discussed by Hatcher et al. (1994) the forms and decoration on the Col/Sil sherds do intimate a central Gaul provenance for these wares.

4.1.2 Place of Origin of the Celsa/Caesaragusta Group

. This group of sherds published by Pérez-Arantegui et al. (1996) is quite different from the Colchester group in terms of chemistry (as seen in Figure 4.8), form, and

	Na_2O	MgO	Al_2O_3	K_2O	CaO	Fe_2O_3	TiO_2
Celsa/Caesaragusta	1.00	2.51	13.24	2.43	11.21	4.91	0.62
Taranto	0.42	3.31	12.70	1.99	12.25	5.66	0.73
Latium/Campania	*na*	3.50	16.94	2.88	13.63	6.59	0.76
Tarsus	0.54	4.84	14.12	2.74	17.65	6.49	0.66
Smyrna	0.71	1.73	20.95	3.97	3.41	4.88	0.88

Table 4.6: Average compositions of 'calcareous' sherds excavated from Spain (Celsa/Caesaragusta) and comparable groups from Italy and the Eastern Mediterranean. The Latium/Campanian lead glazed wares (Italian) were originally published by Picon and Desbat (1986). The black-glazed sherds shown to be from Taranto were originally published by Hatcher et al. (1980). The lead glazed sherd data from Tarsus and Smyrna in the Eastern Mediterranean were published by Hatcher et al. (1994). Note that the low CaO group from Celsa published by Pérez-Arantegui et al. (1996) was omitted from the table for the sake of clarity.

decoration. Unlike the Colchester material, the majority of the Celsa/Caesaragusta glazes are bicoloured with a green exterior and yellow interior. Also, the calcium rich composition of the majority of the sherds further suggests that these vessels represent a production line distinct from the Colchester material with a probable origin of Italy.

The likely Italian origin of these sherds was first assigned by Pérez-Arantegui et al. (1996) through their comparison with data of known origins (see Table 4.6 for compositional comparison of the Celsa/Caesaragusta Group with Italic and Eastern Mediterranean sherds). This provenance is further substantiated by the geology of the area which is dictated by the Appenine range forming a central spine running down the peninsula. In brief, the Appenines are a fold and thrust belt primarily composed of dolomitic limestone rock of marine origin. The clays of the region are made up of various proportions of illite, chlorite, kaolinite, and smectite, together with quartz and relatively high calcium hosted in carbonates (Bianchini et al. 2002).

The dolomitic character of the Caesaragusta/Celsa (henceforth Spanish) sherds is confirmed by the positive correlation between CaO and MgO as may be seen in plot A of Figure 4.8 and enumerated in Table 4.6. Also, as was previously demonstrated by Pérez-Arantegui et al. (1996), the Spanish data shares similarities with vessels from known Italian locals (Plots B and C of Figure 4.8). Additionally, few of the Spanish sherds fall within compositional fields that may be assigned to Eastern Mediterranean

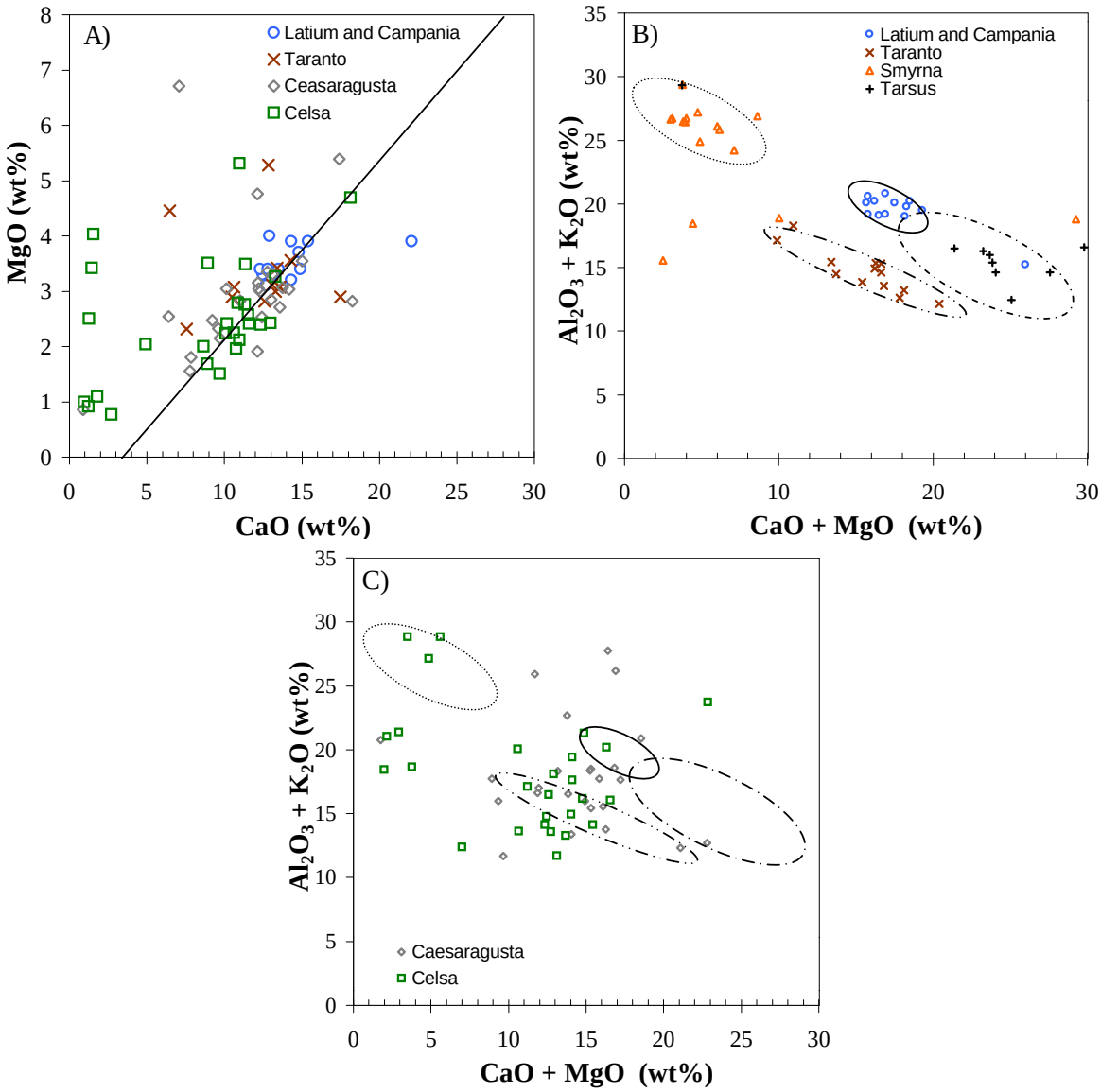

Figure 4.8: Bivariate relationships in the Caesaragusta and Celsa (Northeast Spain) sherds and other reference groups. This series of plots shows data from the Spanish sites compared with sherds of known Italian origins: sites at Taranto and Latium and Campania. Plot A shows the dolomitic character of the sherds with a positive correlation between CaO and MgO. Plots B and C show that the Spanish compositions scatter over both the Latium-Campania and Taranto fields. The line in plot A is simply a visual aid. Also in plot C, the data points of the reference groups were omitted for clarity. The ellipses in Plots B and C show the 90% confidence limits of the reference groups.

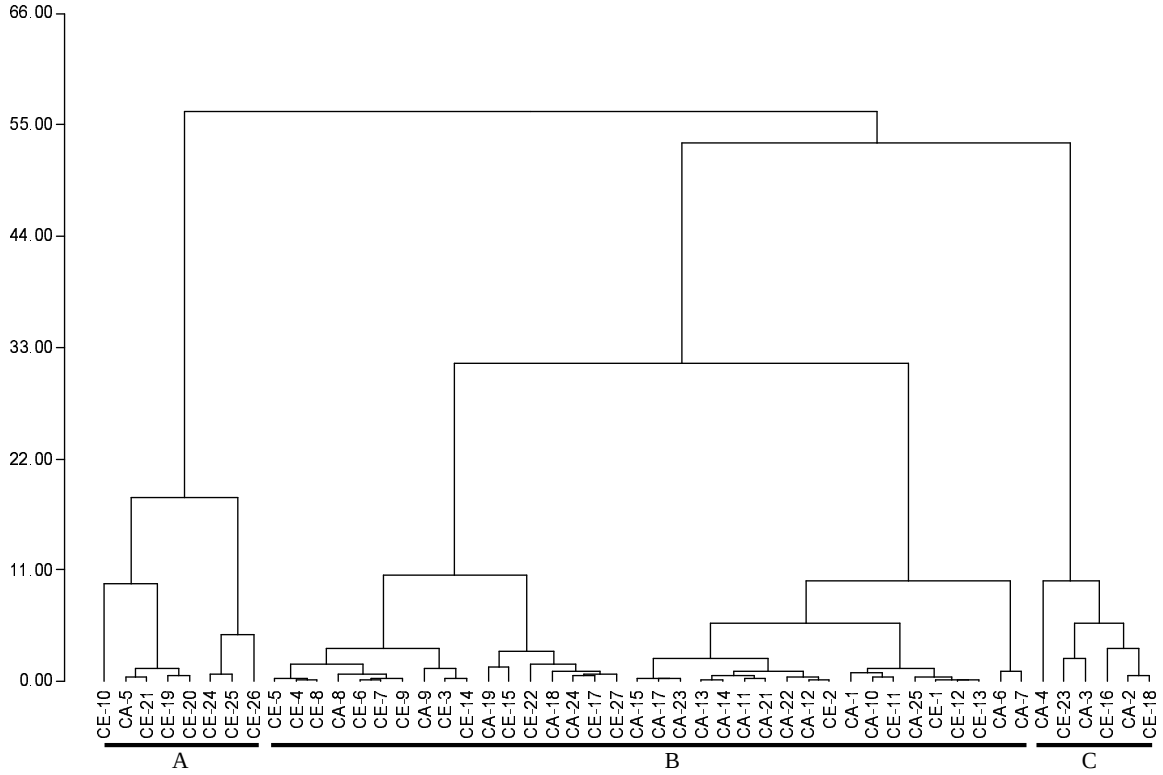

Figure 4.9: Agglomerative hierarchical clustering dendogram of Caesaragusta and Celsa lead glazed sherds showing that the data falls into three groups. The following elements were used in the clustering algorithm: MgO, Al_2O_3, K_2O, CaO, and Fe_2O_3.

locals. For instance, none of the Spanish sherds fall within the 90% confidence limits of the Tarsus group (high CaO with wt%$>$ 15). In comparison with the Smyrnian data, only a handful of the Spanish sherds seem to correspond with this compositional group (characterized by CaO between 0.52-5.80%). It should be noted that these low CaO sherds could alternatively belong to the Col/Sil group discussed in the previous section. Likewise, the further low CaO sherds from Celsa, which may be seen in plots A and C of Figure 4.8 to fall outside the Smyrnian field, have lower Al_2O_3 than the Col/Sil field suggesting that this is a separate group of unknown origin. Beyond these gross divisions, the indiscriminate scatter of the Spanish data across the high calcium reference fields (as seen in plot C of Figure 4.8) makes it difficult to assign the Spanish vessels to specific workshops.

Despite the scatter of the Spanish data, Pérez-Arantegui et al. (1996) did identify

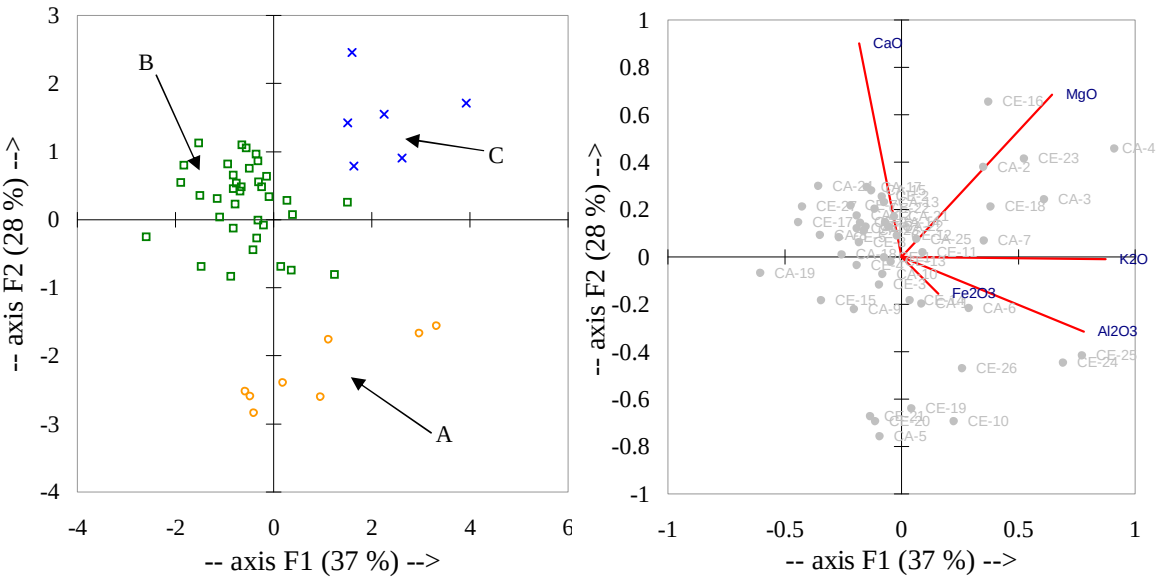

Figure 4.10: Principal component analysis (PCA) of calcareous sherds from Caesaragusta and Celsa based on MgO, Al_2O_3, K_2O, CaO, and Fe_2O_3 as oxide components. The Plot on the left shows the major groups of data: A is characterized by high Al_2O_3 and low CaO, B is high in calcium, C is a splinter group from B with higher MgO. Compositional averages of these groups may be seen in Table 4.7. The plot on the right shows the compositional vectors used to create the PCA plot.

two distinct groupings in these sherds using Ward's clustering methods. The difference between these groups was in their mean Al_2O_3 content (Group 1= 14.6% and Group 2= 11.9%). Also, Pérez-Arantegui et al. (1996) found that these two groups divided very roughly according to find spot. While similar results were obtained here using Ward's method of clustering (see Figure 4.9, the two divisional branches may be seen in the central group labelled B), the difference between the means of these two groups was deemed insignificant according to a Student's t test. Therefore, a division of the data could not be justified in this present study. As a result, these data should be considered as a broad and indiscriminate spread characterized by a CaO range between 4.9–18.3% and a Al_2O_3 range between 9.6–25.7%.

The other groups identified in the dendogram shown in Figure 4.9, which are confirmed via principal component analysis (PCA, Figure 4.10 with chemistry shown in Table 4.7), are a low calcium group (Group A, with a mean CaO of 1.5 ±0.6%) and a high MgO splinter group (Group C, mean MgO= 4.8 ±1.2%). While there is

	MgO	*Al_2O_3*	*K_2O*	*CaO*	*Fe_2O_3*
Group A	*1.82*	*20.04*	*3.11*	*1.48*	*4.95*
σ (n=8)	1.31	4.07	0.69	0.59	0.81
Group B	*2.53*	*14.09*	*2.48*	*10.86*	*4.89*
σ (n=36)	0.52	3.13	0.42	2.09	0.60
Group C	*4.75*	*18.58*	*3.92*	*12.45*	*4.46*
σ (n=6)	1.20	2.50	0.57	3.78	0.73

Table 4.7: Compositional groups identified from PCA and AHC analysis of data from Caesaragusta and Celsa.

not enough data to statistically test whether Group C does indeed form a separate group, the accompanying increase in CaO with MgO suggests that these sherds simply contain a larger percentage of dolomitic limestone than Group B. Group A, however, has a distinct chemical signature which required further comparison to other non-calcareous groups (Figure 4.11 and 4.12). Using Ward's clustering, it was found that the Group A data falls into three distinct fields: three of the data points match with the Smyrna field; one of the sherds falls into the Colchester/Silchester field; and the remaining data form a separate group which is slightly lower in Al_2O_3 than the Colchester/Silchester group and lower in CaO than the Smyrna data. As was discussed previously in the context of the plots shown in Figure 4.8, as of yet, no comparable material has been located for this relatively low Al_2O_3 and low CaO group.

4.1.3 Summary of Previous Work

The data from the literature on lead glazed sherds dating between the 2^{nd}-4^{th} centuries AD divides into five principal compositional fields (Figure 4.13). The low CaO, high Al_2O_3 field is probably from an atelier located in the regions of central Gaul. While this attribution is informed primarily by stylistic arguments, the chemistry of these sherds share many chemical characteristics with Rhenish wares from Jaulge-Villiers-Vineux and Alésia as well as terra sigillata fabrics excavated from Lezoux which corroborates central Gaul as a general area of possible origin. The provenance of the

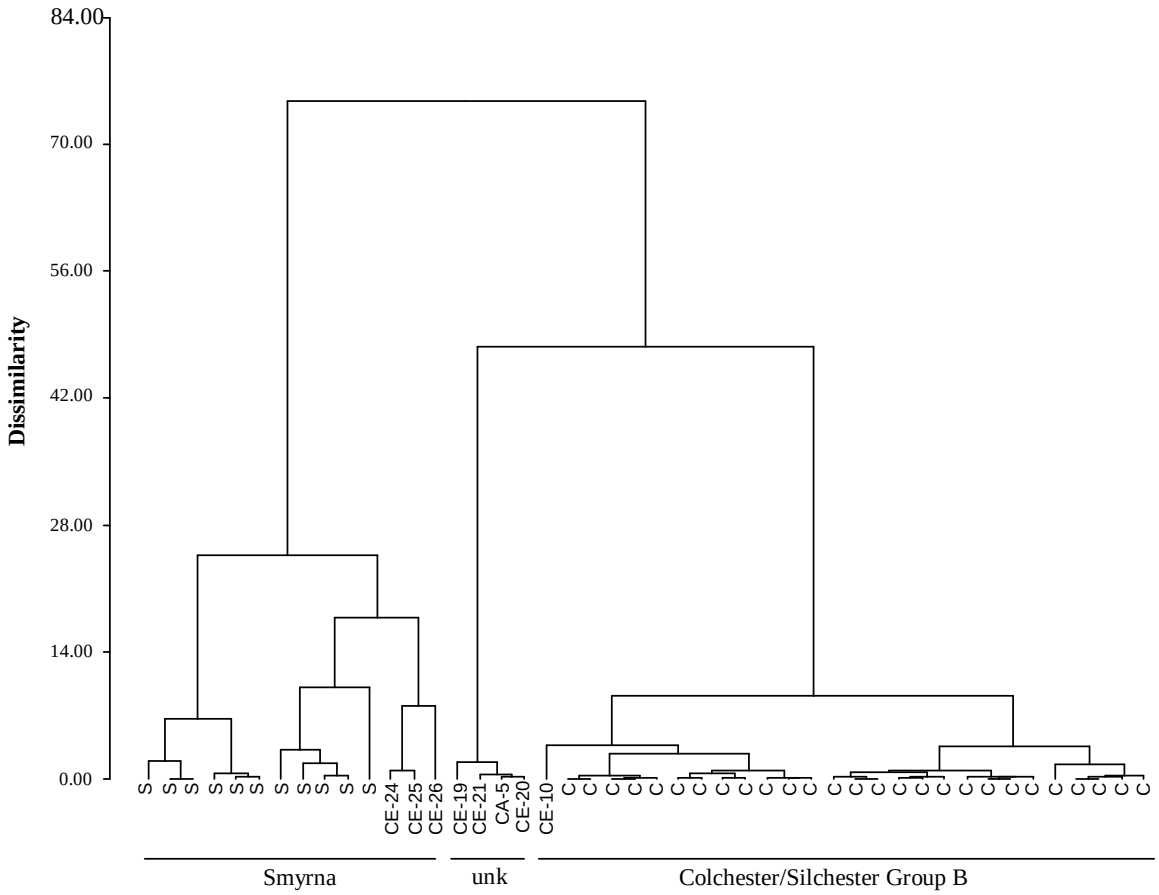

Figure 4.11: Ward's clustering of low calcium Spanish sherds (marked CE and CA) with comparison groups (C= Colchester/Silchester and S= Smyrna).

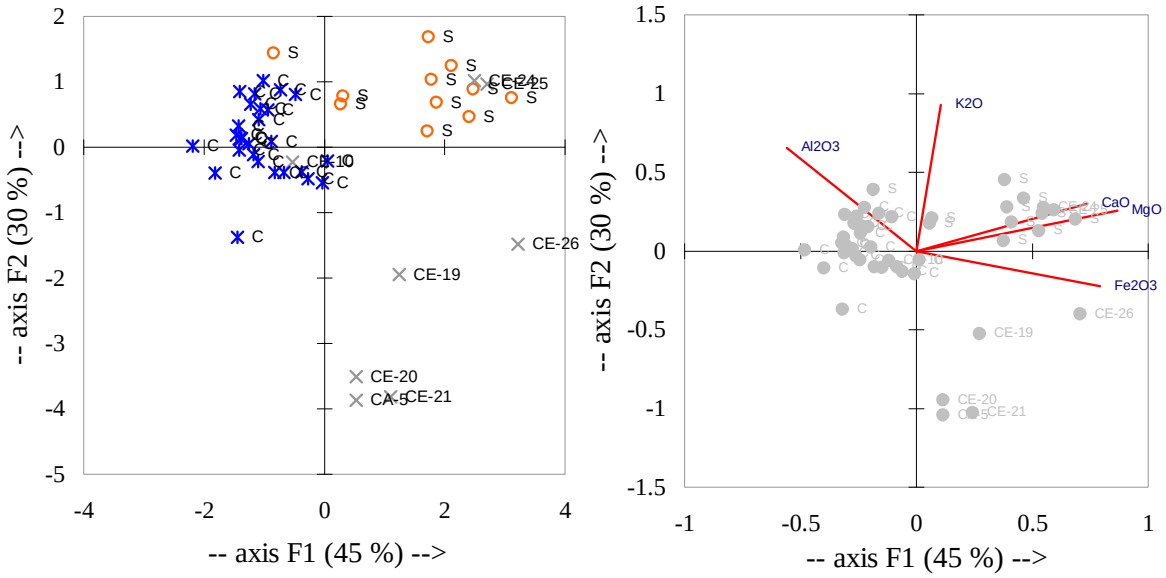

Figure 4.12: PCA of low calcareous sherds from Caesaragusta and Celsa and comparison groups (C= Colchester/Silchester and S= Smyrna).

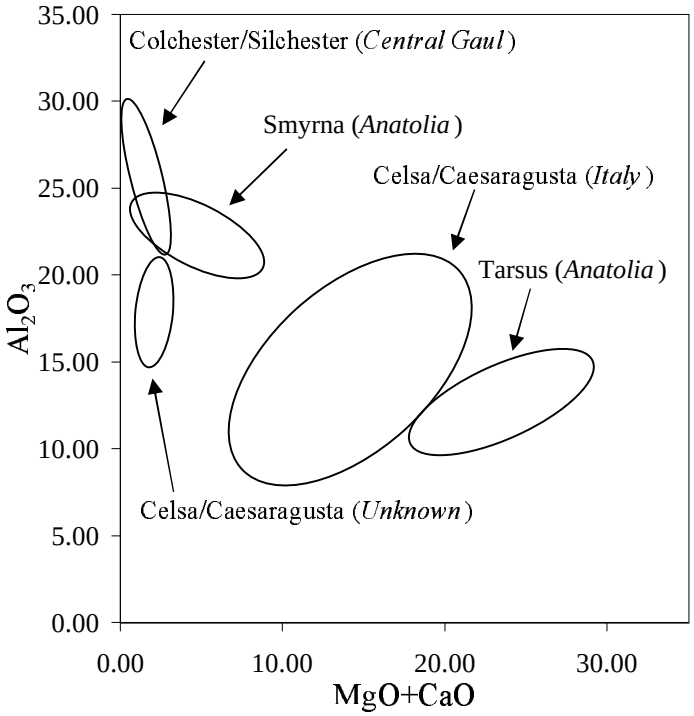

Figure 4.13: 90% confidence ellipses defining the major compositional fields of Roman lead glazed sherds identified by previous studies. For each of the fields, the find spot is labelled with the attributed provenance in parentheses.

other low CaO group, with lower Al_2O_3 than the Col/Sil group, is entirely unknown (marked "unknown" in Figure 4.13). The field labelled Smyrna which has Al_2O_3 content between 20-25% and has CaO up to 10% is from a probable workshop at this Anatolian site. The broadest compositional field is composed of calcareous sherds (CaO= 8-16%) from Celsa and Caesaragusta in Spain. Although these sherds have a likely Italian provenance as deduced by Pérez-Arantegui et al. (1996), a more specific attribution is elusive due to the scatter of these data. Finally, there is a high CaO group (CaO> 14.7%) belonging to the supposed Tarsian atelier.

4.2 New Analyses of Lead Glazed Sherds From Provincial Roman Sites

The ceramics analyzed for this project were excavated from several provincial Roman sites: London, the Upper Moesian sites of Singidunum (in present day Serbia) and

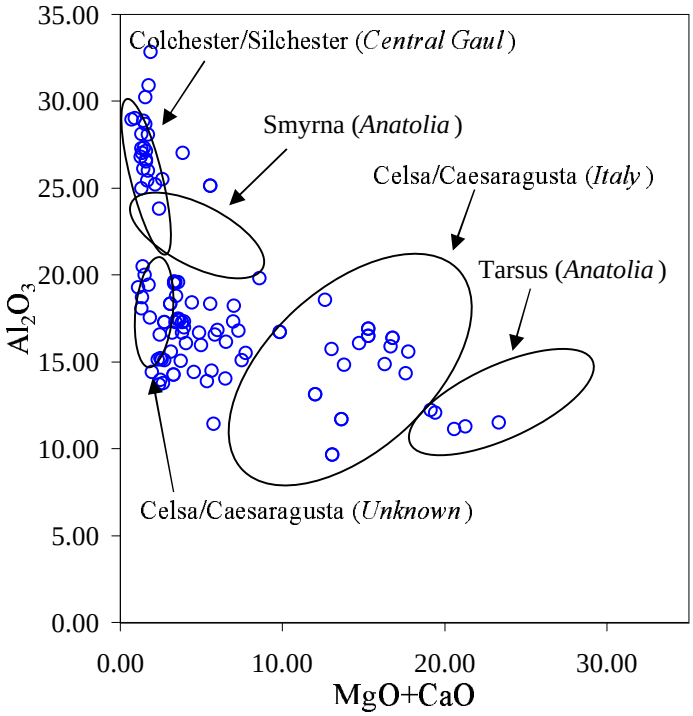

Figure 4.14: Bivariate diagram comparing lead glazed sherds with reference fields.

Diana (Serbia), Ostia (Italy), Carlino (Italy), the Dacian site of Apulum Partos (Romania), and Perge (Anatolia). The majority of the samples may be dated between the 2^{nd} and 4^{th} centuries AD. Since there was no archaeological evidence for local pottery fabrication at any of these sites (with perhaps the exception of Perge in present day Turkey), it was assumed that all wares were imports to their respective find spots.

The preparation and analytical techniques employed in this section are outlined in Appendix A, and the raw ICP-AES data may be found in Appendix C. Although, neither petrographic analysis nor mineralogical identification with SEM and EDX/WDS was performed due to the limited scope of this thesis, these analyses will be conducted prior to publication of the data which will be presented in a more in-depth provenance study. Consequently, any conclusions drawn from these data should be considered as preliminary and employed only to define discrete chemical groups which facilitate the interpretation of the glazing technology of these wares.

The compositional data divides into three main groups according to the Al_2O_3-

(MgO+CaO) discrimination plot (see Figure 4.14). The low CaO sherds divide into a tightly clustered, high Al_2O_3 group (Al_2O_3> 24%) which plots in the central Gaul field (Group 1), and a fragmented group with Al_2O_3 less than 21% and variable CaO up to 8% which plots around the "unknown" field (Group 2). The calcareous sherds plot with the Italian and Tarsian fields identified in the previous section (Group 3).

Group 1 (Al_2O_3> 25%). From these data it is clear that the sherds which plot in the central Gaul field (shown in Figure 4.14) possess a similar chemistry to the Colchester/Silchester group which define this field (see Table 4.8 for comparison of major element chemistry). Moreover, using the comparison index equation 4.1 with major element data, it may be found that these high Al_2O_3 sherds (called group 1 in its entirety) have a 93.3% similarity to the Col/Sil group. This remarkably high index suggests that 93.3% of the group 1 major element data fall within the 90% compositional volume of the Col/Sil field. However, as seen in Figure 4.15, group 1 does not form a chemically homogenous group. Eight of the sherds (labelled group 1b in Figure 4.15) are essentially identical to the Col/Sil group showing similar compositional trends and oxide ratios (see Plots A and B of Figure 4.15). A unique composition is observed for the remainder of the sherds (labelled group 1a in Figure 4.15) which exhibit higher average MgO and lower average iron than the Col/Sil group. These group 1a sherds also show strong correlations between Al_2O_3–Fe_2O_3 and Al_2O_3–MgO (Plots C and D in Figure 4.15) which are not expressed in the group 1b sherds nor with the Col/Sil group. Furthermore, it may be seen in Plots E and F of Figure 4.15 that a series of metals partition with these elements pointing toward a Fe–Mg aluminous phenocryst which is possibly an aluminum rich chlorite. It is not uncommon to find this mineral interstratified with other sheet silicates such as kaolinites or smectites. In addition, if all the Fe_2O_3 and MgO are assumed to partition into chlorite, this phase may be modelled and subtracted from the bulk whole of the clay composition. This reveals a revised composition for these fabrics that is not

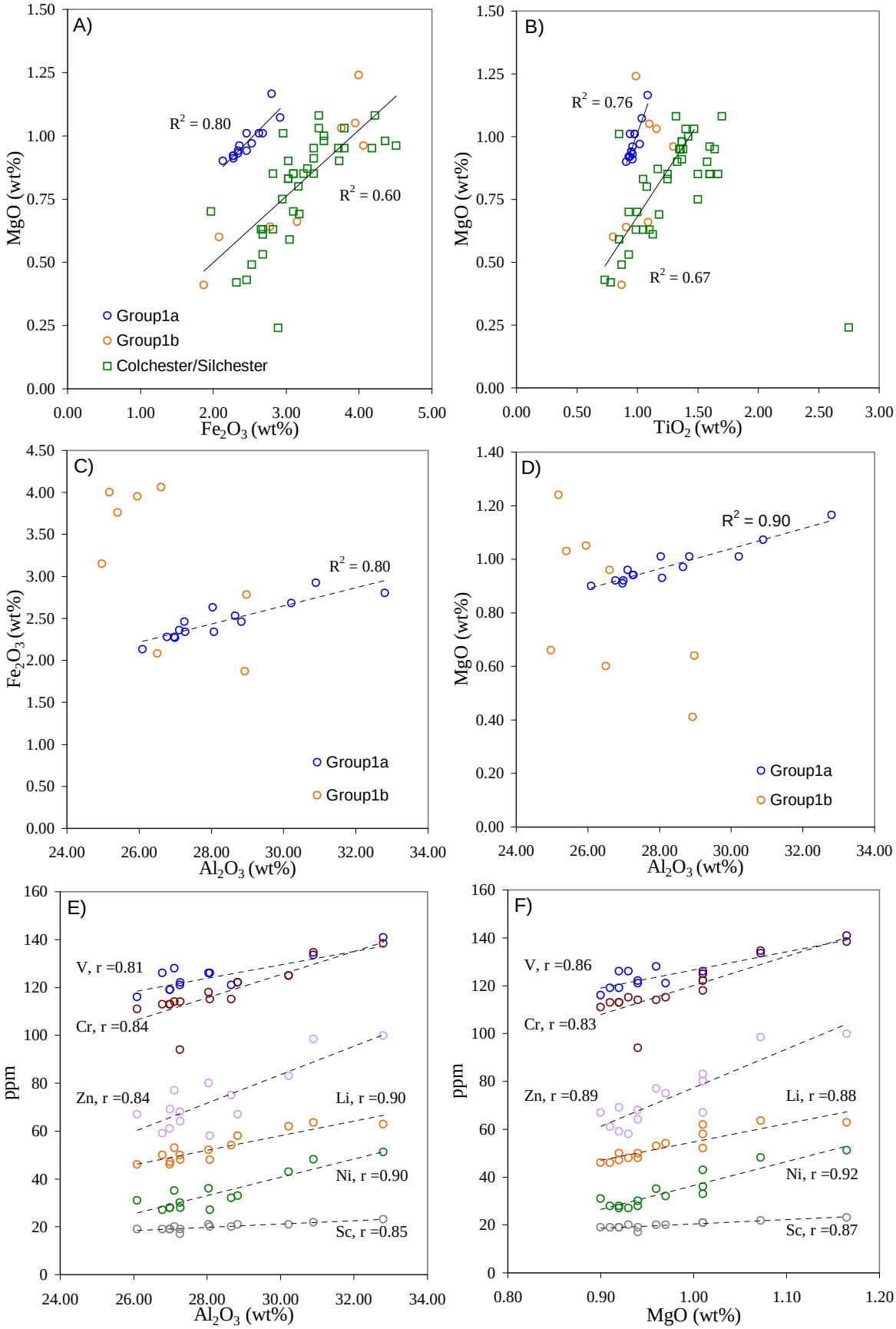

Figure 4.15: Compositional trends exhibited by sherds grouping in the central Gaul field. Only group 1a is shown in plots E and F

	Na_2O	MgO	Al_2O_3	K_2O	CaO	Fe_2O_3	TiO_2
Colchester/Silchester	*0.57*	*0.82*	*25.70*	*3.34*	*0.78*	*3.30*	*1.30*
σ (n=40)	2.67	0.80	0.23	0.44	0.37	0.71	0.36
Group 1a	*0.43*	*0.98*	*28.29*	*3.15*	*0.72*	*2.46*	*0.97*
σ (n=14)	0.11	0.07	1.87	0.69	0.65	0.23	0.05
Group 1b	*0.55*	*0.82*	*26.57*	*3.24*	*0.65*	*3.21*	*1.03*
σ (n=8)	0.42	0.28	1.59	0.56	0.26	0.88	0.17

Table 4.8: Average composition of group 1 and comparison to the Colchester/Silchester group.

	Sherds in Group1
Group1a	D-5315, D-5315a, D-5315b, D-4753, D-5655
	D-5571, D-5571a, D-5571b, D-nonumb, D-202
	D-13355, S-1, S-2, S-5
Group1b	Picon1, Picon2, Picon3, L-LCT84b, L-BGH95
	L-LIM83, L-179 BHS89, D-93-1510

Table 4.9: Sherds belonging to group 1. The sherds are labelled as follows: D are from Diana (Serbia), S are from Singidunum (Serbia), the Picon samples are from the region of Lezoux in central Gaul (France), L are from London (England).

dissimilar to an illite as indicated by the proportions of remaining Al_2O_3 and K_2O.

The sherds that fall into group 1a and group 1b have diverse origins (Table 4.9). It seems that all the sherds that fall into group 1a are from the Iron Gates region of Upper Moesia (Serbia) with find spots from the archaeological sites of Diana and Singidunum. Group 1b includes the majority of the Colchester/Silchester material as well as sherds excavated from London and from the Lezoux region of central Gaul. A single sherd from Diana may be found among this group. With the exception of this one sherd (D-93-1510, which dates to archaeological contexts between the 3^{rd} and 4^{th} centuries A.D.), both groups contain sherds that come from stratigraphic levels which date firmly between the 1^{st} and 2^{nd} centuries AD.

By taking into consideration their common buff colour of these sherds in hand specimen and their monochrome yellow glazes, all of the sherds belonging to both group 1a and group 1b have been identified as being part of the same central Gaul group to which the Col/Sil group also belongs (Symonds 2001). This finding is corroborated by the data shown in Table 4.8 which shows only insignificant differences

between averages for all the groups in question. As was discussed previously in regards to the Col/Sil group, although the chemistries of group 1a and 1b are consistent with what would be expected from this region, there is no specific evidence for lead glaze fabrication in central Gaul. Therefore, other possible sources may not be precluded as the origin of these sherds. For instance, many of the sherds collected from the Serbian and Romanian sites in this thesis could have been produced from the local Danubian clays, which, like the Gaulish clays, are low calcareous illitic clays that can contain significant amounts of quartz (Marković et al. 2004; Müller and Stoffers 1974). It is interesting, following this line of thought, that lead isotope data from group 1a shows that the Pb used in these glazes is from a source found in the Balkans (see section 4.3 of this Chapter for further details). From an archaeological point of view, however, central Gaul represents their most obvious Western source given the large number of terra sigillata workshops in the area making it one of the industrial centers of pottery production in the Roman world.

Group 2 (low CaO, Al_2O_3= 15–20%). These sherds plot around the "unknown" field in Figure 4.14. Unlike the group 1 data, group 2 possesses none of the strong elemental correlations which are indicative of specific mineralogical trends. This makes it more difficult to confirm discrete and homogenous groupings. However, these data may be seen to nominally divide into five subgroups (plots A–D in Figure 4.16 and average data in Table 4.10). The greatest variance in the data may be seen between group 2c and the remainder of the sherds (see plots A, B, and C in Figure 4.16). Group 2c is characterized by its relatively high CaO (CaO= 2.8–5.7%) and low TiO_2 content. Also, in comparison with the other sherds, group 2c only has trace amounts of Sr^{2+} which often substitutes for the Ca^{2+} ion in calcium bearing minerals (see plot D in Figure 4.16). In contrast, group 2a shows a strong correlation between Sr and CaO (r=0.93), and much high Sr values. Also, group 2a separates from the other sherds in terms of its TiO_2 as well as high alkali and Fe_2O_3 levels (plot A in

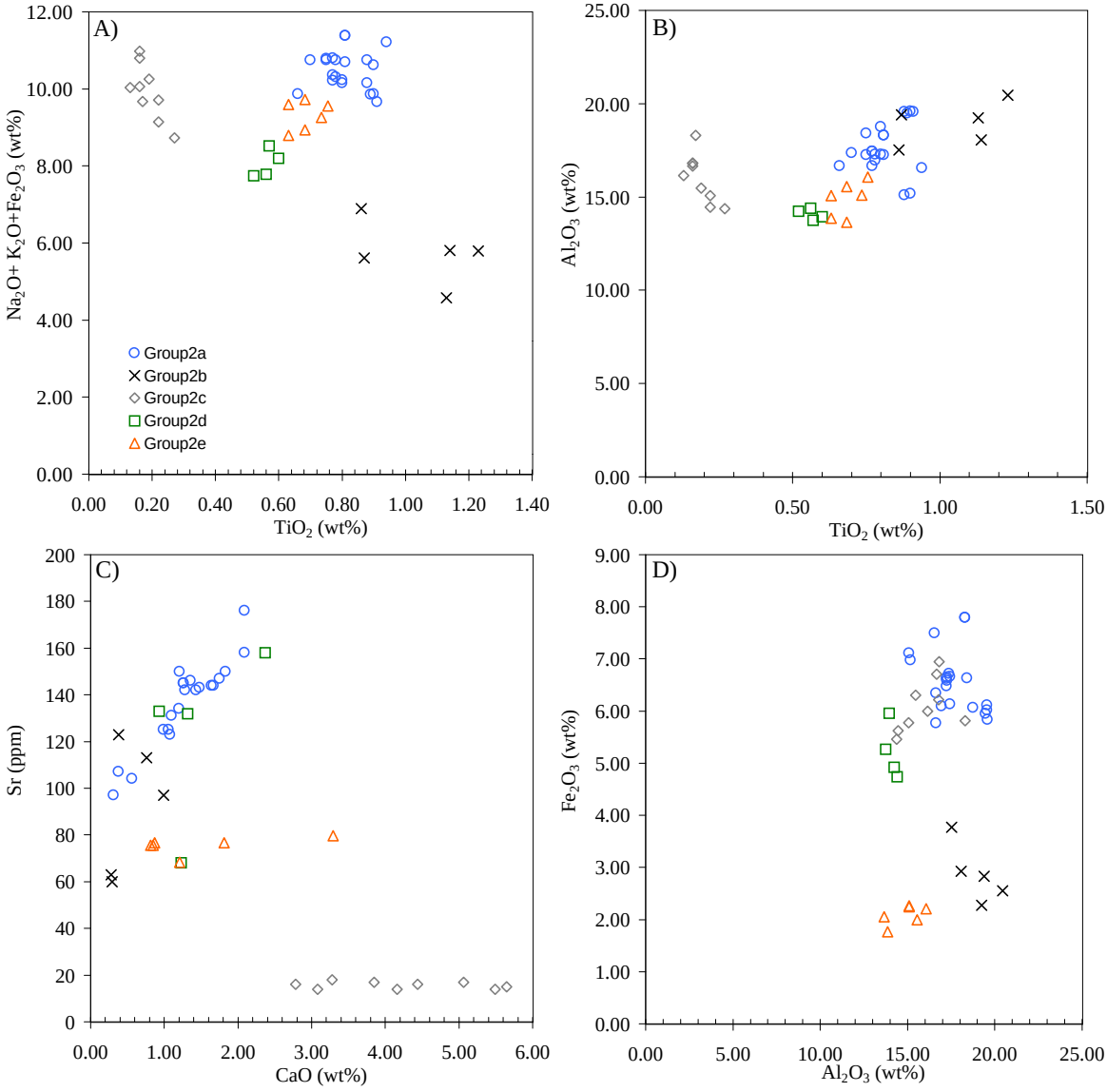

Figure 4.16: Discriminant plots showing the subgroups of group 2.

	Na_2O	MgO	Al_2O_3	K_2O	CaO	Fe_2O_3	TiO_2
Group2a	*1.15*	*2.10*	*17.63*	*2.78*	*1.29*	*6.56*	*0.81*
σ (n=21)	0.36	0.25	1.31	0.33	0.48	0.60	0.07
Group2b	*0.49*	*0.97*	*18.94*	*2.38*	*0.54*	*2.87*	*1.05*
σ (n=5)	0.45	0.18	1.16	0.48	0.32	0.57	0.17
Group2c	*1.26*	*2.01*	*16.01*	*2.58*	*4.20*	*6.09*	*0.19*
σ (n=9)	0.11	0.30	1.28	0.33	1.05	0.50	0.04
Group2d	*0.68*	*1.16*	*14.09*	*2.16*	*1.46*	*5.22*	*0.56*
σ (n=4)	0.33	0.17	0.29	0.26	0.63	0.54	0.03
Group2e	*0.86*	*1.93*	*14.88*	*6.36*	*1.47*	*2.09*	*0.69*
σ (n=6)	0.07	0.24	0.95	0.36	0.97	0.19	0.05

Table 4.10: Average group 2 data.

	Sherds in group 2
Group 2a	L-KWS94, L-LBI95, L-LCT84a, D-94-4736, D-C141/96, D-2553 D-93-573/1/29, D-93-4741, Nat. Museum, S-6, S-7, AP-1131, AP-1270 AP-1850, AP-1694, AP-1797a, AP-1797b, AP-1770, AP-1970, AP-1784
Group 2b	L-Pom79, D-93-2060, D-93-3033, S-3, S-4
Group 2c	D-C135/96, D-nodata, D-93-1709a, D-93-4350, AP-1432, AP-1121 AP-Spoil, AP-2215, AP-1007
Group 2d	O-RZ5636, O-RZ5653, O-RZ5658, O-RZ5258b
Group 2e	C-1, C-2, C-3, C-4, C-5, C-6

Table 4.11: Sherds belonging to group 2. The sherds are labelled as follows: D are from Diana (Serbia), S are from Singidunum (Serbia), L are from London (England), AP are from Apulum Partos in Abulia (Romania), O are from Ostia (Italy), and C are from Carlino (near Trieste, Italy).

Figure 4.16). Groups 2b and 2e separate from the others subgroups due to their low Fe_2O_3 levels as may be seen in Plot D in Figure 4.16. These two subgroups may be discriminated from one another, however, by their alkali content with group 2e showing the higher values (as per plot A and see K_2O levels in Table 4.10). The remaining subgroup, group 2d, shares characteristics with 2e, but possesses a greater amount of Fe_2O_3.

As may be seen in Table 4.11, groups 2a–2c contain sherds from geographically disperse findspots: London, Serbia, and Romania. Also, if the "unknown" low CaO data of Pérez-Arantegui et al. (1996) is considered (discussed in the previous section, see Figure 4.13), then the Tarraconensis region of Spain represents another find spot of these fabrics (see Figure 4.17, the Celsa data from Pérez-Arantegui et al. (1996)

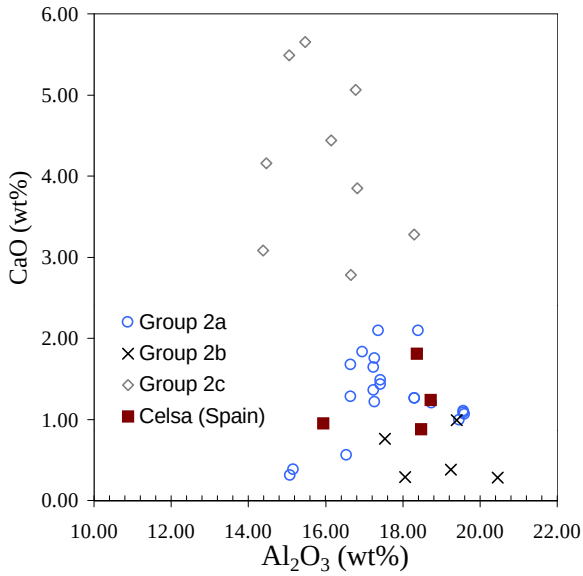

Figure 4.17: Low CaO containing sherds from Spain (the "unknown field" in Figure 4.13) plotting with the other group 2 sherds of contemporary date.

plots close to group 2a in Al_2O_3-CaO space). Groups 2d and 2e contain sherds only from Ostia and Carlino respectively. Since the Ostia and Carlino groups both date to the 5^{th} century AD and, also, possess unique clay chemistries, they probably represent local production at their individual find spots. The data in the 2a–2c groups have dates that range from the 2^{nd}–4^{th} centuries AD. This suggests that the wares which form these subgroups are part of long-lived production lines. Unfortunately, no comparable fabrics of known provenance could be located to pin down the fabrication origin of this material. The archaeological and stylistic features of groups 2a–2c resemble the Group 1a and 1b material – suggesting a central Gaul origin – but it could be equally argued that these sherds represent local production of the Danubian provinces. This scenario is plausible given that the majority of these sherds in groups 2a–2c were excavated in this Serbian region, and that their chemistries are not inconsistent with what would be expected from many Danubian clay deposits.

Group 3 (CaO> 16%). The sherds belonging to this high CaO group plot around the Italian fields in Figure 4.14. These sherds separate into two divisions: one with low Al_2O_3 (Al_2O_3< 12.2%) and high CaO (CaO> 16.2%), and the other with a

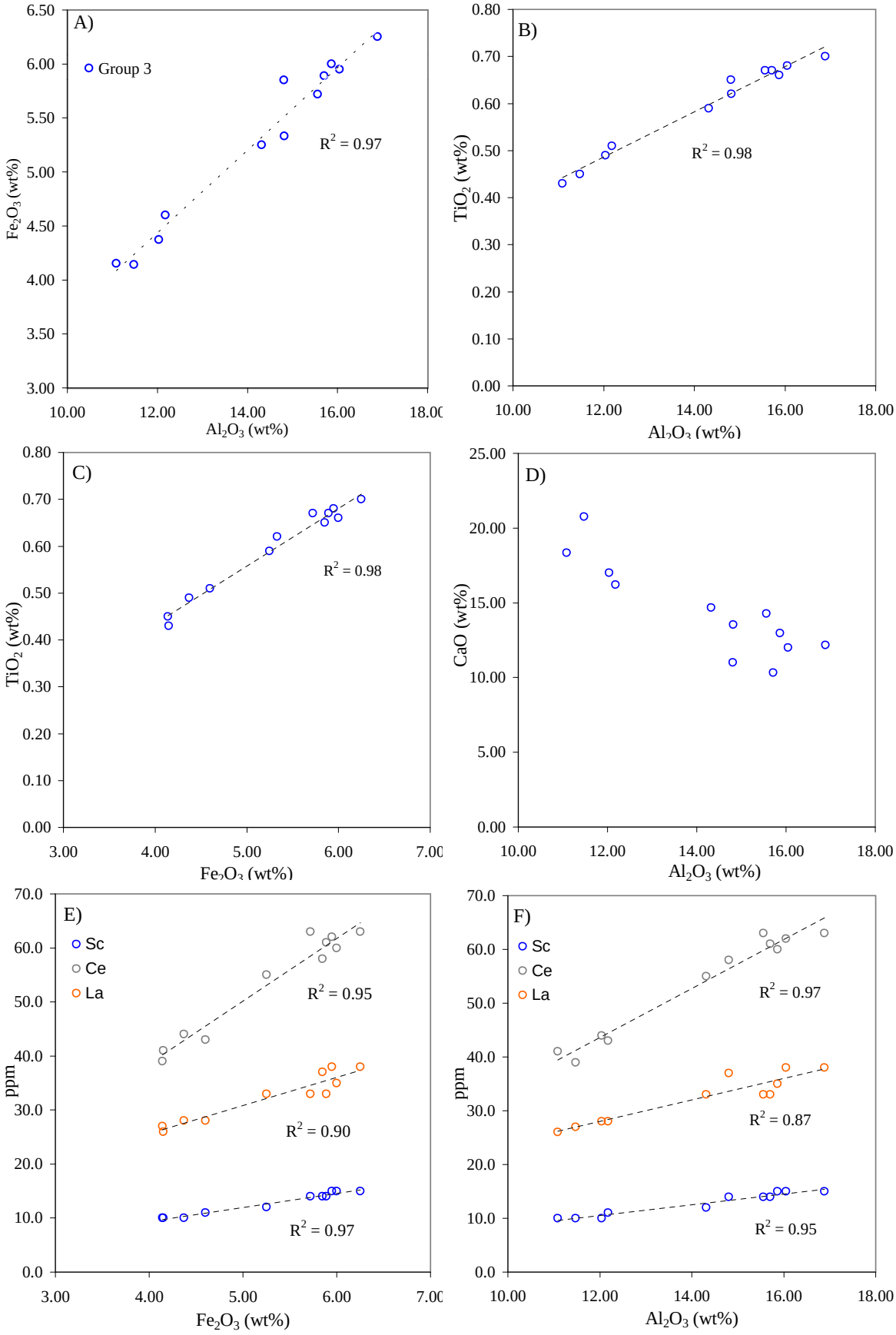

Figure 4.18: Compositional trends exhibited by sherds grouping in the high Ca fields.

	Na_2O	MgO	Al_2O_3	K_2O	CaO	Fe_2O_3	TiO_2
Group 3	*0.96*	*2.90*	*14.18*	*2.52*	*14.52*	*5.29*	*0.59*
σ (n=11)	0.20	0.43	2.09	0.28	3.27	0.82	0.10
Spain	*1.00*	*2.84*	*14.63*	*2.44*	*11.90*	*5.31*	*0.68*
Taranto	*0.42*	*3.31*	*12.70*	*1.99*	*12.25*	*5.66*	*0.73*
Latium/Campania	*na*	*3.50*	*16.94*	*2.88*	*13.63*	*6.59*	*0.76*
Perge-1	*2.52*	*1.66*	*16.68*	*3.72*	*8.20*	*4.39*	*0.57*
Perge-2	*1.32*	*2.79*	*14.82*	*2.94*	*13.55*	*5.33*	*0.62*
Tarsus	*0.54*	*4.84*	*14.12*	*2.74*	*17.65*	*6.49*	*0.66*
Smyrna	*0.71*	*1.73*	*20.95*	*3.97*	*3.41*	*4.88*	*0.88*

Table 4.12: Average composition of group 3 and comparable calcareous fabrics. Data forming the reference groups are compiled from Pérez-Arantegui et al. (1996)(for the Spanish material) and Hatcher et al. (1994) (for the Taranto, Latium/Campania, Tarsus, and Smyrna material). The Perge reference sherds were analyzed during this present study.

lower CaO content (less than 15% CaO). While this is a valid statistical division, the data examined as a whole shows strong correlations between Al_2O_3–Fe_2O_3, Al_2O_3–TiO_2, and TiO_2–Fe_2O_3 (See plots A-C in Figure 4.18). Also, several trace elements (Sc, La, and Ce) show positive correlations to Al_2O_3 and Fe_2O_3 (plots E and F in Figure 4.18) in all the data. These compositional trends demonstrate that the sherds share a common Ti rich alumino-ferrous mineral. While the exact nature of this mineral is not known, it may possibly be associated with an aluminum rich augite that can occur in metamorphosed limestones. More importantly, the presence of this mineralogical trend indicates that these sherds all come from the same general clay source. Plot D in figure 4.18 shows a negative correlation between CaO and Al_2O_3 indicating that Ca is not hosted among the clay minerals and is therefore likely to be associated with a carbonate mineral. This observation, taken together with the overall high calcium content of these fabrics, provides the evidence to suggest that these clays were formed from weathering limestones.

Following the arguments of Pérez-Arantegui et al. (1996), the calcareous fabrics presented here share compositional characteristics with other wares coming from Italy (see Table 4.12 for compositional comparisons). In particular, the sherds share many similarities to those from Latium/Campania (see plots A–D in Figure 4.19). Given

	Sherds in Group 3
Group 3	L-DGH86, L-SWA81, L-SH74, Picon-4, O-Campione1 O-Campione2, O-Campione3, O-RZ5574, O-RZ5637 O-RZ5670, O-RZ5848

Table 4.13: Sherds belonging to group 3. The sherds are labelled with the following prefixes: L are from London (England), Picon are from central Gaul, and O are from Ostia (Italy).

that several of the sherds analyzed in group 3 come from this area, it may be speculated that this region represents the origin of their fabrication. It is certain that the composition of these sherds are unlike those excavated from the Anatolian workshops sites of Perge, Tarsus, and Smyrna (see Table 4.12 and plot A in Figure 4.19).

Group 3 is composed of sherds with find spots from London, central Gaul as well as from the sites of Ostia and Campania (Campione) in Italy (Table 4.13). Although the dates of these sherds range from the 2^{nd} through 5^{th} centuries AD, those from central Gaul and Campania have early dates in the 2^{nd} century, where as the sherds from Ostia date to the 3^{rd} century AD with the exception of RZ5637 which dates to the 5th century. Unfortunately, the sherds from London were found in undatable archaeological contexts, but they are likely to be early examples on account of their decoration and their two toned colouring.

4.2.1 Summary of ICP-OES Analyses

The sherds analyzed for this thesis cluster into eight geochemically distinct groups. The easiest group to discriminate from the others is the high Al_2O_3 group which may be tentatively assigned to a workshop, or workshops, located in central Gaul. This group divides into two subgroups, group 1a and group 1b, following different mineralogical trends. Both of these subgroups contain sherds that date predominantly to the 1^{st}–2^{nd} centuries. The lower Al_2O_3 cluster, collectively labelled as group 2, is geochemically complex but may be seen to divide into five subgroups. Two of these subgroups, 2d and 2e, are composed entirely of sherds excavated from Ostia and Carlino respectively. Both of these groups date to the late antique in the 5^{th} century

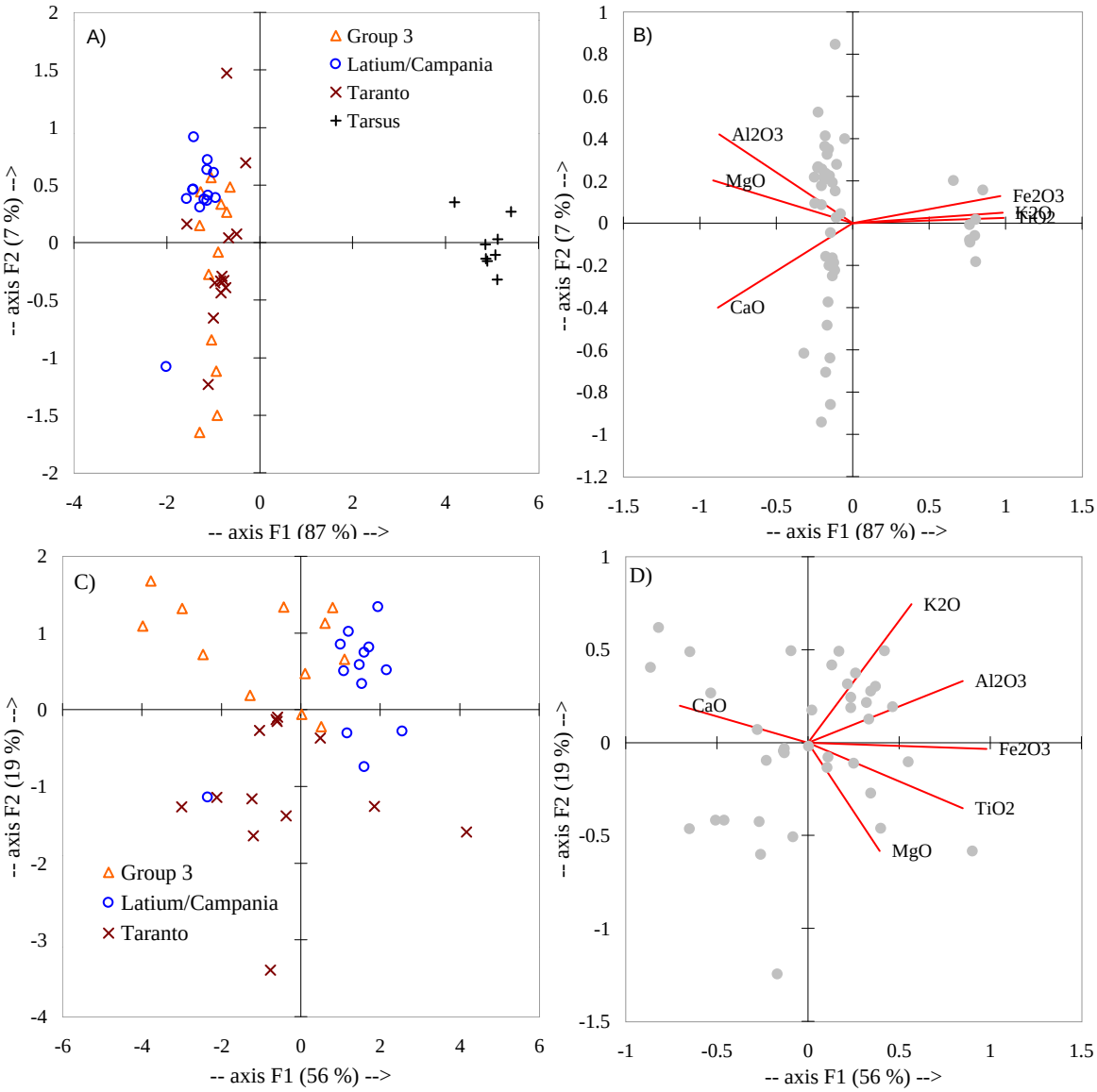

Figure 4.19: Principal component analysis of group 3 sherds with other high Ca groups of known origin using major oxide abundances. Plots B and D show the compositional vectors used to describe the data respectively in plots A and C. Plot A shows that none of the group 3 match with the Anatolian Tarsian group into which the sherds from Perge (analyzed in this study) also fall (see Table 4.12). Plot B shows that group 3 sherds share major oxide characteristics with the Latium/Campanian and Taranto groups.

and are therefore not directly comparable to the earlier sherds. The remainder of the subgroups 2a–c contain sherds that date from the 2^{nd}–4^{th} centuries. Despite having stylistic features consistent with those thought to originate from central Gaul, these sherds have an unknown provenance. Lastly, the high CaO sherds form a single group (called group 3) of probable Italian origins. More specifically, since this cluster shares features with the Latium/Campanian reference group, these sherds are likely products from workshops in these cites. The group 3 sherds date between the 2^{nd}–5^{th} centuries and therefore represents the longest lived clay source discussed in this study.

4.3 Pilot Analyses of Lead Isotope Ratios in Lead Glazes

The aim of these lead isotope analyses was to demonstrate that clusters of lead glazes could be identified with this method which might point toward unique Pb ore bodies exploited for this primary raw material. These data are used to further corroborate and discriminate the groupings presented in the previous section. In addition, this study should be considered as a preliminary effort designed to make these data available to a wider audience.

Representative samples were chosen from each of the groups identified in the previous section. Samples were prepared by flaking or scraping the glaze off the ceramic body. These samples were submitted to the NERC Isotope Geosciences Laboratory of the British Geological Survey (Nottingham, UK) for lead isotope measurement using their thermal ionization mass spectrometer (TIMS). The ratio TIMS data is presented in Table 4.14. The standard lead isotope ratio plots of these data may be seen in Figure 4.20. Matches to known ore sources were made using the OXALID database developed by the Isotrace laboratory formerly of RLAHA, Oxford.

The data presented in Table 4.14 and Figure 4.20 is particularly interesting considering that the sources of lead divide into two main groups which, perhaps incidentally,

Fabric	*Findspot and Sample*	*Earliest Date*	$^{208}Pb/^{206}Pb$	$^{207}Pb/^{206}Pb$	$^{206}Pb/^{204}Pb$	*OXALID Match*
G1a	Diana 5315A	1^{st} c.	2.077853	0.838516	18.695	East Rhodope
G1a	Diana 5571A	1^{st} c.	2.077959	0.838524	18.696	East Rhodope
G1a	Diana 5655	1^{st} c.	2.078262	0.838611	18.695	East Rhodope
G1a	Singidunum S1	2^{nd} c.	2.078117	0.838621	18.695	East Rhodope
G1a	Singidunum S5	2^{nd} c.	2.078079	0.838521	18.697	East Rhodope
G1b	Lezoux Picon 1	1^{st} c.	2.084848	0.844079	18.535	Sardinia?
G1b	Lezoux? Picon 2	1^{st} c.	2.097166	0.850666	18.397	Massif Centrale Mt Noire
G1b	Vichy-S.Remy Picon 3	1^{st} c.	2.072763	0.837223	18.701	Wiesloch - Baden Wurtenberg
G1b	London BGH95	1^{st} c.	2.097767	0.850958	18.407	Massif Central or Wales
G1b	London LCT84B	1^{st} c.	2.085937	0.845579	18.519	Alderley edge
G1b	Diana 93-1510	3^{rd}–4^{th} c.	2.078200	0.838627	18.693	East Rhodope
G2a	Diana 94-4736	1^{st} c.	2.083208	0.841101	18.636	Central Rhodope
G2a	Singidunum S6	2^{nd} c.	2.083037	0.841013	18.639	Central Rhodope
G2a	London LCT84A	2^{nd} c.	2.086694	0.849618	18.406	Mendips
G2a	Apulum Partos 1694	2^{nd} c.	2.085208	0.845363	18.523	Panagyurski (N. Bulgaria)
G2a	Apulum Partos 1131	2^{nd} c.	2.078101	0.838651	18.692	East Rhodope
G2a	London LB195	3^{rd} c.	2.086497	0.849494	18.410	Mendips
G2a	Diana 93-573/1/29	3^{rd}–4^{th} c.	2.086807	0.843684	18.573	Rhodope
G2b	Singidunum S4	2^{nd} c.	2.078216	0.838655	18.694	East Rhodope
G2b	Diana 93-3033	3^{rd}–4^{th} c.	2.085564	0.842920	18.593	Rhodope
G2c	Diana C135/96	1^{st} c.	2.083608	0.841255	18.634	Central Rhodope
G2c	Apulum Partos 1121	2^{nd} c.	2.078802	0.839261	18.678	Rhodope
G2c	Diana 93-4350	3^{rd}–4^{th} c.	2.088847	0.844767	18.551	Rhodope
G2d	Ostia RZ5636	5^{th} c.	2.091079	0.847525	18.467	Massif Central
G2d	Ostia RZ5653	5^{th} c.	2.093840	0.849616	18.416	Massif Central
G2e	Carlino 1	4^{th}–5^{th} c.	2.085829	0.843590	18.571	Sardinia?
G2e	Carlino 4	4^{th}–5^{th} c.	2.084187	0.838329	18.714	Tuscany
G2e	Carlino 5	4^{th}–5^{th} c.	2.086261	0.842864	18.600	Sardinia?
G3	Ostia Campione 1	2^{nd} c.	2.095421	0.851466	18.367	Cumbria or Massif Central
G3	Ostia Campione 3	2^{nd} c.	2.092829	0.851094	18.374	Northumberland or Massif Central
G3	Ostia RZ5574	3^{rd} c.	2.092287	0.849773	18.412	Cumbria Alston
G3	Ostia RZ5670	3^{rd} c.	2.087211	0.846684	18.490	Durham or Massif Central
G3	London SWA81	2^{nd} c.	2.092712	0.850008	18.414	Cumbria Alston
G3	London DGH86	3^{rd} c.	2.084947	0.843607	18.577	Schwarzwald
Tarsus	Perge V24S97-2256	1^{st} c.	2.082409	0.837038	18.736	Central Rhodope

Table 4.14: Lead isotope data of glazes grouped according to fabric type. Matches to Roman Lead anchors and other lead containing metals from the period were made using the OXALID database (Stos 2004).

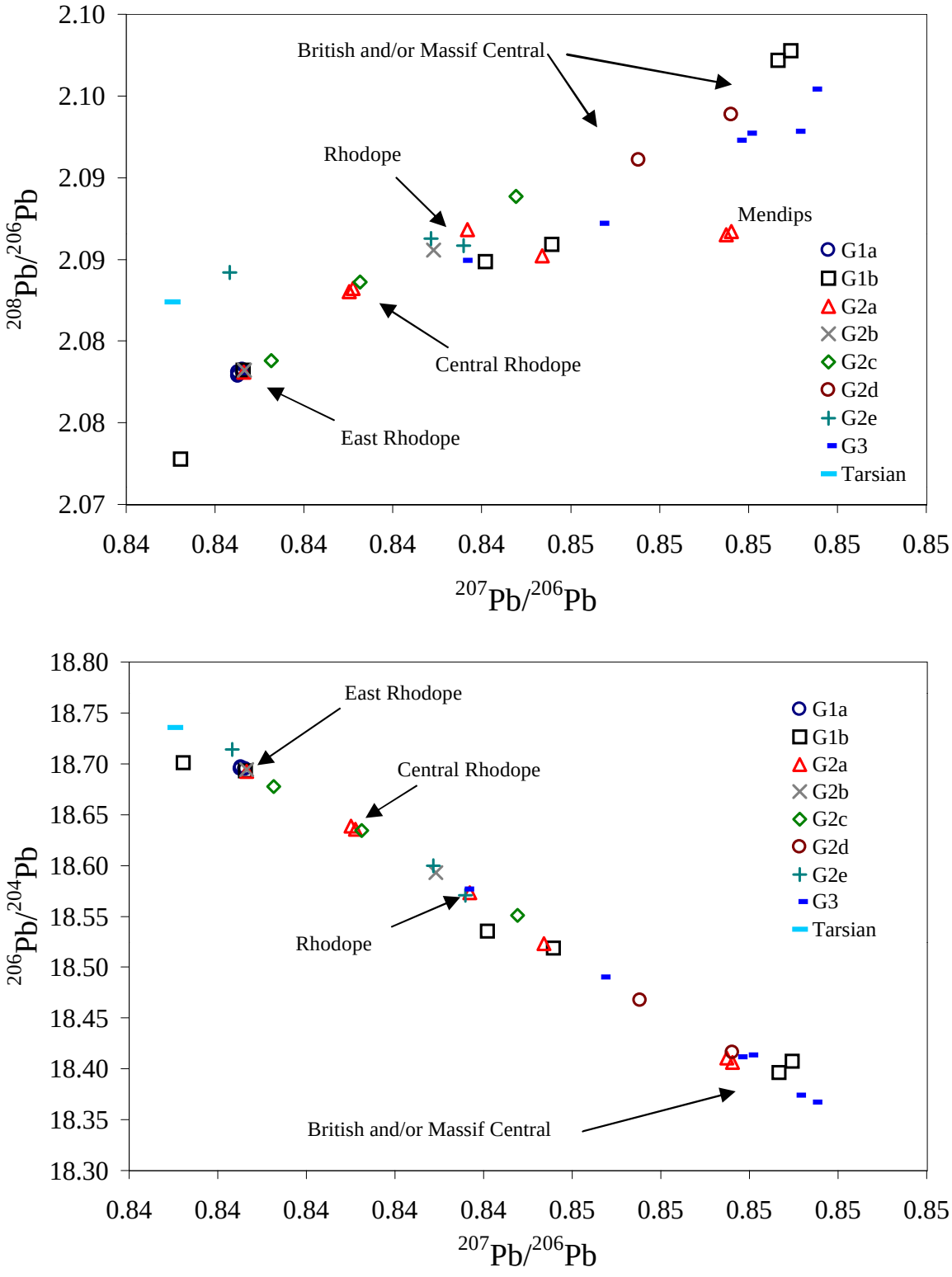

Figure 4.20: Bivariate plots of lead isotope ratios of fabric groups identified in the previous section. Labels show the approximate locations of some of the ore fields (according to the OXALID database) in ratio space.

Probable Fabric Group	*Find Spot and number*	*Probable Provenance*	$^{208}Pb/^{206}Pb$	$^{207}Pb/^{206}Pb$	$^{206}Pb/^{204}Pb$	*OXALID match*
G1b	? RG 64	Central Gaul	2.09597	0.85025	18.419	Sardinia - Ozieri
G1b	Colchester RG 60	Central Gaul	2.09141	0.85157	18.389	Austria?
G1b	Colchester BKC 75 J 188	Central Gaul	2.11004	0.85943	18.225	Tyrol
G3	Colchester RG 83	S. Italy	2.09388	0.85136	18.382	Austria?
G3	? RG 2	S. Italy	2.09590	0.85272	18.343	Tyrol
G3	? RG 3	S. Italy	2.10078	0.85530	18.284	Austria
Tarsian	? RG 10	Asia Minor	2.07117	0.83634	18.748	Rhodope
Tarsian	? RG 9	Asia Minor	2.07297	0.83780	18.702	East Rhodope
Tarsian	Paphos RG 11	Tarsus	2.08731	0.84408	18.581	Sardinia - Capo Marargiu
Tarsian	Tarsus RG 5	Tarsus	2.09551	0.85046	18.427	Sardinia or Anatolia-Izmir
Tarsian	Xanthos RG 8	Asia Minor	2.09898	0.85291	18.368	Sardinia

Table 4.15: Lead isotope data corresponding to the sherds from Hatcher et al. (1994).

also correspond to the find spots for the sherds. Excluding the later pottery from Carlino, it may be seen that the Roman pottery from central Gaul, London, and central Italy all have glazes derived of lead from ores located in Western Europe (Stos 2004). In particular, British and Central Gaul (Massif Central) sources are well represented. The Serbian and Romania sherds, on the other hand, have lead isotope ratios which match sources exclusively from the Rhodope Mountains of Bulgaria. The single sherd from Anatolia (Perge) which falls into the Tarsian compositional field (see Figure 4.14) also seems to possess lead from the Rhodope region. Similar results were obtained from the earlier, but unpublished, Pb isotope ratio study which corresponds to the sherds analyzed by Hatcher et al. (1994). These data, presented in Table 4.15, again show that fabrics which originate in Western Europe have lead sources from European deposits. In these cases, lead sources from Austria, Tyrol, and Sardinia were identified through searching the OXALID database. Sherds that fall into the Tarsian field from Hatcher's data set also possess glazes with Rhodope isotope signatures as well as possible Sardinian signatures.

When combined with the data on fabric composition, this lead isotope data underscores the possibility– mentioned in the previous section– that the Serbian and Romanian sherds represent local production in these respective areas. It should be equally emphasized, however, that lead in the Roman world was a widely transported

item used in the fabrication of a variety of commodities including pipes in buildings, anchors on ships, and, when mined from an argentiferrous ore, in coin alloys. Therefore, there is a distinct probability that lead from the Rhodope region was in wide circulation in Western Europe as well as in Asia Minor during the period in question. Because of these arguments, unfortunately, little may be definitively stated about the origins of the Serbian and Romanian material based on their fabric compositions and glaze isotope signatures.

4.3.1 Conclusions

Additional data is clearly needed to substantiate the trends presented above. Furthermore, it would be potentially illuminating to understand the history of Roman lead exploitation in regards to the ore bodies identified in this study and how these deposits may have related to the provenance of the sherds. Ultimately such information would be useful in reconstructing pottery workshop economies during the Roman period.

Chapter 5

The Technology of Archaeological Lead Glazes

In Chapter 3 the two most viable routes for producing lead glazes were discussed: glazing with either PbO alone or with $PbO{\cdot}SiO_2$ mixtures. On the basis of the microstructural and chemical criteria associated with both of these glazing methods, this chapter will attempt to reconstruct the fabrication processes of a wide selection of archaeological samples ranging from Hellenistic through Islamic contexts. The bulk of this discussion will focus on a comparison of the various Roman glazing techniques as they pertain to each of the compositional groups outlined in Chapter 4. This examination of the chemistry and micro-structural features associated with these glazes constitutes the first comprehensive description of lead glaze technology used by the Romans and their successors.

The chapter begins with a discussion of the differences between glazing using either a non-calcareous fabric (*i.e.*, groups 1 and 2 in Chapter 4) or a calcareous fabric (*i.e.*, group 3 in Chapter 4). This discussion considers both the raw materials and the firing conditions which contribute to the final glaze chemistry. The description of the 2^{nd}–4^{th} century lead glazing technology of the Romans is followed by a re-interpretation of the X-ray fluorescence (XRF) analyses of Hatcher et al. (1994) which includes many early lead glaze wares unavailable to this present study. Finally, the Roman technology at its apogee (*i.e.*, the glazes of the 2^{nd} c. AD) is compared with sherds from the late

antique (5^{th}-7^{th} c. AD) in Italy and Asia Minor, and also from Byzantine, Islamic, and Chinese contexts (7^{th}-14^{th} century AD).

Sample preparation and the electron microprobe (EPMA) methods used to collect the data for this chapter are outlined in Appendix A. For all the glazes, analytical measurements were obtained at the glaze edge as well as at the ceramic interface to assess chemical gradients. On a few representative sherds, full length profiles along cross-sections were collected in order to examine the shape of the gradients. As was discussed in Chapter 3, glaze gradients provide information on raw materials utilized, firing temperatures, and firing times. All the raw EPMA data is presented in Appendix C.

5.1 Fabrication of Roman Lead Glazes: 2^{nd}–4^{th} c. AD

The technology for each of the Roman lead glazes examined in this thesis is summarized in Figure 5.1. The plots shown in this figure are based upon the work presented in Chapter 3 where the two fundamental techniques of glazing with PbO were outlined: 1) applying PbO directly to a fired or unfired ceramic fabric, or 2) the application of a $PbO{\cdot}SiO_2$ mixture or frit. As shown by Hurst and Freestone (1996), these two methods may be differentiated from one another by a simple data reduction procedure: lead oxide and any intentionally added colourant (*i.e.*, CuO) is subtracted from the glaze composition total and the resulting composition is normalised to 100% as shown in equation 5.1.

$$C_i^* = \frac{C_i \cdot 100}{\sum_{i=1}^{N} C_i - (C_{PbO} + C_{CuO})} \tag{5.1}$$

where C_i is the concentration of oxide i in the glaze and C_i^* is the adjusted concentration of oxide i.

After this data treatment, the glaze composition may be directly compared to the fabric composition. If the glaze and fabric chemistries are the same, within

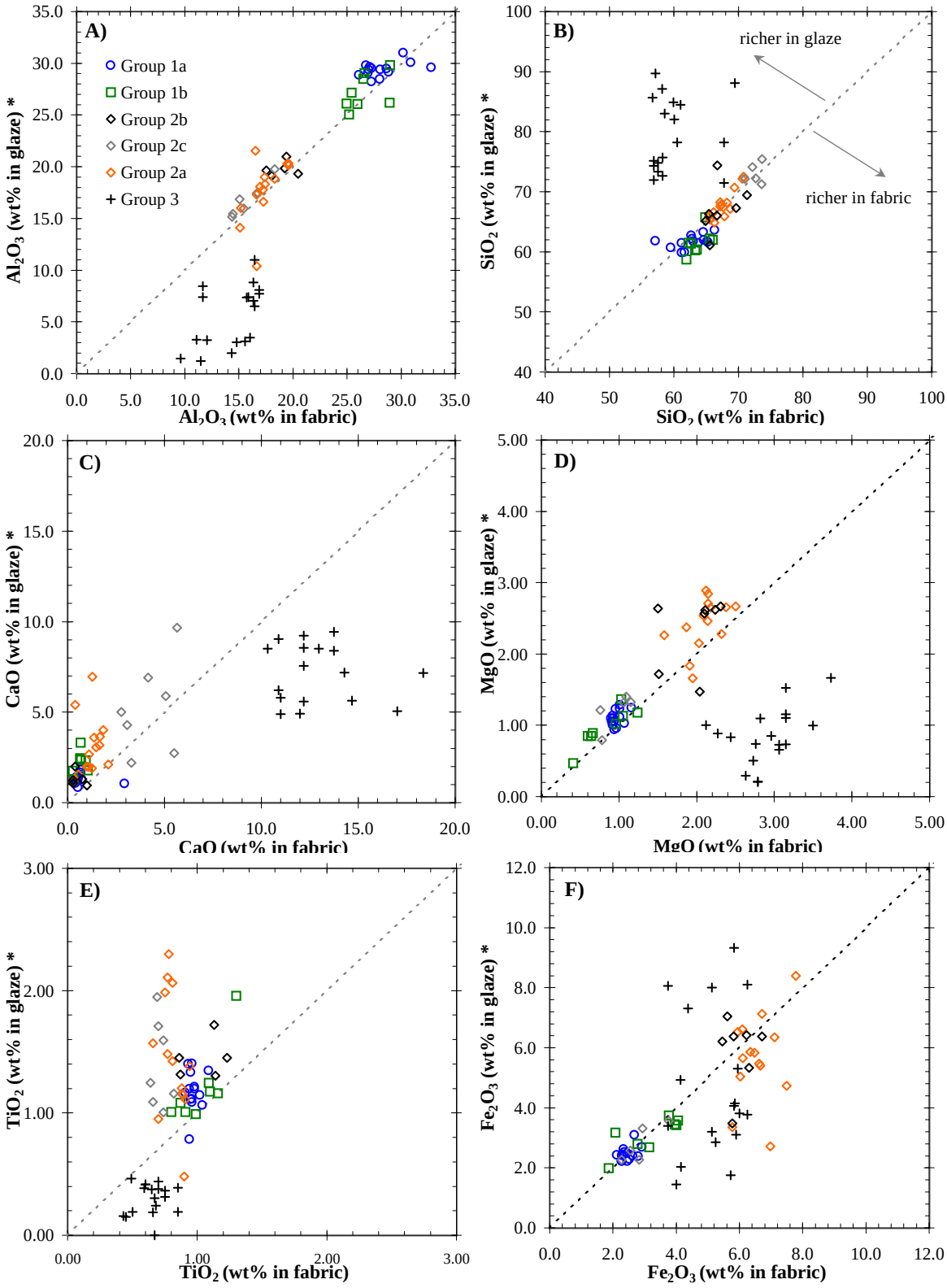

Figure 5.1: Body-glaze comparison plots showing partitioning between glaze and fabric compositions. The glaze data are pre-treated (as denoted by the asterisk) by subtracting PbO and any colourant from the WDS total and normalizing the composition so they can be directly compared to the fabric compositions. If a data point lies on the dotted line (unity slope), then the glaze contains the same proportion of a given oxide as resides in the fabric. As denoted in plot B, if a data point lies to the left of the line, then the glaze is enriched in the particular oxide. Likewise, if a data point lies to the right of the line, then fabric contains a higher concentration of that oxide. Note that Groups 2d and 2e are omitted from these plots because these sherds date to after the 4^{th} century A.D.

experimental error, then this indicates that PbO alone has reacted with the ceramic surface following the mechanism presented in Figure 3.24 in Chapter 3. However, if the proportion of a given oxide is either higher or lower than that of the body, then this points to more complex partitioning mechanisms occurring between the glaze and fabric which are likely associated with a diffusion/dissolution mechanism as presented in Figure 3.39 in Chapter 3. In the case of Figure 5.1, the adjusted glaze composition is plotted against the fabric composition with unity slope demarcated as a dotted line. If a point falls on, or near, unity slope, this indicates that PbO alone was used to create the glaze. If a SiO_2·PbO mixture was applied, SiO_2 levels in the adjusted glaze composition may be seen to be elevated above unity slope together with values below unity slope for the remainder of the oxides (see plot B in Figure 5.1 for further clarification).

The data presented in Figure 5.1 shows that the Roman sherds fall into both categories of the glazing methods discussed in Chapter 3. Furthermore, it may be seen that the data divides into these categories following the ceramic body chemistry: PbO·SiO_2 mixtures appear to be used on the fabrics belonging to the calcareous group 3 fabrics, whereas PbO alone is used on the non-calcareous fabrics of groups 1 and 2. Besides this obvious difference observed between the calcareous and non-calcareous ceramic fabrics, there were no other significant differences in glaze chemistry observed between the fabric subgroups (groups 1a-b and groups 2a-c). The scatter in FeO levels (Plot F of 5.1) observed among the group 3 sherds may be explained by the intentional colouring of some of these glazes with this oxide. Also, the elevated values of TiO_2 above unity slope, seen among the group 1 and 2 sherds (Plot E of 5.1), are likely caused by the poor WDS counting statistics associated with this oxide at these low concentrations (less than 1 % measured). To verify the chemistries of these sherds and to corroborate their methods of manufacture, the two categories of glazing are further explored in the next two sections (5.1.1 and 5.1.3).

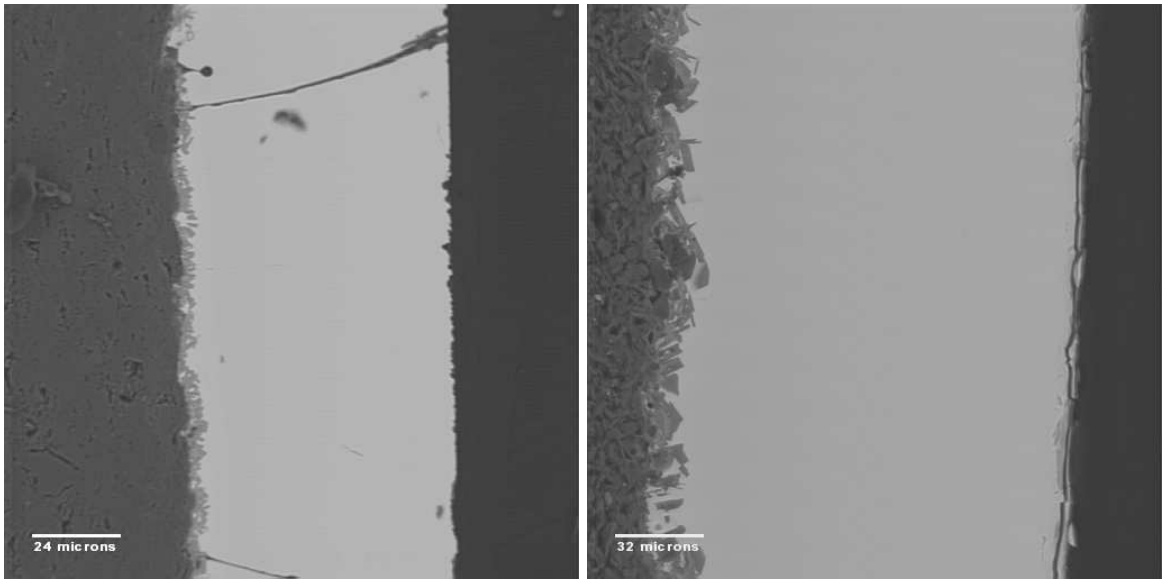

Figure 5.2: Backscatter electron images of glaze cross-sections of S-1 (on left) and S-3 (on right). These images correspond to the profiles shown in Figure 5.3.

5.1.1 Lead Glazes on Non-calcareous Sherds (Fabric Groups 1 and 2)

Two representative sherds were chosen from groups 1 and 2 for the examination of compositional profiles. Through the examination of such profiles, this archaeological material can be compared to the replication experiments presented in Chapter 3. In particular, the experiments presented in section 3.4.1 of Chapter 3 on the fabrication of glazes with shallow and/or flat profiles provide the chemical criteria necessary to assess the chemistry of these glazes.

Microstructural Description and Glaze Chemistry. As may be see in the backscatter electron images shown in Figure 5.2, both of these sherds (S-1, of group 1a, and S-3, of group 2b) have few phenocrysts within the body of the glaze, and a 5-10 μm thick lead feldspar fringe at the interface with the body. These micro-morphological features are typical of the glazes belonging to these two groups (see catalogue in Appendix D for more examples). The profiles, which were collected from the ceramic interface to the edge of the glaze, are presented in Figures 5.3 and 5.4. The S-1 profiles (Figure 5.3) are flat with the exception of Plot C of Figure 5.3 where

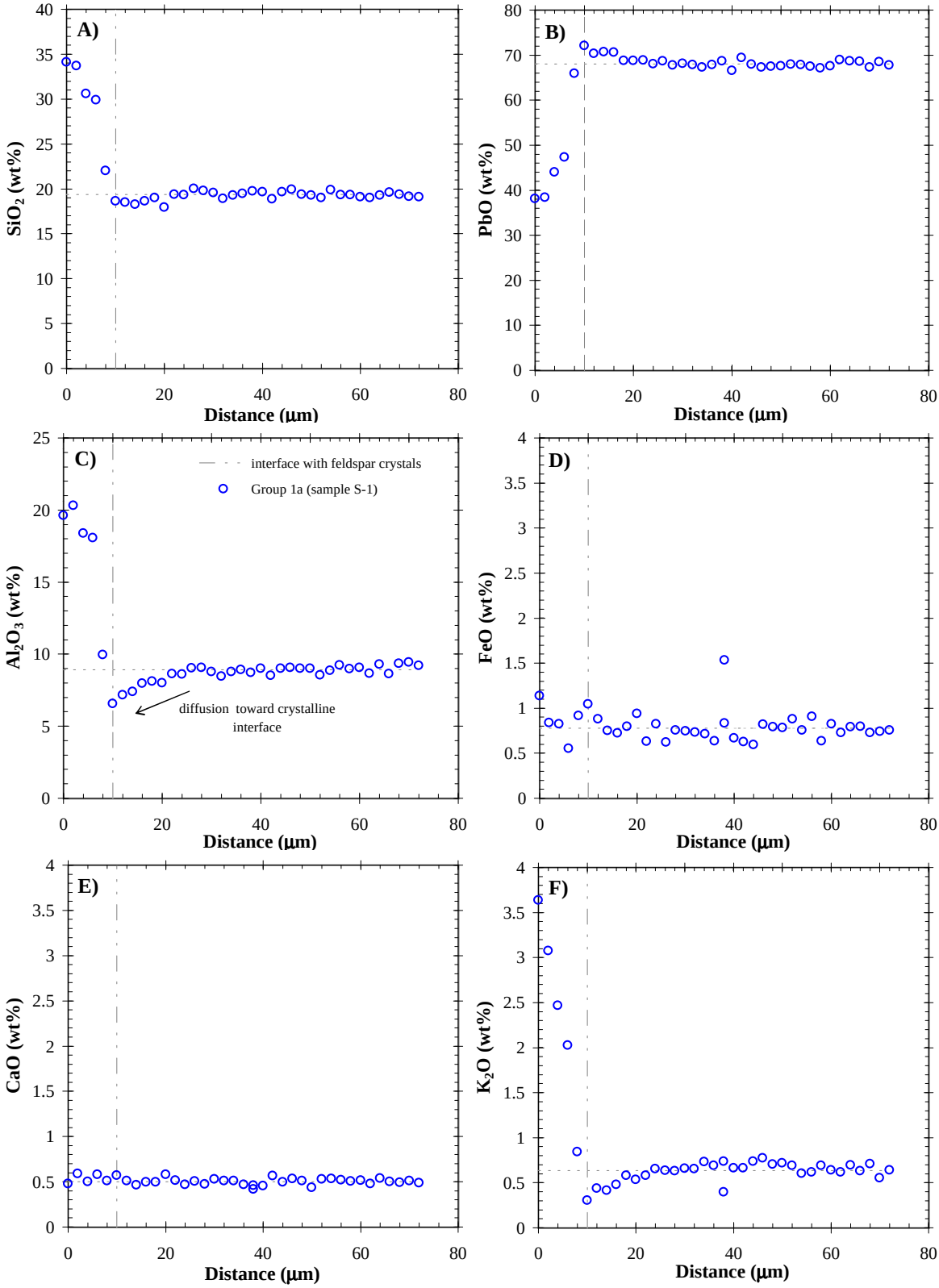

Figure 5.3: Although sample S-1 belongs to group 1a, the flat compositional profiles belonging to this cross-section are typical of most of the sherds belonging to groups 1 and 2 (inclusive of subgroups).

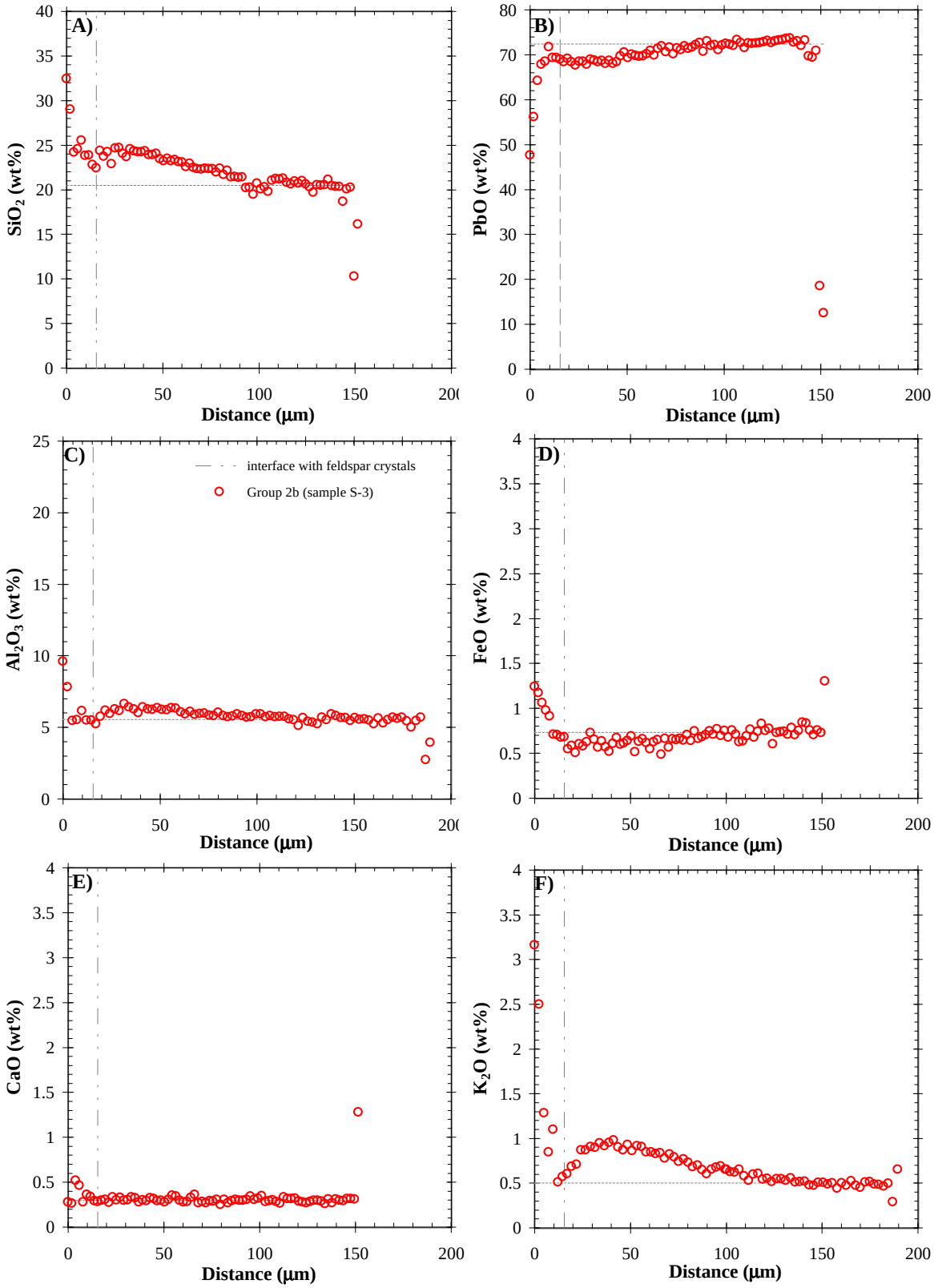

Figure 5.4: Variant profiles of glaze cross-section of a sherd belonging to group 2a. Gradients are likely caused by short dwell times at temperature.

a gradual drop in Al_2O_3 towards the ceramic may be seen to start at approximately 22μm away from the interface. This change in Al_2O_3 is caused by the diffusive growth of the lead feldspar fringe which occurs during cooling (the K_2O profile, Plot F, exhibits the same behaviour confirming the observation). Unlike the S-1 profiles, the SiO_2, Al_2O_3, and K_2O profiles of sample S-3 (Figure 5.4) exhibit shallow diffusion-like gradients in the direction of the ceramic toward the glaze edge. The gradients associated with the formation of feldspars may also be seen in this sample as a decline in concentration towards the ceramic interface as seen by the Al_2O_3 and K_2O profiles in Plots C and F of Figure 5.4 (starting at an approximate distance of 27μm from from the interface). When both the diffusive and feldspar forming gradients are present and of similar magnitude– as they are in the K_2O profile of sample S-3 (Plot F of Figure 5.4)– compositional profiles can take on the shape of a hill. This phenomenon, known as "uphill diffusion" in the literature (see Nishiyama (1998)), is indicative of two, or more, gradients acting in the opposite direction of one another.

While the majority of the glazes in groups 1a-b and 2a-c possess profiles which appear like those belonging to sample S-1 in Figure 5.3, the type of profiles exhibited by S-3 in Figure 5.4 may be found occasionally (approximately 15% of the sherds examined from these groups have S-3 type profiles). Because of their flatness, it is likely that the S-1 profiles formed according to the mechanism outlined for flat profiles in section 3.4.1 of Chapter 3 (i.e., PbO alone applied to the surface). Due to the slight gradients present in the S-3 profiles, however, the formation mechanism of this glaze is not as obvious. Despite showing some diffusive behaviour, the gradients in the S-3 glaze are actually minor and not typical of the gradients that would be expected from glazes formed from $PbO{\cdot}SiO_2$ mixtures. Furthermore, if the ratio of Al_2O_3 to SiO_2 across the glaze section of S-3 is examined (Plot B of Figure 5.5), this ratio remains at approximately 0.3 across the glaze length which is exactly the ratio of Al_2O_3 to SiO_2 in the fabric. The Al_2O_3 to SiO_2 ratio in the S-1 profile (Plot A of Figure 5.5) shows

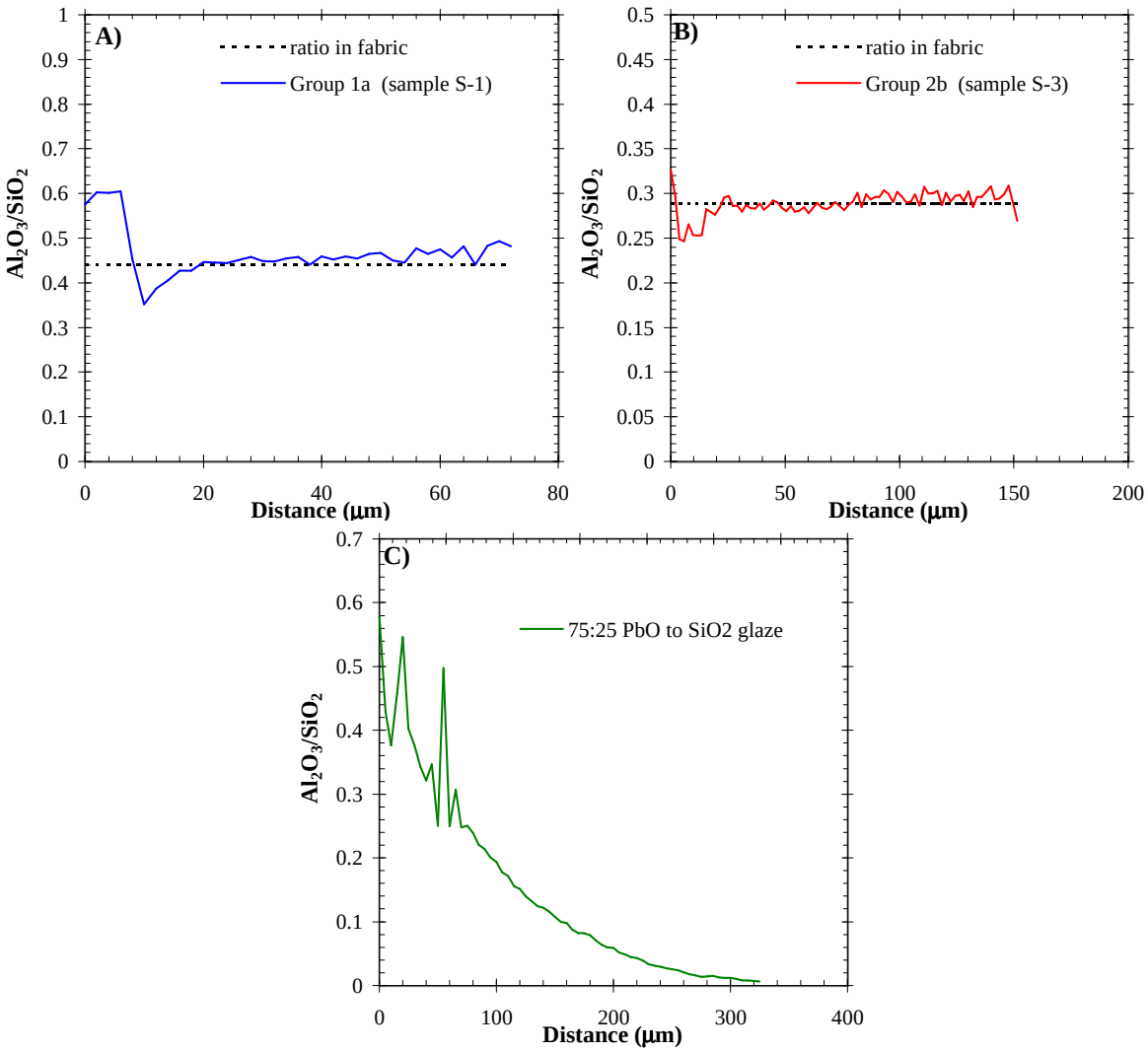

Figure 5.5: Al2O3/SiO2 ratio across cross-sections of samples S-1, S-3, and the 950 ℃ $PbO{\cdot}SiO_2$ replicate sample from section 3.4.2 of Chapter 3.

this same behaviour indicating, for both glazes, that the ceramic body is simply being diluted by PbO. If a $PbO{\cdot}SiO_2$ mixture had been used (as represented by the replicate sample from Chapter 3 presented plot C of Figure 5.5), a consistent Al_2O_3:SiO_2 ratio along these sections would not have been observed. Therefore, based on this ratio data, it seems that PbO alone was used to fabricate the S-3 glaze. The existence of the gradients in this sample could be explained by short dwell times at the maturing temperature as was demonstrated experimentally in section 3.4.1.3 of Chapter 3.

Modelling of Body Fabric Contribution to Glaze Chemistry. Based upon this evidence presented by the profiles, the compositional contribution of the body to the glaze may be modelled by assuming that any of the oxides present in the glaze, besides PbO, come from the ceramic fabric. This modelling process may be described by the following equation.

$$\frac{B_i G_j}{B_j} = G_i^* \tag{5.2}$$

where B_i is the composition of oxide i in the body fabric, B_j is the composition of oxide j in the body fabric known to completely account for amount of oxide j in the glaze which is expressed by G_j. G_i^* is the modelled composition of oxide i in the glaze. By subtracting G_i^* from the measured amount of oxide i in the glaze, G_i, this provides an estimation of the raw glazing material composition, G_i^R, as is shown below.

$$G_i - G_i^* = G_i^R \tag{5.3}$$

This modelling procedure was performed for each glaze analyzed from groups 1 and 2 where the modelled body contribution, as calculated from SiO_2 (calculations using Al_2O_3 produced similar results), was subtracted from the glaze composition at the edge of the cross-section. These results, presented as averages for the two groups, are shown in Table 5.1. The data demonstrates that indeed the majority of the glazing compound was composed of PbO (above 97%). It is also of interest that significant amounts of CaO and Al_2O_3, upwards of 1%, remain after fabric subtraction for both

	Na_2O	MgO	Al_2O_3	PbO	K_2O	CaO	FeO	TiO_2	CuO
Groups 1a-1b	*0.1*	*0.1*	**0.8**	**98.4**	*0.0*	**0.4**	*0.1*	*0.1*	*0.1*
σ	0.1	0.1	0.6	0.8	0.0	0.2	0.1	0.1	0.2
Groups 2a-c	*0.1*	*0.2*	**0.5**	**97.4**	*0.0*	**0.9**	*0.1*	*0.3*	**0.5**
σ	0.1	0.2	0.5	1.5	0.2	0.8	0.3	0.3	0.3

Table 5.1: Group 1 and 2 glaze compositions after subtraction of the wt% of fabric that has diffused into glaze as modelled from the SiO_2 content within the glaze. It is important to note that with the WDS setup at RLAHA, together with the experimental parameters employed, the detection limits for the above major elements are around 0.1 %. However, as a consequence of the problems associated with modelling, a more modest assessment of the data is warranted. As a result, only what are considered to be analytically significant values are presented in bold.

groups in question. Although caution should be exercised in the interpretation of these results, especially considering their poor standard deviations, it may be tentatively posited that the amount of CaO could suggest that the PbO was derived from a purified bone cupel litharge cake. This argument, though, is seriously undermined by the fact that trace phosphate, that would be a biomarker for bone, was not measured in these glazes. Alternatively, these data could indicate hard water (rich in Ca^{2+} ions) mixed with PbO to create an aqueous glazing suspension. As for Al_2O_3, this could be accounted for by the addition of a clay which may have been used as a flocculant in the glaze suspension. However, it is most likely, for both CaO and Al_2O_3, that these results are due to the imperfect methods of modelling and subtraction.

To put the theory that the PbO used in these glazes was derived of detritus from silver cupellation (*i.e.*, from litharge cakes) to a further test, trace element analyses were conducted using long count electron probe microanalysis techniques (two minutes per element). Selected for analysis were oxides believed to partition into litharge during the cupellation of silver bearing argentiferrous ores (Pernicka et al. 1998). Unfortunately, the results obtained from these analyses were ambiguous (see Table 5.2). Although Zn is ubiquitous in all the glazes, and it is certain that this element does not entirely originate from the ceramic fabrics (on average the ceramics possess 90 ppm Zn for both groups 1a-b and 2a-c), it is unclear how it relates to PbO considering there were no observed correlations between Zn and this major element.

Group	*sherd*	*Zn (ppm)*	*Sb (ppm)*	*As (ppm)*	*Sn (ppm)*	*Ag (ppm)*	*S (ppm)*
1a	D202	544	*nd*	56	341	*nd*	*nd*
	D13355	*nd*	*nd*	80	111	*nd*	78
	D5315	302	*nd*	132	*nd*	194	*nd*
	5315a	*nd*	*nd*	287	75	*nd*	*nd*
	5315b	279	*nd*	*nd*	99	117	*nd*
	4735a	764	*nd*	64	272	201	*nd*
	D5655	542	*nd*	*nd*	85	*nd*	*nd*
	NoNum	186	*nd*	*nd*	*nd*	*nd*	*nd*
1b	LCT84b	108	*nd*	2280	*nd*	*nd*	*nd*
	LIM83	196	*nd*	2157	71	*nd*	213
	BGH95	674	*nd*	297	*nd*	*nd*	*nd*
2	LCT84a	522	16699	9363	175	*nd*	*nd*
	S6	1042	*nd*	284	69	*nd*	430
	S3	159	*nd*	814	*nd*	*nd*	*nd*
	NatMus	818	*nd*	324	105	*nd*	185
	C141-96	309	*nd*	198	*nd*	*nd*	388
	LB195	535	5513	3488	66	*nd*	*nd*
	4753b	53	*nd*	193	70	*nd*	*nd*

Table 5.2: Trace metal analyses of elements suspected to be associated with the PbO glazing compound from representative sherds in groups 1 and 2. Elements are reported in parts per million (ppm). Count times of two minutes per element were used with background windows of equal duration. The abbreviation *nd*= none detected.

Also, the occasional traces of Sn, Ag, and S seem to be incidental. Besides Zn, the only elements that seem to be of significance are As and Sb considering they show elevated levels in some samples. However without additional samples, these analyses are of limited value. Therefore, it is necessary to consider these results as negative evidence demonstrating the purity of the PbO used to fabricate the glazes. This also likely means that the PbO was heavily processed to retrieve any metals of economic value prior to its use as a glazing compound. Likewise, it is unlikely, based on these, results that the PbO used on these glazes had anything to do with silver cupellation.

5.1.2 Estimation of Firing Temperatures of the Non-calcareous Sherds

As was shown in the experimental section of Chapter 3, the amount of ceramic fabric digested by a PbO melt increases systematically with temperature. It was also demon-

strated in Chapter 3 that after a relatively short soak at the maturation temperature (around 30 minutes), the glaze achieved a flat profile and did not proceed to digest any more of the body. Lastly, it was found in Chapter 3 that these ceramic reactions with PbO proceeded at the same rate regardless of whether the ceramic was biscuit fired or "raw" prior to the final firing. Therefore, time and ceramic preparation may be considered as only negligible factors contributing to the final glaze chemistry when PbO alone is applied to a ceramic substrate. This experimental evidence provides the necessary information to estimate the average maturation temperatures employed in the firing of archaeological materials. To this end, eight representative sherds from groups 1a and 2a were selected to conduct firing tests to better understand the amount of fabric digestion that takes place with increases in temperature when firing a PbO glaze.

Experimental. Sections (in approximately 1 cm^2 dimensions) were removed from eight ceramics corresponding to fabric groups 1a and 2a (group 1a = D-202, D-5135a, Do-nonumb, D-13355, and group 2a = S-6, Nat. museum, D-C141/96, L-LBI95). The samples were prepared by first grinding the extant glaze off both sides of the section. Then, a water suspension of AnalaR® grade PbO powder (BDH Laboratory Supplies, Poole, UK) was applied to one surface. The sections were subsequently fired at either 750, 800, 900, or 1000℃ with ramps of 10℃/minute and dwell times of 3 hours. Electron microprobe analyses at the glaze edge and at the ceramic interface were collected as per the methods outline in Appendix A. These data were combined with the archaeological glaze data from the two groups. As a combined data set, the log of each data point was normalised by the geometric mean of each oxide group prior to principal component analysis (see Rollinson (1993) page 38 for more on this approach). Principal component analysis (PCA) was used to perform an empirical multicomponent calibration using a polynomial fit to the first principal component of the re-fired sherd data. This PCA approach was used since

it supplied a better description of how overall change occured within the experiment than could be provided by any individual oxide.

Results. The polynomial fits to the re-fired sherd data may be seen in plots A and B of Figure 5.6. For both plots, the first principal component was utilized for the polynomial fit since it contains the primary variance between PbO and the remainder of the oxides associated with the ceramic fabric (see plots B and D of Figure 5.6). This first component essentially describes the amount of fabric digested by the PbO. The resulting empirical equations (shown in the plots) were used to calculate the temperature of each of the sherds from their first principal component.

Plot A shows the data belonging to the group 1 sherds which cluster around an average of 892 ±27 ℃. The group 2 sherds, shown in plot c, are bimodal with one cluster having an average of 935 ±11 ℃ and the other cluster with an average of 1003 ±19 ℃. A further scatter of several sherds may also be seen between 750 and 900 ℃. These temperatures are not surprising and were expected for the kiln technology belonging to this time period. Also, the 900 ℃ mark (around which all the glazes hover) represents a maturation temperature typical of modern lead based glazes which are brought to this point on account of the low viscosity and good wetting characteristics achieved (Peterson 2004). More importantly, however, these data provide an indirect assessment of the typical Roman firing practice for these wares.

5.1.3 Lead Glazes on Calcareous Sherds (Fabric Group 3)

Microstructural Description and Glaze Chemistry. As may be seen in Figure 5.7, the typical archaeological glaze on a calcareous sherd is mostly devoid of crystalline structures within the glass, yet has a thick interaction zone between the glaze and ceramic. The plots in Figure 5.8 show that there are compositional gradients present in each oxide profile indicating the dissolution and diffusion of the ceramic

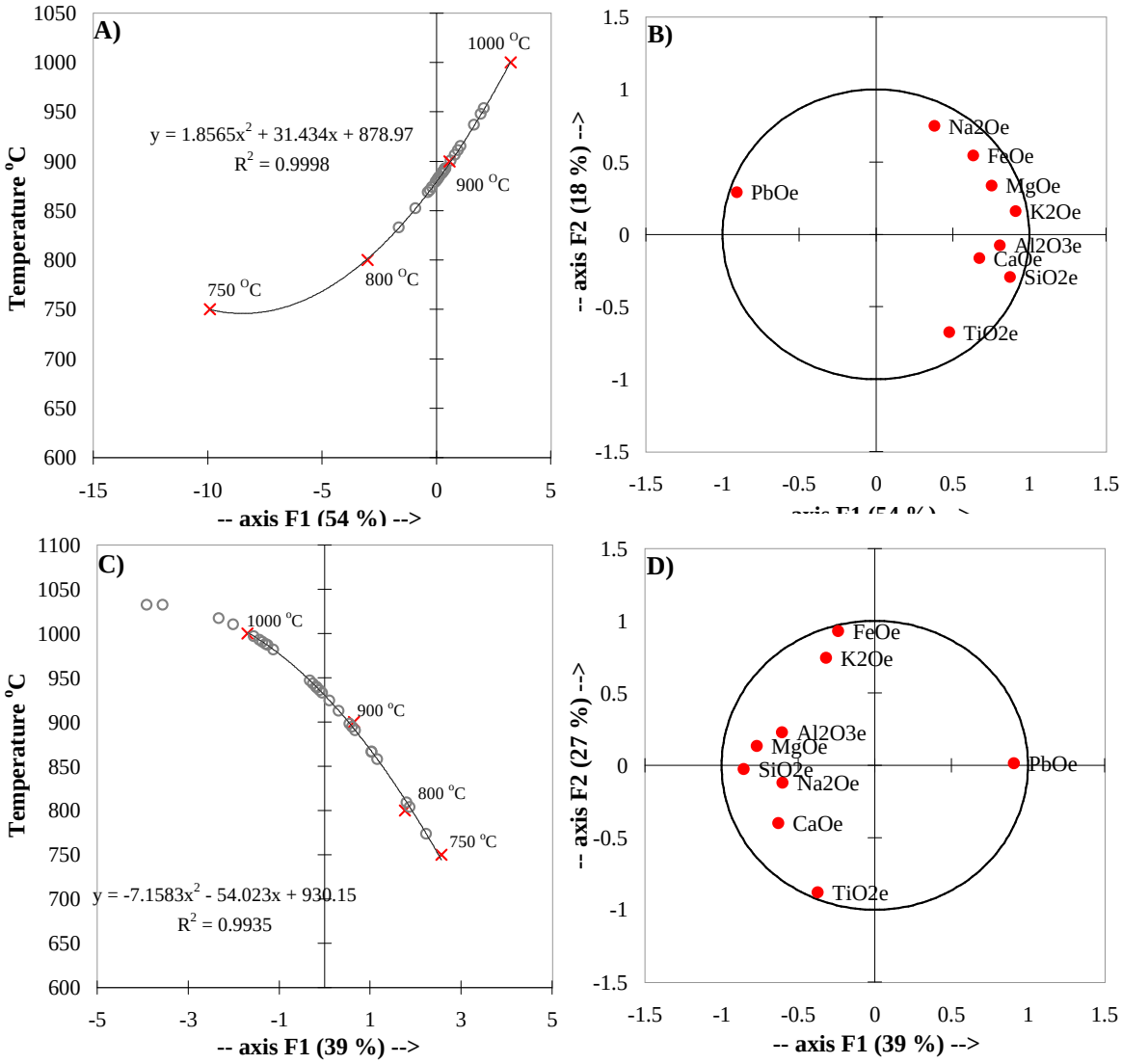

Figure 5.6: Firing temperature estimation of group 1 and 2 sherds by principal component analysis (PCA). Plots A and B correspond to group 1a whereas plots C and D show the data belonging to group 2a. The red x's are the refired sherds. The grey circles are the temperatures associated with each of the archaeological sherds which are calculated from their first principal component using the polynomial fit to the refired sherds (solid line in plots A and C). Note that the *e* after each oxide in plots B and D denote that the exterior glaze analyses were used for the PCA analysis.

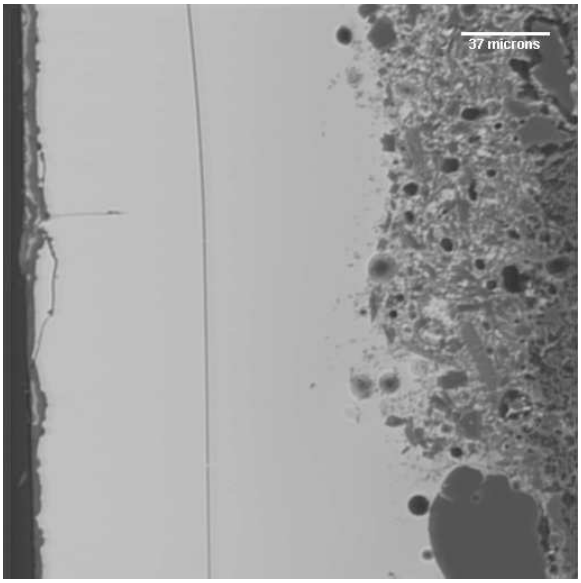

Figure 5.7: Backscatter electron image of a representative glaze on a calcareous sherd (v27). This image corresponds to the profiles shown in Figure 5.8

fabric into the glazing liquid. In this particular sample, it may be seen that all the Al_2O_3 present in the glaze diffuses in from the body reaching nearly 0 wt% at the glaze edge. The SiO_2, FeO, CaO, and K_2O profiles are not as steep as the Al_2O_3 profile and do not terminate at 0 wt% indicating that the diffusion was into a liquid which possibly already contained a certain amount of these oxides. Alternatively, the shape of these profiles may either be a sign that that the glaze was held at temperature for a protracted time, or that the glaze was fired at a relatively high temperature as per the 950℃ profiles presented in Figure 3.35 in Chapter 3. The results presented in 5.8 actually share many characteristics with the Figure 3.35 profiles which were created using $PbO{\cdot}SiO_2$ mixtures on ceramics made from a calcium rich Gault clay. Likewise, with the exception of elevated CaO levels, these archaeological profiles are not dissimilar to those obtained by Molera et al. (2001) who created $PbO{\cdot}SiO_2$ glazes on non-calcareous substrates.

A minor morphological variant to these glazes, present in this set of data only in low numbers, may be seen in Figure 5.9. Unlike the v27 sherd shown in Figure 5.7, this glaze contains a number of $CaMgSiO_3$ (diopside) crystals. These may be

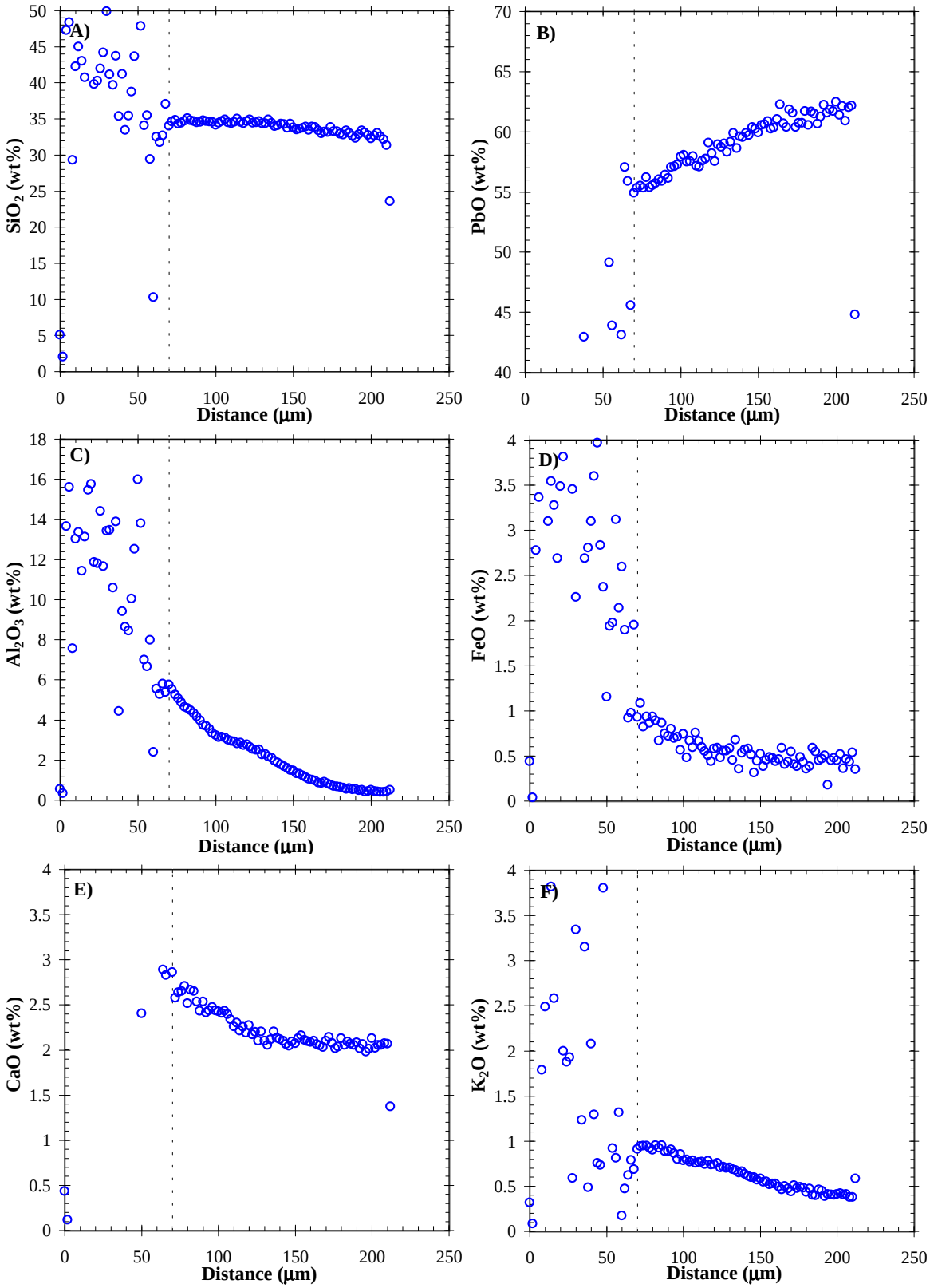

Figure 5.8: Electron microprobe profiles of major elements belonging to a representative glaze on a calcareous sherd (v27).

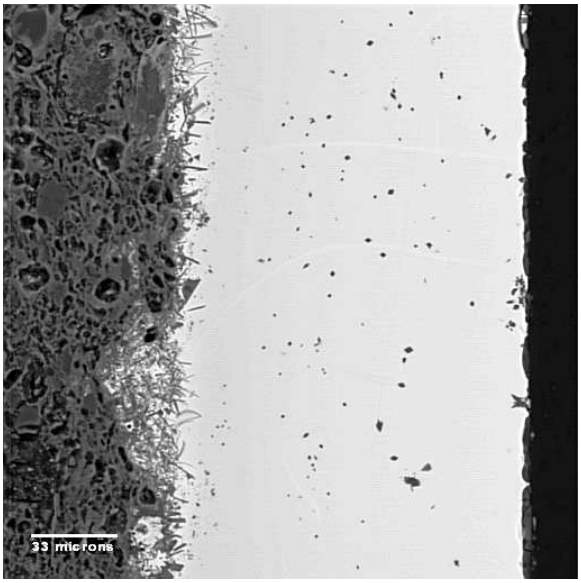

Figure 5.9: Backscatter electron image Picon-4 showing precipitation of diopside crystals within the glass phase of the glaze.

seen both in the backscatter image as fly-like specs throughout the glass phase of the glaze, and in the compositional profiles (Figure 5.10) of CaO, MgO, and SiO_2 shown as slight increases in concentration. Like the v27 example, however, the Al_2O_3 profile (plot A in Figure 5.10) shows a substantial gradient indicating diffusion from the ceramic fabric. However, this gradient terminates at around 3.5% suggesting that this amount of Al_2O_3 was already present in this glaze. While the exact conditions leading to the formation of the diopside crystals are not known, it is likely caused by a slight increase in the CaO and MgO content of the raw materials and/or a slow cooling regime after firing.

Glaze Raw Materials. Because of the sluggish rate of diffusion in glazes created from $PbO{\cdot}SiO_2$ mixtures (as shown experimentally in section 3.4.2 in Chapter 3), it was thought that the dissolution and diffusion of the body fabric would only minimally contribute to the composition at the glaze edge. Therefore the analyses of the glaze edge (show in Table 5.3) should be representative of the raw materials used in fabricating the glaze. What may be immediately gleaned from these data is that the SiO_2 and PbO show a 1:2 wt% ratio in these glazes which is close to the

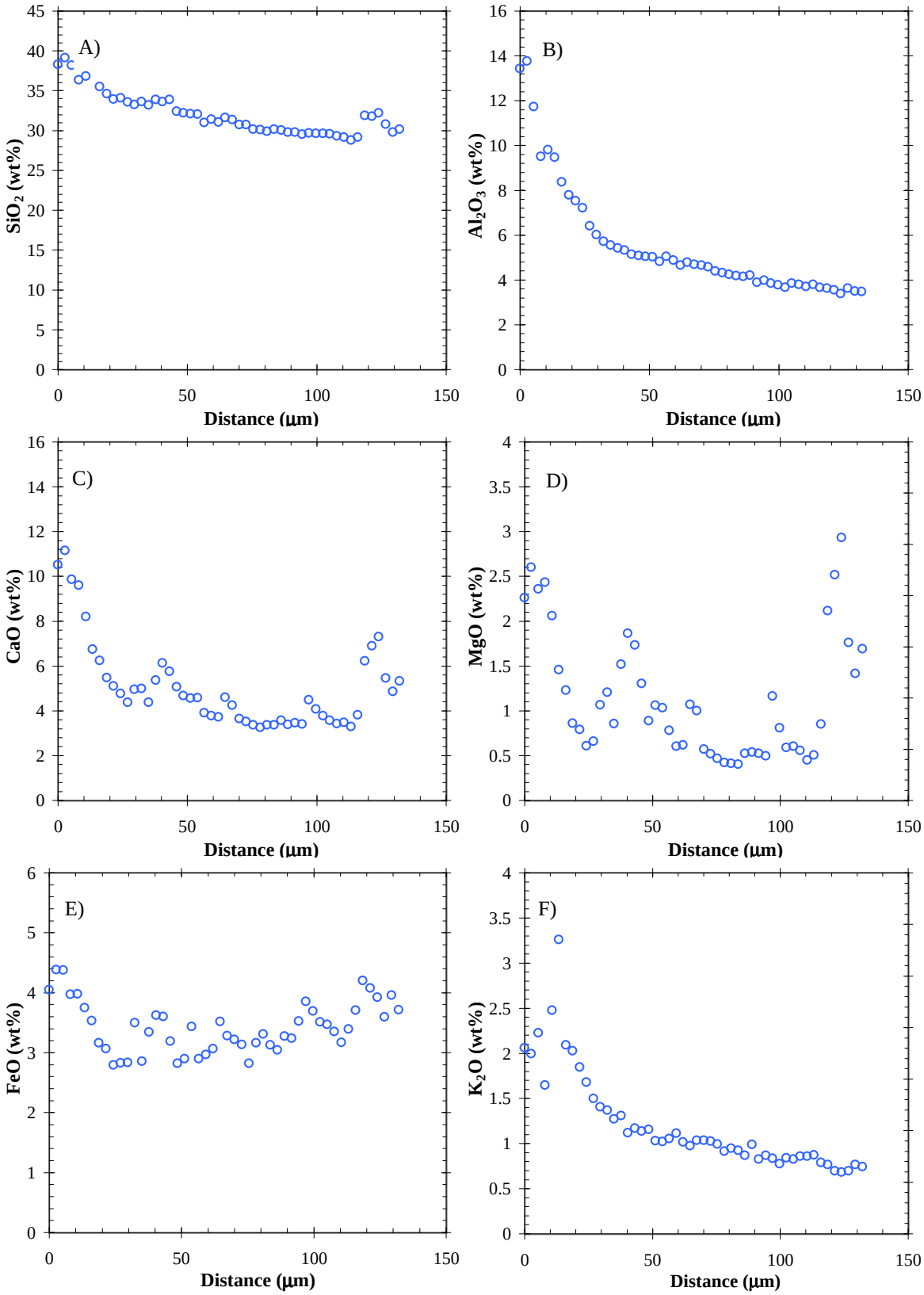

Figure 5.10: Electron microprobe profiles of Picon-4. Note that the PbO profile was been omitted.

Colour	*Sample*	Na_2O	MgO	Al_2O_3	SiO_2	PbO	K_2O	CaO	FeO	TiO_2	CuO
Green	DGH86	0.1	0.3	1.1	29.7	62.0	0.3	2.5	0.6	0.0	1.9
	SWA81	0.2	0.2	1.1	25.1	68.0	0.5	1.5	1.6	0.1	1.5
	SH74	0.2	0.2	2.5	26.4	61.7	0.5	2.9	1.0	0.1	2.7
	Picon4b	0.4	0.6	3.1	29.4	56.2	0.8	3.6	1.5	0.1	2.7
	Camp-2	0.0	0.3	0.6	25.7	68.2	0.3	1.7	0.8	0.1	1.4
	RZ5574	0.2	0.3	1.0	26.1	68.1	0.3	2.2	0.6	0.0	1.2
	RZ5637	0.6	0.7	2.9	29.4	59.2	0.7	3.3	1.5	0.1	1.5
	RZ5670	0.3	0.5	1.3	35.6	57.0	0.6	2.1	1.7	0.2	1.5
	V59	0.3	0.2	3.3	27.9	59.9	0.7	3.5	1.2	0.1	2.6
	V27	0.3	0.3	0.5	30.5	62.2	0.4	2.0	0.5	0.1	2.4
	V83b	0.3	0.1	3.4	31.6	56.6	0.9	2.5	1.4	0.2	3.4
	V69	0.3	0.4	3.9	26.1	61.7	0.5	3.1	1.5	0.1	2.3
Yellow	Picon4	0.3	0.5	3.3	29.7	57.0	0.8	3.1	3.3	0.2	0.3
	Camp-1	0.1	0.3	1.1	28.4	63.5	0.3	1.7	2.5	0.2	0.1
	Camp-3	0.1	0.1	0.4	26.9	68.6	0.2	0.9	1.5	0.0	0.2
	V59b	0.3	0.3	2.8	29.1	59.9	0.6	3.3	3.2	0.1	0.1
	V83	0.5	0.1	3.2	31.1	54.5	1.1	3.9	3.5	0.2	0.1
	V69b	0.3	0.3	2.3	26.9	62.2	0.4	2.0	3.3	0.1	0.1
Average	green	**0.3**	**0.3**	**2.0**	**28.6**	**61.7**	**0.5**	**2.6**	**1.2**	**0.1**	**2.1**
	σ	0.1	0.2	1.2	3.0	4.4	0.2	0.7	0.4	0.05	0.7
	yellow	**0.2**	**0.2**	**2.2**	**28.7**	**60.9**	**0.6**	**2.5**	**2.9**	**0.1**	**0.1**
	σ	0.1	0.1	1.2	1.6	5.0	0.3	1.2	0.8	0.06	0.08

Table 5.3: Group 3 glaze compositions. As is evident from these analyses, the green exterior glazes are coloured with CuO whereas the yellow interior glazes are coloured with Fe_2O_3. Note that any b samples (*i.e.*, V69b) merely represent the opposite side of a glazed sherd where both the green and yellow sides are preserved intact within the resin block.

SiO_2–PbO eutectic residing at 30% SiO_2 (on average SiO_2 is at 32 wt% and PbO is at 68 wt% if normalised). This ratio is remarkably regular throughout the samples studied. A pre-fritting step at a common temperature may provide one explanation for this behaviour. This process can result in a consistent composition at an eutectic due to the tendency of silica-rich earthenware crucibles or frit pans to impart SiO_2 into the glass phase until the eutectic is achieved (known as a "buffering effect", the phenomena was demonstrated experimentally in Figures 3.8 and 3.37 of Chapter 3). It is equally possible that the general practice of glaze fabrication was to create a mixture of PbO (likely in the form of litharge) and SiO_2 (either in the form of quartz pebbles or sand) in a prescribed 1:2 weight ratio with CuO and/or FeO as a colourant.

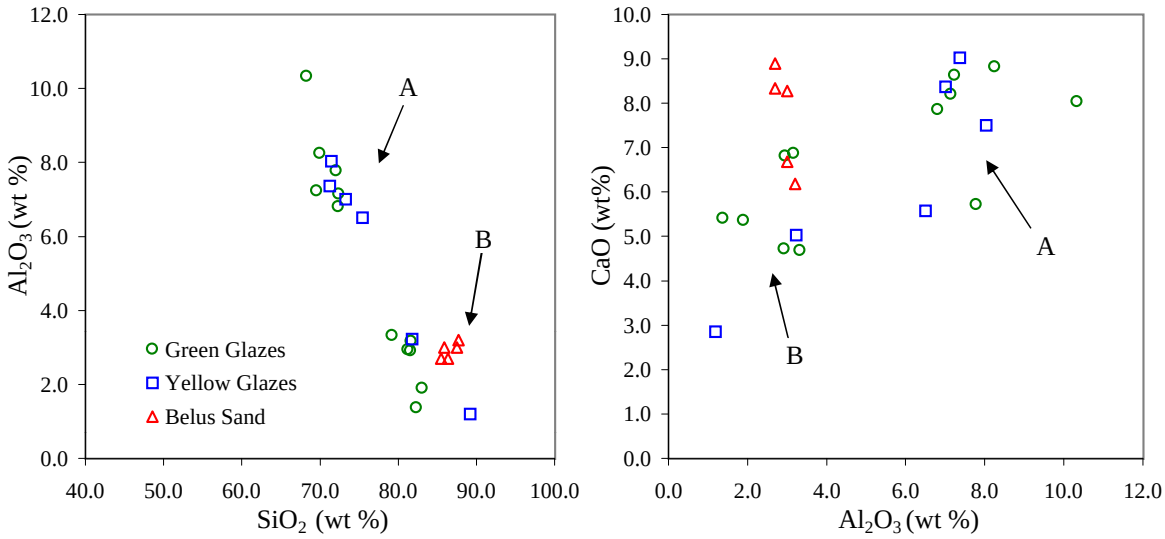

Figure 5.11: $PbO{\cdot}SiO_2$ glazes compared to Belus sand after PbO has been subtracted from the composition and the data has been normalized. See Table 5.4 for the average composition of groups A and B in comparison to the Belus sand samples.

Of additional note is the high CaO content of the glaze compositions in Table 5.3. This amount of calcium is not likely to be due to the contribution of a hard water source because of the relatively high levels throughout the samples. If PbO is subtracted from the compositions presented in Table 5.3, and these data are re-normalised to 100%, this shows the possibility that the Ca is coming into the glaze with the SiO_2 along with Na_2O, MgO, Al_2O_3, and K_2O as minor constituents (see Figure 5.11 and Table 5.4). This finding would imply that the siliceous component of the glaze is possibly a sand. In specific, it appears that this sand could be a coastal river sand containing a proportion of shell as deduced from the amount of CaO present.

As seen in Figure 5.11 the glaze data divides into two groups, one with relatively high Al_2O_3 (above 6.5%) and the other with lower Al_2O_3 (below 3.3%). It should be noted that this division in the data shares no correlation to the amount of Al_2O_3 in the ceramic fabrics which possess a consistent Al_2O_3 composition centered around 14 $\pm$2%. Therefore, this Al_2O_3 is certainly a component of one of the raw materials. If glass making sand samples from the famed Belus River discussed by Pliny (Freestone

		Na_2O	MgO	Al_2O_3	SiO_2	K_2O	CaO	FeO
average	*A*	0.8	0.8	7.6	71.6	1.7	7.8	5.3
	B	0.5	0.8	2.5	82.5	1.0	5.2	3.6
Belus River Sand	*673*	0.9	0.3	3.2	87.8	1.1	6.2	0.5
	674	0.9	0.4	3.0	87.5	1.0	6.7	0.4
	678	0.9	0.5	2.7	85.5	1.0	8.9	0.5
	679	0.8	0.4	3.0	85.9	1.0	8.3	0.5
	681	0.7	0.4	2.7	86.4	0.9	8.3	0.4

Table 5.4: Siliceous component calculated from the glaze data in Table 5.3. Note that the glazes are grouped according to the division in the data seen in Figure 5.11. PbO has been subtracted and the Table 5.3 compositions and re-normalised. Results are compared with coastal river sand (from the Belus River) that contains carbonate shell (Brill 1999). The high average FeO content is likely due to this oxide being intentionally added as a colourant to these glazes.

and Gorin-Rosen 1999) are shown in comparison to the glaze samples (Table 5.4), the low Al_2O_3 group (group B) shares significant similarities with this sand. Likewise, the composition of the group B glazes are not dissimilar to the implied sand compositions of glasses fabricated in the Near East as discussed by Freestone et al. (2000). The high Al_2O_3 glazes (group A), however, are unusual and do not match any typical glass making sands of this period. Although it is possible that this Al_2O_3 content could be the result of clay added to the mixture, which would have aided the application of the glaze onto the ceramic, the similarities with the other oxide components are more suggestive of a sand.

Even though these data imply that shell sand was a raw material, it is clear that additional work is required to confirm this identity. Such work is important as it would point toward a technological connection between lead glazing and Roman glass making practice in terms of raw material choice.

5.1.4 XRF Analyses of Lead Glazes from Hatcher et al. (1994)

The XRF glaze analyses of Hatcher et al. (1994) represent the most comprehensive set of analyses of Roman lead glazes outside this present work. However, as was

briefly alluded to by the authors of this previous study, their analyses were flawed[1] showing spurious concentrations for CaO and K_2O in specific. Furthermore, because of the air path XRF technique employed, detection of light elements (inclusive of SiO_2 and below) was impossible due to severe X-ray attenuation. Lastly, it was noted by Hatcher et al. (1994) that two separate XRF instruments – one in Oxford and the other in Paris – were employed in their study which may have resulted in discrepancies in the data collected at these two locations. These problems with the data were regrettable considering their vast collection of analyses which included lead glazed examples from several of the earliest Eastern Mediterranean workshops dating to the 1st century BC (particulary important are those glazes analyzed in the Louvre, Paris). Since these significant lead glazes were inaccessible for re-analysis under the present study, the data of Hatcher et al. (1994) provides the only information on the earliest lead glazes known.

For the above reasons, an attempt was made to analytically assess and, in a few cases, correct the results of Hatcher et al. (1994). The attempt to reconcile these data was informed by the following points: 1) that any flawed analyses were due to improper matrix corrections (which may be recalculated given a sufficient internal calibration factor); 2) the Colchester/Silchester sherds almost certainly share an identical fabrication to those belonging to group 1 of this present study (*i.e.*, PbO alone on a low calcareous body) given that they are from the same compositional group and share stylistic features; 3) The samples from Tarsus should share similar glaze compositions to the first lead glazes analyzed from this site by Caley (1947).

Correcting the Colchester/Silchester glaze data. Because such an extensive comparative group of sherds with well defined glaze chemistry was studied here (see data presented in Section 5.1.1), a likely glaze composition for the Colch-

[1]Hatcher et al. (1994) states: "An additional problem with high lead glazes is that the lead matrix correction for potassium and calcium is very large, and a given uncertainty in the lead concentration introduces errors several-fold greater into the computed concentrations of these two elements."

ester/Silchester sherds could be modelled for this material based upon the amount of PbO in the glaze (which were assumed to be sound analyses). This modelled composition could then be used as a calibration reference since it is certain that all of the elements, besides PbO, within these glazes resulted from the digestion of the ceramic fabric. Also, as was shown by experimental replication in Chapter 3 and in section 5.1.1 of this Chapter, the relative proportions between oxides in the ceramic and in the glaze remain unchanged when using PbO alone to produce a glaze.

Putting this information to use, a correction factor was obtained for each element analyzed by least squaring the XRF analyses to the modelled glaze compositions as a group using the Solver add-in in Microsoft Excel. This was done using the following equation:

$$G_i^{corr} = G_i F \tag{5.4}$$

where G_i^{corr} is the glaze oxide analysis G_i corrected by factor F. G_i^{corr} was optimized by iteratively changing F (the value of which was arbitrarily chosen at first) until a χ^2 algorithm was minimized.

$$\chi_i^2 = (G_i^{corr} - X_i^{mod})^2 \tag{5.5}$$

where X_i^{mod} is the modelled glaze composition as calculated from the PbO measured by XRF analysis. X_i^{mod} was calculated as follows,

$$X_i^{mod} = \frac{(100\% - C_{PbO})}{\sum_{i=1}^{N} X_i} * X_i \tag{5.6}$$

where C_{PbO}, the measured PbO wt% content in the glaze, is subtracted from 100% and divided by the sum of all the oxide components in the fabric. X_i is the measured composition of oxide i in the ceramic fabric.

Because a single value of F was found for the entire group of data, instead of individual points, the relative elemental proportions between samples remained unaltered. This also meant that the relative proportions of X-ray photon count data

between samples remained unchanged thereby preserving the data integrity. In addition, an attempt was made to estimate SiO_2 content of these sherds. This was accomplished by assuming that all of the Al_2O_3 in a given glaze had been dissolved into the glass phase from the ceramic fabric. By then summing the corrected XRF analyses (CaO, TiO_2, and Fe_2O_3) + CuO and PbO (assumed to be sound analyses) and Al_2O_3, which was calculated from the body, a compositional total is produced that may be subtracted from 100% to give a remainder of SiO_2 + Na_2O + MgO. Since Na_2O + MgO consistently sums to about 1% in the glazes considered in sections 5.1.1 and 5.1.3, this 1% was subtracted from the remainder to give an approximate SiO_2 concentration.

While it is fully acknowledged that these data transformations are not strictly rigorous, and that the interpretation of the resulting data should be used with caution, this manipulation is nevertheless useful to understand the quality of the data of Hatcher et al. (1994) and how these data could be effectively used in the interpretation of technology. It is hoped that by re-assessing these data this might encourage others to engage in a more quantitative study of this important material.

Figure 5.12 shows glaze data of Hatcher et al. (1994) before and after correction. It may be seen that the corrections for both Fe_2O_3 and TiO_2 produced relatively small changes to the data ($F_{Fe_2O_3}$=0.564, and F_{TiO_2}= 0.948). As was expected, the correction factor for CaO (F_{CaO}= 0.045) led to significant changes in the data. However, as is seen in Figure 5.13, these corrected data produce an estimation of SiO_2 that is almost spot-on when compared to the SiO_2 content in the body thereby demonstrating, albeit in an indirect manner, the validity of the corrected data. In addition, the values obtained in this manner match those analyzed in this study for glazes belonging to the same group (group 1b).

Smyrna/Calzomenae and Tarsus. Smyrna and Tarsus are among the first known production sites for lead glazed wares dating, at their earliest, to the 1^{st} cen-

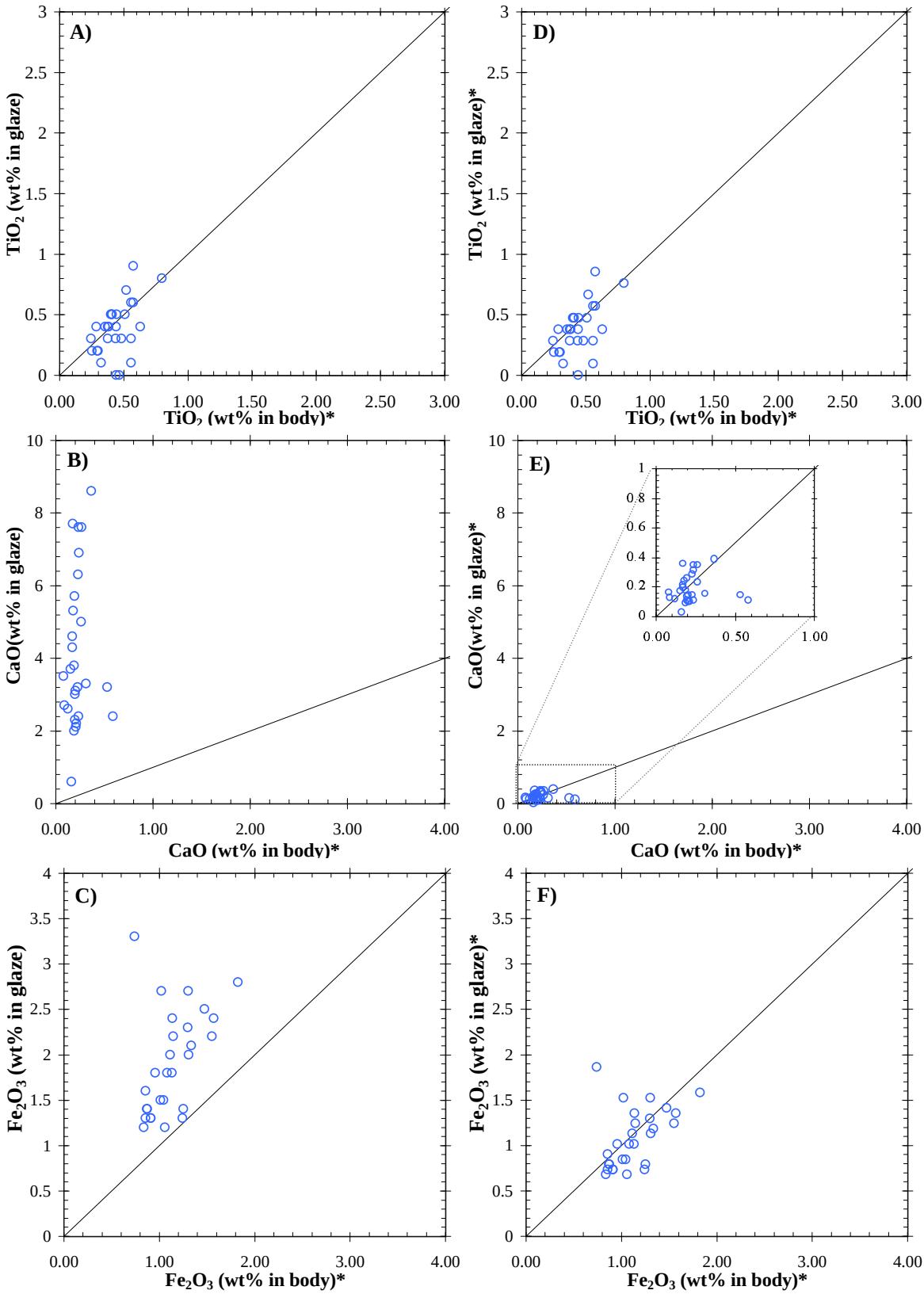

Figure 5.12: Hatcher glaze data plotted against body composition before (plots A–C) and after (D–F) correction. The diagonal line is unity slope. The asterisk next to the wt% in body label denotes that this composition was modelled based on the analyzed PbO concentration by XRF. The asterisk next to the wt% in glaze label denotes that these are the corrected analyses of the glaze compositions.

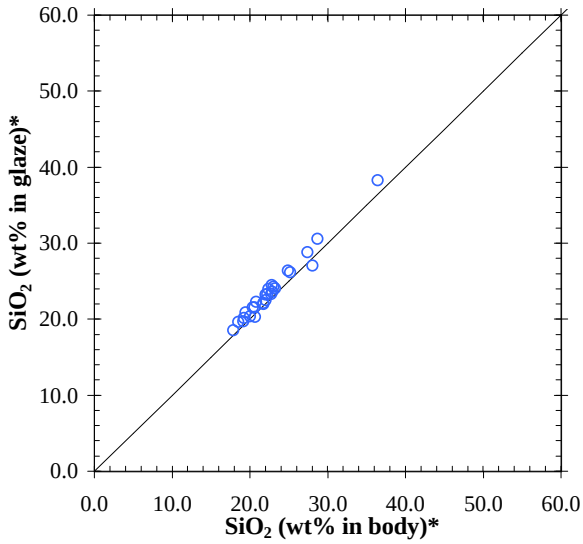

Figure 5.13: Estimated SiO_2 content in the Hatcher glaze data plotted against measured SiO_2 in the ceramic fabric.

tury BC (Hochuli-Gysel 1977). Also, the ceramic groups identified by Hatcher et al. (1994) as coming from these sites were the only sherds with a probable provenance. Therefore, from the Hatcher corpus, only these glazes were assessed to evaluate fabrication technology.

Unlike the Colchester/Silchester data, when the Tarsus glaze data of Hatcher et al. (1994) was compared to the Tarsian vessels previously published by Caley (1947), these data did not seem to have specious Fe_2O_3 or CaO content. Also when compared with other glazes applied to calcareous substrates, such as those on the vessels from Italy (discussed in the previous section), the compositions of these glazes were not dissimilar to Hatcher's Tarsus data. Based on these observations, it was thought probable that the Tarsus XRF analyses were an accurate representation of the chemistry of these glazes. By association, it was also though the Smyrnian data was also correct considering that these sherds, together with the Tarsus sherds, were all run together on the XRF spectrometer at the Louvre. Because, the Colchester/Silchester material was run separately from these other analyses in Oxford, it was though that they may have been subjected to a peculiar user error. As a consequence, the uncorrected glaze analyses for Tarsus and Smyrna were chosen for plotting in Figure

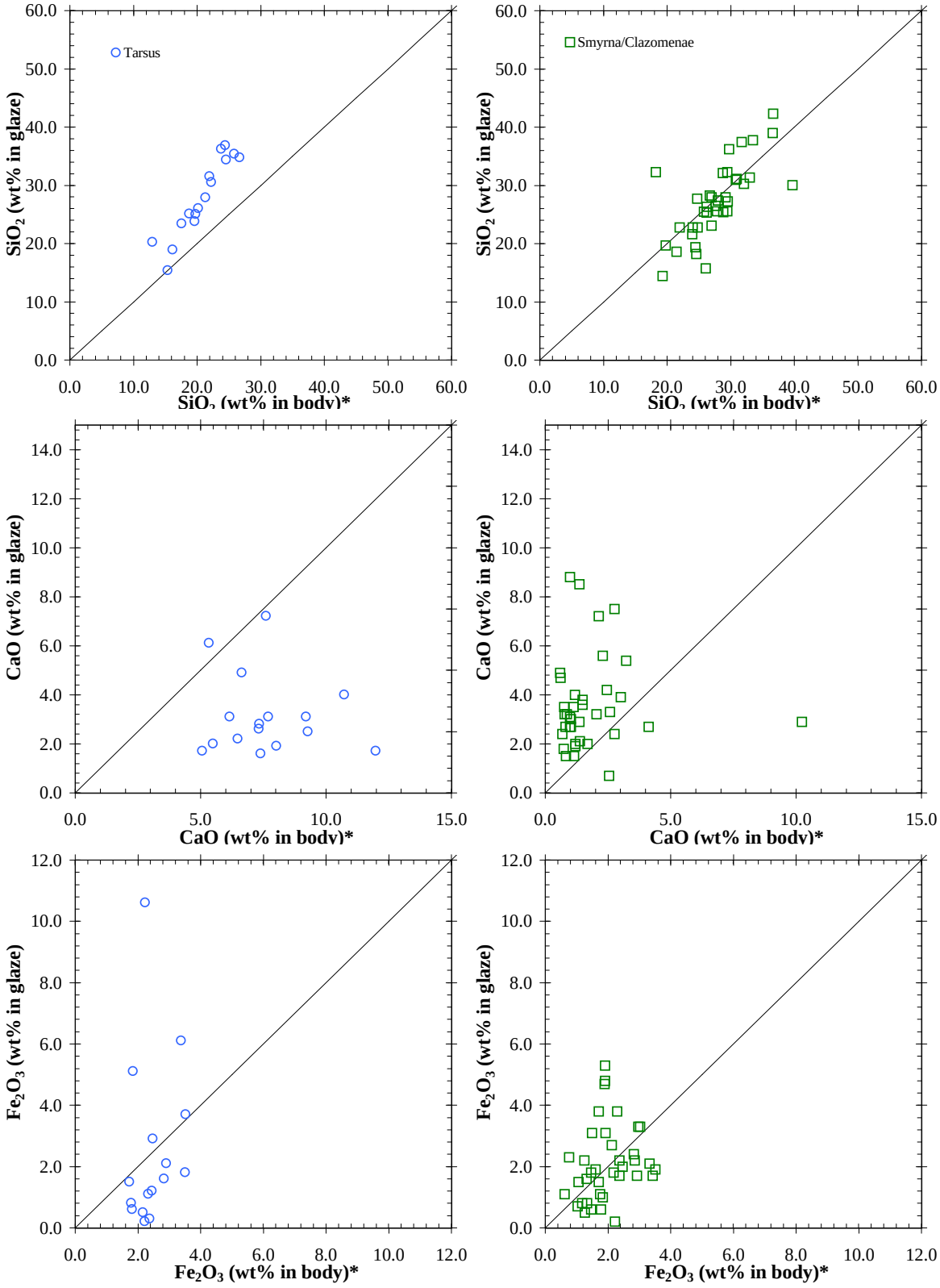

Figure 5.14: Tarsus (blue circles) and Smyrna/Clazomenae (green squares) glaze data plotted against their body compositions adjusted by equation 5.6(demarcated with an asterisk).

5.14. In these plots body compositions were adjusted with equation 5.6 in order to be directly compared with the glaze compositions.

As shown in plots of Tarsus data (plots with blue circles in Figure 5.14) these sherds were likely glazed with a $PbO{\cdot}SiO_2$ mixture or frit as is shown by the SiO_2 values above unity slope and the CaO and Fe_2O_3 contents below unity slope. The few data points above unity slope in the Fe_2O_3 plot are probably associated with glazes intentionally coloured with a Fe compound. Further modelling to understand the relationship between PbO and SiO_2 was not possible with this Tarsian data since there was not a single measured oxide which could be demonstrated to enter the glaze from the ceramic fabric alone. In contrast to the Tarsus data, the Smyrna/Clazomenae data (shown in plots D–F) clearly show that only PbO was used in the glaze as shown by the data points laying directly on unity slope in both the SiO_2 and Fe_2O_3 plots. The CaO plot is interesting in that it shows elevated CaO levels (at 2.4 $\pm$1.8% above unity slope) which is similar to the elevated CaO values observed in the group 1 data of this present study.

While interpretation of these data is necessarily kept at a minimum, it is revealing as it establishes that both the glazing methods found to be used in the 2^{nd} century AD were already in place during the nascent period of lead glazing in the East. While it is not certain whether there is a direct link between the Smyrna glazing method and that used in the later Gallic contexts, this possibility cannot be ruled out. It is more probable that there is a connection between the methods used in the fabrication of both the Tarsus vessels and those thought to be produced in Italy given the relative complexity of the fabrication method and its possible material similarities to glass making as discussed in the previous section.

It should be noted that this interpretation of the data of Hatcher et al. (1994) is different than that of Paynter (2001) who thought that glazes from Colchester, Smyrna, and Tarsus were all produced using $PbO{\cdot}SiO_2$ mixtures. Also, based on the

high calcium content of all of these glazes, Paynter (2001) suggested that the SiO_2 source was a sand similar to the Belus sand used to make mixed alkali glasses during the Roman period. However, because Paynter (2001) did not have at her disposal comparative material to assess the quality of the Colchester sherds, the assessment that these sherds were glazed with a $PbO{\cdot}SiO_2$ mixture may be ruled out. Also, the modelling procedure used in this present study confirms that the technology used on the Smyrnian sherds was PbO alone. However, as suggested by Paynter (2001), the FeO and CaO content of the Tarsian data does lead one to believe that the source of SiO_2 in these sherds was a sand.

5.1.5 Summary of Lead Glazing During the Roman period: 1st Century BC– 4th Century AD

The fabrication of lead glazes from the Hellenistic through late Roman periods falls into two basic categories. First, in the case of the Smyrna vessels and the sherds from Gaul, it now has been demonstrated that PbO was applied directly to what was probably, based on archaeological evidence, a biscuit fired ceramic (Atik 1995). This was technologically possible since these fabrics possessed high quartz content which drove the reaction with PbO. Second, the Tarsian and Italian glazes are likely derived from earlier glass making and glazing traditions where a flux (traditionally a K_2O or Na_2O alkali, PbO in these glazes) is mixed with sand or quartz pebbles to create a vitreous material. This connection between the alkali glazes and the Hellenistic invention of lead glazes is underpinned by the incorporation of what may be a calcium rich sand which was utilized for glass making in the Near East. While it is mere speculation that the source of the sand is identical in both cases, the deliberate technological choice of this specific raw material type is intriguing.

5.2 After the Roman Empire: Lead Glazes from Europe, the Middle East, and China

In an attempt to trace the development of lead glaze technology after the Roman period, a brief and very general survey was conducted to trace the chemistries of late antique European lead glazes (after the 4^{th} century AD) and Byzantine and Islamic glazes (after the 7^{th} century AD). Applying the same methodology as used for the Roman data, PbO was subtracted from the glaze analyses and these data were re-normalised in order to compare body compositions with the glazes (for the raw data see Appendix C). The aim of this work was twofold. First, it was desirable to understand the legacy of the Roman lead glaze technology after the 4^{th} century. Second, because it has been suggested by Hayes (1992), among others, that lead glaze technology arrived in Byzantine Saraçhane from the late antique European centres, it was thought necessary to test this hypothesis with analytical data. Also, for the sake of comparison, these results were evaluated with new analyses of some Chinese Tang *Sancai* ware (datable to between the 9^{th} century) originally published by Rawson et al. (1988).

5.2.1 European Late Antique Lead Glazes

Most of the European late antique sherds analyzed were from Italy with the exception of one central European sherd from Oberleis (in present day Germany) which dates to the late 4^{th} century. The other sherds included examples of 5^{th} century glazed wares from Ostia and Carlino, 4–7^{th} century sherds from the site of Aosta, and 8–10^{th} century examples of the so-called forum ware from Otranto (see Table 5.5). All of these examples may be considered to be coarse wares that were of purely utilitarian function. Most of these sherds were composed of silica-rich non-calcareous fabrics with

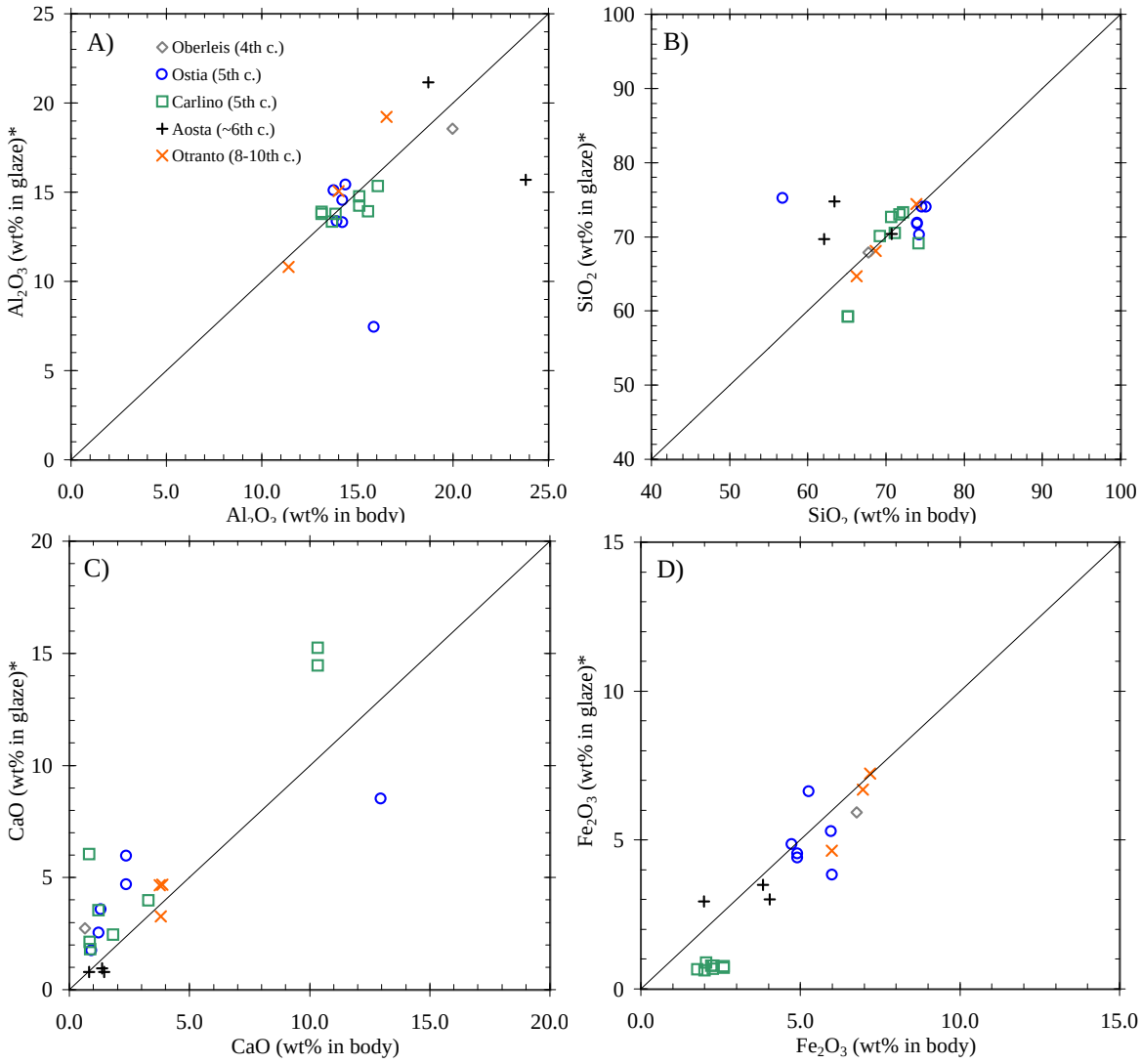

Figure 5.15: A sample of late antique glaze analyses (after PbO has been subtracted away and data normalised) plotted against their body compositions. With the exception of the single sherd from Oberleis, the glazes shown in plots A–D were excavated from sites in Italy.

Sample	*Find Spot*		*Date (A.D.)*	*Vessel Type*	Na_2O	MgO	Al_2O_3	SiO_2	K_2O	CaO	FeO	TiO_2
Oberleis	Central Europe	Germany	4^{th}	mortarium	0.2	0.9	20.0	67.7	2.7	0.7	6.8	0.9
M.11	Aosta	Italy	4-5^{th} c.	mortar	0.7	0.6	18.7	70.7	5.6	0.8	2.0	0.4
M.16	Aosta	Italy	5-7^{th} c.	mortar	1.0	1.2	25.5	62.1	3.6	1.4	3.8	0.7
M.25	Aosta	Italy	4-7^{th} c.	mortar	0.9	1.1	23.8	63.4	3.6	1.4	4.0	1.3
RZ5636	Ostia	Italy	5^{th} c.	coarse ware	0.8	1.0	14.2	74.0	2.0	2.4	4.9	0.5
RZ5637	Ostia	Italy	5^{th} c.	coarse ware	1.1	3.7	15.9	56.8	2.4	13.0	6.0	0.7
RZ5653	Ostia	Italy	5^{th} c.	coarse ware	0.2	1.3	13.9	74.6	2.0	1.2	6.0	0.6
RZ5658a	Ostia	Italy	5^{th} c.	coarse ware	1.0	1.1	14.4	75.2	2.1	0.9	4.7	0.6
RZ5658b	Ostia	Italy	5^{th} c.	coarse ware	0.7	1.3	13.8	74.3	2.5	1.3	5.3	0.6
1	Carlino	Italy	5^{th} c.	coarse ware	0.8	2.1	13.9	71.1	6.2	3.3	1.8	0.6
2	Carlino	Italy	5^{th} c.	coarse ware	0.9	1.6	13.7	74.1	5.9	0.8	2.0	0.7
3	Carlino	Italy	5^{th} c.	coarse ware	0.9	1.7	15.1	72.2	6.2	0.8	2.2	0.7
4	Carlino	Italy	5^{th} c.	coarse ware	0.9	1.9	15.1	71.7	6.4	0.9	2.3	0.6
5	Carlino	Italy	5^{th} c.	coarse ware	0.8	2.3	16.1	69.2	6.6	1.8	2.2	0.8
6	Carlino	Italy	5^{th} c.	coarse ware	0.8	1.9	15.5	70.6	7.0	1.2	2.0	0.7
7A	Carlino	Italy	6–7^{th} c.	coarse ware	0.9	1.7	13.1	65.1	5.1	10.3	2.6	0.5
US55	Otrano	Italy	8–10^{th} c.	forum ware	0.5	2.0	11.4	73.9	1.7	3.8	6.0	0.6
US1040	Otrano	Italy	8–10^{th} c.	forum ware	0.8	2.1	16.5	66.2	2.3	3.8	7.2	0.8
US1489	Otrano	Italy	8–10^{th} c.	forum ware	0.6	2.6	14.0	68.7	2.1	3.9	7.0	0.7

Table 5.5: Late antique glazed sherds excavated from sites in Italy and Europe.

the exception of two sherds (RZ5637 from Ostia and sample 7 from Carlino) which contained appreciable amounts of calcium (see Table 5.5 for body compositions).

As can be seen in the glaze/body plots A–D in Figure 5.15, most of the data from the main oxide components (Al_2O_3, SiO_2, CaO, and Fe_2O_3) lay on unity slope showing that these glazes utilized PbO alone as the glazing compound. However three exceptions to this trend may be observed. As is most evident in Plot B of Figure 5.15, three of the sherds have SiO_2 values above unity slope indicating that a $PbO{\cdot}SiO_2$ mixture was likely used on these samples. One of these sherds from Ostia (RZ5637) was made of a calcareous fabric and was thus in keeping with the earlier tradition of glazing these fabric types with $PbO{\cdot}SiO_2$ mixtures. The other two sherds from Aosta (M.16 and M.25) were more unusual considering that they were made of non-calcareous fabrics. As was observed with the non-calcareous Roman material discussed in section 5.1.1, CaO is also at slightly elevated levels in all these glazes (see Plot C of Figure 5.15) suggesting a possible calcified water source used in the application of the PbO. Most importantly, though more samples could prove this trend to be false, the majority of these data demonstrated that glazing with $PbO{\cdot}SiO_2$ mixtures during the late 4^{th}–10^{th} centuries was largely abandoned on the Italian peninsula. This trend is accompanied by a reduced use of calcareous clays in these samples (with the exception of sample Carlino 7 which was fabricated with a calcareous clay and PbO only).

5.2.2 Byzantine and Islamic Lead Glazes

The Byzantine and Islamic sherds represent a broad array of examples from each of these religious cultures dating from around the 7-8^{th} century through to the 14^{th} century AD (Armstrong et al. 1997; Mason 1994). The listing of these sherds together with their fabric analyses (as determined by SEM/EDS) may be seen in Table 5.6. In Al_2O_3-CaO space (see Figure 5.16), the samples may be seen to divide nominally

Sherd	Apprx. Date	Context	Na_2O	MgO	Al_2O_3	SiO_2	K_2O	CaO	FeO	TiO_2
SA99RD37	~7-8th c.	Byz	1.5	3.2	16.0	66.1	3.0	1.9	7.6	0.8
SA2000RD7	~7-8th c.	Byz	1.2	4.4	18.5	55.6	3.6	8.3	7.7	0.8
CR9550	9-10th c.	Byz	0.4	0.2	29.6	65.7	0.8	1.0	1.6	0.8
CR9551	9-11th c.	Byz	0.2	0.6	19.6	75.8	1.4	0.5	1.0	0.9
Mango	9-10th c.	Byz	0.4	0.6	27.4	63.3	0.7	1.9	3.0	2.7
Mangob	9-10th c.	Byz	0.4	0.7	30.7	61.9	0.7	3.2	1.4	1.0
CR9560	10-11th c.	Byz	0.3	0.5	25.1	69.5	0.4	1.1	1.7	1.2
CR9559	10-11th c.	Byz	0.3	0.6	25.8	67.3	0.8	1.0	3.3	0.9
SA2000JP40A	11-12th c.	Byz	1.6	2.4	18.2	77.9	3.4	4.6	6.9	0.7
SA2000JP40B	11-12th c.	Byz	1.1	3.4	19.8	75.8	4.1	5.2	8.2	0.8
CR9561	11th c.	Byz	2.2	2.5	20.7	55.9	3.9	4.0	8.3	1.8
CR9562	11th c.	Byz	0.7	1.6	21.9	59.1	3.9	4.2	7.5	0.8
SA2000JP42	12th c.	Byz	1.6	2.4	17.3	63.2	3.3	4.6	6.5	0.7
CR9549	12-13th c.	Byz	1.5	7.3	13.1	52.2	2.5	16.0	6.6	0.7
CR9564		Byz	1.2	3.3	14.5	63.0	2.6	8.0	6.6	0.7
CR9567		Byz	1.9	6.1	14.5	50.1	2.9	16.8	6.9	0.7
CR9563	13th c.	Byz	0.7	3.7	15.0	45.4	1.9	25.4	7.1	0.6
CR9548	13th c.	Byz	2.2	4.6	12.6	49.0	2.6	22.8	5.4	0.5
CR9548b	13th c.	Byz	2.2	4.6	12.6	49.0	2.6	22.8	5.4	0.5
988.117.43	8th c.	Islamic	1.5	4.5	11.4	51.3	1.5	22.5	6.4	0.8
988.117.30	8th c.	Islamic	1.1	0.6	29.3	66.2	0.8	0.3	2.0	1.2
988.117.42	8th c.	Islamic	1.6	3.7	12.1	56.5	1.2	18.3	5.7	0.9
BA-716	8-9th c.	Islamic	1.2	7.5	13.2	49.2	1.7	19.9	6.4	0.6
923.34.47	8-9th c.	Islamic	2.0	5.9	13.2	57.7	3.2	11.5	5.5	0.7
BA-952	8-9th c.	Islamic	1.9	7.7	12.2	52.6	1.4	17.6	5.7	0.9
909.38.5	10th c.	Islamic	1.8	3.6	14.5	53.2	2.8	16.1	6.8	1.0
909.43.42	14th c.	Islamic	2.3	3.3	17.4	52.3	1.6	6.0	10.7	4.7
909.43.43	14th c.	Islamic	1.8	2.7	16.0	61.1	1.4	5.7	8.6	1.6

Table 5.6: Body fabric analyses of Byzantine (Byz.) and Islamic sherds.

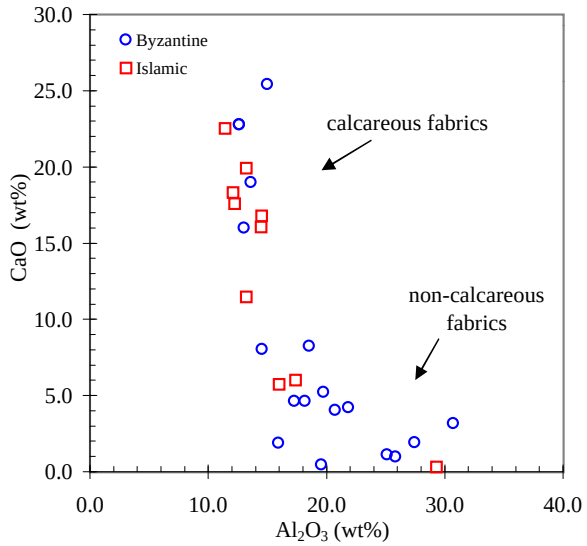

Figure 5.16: Al_2O_3-CaO bivariate plot of Byzantine and Islamic body fabrics.

into two compositional groups. A low calcium group ($<$ 8% CaO with variable Al_2O_3 between 11-31 wt%) contains mostly sherds from Byzantine contexts. Two Islamic sherds in this group (samples 909.43.42 and 909.43.43) date to late Mamluk contexts (14^{th} c.). The other Islamic sherd in this group (988.117.30) is an unusual low calcareous fabric of the 8^{th} century. The other group is high in calcium ($>$ 15% CaO with Al_2O_3 between 10 and 15 wt%). This group contains the majority of Islamic sherds together with the remainder of the Byzantine sherds. The Byzantine sherds in this group are all late dating between the 12–13^{th} centuries.

When the body compositions of these sherds are plotted against their adjusted glaze analyses (PbO subtracted from the total and the data re-normalised), it may be immediately gleaned that the results for these Byzantine and Islamic sherds contrast sharply with the European late antique glazed wares (Figure 5.17). As shown in Figure 5.17, the Byzantine and Islamic data in these body/glaze plots do not, for the most part, fall on unity slope. In particular, if plot B of Figure 5.17 is examined, it may be seen that all but three of the sherds have SiO_2 values above their body compositions showing that these glazes were derived of mixtures of PbO and SiO_2 (in the form of either sand or quartz pebbles). The three sherds falling on unity slope

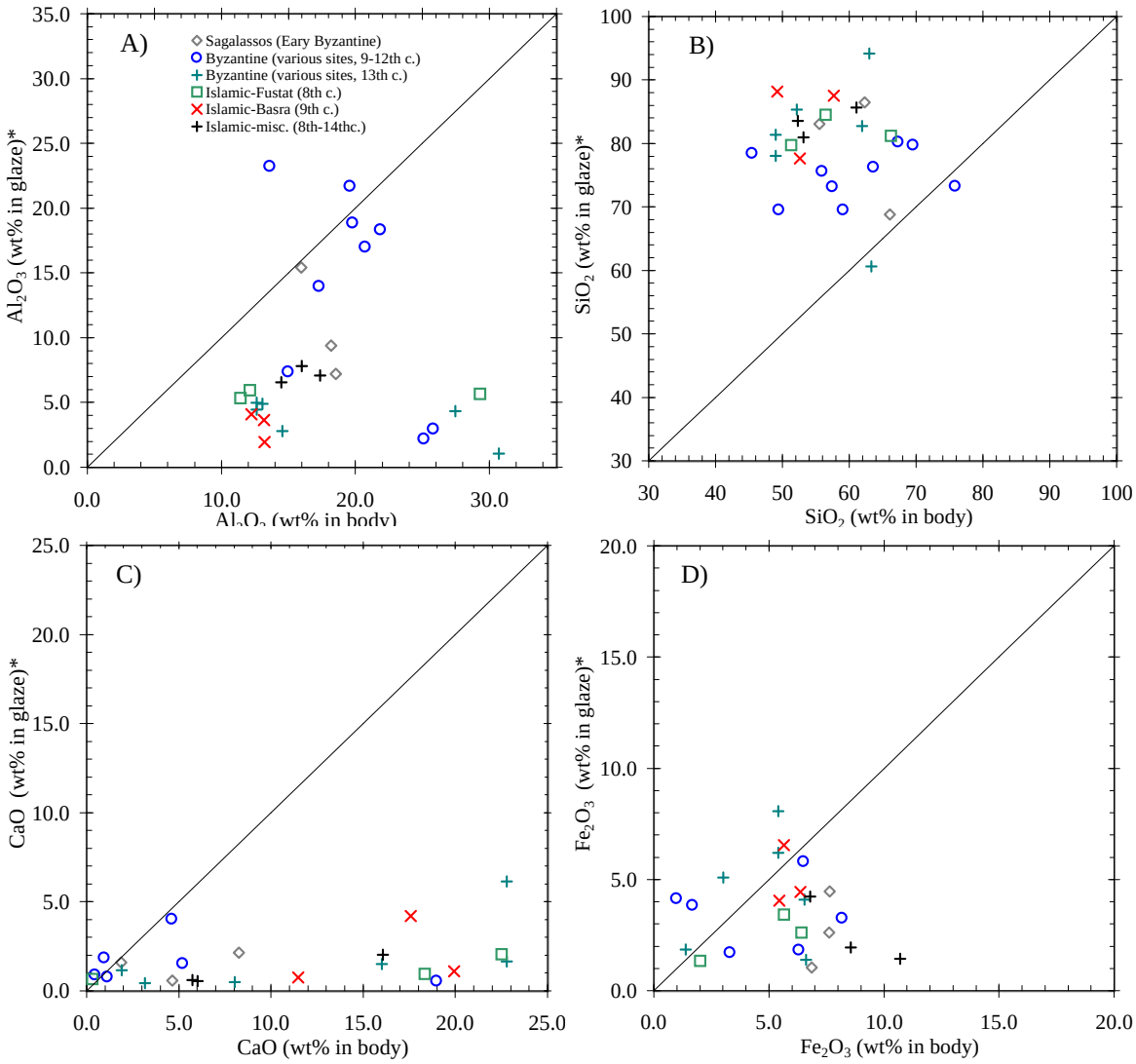

Figure 5.17: Sampling of Byzantine and Islamic glaze analyses plotted against their body compositions. The values

(SA99RD37, CR9551, and Mango) all are composed of low CaO body fabrics.

To further assess the chemistry of these glazes the dissolved body composition was modelled (from the Al_2O_3 content in the glaze as per equations 5.2 and 5.3) and subtracted from the glaze composition. It may be seen that the majority of the glazes cluster around 75% PbO (see Figure 5.18) which resides slightly below the SiO_2–PbO eutectic at 30% SiO_2. The Islamic sherds examined are particularly interesting considering that they cluster tightly around values of 26 ±2% SiO_2 and 72

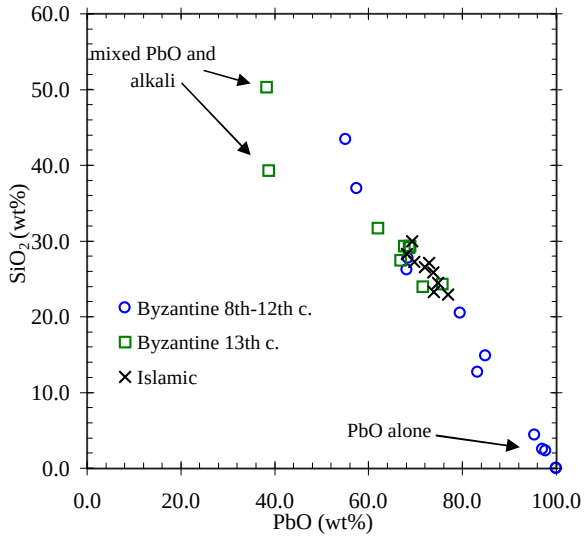

Figure 5.18: Discriminant plot of Byzantine and Islamic glazes after body contributions have been subtracted away.

±2% PbO, yet their dates range from 8^{th} century (from Fustat, Egypt) through 14^{th} century Mamluk contexts. While a specific explanation for this uniform behaviour will not be posited here, it is likely that these compositions result from buffering effects of the silica in the body fabrics (as discussed previously in Chapter 3 in Figures 3.8 and 3.37 and above in section 5.1.3). Other unusual compositions observed in these data are the relatively low lead values (∼40%) of two late Byzantine sherds (samples CR9565 and Mango, marked as mixed alkali and PbO in Figure 5.18) which also show high alkali content (around 8–11% Na_2O). While lead alkali glazes were certainly present in Islamic context of the same period, they were most often associated with tin-opacification and exhibited lead levels of around 30%. Even so, non-opacified and mixed high lead and alkali glazes in Byzantine contexts have been previously reported by Henderson and Mango (1995).

5.2.3 Chinese Sancai Ware

SEM/EDS body analyses for the Sancai studied here may be seen in Table 5.7. All of these glaze are formed from white bodied fabrics with high Al_2O_3 and SiO_2 compositions. When these body analyses are plotted against their glazes (presented in

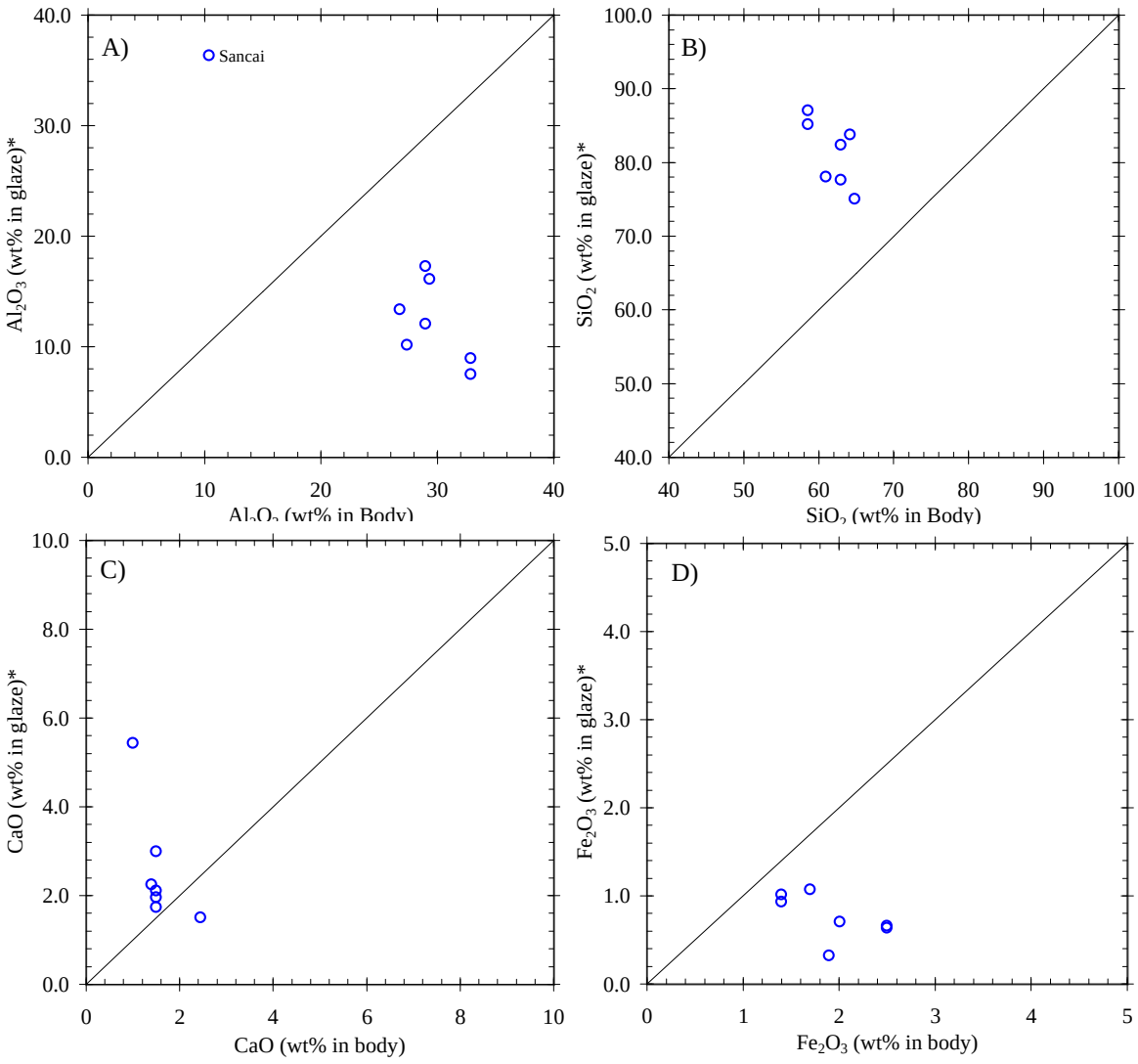

Figure 5.19: Examples of Chinese Sancai ware glazes plotted against their body compositions.

	Na_2O	MgO	Al_2O_3	SiO_2	K_2O	CaO	FeO	TiO_2
25968T	1.0	0.5	29.0	63.0	2.1	1.5	1.4	1.3
25969R	0.7	0.6	32.9	58.6	1.6	1.5	2.5	1.2
25971S	0.7	0.5	27.4	64.2	2.4	1.4	1.7	1.3
25970OU	0.6	0.5	26.8	64.8	2.5	1.0	1.9	1.3
Sherd C	0.9	1.0	29.4	61.0	2.2	2.5	2.0	1.1

Table 5.7: Sancai body analyses. Note that Sherd C is an unpublished Sancai sherd courtesy of N. Wood.

	Na_2O	MgO	Al_2O_2	SiO_2	PbO	K_2O	CaO	Fe_2O_2	TiO_2	CuO
25968T	0.0	0.2	0.0	21.6	71.1	0.0	0.5	0.1	0.3	6.3
25968Tb	0.0	0.2	0.0	28.6	64.0	0.1	0.7	0.2	0.4	5.7
25969R	0.1	0.4	0.0	35.5	61.2	0.2	0.7	0.2	0.3	1.4
25969Rb	0.0	0.4	0.0	32.1	63.0	0.1	1.1	0.2	0.2	3.0
25971S	0.1	0.5	0.0	29.4	65.6	0.1	0.8	0.3	0.2	3.0
25970OU	0.6	0.5	0.0	23.0	71.9	1.2	2.4	0.0	0.4	0.0
Sherd C	0.1	0.4	0.0	36.3	60.9	0.1	0.3	0.1	0.5	1.3
average	**0.1**	**0.4**	**0.0**	**29.5**	**65.4**	**0.3**	**0.9**	**0.2**	**0.3**	**2.9**
σ	0.2	0.1	0.0	5.7	4.5	0.4	0.7	0.1	0.1	2.3

Table 5.8: Sancai glaze analyses after body contribution has been calculated from the amount of Al_2O_3 in the glaze and subtracted. The *b* after several of the samples denotes the glaze analysis on the verso side of the sherd. All the data has been normalised.

Figure 5.19) this shows that the raw materials were likely comprised of a SiO_2·PbO mixture. The plots of Al_2O_3, SiO_2 and Fe_2O_3 (Plots A, B, and D of Figure 5.19) all demonstrate characteristic features of SiO_2·PbO glazes with the data for SiO_2 laying above unity slope, and Fe_2O_3 and Al_2O_3 laying below unity slope. Furthermore, CaO lay slightly above unity slope which, given the relatively low values, may be accounted for by a hard water source possibly used in the glazing process. The contribution of the body composition to the glaze was also modelled and subtracted from the glaze compositions (measured at glaze edge). These results, which are shown in Table 5.8, corroborate that the glazing mixture was PbO and likely sand mixture as denoted by the relatively high CaO and Fe_2O_3 levels. It is also clear that the *Sancai* were coloured by Cu compounds as indicated by the high CuO levels in the normalised glaze results.

5.2.4 Conclusions on Late Antique European, Byzantine, Islamic and Chinese Lead Glazing Techniques

By comparing the late antique European lead glazes with the Byzantine and Islamic ones, these data show that it is not likely that the early Byzantine technology was inherited from the Europeans. That the Byzantine and Islamic lead glaze technology utilized SiO_2·PbO mixtures is interesting considering that this technology had long since died out in this region prior to its Byzantine re-introduction. These facts suggest one of two possibilities: 1) the technology was re-invented at this point in time, or 2) the technology arrived into Asia Minor from the Far East. The data from the *Sancai* wares suggest that this later possibility is viable, considering that these Chinese vessels also utilized SiO_2·PbO mixtures as glazing compounds. Furthermore, the date of production of the *Sancai* fits nicely with the date of re-introduction of lead glazes into Asia Minor. It is equally interesting to note that like the Sancai, the first Byzantine lead glazed sherds were produced using high white firing and high Al_2O_3 bodies. However, this particular technological connection between China and Mediterranean still needs considerable verification. In particular, it would be useful to compare Central Asian glazed wares from this period to the Chinese and Byzantine/Islamic lead glazes.

Chapter 6

Synthesis and Conclusions

The primary aim of this thesis has been to define the technological style of Roman lead glazed ceramics (see Chapter 1 section 1.1 for definition of technological style). Of critical importance to this exercise was the introduction of a corpus of new analyses – of both ceramic bodies and glazes – that spanned the geographical reaches and duration of the Roman Empire (see Appendix C for listing of all the sherds studied and their chemistry). Analyses of sherds from Late Antique European, Byzantine, Islamic, and Tang Chinese contexts were also conducted in order to elucidate their possible connection to the Roman tradition. To assess the technological style for these above samples, a series of replication experiments were conducted. These replication experiments (presented in Chapter 3) were designed to evaluate the chemical and microstructural features that would be obtained by each of the possible material and technological choices available to a potter producing lead glazes (as outlined in Figure 1.2 of Chapter 1). By comparing these replicated glazes to archaeological artifacts, the procedures likely utilized in glaze fabrication were established.

The chief analytical techniques employed in this study were inductively coupled plasma atomic emission spectroscopy (ICP-AES), for the body analyses, and electron probe microanalysis (EPMA), for the glaze analyses. The body analyses were used in a preliminary provenance study (Chapter 4) to define discrete compositional groupings of sherds that likely belonged to a common line of production. The glaze analyses were

used to understand how the raw glaze materials reacted with the ceramic body to form the final glaze composition (Chapter 5). To this end, EPMA analyses were conducted at glaze edges and at the interface between the glaze and the ceramic body. Also, profiles were obtained along glaze cross-sections to examine compositional gradients. The shape of these gradients were found to be indicative of certain combinations of raw glaze materials.

In this final chapter, the findings on the technological style of lead glazes are drawn together and summarized. In the first section (section 6.1), the results from the replication experiments are reviewed. This is followed by a discussion on the types of glazes recognized among the archaeological material and the raw materials employed in their fabrication (section 6.2). Lastly, some of the archaeological implications of this study are followed by recommendations for future research (section 6.3).

6.1 Replication

The replication work of Chapter 3, to a large extent, was built on the thesis of Molera (1996). In this previous study, the reactions between $PbO{\cdot}SiO_2$ glaze mixtures and earthenware ceramics were thoroughly examined. Although, experiments were conducted in this present study to confirm the results of Molera (1996) (as in section 3.4.2 in Chapter 3), most of the work here focused on the reactions between PbO alone and earthenware ceramics which hitherto had been unstudied. Of particular importance, it was discovered that the glazes made with PbO alone and $PbO{\cdot}SiO_2$ mixtures followed two distinct reaction paths that resulted in different compositional profiles (see Figures 3.24 and 3.39 which diagram, respectively, these reaction paths). When glazing with PbO alone, it was found that flat compositional profiles were created (as seen in Figure 3.19). However, when using $PbO{\cdot}SiO_2$ glaze mixtures, it was found that compositional profiles with steep gradients indicative of diffusion were produced. Based on these diagnostic features for each of these raw material

combinations, the glazes on the archeological sherds could be classified according to whether they were made from PbO alone or with $PbO{\cdot}SiO_2$ mixtures.

Several other characteristic chemical features were determined by using PbO alone. For instance, the chemical composition of the glaze remained the same, at a given maturing temperature, regardless of whether the ceramic had been raw or biscuit-fired prior to the glaze application (see Table 3.4 in Chapter 3 for these results). Furthermore, this composition remained the same regardless of whether or not clay was mixed with PbO as a flocculant. A linear relationship was also discovered between the firing temperature and the amount of PbO reacted with the ceramic (as seen in Figure 3.18 of Chapter 3). This particular feature of PbO glazed sherds meant that firing temperatures could be estimated for archaeological sherds (with glazes of this type) based on the amount ceramic dissolved by PbO.

With $PbO{\cdot}SiO_2$ applied to calcareous clays, it was established that instead of producing sanidine-like lead feldspars as were found on the non-calcareous clays of Molera (1996), wollastonite crystals instead formed at the interface between the ceramic and the glaze (see section 3.4.2.1 of Chapter 3). It was also found that it is possible to obtain qualitative information on possible firing temperatures of these glaze types based on the univariate box plots of SiO_2 content as shown in Figures 3.8 and 3.37 in Chapter 3. These plots demonstrated that with increasing temperature, the glaze composition was driven toward the PbO-SiO_2 eutectic residing at 30% SiO_2. The compositional profiles of these glazes (shown in Figure 3.35 of Chapter 3) demonstrated (with the exception of the 1050°C profile) that diffusion in these glazes was sluggish due to the high viscosity of the melts. This meant that the composition at the very edge of the glaze approximated the combined composition of the raw materials for the temperature range between 750 and 950°C. This edge value was therefore found to be useful for estimating the raw material compositions in archaeological glazes (in section 5.1.3 of Chapter 5).

6.2 Glaze Types Recognized and Raw Materials Utilized

Based on the replication work of Chapter 3, it was seen that the archaeological material (presented in Chapter 5) divided into both of the glazing categories outlined: using PbO alone or with $PbO{\cdot}SiO_2$ mixtures (see Figure 5.1). The 2^{nd}-4^{th} century sherds composed of calcareous fabrics, namely those with a likely Italian provenance, were glazed with $PbO{\cdot}SiO_2$ mixtures. Non-calcareous sherds of the same period, such as those with a suspected provenance of central Gaul, were glazed with PbO alone. The re-analysis of the XRF analyses of lead glazes of Hatcher et al. (1994), showed this same trend with the calcareous sherds of Tarsus being glazed with $PbO{\cdot}SiO_2$ mixtures, and the non-calcareous sherds of Colchester/Silchester as well as those from Smyrna/Clazomenae being glazed with PbO alone (see Figures 5.12 and 5.13).

Attempts were also made at retrieving the compositions of raw materials used in these Roman glazes by a variety of data reduction proceedures (see sections 5.1.1 and 5.1.3 of Chapter 5). For the PbO glazed sherds, it was found that very pure sources of PbO were utilized which possessed few trace elements which would have been suggestive of the material origins of this oxide. The $PbO{\cdot}SiO_2$ glazed sherds were more interesting in that these analyses revealed that the source of silica was probably a calcareous sand.

The results for samples after the Roman Empire showed that the glazes from Late Antique European contexts (mostly from Italy) were made from PbO alone (see Figure 5.15). The remainder of these post-Roman sherds (those from Byzantine, Islamic, and Chinese contexts) were primarily created from $PbO{\cdot}SiO_2$ mixtures. It is significant that for the Byzantine and Islamic samples, the glaze raw materials did not correspond to the body chemistry as had been the case for the Roman material. As shown by Figure 5.16 of Chapter 5, both calcareous and non-calcareous ceramics were used as substrates for glazes made from $PbO{\cdot}SiO_2$ mixtures.

6.3 Archaeological Implications and Future Research

The main contribution this thesis hopes to have made to the archaeology of Roman lead glazed ceramics is that it provides the most comprehensive chemical description of this material to date. However, this thesis leaves many questions about lead glazed ceramics unanswered opening this subject to further refinement. For instance, little is yet known about the 'discovery' of lead glazing and how this technology might have related to either the earlier glazing traditions using alkaline plant ash fluxes or metallurgical processes such as the cupellation of silver from argentiferrous ores. Also, research on the sources of raw material used in these glazes is still in its infancy. Although, some lead isotope work was presented in section 4.3 of Chapter 4, many more of these analyses are needed in order to understand the source of PbO used in these glazes. Likewise, although a connection between lead glazing and glass-making has been tentatively posited by virtue of the calcareous sand used in the fabrication of these materials (see section 5.1.3 of Chapter 5), this subject deserves to be investigated further and would certainly benefit from a study using Sr and O isotopes as was proven effective by Freestone et al. (2003).

Despite these open questions, several important aspects about lead glazes have been revealed in this study. It has been established in Chapter 4 that there were at least eight geochemically distinct clays used in the fabrication of lead glazed vessels between the 1^{st} century BC and the 4^{th} century AD as determined from the combined data set of sherds analysed by ICP-AES in this present study, and those previously analysed by Hatcher et al. (1994) as well as Pérez-Arantegui et al. (1996). It is doubtful that each of these groups represents a unique workshop. Rather, it seems that there were probably five main centers which utilized more than one clay type during their existence. These five centers included a likely central Gaul workshop defined by sherds found near London, a possible workshop along the Danube which provided these wares to the Dacia Repensis and Upper Moesian areas of the Roman

Empire, an Italian centre at either Campania or Latium, and Anatolian workshops at Tarsus and Smyrna. However, to allow for a more specific assessment of the provenance of these sherds, a thorough petrographic examination of these fabrics is required.

As concerns the technological transfer of lead glaze technology from Anatolia to the Western Mediterranean during the early Roman period, the data presented in Chapter 5 demonstrates that the Tarsian glaze technology of applying $PbO{\cdot}SiO_2$ mixtures or frits to calcareous clays was also found to be used in Italy on her calcareous clays. Likewise, the technology of employing PbO alone on non-calcareous clays discovered on sherds from Smyrna was again found on the non-calcareous clays of central Gaul. Whether these findings represent actual technological transfer or are rather coincidental discoveries imposed by the chemical behaviours of the raw materials is an open debate. Equally ambiguous is the inheritance of lead glazes by Byzantine and Islamic artisans. While it remains a possibility that the technology of lead glazing was a holdover from Roman times in Europe and the Mediterranean, the chemistry of the Byzantine and Islamic lead glazed vessels shares much more in common with Chinese lead glaze wares which were made from white firing bodies glazed with $PbO{\cdot}SiO_2$ mixtures (as was discussed in section 5.2.4). It seems certain, however, that with a possible study on the social history of lead glazes, the data presented here would help to illuminate technological changes for this material over the nine-hundred years covered by this thesis.

Appendix A

Analytical Techniques

The diverse techniques and instruments employed in this thesis reflect the multidisciplinary and collaborative nature of archaeological materials research. The chemical composition of ceramics in this study was determined through inductively coupled plasma atomic emission spectroscopy (ICP-AES) performed by Dr. N.J. Walsh at the Department of Geology, Royal Holloway, University of London. High temperature synchrotron radiation X-ray diffraction (HT-SRXRD), which was used to determine the mechanism of reaction between PbO and a fireclay refractory, was conducted Dr. T. Pradell at the CERN Synchrotron facility in Grenoble, France. Traditional X-ray diffraction was performed on the Philips PW1729 at the Department of Materials Science at the University of Oxford. The bulk of the research for this thesis utilized electron probe microanalysis (EPMA) techniques which were performed on our in-house Cameca SU30 probe and on the Jeol JXA 8800 Superprobe located at Materials Science's Begroke Facility. Although some of these analytical techniques were discussed within the body of the thesis (namely HT-SRXRD in section 3.4.1.4 of Chapter 3 and XRD in section 3.4.1 of Chapter 3), the two most commonly used analytical procedures (ICP-AES and EPMA) are outlined below.

A.1 Electron Beam Methods and Procedures

The electron probe is a state-of-the-art instrument for obtaining spatially resolved (on the order of a μm) quantitative chemical information on both major and minor elements. It is one of the workhorse analytical technique for solid state materials science and mineralogical studies. Since the mechanics of this analysis technique are well known and have been thoroughly described elsewhere, only a brief introduction to the subject will be presented here as it applies to glasses and ceramics (Goldstein et al. 1992).

Electrons for both imaging and analysis are produced by thermionic emission from a tungsten filament in an electron gun. These electrons are accelerated and passed through an electromagnetic condenser and objective lenses to produce a coherent electron beam. The beam, which can be focused to a diameter less than a μm, interacts with the sample allowing it to be either imaged or analyzed. For imaging (the scanning electron microscope (SEM) part of the instrument), the beam is scanned over the sample surface and secondary electrons or backscatter electrons are monitored. Secondary electron images are used to examine surface morphologies including relative roughness. Backscatter electron images show compositional variation by gray-scale contrast (*eg.*, the lighter the gray, the heavier the atomic number). For quantitative analysis (known as electron probe microanalysis, EPMA), characteristic X-Rays are detected by energy dispersive (EDS) or wavelength dispersive spectrometers (WDS).

A.1.1 Sample Preparation

Using a standard procedure describe previously, samples were prepared for EPMA by mounting the ceramic/glaze cross-sections in epoxy resin (Shortland 2000). After curing, samples were ground to mirror finish using a series of lapping wheels with increasingly smaller diamond grits down to a 0.25 μm grit. After polishing, samples

were soaked in diethyl ether and wiped down using lens tissue prior to being coated with carbon using a sputter evaporation system.

A.1.2 Analytical Procedure

Throughout this study, WDS measurements are the quoted values unless otherwise indicated. Typical conditions of analysis were 20 second count times per element with an acceleration voltage of 15 keV, a beam current of 10 nA, and a beam size regulated between 1 and 3μm. These conditions were found to be well suited to obtaining precision analyses on a standard high lead alumino-silicate glass (DLH1) made bespoke for RLAHA.

Calibration on RLAHA's Cameca SU30 was performed on a set of mineral and metal standards prepared by P&H Developments Ltd. A set of typical standard conditions are presented in table A.1. The standard deviation σ and the average number of counts was calculated from at least five positions on each standard.

Crystal	*Element*	*Standard*	*X-ray line*	*Pos. (2Θ)*	*counts/sec/nA*	σ
TAP	Na	albite	Kα	0.46358	27.44	1.19
	Mg	periclase	Kα	0.38507	374.18	0.31
	Al	orthoclase	Kα	0.32467	79.51	0.29
	Si	albite	Kα	0.27741	179.28	0.39
LIF	Ti	TiO_2	Kα	0.68272	83.98	0.24
	Cu	CuO	Kα	0.38252	79.26	0.79
	Fe	FeO	Kα	0.48082	127.86	0.52
PET	Pb	PbTe	Mα	0.60316	34.07	0.04
	K	orthoclase	Kα	0.42735	61.37	0.27
	Ca	wollastonite	Kα	0.38381	206.75	0.1

Table A.1: Standard calibration conditions on Cameca SU30

Evaluation of the quality of the calibration was made by comparing the quoted assay values of the DLH1 secondary standard to the values obtained by probe analysis. Secondary standard analyses were deemed to be acceptable if they were between 99-101%. The DLH1 standard was analysed prior to each session on the electron microprobe to check for instrument drift. A running tab of a significant number of

standard and archaeological sample points (from both the edge and ceramic interface of the glazes) collected on the Cameca SU30 can be seen in figure A.1. The run number in figure A.1 gives the number and order of analyses over a period of two months and therefore provides a sense of the long term precision and accuracy obtainable on the Cameca Su30. The precision of the instrument can be further accessed in table A.2 where the running average and standard deviation of DLH1 from this study (both on the Cameca SU30 and the Jeol 8800) is compared with the assay values and those independently determined on the British Museum's Jeol JSM840 EDX system and the University of Barcelona's Cameca SU50 microprobe.

A.2 ICP-AES

Approximately 1 gram was removed from each sherd. All outside surfaces, including the glaze, were removed by grinding before the sherd was pulverized in a mortar. Standard ceramic samples (MINTEK SARM 69 and KN Sherd) were randomly interspersed between the experimental samples to check the precision and consistency of the measurements. These powdered samples were sent to Dr. J.N. Walsh of the Department of Geology, Royal Holloway, University of London for further preparation and analysis. The resulting powdered samples were digested in 2:1 mixture of hydroflouric acid (HF) and hyproclorate ($HClO_4$) and then evaporated to dryness. The resulting residue was re-dissolved in 10% hydrochloric acid (HCl) and analyzed on a Philips PV8060 ICP-AES. The data output submitted to the laboratory was with elements Al, Fe, Mg, Na, Ca, K, Ti, P, and Mn reported in wt%, and Ba, Ce, Co, Cr, Cu, La, Li, Ni, Nb, Sc, Sr, V, Y, Zn, and Zr reported in parts per million g/g. Detection limits of this instrument are reported between 5- 10 ppm. The average and standard deviation for the standard analyses are shown in Table A.3 compared to target values for major elements. Minor element standard data is shown in Table

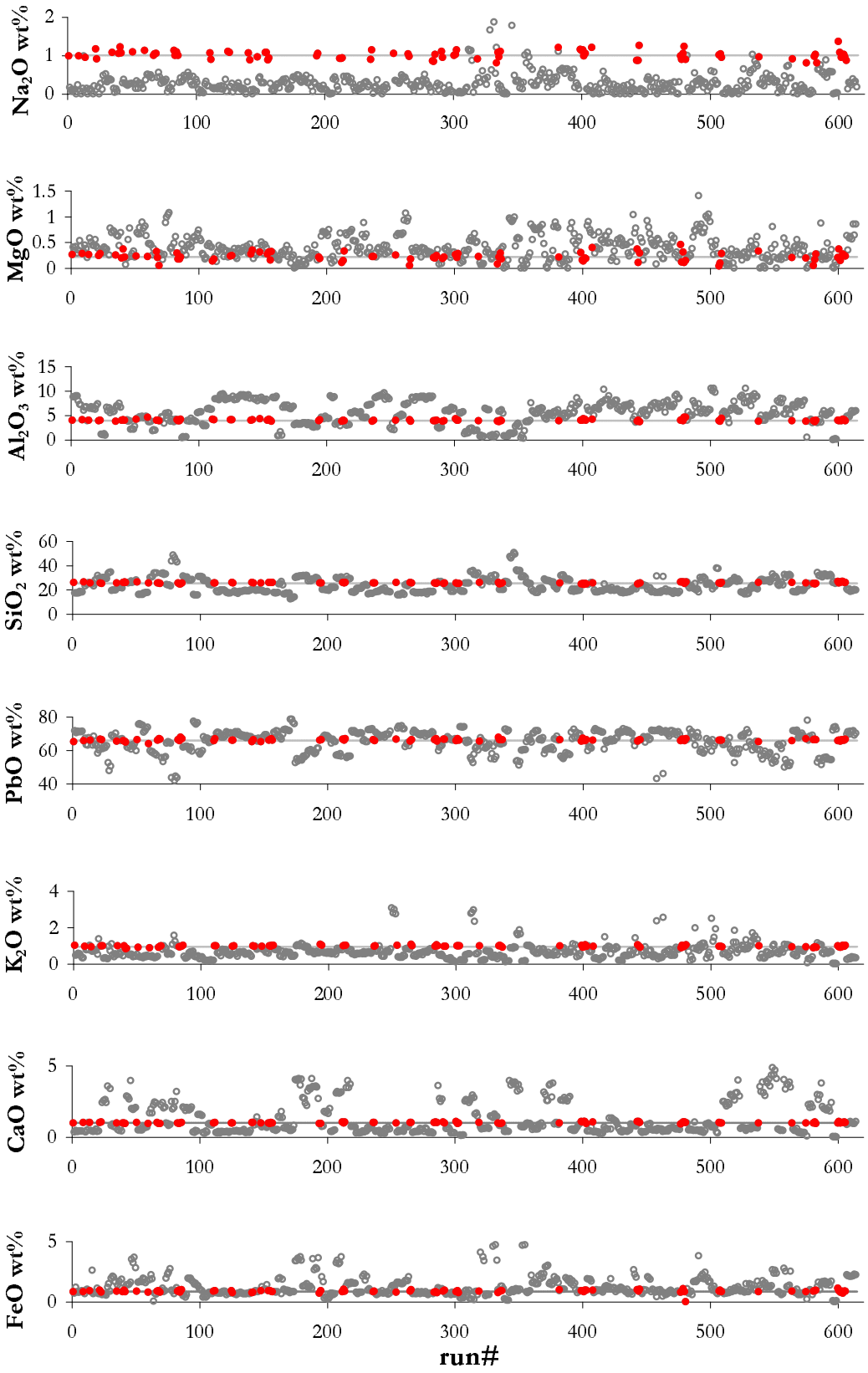

Figure A.1: Probe points on archaeological samples (grey open circles) and DLH1 standard (red circles).

A.4. All data reduction and statistical analyses were performed in Microsoft Excel using the XLSTAT statistical analysis add-in.

Instrument location		Na_2O	MgO	Al_2O_3	SiO_2	PbO	K_2O	CaO	FeO	TiO_2	CuO	*Total*
(1) RLAHA	mean (82)	1.02	0.22	3.99	25.56	66.08	0.97	1.00	0.86	0.03	0.02	99.75
	σ (82)	0.11	0.08	0.18	0.49	0.62	0.05	0.04	0.12	0.04	0.04	
(2) Begbroke	mean (25)	1.11	0.22	4.31	26.28	66.27	1.04	1.04	0.79	0.01	0.15	101.21
	σ (25)	0.06	0.03	0.27	0.63	1.39	0.06	0.07	0.17	0.02	0.23	
(3) Barcelona	mean (20)	1.09	0.21	3.81	25.86	66.19	0.97	1.00	0.91	0.00	0.00	100.04
	σ (20)	0.05	0.04	0.11	0.19	0.50	0.04	0.06	0.04	0.00	0.00	
(4) British Museum	mean (3)	1.01	0.33	3.98	24.96	67.04	0.96	1.04	0.98	0.00	0.00	100.97
	σ (3)	0.07	0.05	0.06	0.15	0.16	0.06	0.07	0.06	0.00	0.00	
Target		**1.00**	**1.00**	**4.00**	**26.00**	**65.00**	**1.00**	**1.00**	**1.00**	**0.00**	**0.00**	

Table A.2: Running Average of the DLH1 glass standard on Oxford's Cameca Su30 (1) and Jeol JXA8800 (2) compared with the University of Barcelona's Cameca Su50, The British Museum's Jeol JSM840 (EDX), and target assay.

		Al_2O_3	Fe_2O_3	MgO	CaO	Na_2O	K_2O	TiO_2	P_2O_5
SARM 69	Average	14.03	7.25	1.83	2.27	0.75	1.92	0.70	0.23
	σ	0.31	0.22	0.03	0.05	0.01	0.05	0.01	0.01
	Relative σ	2.21	2.99	1.84	2.31	1.46	2.36	1.76	2.28
	Target value	14.40	7.18	1.85	2.37	0.79	1.96	0.78	0.28
KN	Average	13.98	7.45	5.37	10.78	0.91	2.51	0.65	0.19
	σ	0.23	0.14	0.07	0.22	0.02	0.04	0.02	0.01
	Relative σ	1.61	1.90	1.31	2.05	1.85	1.72	2.54	2.82
	Target value	13.75	7.69	5.41	10.92	0.88	2.33	0.64	

Table A.3: Major element compositions and standard deviation statistics for the SARM 69 and KN standards by ICP-AES.

		Ba	Co	Cr	Cu	Li	Ni	Sc	Sr	V
SAS	Average	508.50	22.67	193.83	46.67	24.00	53.67	18.83	110.50	140.17
	σ	17.66	1.03	4.07	1.75	0.00	1.03	0.41	1.87	1.72
	Relative σ	3.47	4.56	2.10	3.75	0.00	1.92	2.17	1.69	1.23
	Target value	518.00	28.00	223.00	46.00		53.00	20.00	109.00	157.00
KN	Average	345.20	27.40	328.80	71.60	52.80	321.00	19.20	310.20	138.20
	σ	3.42	1.95	10.47	1.67	0.45	2.83	0.45	2.28	2.77
	Relative σ	0.99	7.11	3.19	2.34	0.85	0.88	2.33	0.74	2.01
	Target value	344.67	28.33	273.00	70.67	46.67	319.00	19.67	313.33	144.33

		Y	Zn	Zr*	La	Ce	Nd	Sm	Eu	Dy	Yb	Pb
SAS	Average	26.17	65.83	75.83	27.83	59.00	30.23	5.55	1.24	4.50	2.60	15.39
	σ	0.41	0.98	16.70	1.17	4.52	1.69	0.18	0.07	0.15	0.06	2.14
	Relative σ	1.56	1.49	22.03	4.20	7.66	5.59	3.23	6.02	3.44	2.43	13.89
	Target value	29.00		271.00		67.00	30.00					
KN	Average	22.20	122.20	32.40	26.20	41.60	28.43	3.94	1.15	3.46	1.84	19.11
	σ	0.45	0.84	8.32	1.10	4.51	1.90	1.10	0.15	0.11	0.05	0.91
	Relative σ	2.01	0.68	25.69	4.18	10.83	6.68	27.78	12.75	3.30	2.98	4.78
	Target value	22.00	118.00	35.33	29.33	49.33	24.67	6.00	0.93	3.83	1.57	

Table A.4: Trace element ICP-AES data for the SARM 69 and KN standards. Values are reported in parts per million (ppm)

Appendix B

Diffusive Dissolution Model

The numerical model outlined in this appendix intends to describe two critical steps of the glaze formation process: the dissolution of the ceramic material and its diffusion into a bulk glass melt. This model relates to work presented in the experimental program of Chapter 3 and, to a minor extent, the interpretation of archaeological material in Chapter 5.

Following geological models of magma flows, the diffusive dissolution (D-D) model describes the mass movements that contribute to the ultimate chemical composition and physical structure of an archaeological glaze. The D-D model is based on the chemical activities in molten glass as well as the classical physical laws governing diffusive movement. Thus, by fitting the D-D model to experimentally acquired concentration profiles from glaze cross-sections, in-depth information of the stoichiometries of the formation reactions, the formation rates, and body dissolution rates can be obtained (Lasaga 1979; Chakraborty et al. 1995a; Chakraborty et al. 1995b). Further evidence on the temperature and duration of firing may be extracted by correlating the coefficients of diffusion to the viscosity of the melt through Tamman-Fulcher-Vogel relations (TFV) and Einstein-Stokes/Erying equations (Liang et al. 1996). Through this model, approaches will be presented to chemically describe the development of a glaze microstructure, to evaluate raw material compositions, and to approximate temperatures and durations of firing.

In the most simplistic case (*i.e.*, one diffusing species and a solvent), the ceramic will dissolve forming a concentration c of species i which diffuses following the expression

$$\frac{\partial c_i}{\partial t} = D_i \frac{\partial^2 c_i}{\partial x^2} + V \frac{\partial c_i}{\partial x} \tag{B.1}$$

where D is the diffusion coefficient, x is the displacement distance, and V is the dissolution rate (Zhang et al. 1989; Liang 1999). This expression has the exact analytical solution of

$$c_i = c_\infty + (c_0 - c_\infty) erfc\Big(\frac{x}{2\sqrt{D_i t}} + \alpha\Big)[erfc(\alpha)] \tag{B.2}$$

where c_i is the concentration of a given component at position x, c_∞ is the initial concentration, and C_0 is the concentration at the interface. The dimensionless parameter α expresses the degree of chemical saturation at the solid-liquid interface and is equal to

$$\alpha = V\sqrt{\frac{t}{D_i}} \tag{B.3}$$

A compositional profile of the diffusing component obtained by an electron microprobe traverse of a glaze cross-section can easily be fit to B.2 as a function of the unknown quantities D, t, and α through an iterative non-linear least-squares routine (de Levie 2001). However, the parameters D and t cannot be separated from each other by least-squaring. Therefore literature values (Matousek 1975; Langanke and Schmalzried 1979; Petusky 1980; Petusky and Schmalzried 1980; Schmalzried et al. 1981), and estimations of D from the Einstein-Stokes equation must be plugged into B.2 to retrieve time. Einstein-Stokes is given by

$$D_i = \frac{k_B T}{6\pi\eta a} \tag{B.4}$$

where k_B is the Boltzmann constant, T is absolute temperature, η is the melt viscosity, and a is the radius of the diffusion ion. Einstein's formulation is based on a non-interactive hard-sphere model of Brownian movement. Erying in 1936 developed a

similar equation that related absolute reaction rates to the viscosity of the solution.

$$D_i = \frac{k_B T}{a\eta} \tag{B.5}$$

where a is the mean jump distance of the diffusing species (Eyring 1936). Care must be taken in estimating the jump distance or the ion radius since these are based on the particular silicate structural units that are formed under ceramic-glass reaction.

Equations B.1-B.5 are appealing because of their simplicity. However, as they assume an ideal binary system, deviations may occur when attempting to apply these to real multi-component systems. This is due to the fact that diffusion is a consequence of not only thermodynamic and compositional gradients, but also the direction of mass flow (Cooper and Varshneya 1968). As can often be the case in multi-component systems, competing flows of individual components may lead to diffusion phenomena that are not explainable under a binary model.

B.1 Multi-component Diffusion

In the process of mass transfer, movement will occur by either convection or diffusion. As the relatively low liquid temperatures of lead silicates (700-1000 ℃), where surface reactions are sluggish and temperature gradients minimal, the dominant mechanisms of transfer will be through diffusion (Liang 1999). As subsets of diffusion there are three types: trace, self, and chemical (Kress and Ghioroso 1995). Trace diffusion refers to the diffusive behavior of a single component at infinite dilution. Self-diffusion characterizes the random movement of a single component in a homogenous system. In chemical diffusion, the type of interest here, transport is driven by a concentration gradient, which is a function of the linear combination of all the chemical potentials in the system (Gupta and Cooper 1971). When a system is comprised of more than two components it is termed multi-component, and it exhibits more complicated behaviors than those exhibited in a binary system. With two or more diffusing species,

chemical reactions and interacting diffusional flows may produce counter currents and co-currents (Leaist and Noulty 1985). If these coupling phenomena are strong enough, the gradient of one component can control the transport of another. Therefore, in multi-component systems, the flux of a component is not only dependent of its own concentration gradient, but also on all the concentration gradients in a system. As of recently, multi-component diffusion has received considerable attention in geochemical circles (Zhang et al. 1989; Liang et al. 1997; Mungall et al. 1998; Nishiyama 1998; Liang 2000). Its history, however, can be traced back to Onsager (1945) whose classic paper in 1945 placed multi-component diffusion on firm theoretical grounds, and sparked an extensive discussion on the subject in the field of irreversible thermodynamics.

B.1.1 *EBDC* Diffusion and Matrix Diffusion

Multi-component diffusion may be described through an expanded form of Fick's Laws (Crank 1975). As has already been shown in equations B.1-B.3, the easiest way to describe a diffusing system is through a binary case (Cooper and Varshneya 1968; Zhang et al. 1989). Extending this binary case, and "effectively" binary diffusion coefficient (*EBDC*) model can be formed by reducing the multi-component melt into a pseudo-binary composition. In the *EBDC* model, one of the components is treated as an element of primary interest and the others are taken together as the second, solvent-like, component. Using this approach, *EBDC*s may be found for every component in a system. Therefore, in an *EBDC* model, all components obey the following equation

$$J_i = -\mathbf{D}_i^{EBDC} \nabla c_i \tag{B.6}$$

where $\mathbf{D}_i^{EBDC}$ is the effective binary diffusion coefficient.

In terms of mathematical simplicity, the *EBDC* flux equation has many advantages. If the mass conservation is combined with equation B.6, then the more useful

Fick's second law may be obtained.

$$\frac{\partial c_i}{\partial t} = \frac{\partial\Big(\mathbf{D}_i^{EBDC}\frac{\partial c_i}{\partial x}\Big)}{\partial x} \tag{B.7}$$

where $\mathbf{D}_i^{EBDC}$ in this case is a concentration weighted average.

$$\mathbf{D}_i^{EBDC} = \frac{\sum_{i=1}^{n}\mathbf{D}_i\frac{\partial c_i}{\partial x}}{\sum_{i=1}^{n}\frac{\partial c_i}{\partial x}} \tag{B.8}$$

Taking as boundary conditions the case of diffusion from a constant concentration at an internal frame of reference[1], the following solution may be obtained which is the equivalent of equation B.2 without taking into consideration dissolution processes (Crank 1975; Zhang et al. 1989).

$$\frac{C - C_\infty}{C_0 - C_\infty} = erfc\Big(\frac{x}{2\sqrt{\mathbf{D}_i^{EBDC}t}}\Big) \tag{B.9}$$

Using $EBDC$s assumes that diffusing components are unaffected by chemical coupling and concentration gradients (Kress and Ghioroso 1995). As a first approximation, this assumption is useful in its ability to broadly characterize individual compositional profiles. Almost any compositional profile can be fitted with B.9 provided it contains no extrema indicative of coupled behavior. Despite this, the $EBDC$ approach does not proved a route towards an accurate diffusion model for multicomponent systems. For instance, the $EBDC$ model implies that the diffusion of a single component is simply a function of its own concentration gradient. This, however, is impossible unless the unlikely situation occurs where all components diffuse at the same rate (Trial and Spera 1994). The $EBDC$ for a given component can vary by an order of magnitude depending on the speed and coupling effect of a counter-diffusing component (Liang et al. 1996). Furthermore, the $EBDC$ model is unable

[1] $x = \infty : C|_{x=\infty} = C_\infty, t > 0$
at
$x = 0 : \mathbf{D}_i\frac{\partial c_i}{\partial x}|_{x=\infty} = 0, t > 0$

to predict the shape of some profiles, such as in the common case of "uphill diffusion" where the movement of a component is in the opposite direction of its diffusion gradient (Zhang et al. 1989).

To solve the problems inherent to the effectively binary approach Onsager(Onsager 1945) modified Fick's first law such that the flux of any species i would be a linear combination of all the concentration gradients in a system, viz.

$$J_i = \frac{\partial c_i}{\partial t} = -\sum_{j=1}^{n-1} \mathbf{D}_{ij}^{k} \nabla C_j \tag{B.10}$$

where J_i, ∇c_i, t, n, $\mathbf{D}_{ij}^{k}$, and C_j are respectively the flux, the concentration gradient of component i, time, the number of components in the system, the multi-component diffusion coefficients independent of the concentration gradient for which k is the dependent component, and the concentration if component j. Also in B.10, there are only n-1 elements of C that are independent, since the nth component can be determined by mass balance. In the computationally rigorous approach of Onsager and later Darken (1948), who worked on non-electrolyte systems, particular combinations of the diffusion coefficients governing the mass transfer diagonalize in a diffusion matrix [**D**] forming eigenvalues (coupled diffusion coefficients). The matrix of diffusion coefficients $\mathbf{D}_{ij}^{k}$ are give the matrix notation of [**D**]. In matrix notation B.10 becomes

$$\mathbf{J} = [\mathbf{D}]\nabla\mathbf{c} \tag{B.11}$$

where **c** is the column vector of n component concentrations, and [**D**] is the $(n-1) \times (n-1)$ square matrix of diffusion coefficients.

The [**D**] matrix can completely describe a multi-component system if the concentration profiles are known for each of the components. Applying the concept, Schut and Cooper (Schut and Cooper 1982) found that in compositional space (a bivariate plot of the concentration profiles of two coupled components) the diffusion profile appears as an s-shape in a liquid-liquid interface system. Contained in this path are

all the concentration loci encountered between end component concentrations. In figure, a schematic of the diffusion path between end compositions A and B of two components C_1 and C_2, the typical S-shaped curve can be described by a vector $\overrightarrow{AB}$ joining the end compositions. This diffusion direction vector may be broken into components known as the eigenvectors $v1$ and $v2$ (dashed lines in figure) of [**D**]. The eigenvectors characterize the chemical interaction between components and the competing flow influence of one component over another. From the magnitude of these interactions, the coupled diffusion coefficient, otherwise called the eigenvalues in this problem, may be calculated. If the curve us not s-shaped, thus suggests that $\overrightarrow{AB}$ itself is an eigenvector of [**D**], and thus behaves in a binary manner suggesting no chemical interaction.

B.1.2 Constructing [D]

There are several methods for determining [**D**] that employ standard procedures of linear algebra. Here the two stage methods outlined by Gupta and Cooper (Gupta and Cooper 1971) and Trial and Spera (Trial and Spera 1994) are used, and for a fuller description of the mathematics the reader should refer to them. In the first stage, individual elements of the model equation are seeded with estimations of the values of those elements. In the second stage the model is optimized using a χ^2 merit function to find the eigenvalues and starting concentrations.

The basic elements of [**D**] can be calculated using the matrix operation

$$[\mathbf{D}] = [P][\Lambda][P]^{-1} \tag{B.12}$$

where $[P]$ is the square matrix of eigenvectors, $[\Lambda]$ is the matrix of eigenvalues, and $[P]^{-1}$ is the inverse of the eigenvector matrix. Combining this expression with Fick's flux equation (B.10 and B.11) the following can be obtained

$$[P]^{-1}\mathbf{J} = [\Lambda][P]^{-1}\frac{\partial \mathbf{c}}{\partial x} \tag{B.13}$$

In equation B.13, the experimentally obtained vector $\mathbf{c}$ may be transformed by the eigenvector matrix such that

$$\mathbf{u} = [P]\mathbf{c} \tag{B.14}$$

where $\mathbf{u}$ is the "transformed" column vector of concentration. This transformation is the equivalent of rotating the frame of reference if compositional space such that one axis is parallel to the directional vector (see figure). In this manner the direction vector $\overrightarrow{AB}$ becomes a basis vector of component 1 (now C_2^* in figure), and component 2 (now C_1^* in figure) becomes normal to component 1. In terms of the end member concentrations (points A and B), the concentration of C_1^* are the same at both points. Because of this, the couple has been transformed to appear as if it were a binary system for which C_2^* is the diffusing component. This transformed matrix effectively decouples the concentrations and allows them to be calculated separately form one another. Besides allowing the diffusion matrix to be solved, this transformation can aid in predicting stoichiometries of the coupling reactions.

Analogous to the derivation of the Fick's second law of diffusion in the binary case (that is from equation B.7), equations B.13 and B.14 may be combined together and with mass balance to obtain the following

$$\frac{\partial \mathbf{u}}{\partial t} = \frac{\partial\left([\Lambda]\frac{\partial \mathbf{u}}{\partial x}\right)}{\partial x} \tag{B.15}$$

for which the general solution is

$$\mathbf{u} = \mathbf{u}_\infty + [F](\mathbf{u}_0 - \mathbf{u}_\infty) \tag{B.16}$$

where $\mathbf{u}_0$ is the transformed interface vector column of concentration, $\mathbf{u}_\infty$ is the transformed initial vector column of concentration, and $[F]$ is a linear operator that contains the elements of time, position, and the eigenvalues of diffusion. If equation B.14 is substituted into B.16 then the following may be written

$$\mathbf{c} = \mathbf{c}_\infty + [P][F][P]^{-1}(\mathbf{c}_0 - \mathbf{c}_\infty) \tag{B.17}$$

where $\mathbf{c}_\infty$ is the interface concentration vector matrix, $\mathbf{c}_\infty$ is the initial concentration vector matrix and $[F]$ (for an infinite diffusion length ternary system) is

$$[F] = \begin{pmatrix} erfc\Big(\frac{x}{\sqrt{2\lambda_{11}t}} + \alpha_{11}\Big)erfc(\alpha_{11})^{-1} & 0 \\ 0 & erfc\Big(\frac{x}{\sqrt{2\lambda_{22}t}} + \alpha_{22}\Big)erfc(\alpha_{22})^{-1} \end{pmatrix} \quad \text{(B.18)}$$

Thus in expanded form, B.17 becomes

$$c_i = c_{i\infty} + \sum_{l=1}^{n-1}\sum_{m=1}^{n-1} P_{ij} erfc\Big(\frac{x}{\sqrt{2\lambda_j t}} + \alpha_j\Big)erfc(\alpha_j)^{-1}P_{ij}^{-1}(c_{i0} - c_{i\infty}) \quad \text{(B.19)}$$

In equation B.19 the unknowns are P_{ij}, λ_j, α_j and, if considering archaeological samples, time t. Recall that α_j is the dimensionless dissolution parameter from B.2. Equation B.19 is solved by fitting the unknowns to experimental profiles using a χ^2 merit function.

The χ^2 function is composed of vector components, the experimentally measured concentration y_i, the concentration c_i determined from B.19, time t and the standard deviation of the measured concentration value σ_{ij}.

$$\chi^2 = \sum_{l=1}^{n-1}\sum_{m=1}^{n-1}\Big(\frac{y_i(x,t) - c_i(P_{ij};x,t)}{\sigma_{ij}}\Big)^2 \quad \text{(B.20)}$$

Since none of the eigenvalues, nor eigenvectors, are known there can be several correct non-unique values of the individual vectors composing the P matrix. Therefore the model equation B.19 needs to be seeded with predictions of the eigenvalues and eigenvectors of the system. Literature values for diffusion coefficients greatly aid in determining the eigenvalues. However, for the eigenvector matrix, individual P_is have to be optimized one at a time to yield a best-fit value. This can be accomplished through an optimization program such as the Solver add-in in Microsoft Excel.

Appendix C

Data Tables

Table C.1: Archaeological samples

Sample	Find Spot	Type	Earliest Date (AD)	Latest Date (AD)	Contact/Reference
BGH95	London	Roman	70	100	R. Symonds, MoLAS
DGH86	London	Roman	270	400	R. Symonds, MoLAS
ER	London	Roman	no data	no data	R. Symonds, MoLAS
KWS94	London	Roman	100	120	R. Symonds, MoLAS
LBI95	London	Roman	250	300	R. Symonds, MoLAS
LCT84a	London	Roman	200	250	R. Symonds, MoLAS
LCT84b	London	Roman	70	100	R. Symonds, MoLAS
LIM83	London	Roman	no data	no data	R. Symonds, MoLAS
179 BHS89	London	Roman	no data	no data	R. Symonds, MoLAS
SWA81	London	Roman	180	230	R. Symonds, MoLAS
SH74	London	Roman	no data	no data	R. Symonds, MoLAS
Pom79	London	Roman	no data	no data	R. Symonds, MoLAS
5315	Diana	Roman	85	117	R. Symonds, MoLAS
5315a	Diana	Roman	85	117	R. Symonds, MoLAS
5315b	Diana	Roman	85	117	R. Symonds, MoLAS
4753	Diana	Roman	85	117	R. Symonds, MoLAS
5655	Diana	Roman	85	117	R. Symonds, MoLAS
5571	Diana	Roman	85	117	R. Symonds, MoLAS
5571a	Diana	Roman	85	117	R. Symonds, MoLAS
5571b	Diana	Roman	85	117	R. Symonds, MoLAS
no number	Diana	Roman	100	150	R. Symonds, MoLAS
202	Diana	Roman	no data	no data	R. Symonds, MoLAS
13355	Diana	Roman	150	200	R. Symonds, MoLAS
C 135/96	Diana	Roman	85	117	R. Symonds, MoLAS
94-4736	Diana	Roman	50	100	R. Symonds, MoLAS
no data	Diana	Roman	no data	no data	R. Symonds, MoLAS
C 141/96	Diana	Roman	no data	no data	R. Symonds, MoLAS
2553	Diana	Roman	3^{rd} C.	4^{th} C.	R. Symonds, MoLAS
93-573/1/29	Diana	Roman	3^{rd} C.	4^{th} C.	R. Symonds, MoLAS
93-1709a	Diana	Roman	3^{rd} C.	4^{th} C.	R. Symonds, MoLAS
93-1510	Diana	Roman	3^{rd} C.	4^{th} C.	R. Symonds, MoLAS
93-2060	Diana	Roman	3^{rd} C.	4^{th} C.	R. Symonds, MoLAS
93-4350	Diana	Roman	3^{rd} C.	4^{th} C.	R. Symonds, MoLAS
93-4741	Diana	Roman	3^{rd} C.	4^{th} C.	R. Symonds, MoLAS
93-3033	Diana	Roman	3^{rd} C.	4^{th} C.	R. Symonds, MoLAS
Nat.museum	no data	Roman	no data	no data	R. Symonds, MoLAS
S-1	Singidunum	Roman	150	200	R. Symonds, MoLAS
S-2	Singidunum	Roman	150	200	R. Symonds, MoLAS
S-3	Singidunum	Roman	150	200	R. Symonds, MoLAS
S-4	Singidunum	Roman	150	200	R. Symonds, MoLAS
S-5	Singidunum	Roman	150	200	R. Symonds, MoLAS
S-6	Singidunum	Roman	150	200	R. Symonds, MoLAS
S-7	Singidunum	Roman	150	200	R. Symonds, MoLAS
1432	Apulum Partos	Roman	2^{nd} C.		R. Symonds, MoLAS

Table C.1: continued...

Sample	Find Spot	Type	Earliest Date (AD)	Latest Date (AD)	Contact/Reference
1131	Apulum Partos	Roman	2^{nd} C.		R. Symonds, MoLAS
1121	Apulum Partos	Roman	2^{nd} C.		R. Symonds, MoLAS
1270	Apulum Partos	Roman	2^{nd} C.		R. Symonds, MoLAS
Spoil	Apulum Partos	Roman	2^{nd} C.		R. Symonds, MoLAS
1850	Apulum Partos	Roman	2^{nd} C.		R. Symonds, MoLAS
1694	Apulum Partos	Roman	2^{nd} C.		R. Symonds, MoLAS
1797b	Apulum Partos	Roman	2^{nd} C.		R. Symonds, MoLAS
1770	Apulum Partos	Roman	2^{nd} C.		R. Symonds, MoLAS
2215	Apulum Partos	Roman	2^{nd} C.		R. Symonds, MoLAS
1970	Apulum Partos	Roman	2^{nd} C.		R. Symonds, MoLAS
1797	Apulum Partos	Roman	2^{nd} C.		R. Symonds, MoLAS
1007	Apulum Partos	Roman	2^{nd} C.		R. Symonds, MoLAS
1784	Apulum Partos	Roman	2^{nd} C.		R. Symonds, MoLAS
V59	Celsa	Roman	44BC	100	Pérez-Arantegui (1996)
V45	Celsa	Roman	44BC	100	Pérez-Arantegui (1996)
V27	Celsa	Roman	44BC	100	Pérez-Arantegui (1996)
V83	Celsa	Roman	44BC	100	Pérez-Arantegui (1996)
V46	Caesaraugusta	Roman	19BC	100	Pérez-Arantegui (1996)
V69	Caesaraugusta	Roman	19BC	100	Pérez-Arantegui (1996)
Picon1	Lezoux	Roman	1st C.		Pérez-Arantegui (1996)
Picon2	Lezoux	Roman	1st C.		Pérez-Arantegui (1996)
Picon3	Vichy/S.Remy	Roman	1st C.		Pérez-Arantegui (1996)
Picon4	Italy?	Roman	3^{rd} C.		Pérez-Arantegui (1996)
V.24S.97-2256	Perge	Roman	1st C.		P. Degryse, Leuven
V.2S.92	Perge	Roman	1st C.		P. Degryse, Leuven
SA99RD37	Sagalassos	Roman	L. Roman	E. Byzan.	P. Degryse, Leuven
SA2000RD7	Sagalassos	Roman	L. Roman	E. Byzan.	P. Degryse, Leuven
SA2000JP40A	Sagalassos	Roman	11^{th} C.	12^{th} C.	P. Degryse, Leuven
SA2000JP40B	Sagalassos	Roman	11^{th} C.	12^{th} C.	P. Degryse, Leuven
SA2000JP42	Sagalassos	Roman	11^{th} C.	12^{th} C.	P. Degryse, Leuven
US55	Otranto	Roman	8^{th} C.	10^{th} C.	P. Arthur
US1040	Otranto	Roman	8^{th} C.	10^{th} C.	P. Arthur
US1489	Otranto	Roman	8^{th} C.	10^{th} C.	P. Arthur
Oberless	Erustbrunn	Roman	4^{th} C.		P. Arthur
M.11	Saraillon (Aosta)	Roman	4^{th} C.	5^{th} C.	M. Gulmini, Torino
M.16	Villenueve	Roman	5^{th} C.	7^{th} C.	M. Gulmini, Torino
M.25	Aosta	Roman	4^{th} C.	7^{th} C.	M. Gulmini, Torino
Campione1	Ostia	Roman	160	180	A. Gallina, Ostia
Campione2	Ostia	Roman	160	180	A. Gallina, Ostia
Campione3	Ostia	Roman	160	180	A. Gallina, Ostia
RZ5574	Ostia	Roman	3^{rd} C.		A. Gallina, Ostia
RZ5636	Ostia	Roman	450	500	A. Gallina, Ostia
RZ5637	Ostia	Roman	450	500	A. Gallina, Ostia
RZ5653	Ostia	Roman	450	500	A. Gallina, Ostia
RZ5658a	Ostia	Roman	450	500	A. Gallina, Ostia
RZ5658b	Ostia	Roman	450	500	A. Gallina, Ostia
RZ5670	Ostia	Roman	3^{rd} C.		A. Gallina, Ostia
RZ5848	Ostia	Roman	2^{nd} C.	3^{rd} C.	A. Gallina, Ostia
1	Carlino	Roman	4^{th} C.	5^{th} C.	A. Gallina, Ostia
2	Carlino	Roman	4^{th} C.	5^{th} C.	A. Gallina, Ostia
3	Carlino	Roman	4^{th} C.	5^{th} C.	A. Gallina, Ostia
4	Carlino	Roman	4^{th} C.	5^{th} C.	A. Gallina, Ostia
5	Carlino	Roman	4^{th} C.	5^{th} C.	A. Gallina, Ostia
6	Carlino	Roman	4^{th} C.	5^{th} C.	A. Gallina,Ostia
7	Carlino	Roman	4^{th} C.	5^{th} C.	A. Gallina, Ostia
CR9550	Lakedaimon	Byzantine	9^{th} C.	10^{th} C.	Armstrong (1997)
CR9551		Byzantine	9^{th} C.	11^{th} C.	Armstrong (1997)
CR9548		Byzantine	13^{th} C.		Armstrong (1997)
CR9549		Byzantine	12^{th}	13^{th}	Armstrong (1997)
CR9560	Constantinople	Byzantine	10^{th}	11^{th}	Armstrong (1997)
CR9561		Byzantine	11^{th} C.		Armstrong (1997)
CR9559		Byzantine	10^{th}	11^{th}	Armstrong (1997)

Table C.1: continued...

Sample	Find Spot	Type	Earliest Date (AD)	Latest Date (AD)	Contact/Reference
CR9562		Byzantine	11^{th} C.		Armstrong (1997)
CR9564	Lakedaimon	Byzantine			Armstrong (1997)
CR9563		Byzantine	13^{th} C.		Armstrong (1997)
CR9567		Byzantine			Armstrong (1997)
Mango		Byzantine	9^{th} C.	10^{th} C.	Henderson (1995)
988.117.43	Fustat	Islamic	8^{th} C.		Mason (1994)
988.117.49	Fustat	Islamic	8^{th} C.		Mason (1994)
988.117.30	Fustat	Islamic	8^{th} C.		Mason (1994)
988.117.53	Fustat	Islamic	8^{th} C.		Mason (1994)
988.117.42	Fustat	Islamic	8^{th} C.		Mason (1994)
BA-525	Basra	Islamic	8^{th} C.	9^{th} C.	Mason (1994)
BA-716	Basra	Islamic	8^{th} C.	9^{th} C.	Mason (1994)
923.34.47	Basra	Islamic	8^{th} C.	9^{th} C.	Mason (1994)
BA-952		Islamic	8^{th} C.	9^{th} C.	Mason (1994)
909.43.42		Islamic	14^{th} C.		Mason (1994)
909.43.43		Islamic	14^{th} C.		Mason (1994)
909.38.5		Islamic	10^{th} C.		Mason (1994)
25968T		Chinese	$\sim 9^{th}$		Rawson et al. (1988)
25969R		Chinese	$\sim 9^{th}$		Rawson et al. (1988)
25971S		Chinese	$\sim 9^{th}$		Rawson et al. (1988)
25970OU		Chinese	$\sim 9^{th}$		Rawson et al. (1988)
Sherd C		Chinese	$\sim 9^{th}$		N. Wood

Table C.2: Major element ICP-AES and EDS analyses of archaeological bodies. Analyses marked with asterisk are done by EDS.

Sample	Na_2O	MgO	Al_2O_3	SiO_2	K_2O	CaO	Fe_2O_3	TiO_2	P_2O_5	MnO
BGH95	0.51	1.05	25.96	62.63	3.84	0.70	3.95	1.10	0.22	0.04
DGH86	0.89	3.50	15.56	56.70	2.37	14.29	5.72	0.67	0.21	0.09
ER	2.01	5.53	11.26	56.77	1.69	15.75	5.66	0.59	0.64	0.10
KWS94	0.43	1.91	16.55	68.71	3.29	0.56	7.49	0.94	0.10	0.02
LBI95	0.44	2.03	15.09	70.78	3.20	0.31	7.11	0.88	0.13	0.03
LCT84a	0.43	2.14	15.17	70.62	3.20	0.38	6.98	0.90	0.14	0.04
LCT84b	0.63	1.03	25.41	63.52	3.63	0.65	3.76	1.16	0.18	0.03
LIM83	0.25	0.66	24.97	66.04	2.85	0.67	3.15	1.09	0.31	0.01
179 BHS89	0.26	0.64	28.98	63.29	2.75	0.29	2.78	0.91	0.07	0.03
SWA81	0.89	2.76	16.05	58.53	2.85	11.99	5.95	0.68	0.22	0.078
SH74	0.75	2.73	15.71	60.50	3.08	10.33	5.89	0.67	0.26	0.08
Pom79	0.13	0.76	19.24	73.68	2.18	0.38	2.27	1.13	0.22	0.01
5315	0.39	0.93	28.08	63.80	3.04	0.41	2.34	0.96	0.05	0.00
5315a	0.44	0.94	27.26	64.57	2.90	0.41	2.46	0.95	0.06	0.01
5315b	0.38	0.94	27.28	64.66	2.84	0.54	2.34	0.95	0.06	0.01
4753	0.34	0.90	26.10	66.33	2.69	0.54	2.13	0.91	0.05	0.01
5655	0.34	0.91	26.98	65.15	2.86	0.45	2.28	0.96	0.06	0.01
5571	0.39	0.97	28.66	62.86	2.86	0.61	2.53	1.02	0.09	0.01
5571a	0.39	0.92	26.78	65.29	2.96	0.39	2.28	0.94	0.04	0.01
5571b	0.38	1.01	28.84	62.69	3.13	0.45	2.46	0.98	0.05	0.01
no number	0.53	1.01	28.04	63.01	2.91	0.71	2.63	0.98	0.17	0.01
202	0.37	0.92	27.00	61.19	2.80	2.95	2.27	0.93	1.56	0.01
13355	0.71	0.96	27.11	61.64	5.43	0.67	2.36	0.96	0.14	0.02
C 135/96	1.07	2.31	18.30	65.40	2.79	3.28	5.81	0.82	0.17	0.05
94-4736	1.22	2.29	18.75	66.51	2.95	1.20	6.06	0.80	0.16	0.06
no data	1.44	1.51	14.46	69.65	2.08	4.16	5.62	0.74	0.22	0.119
C 141/96	1.02	2.30	19.60	66.07	3.01	1.06	5.83	0.90	0.17	0.04
2553	1.27	1.52	17.27	68.82	2.23	1.21	6.65	0.80	0.15	0.081
93-573/1/29	1.46	1.87	18.31	66.12	2.13	1.26	7.79	0.81	0.20	0.054
2553	1.27	1.52	17.27	68.82	2.23	1.21	6.65	0.80	0.15	0.081
93-573/1/29	1.46	1.87	18.31	66.12	2.13	1.26	7.79	0.81	0.20	0.054
93-1709a	1.21	2.04	15.06	66.74	2.72	5.49	5.78	0.64	0.22	0.103
93-1510	0.52	0.60	26.51	65.57	2.71	1.03	2.08	0.80	0.16	0.020
93-2060	1.13	1.09	17.53	72.72	1.99	0.76	3.77	0.86	0.12	0.028
93-4350	1.35	1.50	14.38	71.32	1.92	3.08	5.46	0.66	0.27	0.064
93-4741	1.62	1.58	17.37	67.28	2.41	2.09	6.72	0.70	0.18	0.053
93-3033	0.81	0.78	19.39	72.17	1.97	0.99	2.83	0.87	0.16	0.030
Nat.museum	0.86	2.50	19.57	65.44	2.78	1.08	6.02	0.91	0.79	0.05
S-1	0.49	1.07	30.90	59.53	3.16	0.70	2.92	1.04	0.18	0.01
S-2	0.55	1.17	32.80	57.13	3.55	0.73	2.80	1.09	0.17	0.01
S-3	0.19	1.15	20.46	70.99	3.05	0.28	2.55	1.23	0.06	0.04
S-4	0.18	1.06	18.06	73.57	2.69	0.29	2.93	1.14	0.05	0.03
S-5	0.33	1.01	30.22	61.23	2.92	0.57	2.68	0.94	0.09	0.01
S-6	1.05	2.32	19.57	65.63	2.99	1.10	6.11	0.88	0.26	0.09
S-7	0.89	2.38	19.47	66.25	3.01	0.99	5.95	0.89	0.13	0.038
1432	1.29	2.11	16.14	66.37	2.75	4.44	6.00	0.69	0.13	0.079
1131	1.11	2.35	18.40	65.50	3.01	2.09	6.63	0.75	0.11	0.048
1121	1.21	2.19	16.82	65.07	2.82	3.85	6.95	0.78	0.16	0.148
1270	1.33	2.13	17.43	67.87	2.76	1.43	6.13	0.77	0.10	0.046
Spoil	1.17	2.24	16.78	64.89	2.67	5.06	6.22	0.74	0.16	0.074
1850	1.36	2.18	17.24	67.20	2.80	1.64	6.62	0.75	0.14	0.068
1694	1.40	1.95	16.65	69.37	2.69	1.28	5.77	0.66	0.19	0.042
1797b	1.32	2.15	16.65	68.22	2.70	1.67	6.34	0.77	0.11	0.066
1770	1.28	2.15	17.43	67.19	2.86	1.48	6.66	0.77	0.13	0.055
2215	1.36	2.11	16.66	66.68	2.73	2.78	6.71	0.70	0.16	0.115
1970	1.45	2.09	17.25	67.63	2.76	1.36	6.48	0.81	0.12	0.051
1797a	1.36	2.20	17.28	67.05	2.81	1.75	6.58	0.78	0.12	0.069
1007	1.22	2.10	15.47	65.54	2.73	5.65	6.30	0.69	0.19	0.111
1784	1.47	2.12	16.96	67.81	2.74	1.83	6.09	0.78	0.12	0.084
V59	1.12	3.06	16.36	57.54	2.22	13.75	5.13	0.75		0.07
V45	1.58	4.03	25.09	57.11	3.78	1.56	5.64	1.09		0.119
V27	1.15	2.12	9.61	69.46	2.13	10.99	4	0.5		0.037
V83	0.92	2.79	11.65	67.74	1.63	10.88	3.74	0.60		0.05
V46	1.78	2.5	15.01	69.23	3.65	1.27	5.75	0.74		0.068

Table C.2: continued...

Sample	Na_2O	MgO	Al_2O_3	SiO_2	K_2O	CaO	Fe_2O_3	TiO_2	P_2O_5	MnO
V69	1.16	3.15	16.46	58.23	2.06	12.18	5.83	0.85		0.08
Picon1	1.47	1.24	25.18	62.27	3.76	0.93	4.00	0.99	0.12	0.038
Picon2	0.64	0.96	26.61	61.90	3.78	0.64	4.06	1.30	0.07	0.039
Picon3	0.12	0.41	28.93	64.84	2.60	0.30	1.87	0.87	0.05	0.011
Picon4	0.95	3.15	16.89	56.85	2.72	12.18	6.25	0.70	0.23	0.078
V.24S.97-2256	1.32	2.79	14.82	58.40	2.94	13.55	5.33	0.62	0.17	0.062
V.2S.92	2.52	1.66	16.68	61.86	3.72	8.20	4.39	0.57	0.35	0.050
V.2S.92b	2.52	1.66	16.68	61.86	3.72	8.20	4.39	0.57	0.35	0.050
SA99RD37	1.53	3.15	15.95	65.78	2.97	1.88	7.61	0.81	0.17	0.146
SA2000RD7	1.20	4.41	18.53	55.16	3.63	8.25	7.65	0.78	0.30	0.092
SA2000JP40A	1.57	2.40	18.18	61.97	3.37	4.64	6.86	0.71	0.18	0.117
SA2000JP40B	1.06	3.39	19.77	57.19	4.14	5.22	8.17	0.78	0.19	0.093
SA2000JP42	1.58	2.37	17.29	63.36	3.28	4.62	6.50	0.72	0.17	0.112
US55	0.49	2.02	11.40	73.91	1.70	3.76	5.99	0.58	0.09	0.060
US1040	0.83	2.08	16.52	66.22	2.26	3.80	7.19	0.76	0.18	0.162
US1489	0.63	2.63	14.01	68.69	2.08	3.87	6.96	0.74	0.17	0.218
Oberless	0.23	0.88	19.97	67.73	2.69	0.65	6.77	0.93	0.10	0.050
M.11*	0.75	0.56	18.70	70.71	5.60	0.81	1.97	0.41		
M.16*	1.01	1.19	25.48	62.08	3.64	1.44	3.82	0.67		
M.25*	0.95	1.05	23.80	63.39	3.56	1.36	4.04	1.26		
Campione1	0.84	2.44	12.04	60.07	2.48	17.01	4.37	0.49	0.18	0.078
Campione2	1.42	2.96	14.32	58.16	2.09	14.67	5.25	0.59	0.46	0.081
Campione3	0.75	2.63	11.48	57.11	2.22	20.75	4.14	0.45	0.40	0.072
RZ5574	0.81	2.27	11.09	59.90	2.53	18.35	4.15	0.43	0.40	0.066
RZ5636	0.84	0.96	14.24	74.01	1.98	2.37	4.92	0.52	0.07	0.088
RZ5637	1.10	3.73	15.87	56.84	2.43	12.97	6.00	0.66	0.31	0.090
RZ5653	0.20	1.27	13.94	74.60	2.04	1.23	5.96	0.60	0.10	0.057
RZ5658a	0.96	1.06	14.40	75.16	2.09	0.93	4.74	0.56	0.06	0.036
RZ5658b	0.71	1.33	13.76	74.28	2.54	1.32	5.27	0.57	0.11	0.106
RZ5670	1.09	2.82	14.81	61.02	2.49	11.00	5.85	0.65	0.18	0.088
RZ5848	1.02	2.94	12.18	59.72	2.45	16.20	4.60	0.51	0.26	0.121
Carlino1	0.85	2.09	13.86	71.11	6.17	3.29	1.77	0.63	0.12	0.111
Carlino2	0.94	1.60	13.65	74.15	5.94	0.82	2.05	0.68	0.06	0.107
Carlino3	0.86	1.75	15.09	72.19	6.16	0.85	2.25	0.73	0.05	0.080
Carlino4	0.93	1.89	15.08	71.73	6.40	0.87	2.27	0.63	0.08	0.117
Carlino5	0.79	2.28	16.06	69.23	6.56	1.81	2.20	0.76	0.18	0.130
Carlino6	0.78	1.94	15.55	70.63	6.96	1.21	2.00	0.68	0.14	0.118
Carlino7	0.88	1.70	13.11	65.10	5.06	10.34	2.60	0.54	0.57	0.099
CR9550*	0.4	0.2	29.6	65.7	0.8	1.0	1.6	0.8		
CR9551*	0.24	0.59	19.58	75.83	1.42	0.46	0.98	0.91		
CR9548*	2.21	4.63	12.64	48.96	2.56	22.78	5.41	0.51		
CR9549*	1.53	7.34	13.06	52.16	2.49	16.01	6.55	0.66		
CR9560*	0.29	0.47	25.11	69.54	0.43	1.11	1.69	1.18		
CR9561*	2.18	2.51	20.74	55.89	3.92	4.02	8.34	1.79		
CR9559*	0.30	0.56	25.83	67.31	0.84	0.96	3.31	0.85		
CR9562*	0.65	1.62	21.87	59.11	3.87	4.20	7.48	0.82		
CR9564*	1.22	3.26	14.54	63.02	2.65	8.03	6.62	0.67		
CR9563*	0.72	3.70	14.99	45.43	1.87	25.43	7.08	0.63		
CR9567*	1.87	6.12	14.49	50.08	2.86	16.78	6.93	0.68		
Mango*	0.41	0.57	27.45	63.27	0.74	1.91	3.01	2.70		
Mangob*	0.41	0.69	30.71	61.90	0.73	3.17	1.39	0.96		
988.117.43*	1.50	4.54	11.44	51.34	1.49	22.52	6.42	0.75		
988.117.49*	1.59	3.00	11.30	59.19	1.71	17.37	5.03	0.81		
988.117.30*	1.1	0.6	29.3	66.2	0.8	0.3	2.0	1.2		
988.117.53*	2.66	0.68	23.61	65.40	1.24	1.56	3.30	1.55		
988.117.42*	1.64	3.71	12.11	56.47	1.21	18.33	5.66	0.88		
BA-525*	1.60	7.94	13.68	49.74	1.47	18.73	6.21	0.64		
BA-716*	1.23	7.47	13.21	49.20	1.67	19.93	6.36	0.62		
923.34.47*	2.02	5.85	13.19	57.71	3.23	11.49	5.45	0.66		
BA-952*	1.91	7.69	12.24	52.63	1.42	17.59	5.66	0.86		
909.43.42*	2.32	3.27	17.38	52.28	1.57	6.02	10.71	4.71		
909.43.43*	1.80	2.69	15.99	61.09	1.41	5.74	8.55	1.56		
909.38.5*	1.79	3.58	14.48	53.18	2.83	16.07	6.80	0.95		
25968T*	1.0	0.5	29.0	63.0	2.1	1.5	1.4	1.3		
25969R*	0.7	0.6	32.9	58.6	1.6	1.5	2.5	1.2		

Table C.2: continued...

Sample	Na_2O	MgO	Al_2O_3	SiO_2	K_2O	CaO	Fe_2O_3	TiO_2	P_2O_5	MnO
25971S*	0.7	0.5	27.4	64.2	2.4	1.4	1.7	1.3		
25970OU*	0.6	0.5	26.8	64.8	2.5	1.0	1.9	1.3		
Sherd C*	0.9	1.0	29.4	61.0	2.2	2.5	2.0	1.1		

Table C.3: Trace element analyses (ppm) of body fabrics by ICP-AES: set 1.

Sample	Ba	Co	Cr	Cu	Li	Ni	Sc	Sr	V	Y	Zn
BGH95	524	15	94	42	130	39	16	114	88	48	126
DGH86	387	11	121	55	71	53	14	411	119	25	101
ER	439	19	217	323	24	190	15	367	96	23	78
KWS94	414	12	131	31	79	38	18	104	160	14	84
LBI95	411	18	122	41	82	53	17	97	141	27	88
LCT84a	437	23	134	161	78	67	18	107	150	37	105
LCT84b	540	11	90	32	127	38	17	116	85	46	133
LIM83	525	5	80	31	77	36	17	87	84	32	97
179 BHS89	629	8	96	28	67	34	22	80	100	67	82
SWA81	361	11	91	110	72	57	15	383	135	24	84
SH74	364	13	123	48	66	56	14	372	128	21	97
Pom79	340	10	141	53	57	50	18	123	129	19	90
5315	575	1	115	43	48	27	20	102	126	17	58
5315a	574	2	94	28	50	30	17	94	121	13	68
5315b	547	1	114	47	48	28	19	96	122	16	64
4753	519	3	111	52	46	31	19	97	116	19	67
5655	522	14	113	39	46	28	19	97	119	18	61
5571	540	21	115	39	54	32	20	102	121	17	75
5571a	548	21	113	43	50	27	19	95	126	16	59
5571b	595	44	122	50	58	33	21	106	122	21	67
no number	596	3	118	48	52	36	21	119	126	18	80
202	563	2	113	48	47	28	19	134	119	16	69
13355	668	10	114	22	53	35	20	118	128	21	77
C 135/96	514	25	153	65	74	105	18	141	127	29	113
94-4736	539	19	150	43	71	105	18	134	125	28	115
no data	480	14	89	39	44	48	14	151	89	33	83
C 141/96	559	35	180	37	80	121	20	125	147	34	127
Nat.museum	705	41	181	46	80	127	20	123	146	35	131
S-1	583	31	135	57	63	48	22	119	133	23	98
S-2	680	13	138	54	63	51	23	127	141	24	100
S-3	455	30	351	35	178	212	21	63	130	40	428
S-4	408	38	328	57	182	194	21	60	132	37	430
S-5	509	3	125	48	62	43	21	100	125	17	83
S-6	592	28	176	54	77	120	20	131	141	32	132
S-7	535	21	166	48	79	117	20	125	148	33	124
Picon1	717	13	66	28	154	29	12	157	63	32	124
Picon2	724	26	83	54	97	43	18	109	103	40	135
Picon3	345	5	49	26	69	22	14	66	55	60	64
Picon4	338	13	129	135	65	64	15	394	139	23	100
Picon4b	338	13	129	135	65	64	15	394	139	23	100
V.24S.97-2256	583	18	198	191	55	172	13	680	97	27	88
V.2S.92	953	14	176	424	56	136	9	1037	69	28	111
V.2S.92b	953	14	176	424	56	136	9	1037	69	28	111
SA99RD37	1094	28	266	69	61	236	16	1071	133	32	110
SA2000RD7	1204	21	199	119	69	197	16	1094	123	34	134
SA2000JP40A	601	17	133	38	63	93	18	118	106	21	96
SA2000JP40B	869	21	137	48	57	95	18	273	130	27	118
SA2000JP42	573	16	130	32	59	91	17	115	97	19	92
US55	214	13	156	73	63	127	13	124	105	20	86
US1040	428	20	141	33	58	130	16	194	116	46	100
US1489	273	28	239	55	81	192	16	136	117	33	139
Oberless	409	15	118	78	63	56	18	56	112	37	102
Campione1	308	8	100	130	49	49	10	482	82	20	78
Campione2	433	10	101	116	60	55	12	602	95	23	88
Campione3	271	7	93	32	50	46	10	455	66	20	75
RZ5574	295	6	83	88	47	40	10	650	82	19	81
RZ5636	474	6	69	28	41	33	11	158	95	25	62
RZ5636b	474	6	69	28	41	33	11	158	95	25	62
RZ5637	311	15	122	166	60	56	15	370	143	25	103
RZ5653	281	23	82	46	61	54	15	68	101	42	98
RZ5658a	597	7	66	29	48	37	11	133	93	28	64
RZ5658b	680	15	90	25	45	55	11	132	107	36	87
RZ5670	340	11	108	126	59	52	14	384	132	21	87
RZ5848	770	11	100	153	53	53	11	636	108	19	97

Table C.4: Trace element analyses (ppm) of body fabrics by ICP-AES: set 2.

Sample	Zr*	La	Ce	Nd	Sm	Eu	Dy	Yb	Pb
BGH95	109	77	143	81	12.5	1.5	7.6	3.4	956
DGH86	63	33	63	35	5.3	1.4	3.7	2.0	1170
ER	74	22	44	24	3.6	1.1	3.3	1.9	49
KWS94	85	32	60	33	4.2	1.2	3.0	1.9	415
LBI95	75	42	84	44	7.5	1.6	4.5	2.6	508
LCT84a	97	44	91	47	8.5	1.7	5.8	3.1	6582
LCT84b	133	79	145	82	12.5	1.6	7.5	3.3	3221
LIM83	121	67	121	69	9.8	1.7	5.7	2.6	542
179 BHS89	133	121	180	126	19.5	2.9	11.2	5.0	966
SWA81	87	38	62	40	5.8	1.2	4.6	2.5	2688
SH74	56	33	61	35	4.7	1.0	3.3	1.7	294
Pom79	96	50	88	51	6.4	1.0	3.6	1.9	2455
5315	90	29	50	30	3.2	0.8	2.7	1.7	1187
5315a	63	24	43	25	2.9	0.7	2.2	1.5	2814
5315b	72	29	52	30	3.4	1.1	2.7	1.6	8759
4753	99	28	51	30	2.8	1.0	3.0	1.8	19447
5655	85	27	52	28	2.1	0.8	2.9	1.8	4231
5571	96	27	49	28	0.7	0.9	2.8	1.8	1981
5571a	89	27	49	28	0.6	0.7	2.6	1.6	620
5571b	111	31	57	33	1.3	1.1	3.4	2.0	1093
no number	90	31	53	33	4.0	1.2	3.2	1.8	334
202	74	29	51	30	4.1	1.1	2.7	1.5	3046
13355	79	29	51	31	2.5	0.8	3.3	1.9	1330
C 135/96	69	44	81	46	5.3	1.5	4.7	2.4	6897
94-4736	46	45	83	47	7.0	1.5	4.6	2.5	278
no data	54	40	67	42	7.1	1.5	5.1	2.5	1604
C 141/96	99	46	86	49	4.5	1.7	5.1	3.0	420
Nat.museum	122	48	93	51	4.2	1.7	5.8	3.3	5237
S-1	126	31	56	33	1.6	1.0	3.6	2.1	3797
S-2	105	32	60	34	2.3	1.2	3.8	2.3	3921
S-3	111	56	95	59	5.7	1.7	6.3	3.3	1198
S-4	109	51	91	54	3.2	1.7	6.0	3.0	25405
S-5	94	26	48	27	3.2	0.9	2.7	1.6	1762
S-6	71	47	88	50	6.5	1.6	5.1	2.8	6641
S-7	108	53	89	55	9.3	1.7	5.8	3.1	530
Picon1	270	84	132	84	9.8	1.7	5.6	2.7	396
Picon2	150	102	163	104	16.1	2.6	8.2	3.1	527
Picon3	128	128	195	131	24.5	2.2	10.9	4.7	596
Picon4	74	38	63	40	5.1	1.2	4.4	2.4	9373
Picon4b	74	38	63	40	5.1	1.2	4.4	2.4	9373
V.24S.97-2256	138	88	122	87	7.3	1.7	4.8	2.5	3346
V.2S.92	160	122	161	119	9.9	1.9	4.6	2.5	13202
V.2S.92b	160	122	161	119	9.9	1.9	4.6	2.5	13202
SA99RD37	167	129	173	127	12.3	2.5	6.2	3.0	375
SA2000RD7	241	174	214	169	14.1	2.8	6.2	3.2	546
SA2000JP40A	58	42	68	44	7.2	1.4	4.5	2.3	848
SA2000JP40B	23	53	91	56	9.6	1.7	6.1	2.7	833
SA2000JP42	56	43	73	44	7.3	1.4	4.3	2.2	740
US55	71	31	50	32	3.7	0.9	3.5	2.1	9377
US1040	173	63	106	67	10.3	2.1	7.8	4.0	893
US1489	120	44	77	47	6.3	1.5	6.3	3.3	5554
Oberless	38	53	94	57	10.3	1.7	7.2	3.4	263
Campione1	51	28	44	30	4.4	0.9	3.9	2.0	4492
Campione2	68	33	55	35	4.9	1.1	4.4	2.2	3538
Campione3	50	27	39	29	4.6	1.0	3.7	1.8	2559
RZ5574	46	26	41	28	4.3	0.9	3.7	1.8	11622
RZ5636	125	61	98	62	8.4	1.4	4.6	2.2	1819
RZ5636b	125	61	98	62	8.4	1.4	4.6	2.2	1819
RZ5637	69	35	60	37	5.3	1.2	4.8	2.5	11668
RZ5653	81	59	64	61	7.5	1.5	6.0	3.4	12103
RZ5658a	132	68	118	69	9.7	1.7	5.3	2.5	1978
RZ5658b	101	73	89	75	9.2	1.8	6.4	3.1	1386
RZ5670	67	37	58	39	5.8	1.2	4.3	2.2	6423
RZ5848	58	28	43	30	3.8	0.9	3.8	2.0	8480

Table C.5: WDS analyses collected at the interior of archaeological glaze cross-sections. Each analysis represents the average of at least six points.

Sample	Na_2O	MgO	Al_2O_3	SiO_2	PbO	K_2O	CaO	Fe_2O_3	TiO_2	CuO	Total
BGH95	0.46	0.41	10.19	22.22	62.89	1.77	0.70	1.10	0.37	0.19	100.30
DGH86	0.45	0.78	6.38	33.93	50.17	0.92	4.14	1.19	0.00	0.40	98.34
ER	9.69	3.42	7.60	61.01	0.25	4.04	6.95	3.46	0.40	2.56	99.54
KWS94	0.13	0.78	5.96	25.31	61.67	0.68	0.52	1.80	0.42	0.02	97.30
LBI95	0.30	0.76	5.97	29.61	59.24	1.03	0.39	2.12	0.41	0.03	99.86
LCT84a	0.13	0.86	4.47	21.32	64.30	1.08	0.83	2.46	0.27	0.00	97.41
LCT84b	0.29	0.61	8.38	20.68	65.36	0.90	0.75	1.26	0.32	0.08	98.63
LIM83	0.08	0.26	7.64	20.22	66.24	0.85	1.17	1.03	0.38	0.26	98.13
179 BHS89	0.15	0.25	8.82	17.85	69.91	0.83	0.55	0.83	0.21	0.12	99.52
SWA81	0.86	2.04	10.62	43.82	30.80	4.42	5.79	0.98	0.09	0.29	99.71
SH74	0.31	0.29	4.93	32.34	55.19	0.88	3.40	0.93	0.13	0.05	98.46
Pom79	0.11	0.27	5.15	22.37	70.27	0.38	0.52	0.73	0.43	0.87	101.10
5315	0.20	0.48	7.64	19.55	69.32	0.54	0.77	0.88	0.44	0.03	99.85
5315a	0.11	0.54	7.23	18.82	71.00	0.31	0.28	0.90	0.39	0.02	99.59
5315b	0.06	0.43	6.14	18.55	72.07	0.29	0.36	0.88	0.51	0.07	99.35
4753	0.19	0.35	7.26	19.20	70.61	0.65	0.44	0.66	0.13	0.13	99.61
5655	0.18	0.41	8.84	20.05	68.83	0.79	0.39	0.73	0.43	0.13	100.81
5571	0.16	0.34	6.95	18.99	70.54	0.55	0.67	0.72	0.37	0.04	99.31
5571a	0.08	0.45	6.79	17.87	71.74	0.45	0.42	0.94	0.33	0.04	99.12
5571b	0.12	0.54	6.25	18.85	70.75	0.17	0.49	1.10	0.58	0.09	98.94
no number	0.20	0.50	7.00	18.68	70.66	0.55	0.62	0.83	0.39	0.00	99.42
202	0.13	0.38	7.66	19.75	68.56	0.76	0.31	0.66	0.29	0.05	98.55
13355	0.10	0.42	7.05	18.13	71.55	0.48	0.52	0.88	0.41	0.03	99.57
C 135/96	0.53	0.83	6.23	21.76	67.99	0.61	0.69	1.77	0.33	0.32	101.06
94-4736	0.40	0.82	5.79	22.15	66.91	0.67	0.96	1.82	0.38	0.17	100.08
no data	0.47	0.65	7.78	34.17	51.26	0.80	2.77	2.63	0.53	0.15	101.21
C 141/96	0.34	0.86	7.05	20.86	67.37	1.06	0.58	2.11	0.21	0.14	100.58
2553	0.52	0.64	5.92	24.78	63.88	0.12	0.94	0.71	1.39	0.30	99.20
93-573/1/29	0.41	0.74	5.83	21.32	67.49	0.25	0.51	0.44	2.22	0.30	99.51
93-1709a	0.27	0.57	6.97	31.20	58.57	0.26	1.01	0.53	1.37	0.54	101.28
93-1510	0.07	0.26	7.28	20.38	70.87	0.10	0.50	0.28	0.70	0.30	100.74
93-2060	0.47	0.42	5.37	22.54	69.69	0.10	0.53	0.47	0.99	0.34	100.92
93-4350	0.27	0.61	5.11	21.80	68.38	0.09	1.16	0.38	1.93	0.30	100.04
93-4741	0.44	0.88	6.69	26.93	60.65	0.10	0.99	0.42	2.62	0.38	100.10
93-3033	0.26	0.20	5.64	21.44	72.00	0.08	0.27	0.77	0.40	0.22	101.27
Nat.museum	0.17	0.98	5.86	24.96	65.26	0.44	0.92	1.79	0.45	0.06	100.89
S-1	0.18	0.48	7.23	18.34	71.73	0.45	0.51	0.90	0.28	0.03	100.14
S-2	0.12	0.46	6.83	18.12	71.72	0.34	0.57	0.91	0.42	0.05	99.53
S-3	0.07	0.37	5.54	23.57	66.79	0.66	0.35	0.87	0.37	0.05	98.64
S-4	0.11	0.45	6.76	29.55	61.15	0.90	0.45	0.84	0.43	0.00	100.63
S-5	0.12	0.44	7.43	18.33	71.10	0.37	0.41	0.84	0.34	0.00	99.39
S-6	0.39	0.79	5.80	20.99	67.06	0.65	0.89	1.96	0.29	0.17	98.99
S-7	0.39	1.04	6.19	25.91	62.62	0.57	0.81	2.14	0.41	0.06	100.15
Spoil	0.75	0.78	6.64	25.59	62.57	0.23	2.56	0.94	1.21	0.25	101.50
1850	0.76	0.93	6.77	26.45	61.75	0.17	1.16	0.96	1.69	0.36	101.00
1694	1.12	0.65	5.88	31.31	56.22	0.87	2.49	1.00	1.49	0.40	101.43
1797b	0.53	1.14	7.35	29.35	56.57	0.12	1.54	0.70	1.86	0.41	99.57
1770	0.78	1.35	9.00	34.12	49.01	0.04	1.36	1.15	2.95	0.40	100.16
2215	1.07	0.93	9.02	33.59	49.91	0.07	1.82	1.71	2.02	0.31	100.45
1970	0.72	0.94	6.88	28.48	58.59	0.40	1.25	1.10	2.08	0.35	100.79
1797	0.72	0.93	6.99	28.59	57.13	0.13	1.41	1.38	2.06	0.37	99.71
1007	1.18	2.17	6.21	31.35	51.00	0.57	5.13	1.42	1.81	0.28	101.12
1784	0.78	1.41	8.44	31.17	50.84	0.11	1.65	1.97	2.33	0.33	99.02
V59	0.43	0.18	4.88	27.31	57.38	0.59	3.84	1.26	0.19	1.63	97.68
V59b	0.35	0.37	5.63	31.11	53.85	0.85	4.51	2.48	0.19	0.05	99.39
V45	0.38	0.74	5.92	18.56	70.01	0.66	0.60	1.65	0.19	0.07	98.78
V45b	0.43	0.76	6.40	20.93	66.71	0.78	0.86	2.10	0.16	0.06	99.19
V27	0.63	0.10	4.96	31.43	55.81	0.74	2.63	1.03	0.22	1.12	98.66
V27b	0.61	0.15	5.01	28.43	57.78	0.63	2.68	1.86	0.25	0.05	97.44
V83	0.30	0.05	4.24	27.84	57.85	0.36	3.32	1.45	0.24	2.05	97.69
V83b	0.51	0.54	5.00	31.74	54.71	0.93	3.51	1.55	0.19	2.20	100.90
V46	0.53	0.71	6.21	19.62	69.44	0.92	0.49	1.55	0.13	0.11	99.71
V69	0.45	0.19	4.65	27.99	59.77	0.57	2.80	2.78	0.21	0.01	99.43
V69b	0.32	0.20	5.20	26.39	60.99	0.49	3.47	1.49	0.33	1.03	99.90

Table C.5: continued...

Sample	Na_2O	MgO	Al_2O_3	SiO_2	PbO	K_2O	CaO	Fe_2O_3	TiO_2	CuO	Total
Picon1	0.77	0.38	8.65	21.65	63.10	1.35	0.68	1.19	0.31	0.16	98.24
Picon2	0.32	0.23	8.55	17.30	69.62	0.90	0.62	0.87	0.27	0.05	98.73
Picon3	0.11	0.20	8.00	24.50	62.88	0.66	0.50	0.72	0.35	0.32	98.24
Picon4	0.52	0.32	5.90	32.08	51.86	0.99	3.69	1.71	0.31	0.58	97.96
Picon4b	0.54	0.59	5.98	31.54	51.85	1.13	3.83	1.53	0.18	1.34	99.14
V.24S.97-2256	0.65	0.40	3.69	32.45	53.46	1.07	3.08	1.32	0.13	1.19	97.44
V.2S.92	0.59	0.25	5.54	32.14	55.18	0.64	2.06	1.57	0.28	0.11	98.37
V.2S.92b	0.66	0.32	4.48	34.70	54.07	0.68	2.45	0.87	0.14	2.45	100.85
SA99RD37	0.33	1.12	5.86	28.25	60.60	0.59	0.94	0.96	0.15	0.03	98.81
SA2000RD7	0.31	0.71	6.94	48.28	36.94	1.79	2.66	0.40	0.13	0.45	98.61
SA2000JP40A	0.32	0.34	15.75	35.64	44.05	1.67	0.35	0.42	0.19	0.05	98.78
SA2000JP40B	0.26	0.37	7.25	28.68	61.13	0.31	1.04	0.23	0.03	0.06	99.37
SA2000JP42											
US55	0.38	0.80	6.31	35.92	51.37	1.41	1.90	2.05	0.34	0.04	100.52
US1040	0.24	0.54	4.86	19.84	70.35	0.28	0.97	2.15	0.31	0.00	99.53
US1489	0.28	0.83	5.54	29.90	58.50	0.52	1.57	2.42	0.45	0.01	100.02
Oberless	0.12	0.65	7.42	32.30	54.71	0.44	1.20	2.46	0.94	0.06	100.30
M.11	0.20	0.55	5.10	22.65	70.47	0.29	0.29	1.19	0.25	0.04	101.04
M.16	0.24	0.40	5.22	20.05	72.17	0.30	0.26	1.39	0.23	0.07	100.50
M.25	0.44	0.39	5.30	22.84	69.96	0.69	0.25	0.90	0.26	0.31	101.33
Campione1	0.32	0.57	4.65	30.48	57.34	0.73	3.29	2.07	0.11	0.14	99.69
Campione2	0.23	0.43	4.41	28.74	58.00	0.62	3.67	2.02	0.16	0.17	98.45
Campione3	0.27	0.43	3.27	28.69	61.67	0.65	2.36	0.94	0.06	1.51	99.85
RZ5574	0.24	1.01	3.79	28.64	60.52	0.56	3.37	1.21	0.10	0.75	100.19
RZ5636	0.79	0.44	9.86	39.93	41.95	2.61	2.18	1.62	0.21	0.05	99.64
RZ5636b	0.52	0.49	7.45	34.19	49.54	1.11	2.00	2.08	0.42	0.11	97.92
RZ5637	0.75	0.34	7.49	32.26	50.00	1.43	4.58	1.82	0.34	0.66	99.65
RZ5653	0.20	0.48	6.28	33.76	54.03	1.11	0.96	1.86	0.22	0.10	99.00
RZ5658a	0.52	0.47	6.46	33.53	55.22	0.87	0.68	1.65	0.26	0.22	99.88
RZ5658b	0.60	0.68	8.59	41.92	43.02	1.88	1.48	1.77	0.43	0.10	100.46
RZ5670	0.63	0.27	6.29	39.35	46.49	1.38	3.64	1.61	0.19	0.74	100.59
RZ5848											
Carlino1	0.58	0.98	6.19	31.06	56.85	0.87	1.70	2.28	0.35	0.08	101.33
Carlino2	0.79	0.83	8.20	41.82	43.78	1.35	1.34	2.18	0.43	0.03	101.29
Carlino3	0.50	0.51	4.57	26.80	66.36	0.68	0.44	0.97	0.17	0.08	101.32
Carlino4	0.48	0.75	6.35	32.29	56.63	0.80	0.69	1.96	0.44	0.10	100.56
Carlino5	0.30	0.79	4.94	23.67	66.84	0.49	0.84	1.93	0.24	0.09	100.33
Carlino6	0.43	0.78	5.66	29.47	60.00	0.77	1.44	1.38	0.26	0.01	100.58
Carlino7A	0.37	0.89	6.10	26.16	56.64	0.84	6.52	2.41	0.31	0.07	100.61
Carlino7B	0.43	0.82	6.29	25.80	57.45	0.95	5.92	1.95	0.35	0.02	100.21
CR9550	0.19	0.39	3.09	35.96	56.36	1.54	2.07	0.50	0.14	1.04	101.27
CR9551	0.05	0.14	5.59	23.03	70.70	0.30	0.10	0.33	0.33	0.29	100.86
CR9548	0.07	0.29	6.36	26.51	64.10	0.24	0.30	0.53	0.46	3.29	102.13
CR9548b											
CR9549	0.18	0.41	4.29	38.27	53.22	1.17	0.57	1.50	0.29	0.05	99.95
CR9560	0.99	0.23	6.79	31.07	53.82	0.73	0.97	5.52	0.19	0.11	100.42
CR9561	0.62	0.41	7.50	33.09	56.76	1.13	0.69	0.51	0.10	0.41	101.23
CR9559	1.19	0.13	7.22	32.29	55.41	0.85	1.23	2.17	0.15	0.23	100.87
CR9562	0.28	0.56	5.47	22.53	65.29	0.27	1.10	1.55	0.53	5.72	103.31
CR9564	0.06	0.05	4.92	30.98	64.52	0.57	0.41	0.09	0.05	0.21	101.86
CR9563	0.61	0.32	6.44	35.17	49.63	2.04	4.44	1.42	0.27	0.07	100.40
CR9567	0.36	0.25	3.38	31.02	63.32	0.44	1.46	0.41	0.14	0.29	101.07
Mango	9.34	0.42	7.12	43.44	23.24	0.89	2.68	11.88	0.35	0.22	99.57
Mangob	0.53	0.08	4.69	33.25	56.50	0.30	0.96	3.38	0.08	0.22	99.99
988.117.43	0.81	0.21	3.34	31.61	60.11	0.89	1.35	2.14	0.23	0.23	100.92
988.117.49											
988.117.30	0.22	0.14	7.64	30.92	58.60	0.24	0.51	1.94	0.53	0.23	100.96
988.117.53	3.05	0.19	3.00	48.92	35.15	2.40	1.98	0.79	0.32	0.30	96.10
988.117.42	0.51	0.22	4.38	30.99	60.75	0.58	1.03	0.56	0.31	1.34	100.66
BA-525											
BA-716	0.36	0.33	1.21	26.87	66.32	0.41	1.56	0.82	0.03	4.83	102.74
923.34.47	0.46	0.28	4.47	31.69	60.45	0.50	1.10	0.41	0.13	2.54	102.02
BA-952	1.51	0.54	3.44	36.08	51.12	2.42	2.94	1.06	0.36	2.22	101.70
909.43.42	0.24	0.17	4.49	37.58	54.35	0.40	0.56	1.51	0.21	0.42	99.93
909.43.43	0.42	0.28	6.54	40.09	51.95	0.67	0.93	0.89	0.38	0.54	102.67

Table C.5: continued...

Sample	Na_2O	MgO	Al_2O_3	SiO_2	PbO	K_2O	CaO	Fe_2O_3	TiO_2	CuO	Total
909.38.5	0.72	0.13	3.21	28.26	62.99	0.55	1.87	1.29	0.51	2.46	101.98
25968T	0.19	0.29	6.74	30.27	57.57	0.14	0.78	0.35	0.34	3.46	100.11
25968Tb	0.40	0.23	7.80	33.36	54.21	0.29	0.84	0.38	0.39	2.53	100.42
25969R	0.28	0.27	7.89	32.60	57.05	0.47	1.09	0.16	0.24	0.45	100.49
25969Rb	0.27	0.29	7.29	32.20	56.08	0.27	1.25	0.31	0.19	1.78	99.92
25971S	3.00	4.54	0.99	54.01	24.76	3.25	6.66	0.45	0.19	0.26	98.10
25970OU	3.31	2.43	1.10	55.55	28.02	3.76	3.61	0.28	0.18	0.30	98.52
Sherd C											

Table C.6: WDS analyses collected at the edge of archaeological glaze cross-sections. Each analysis represents the average of at least six points.

Sample	Na_2O	MgO	Al_2O_3	SiO_2	PbO	K_2O	CaO	Fe_2O_3	TiO_2	CuO	Total
BGH95	0.26	0.31	7.13	16.80	72.47	0.63	0.65	0.95	0.32	0.33	99.85
DGH86	0.14	0.35	1.08	29.66	61.96	0.30	2.49	0.61	0.00	1.90	98.48
ER	9.06	3.71	2.64	70.19	0.18	2.96	6.06	1.28	0.27	3.15	99.49
KWS94	0.10	0.59	6.97	21.74	66.29	0.55	0.50	1.53	0.45	0.05	98.77
LBI95	0.22	0.70	4.59	23.56	65.50	0.62	0.39	2.06	0.38	0.02	98.03
LCT84a	0.14	0.68	4.45	20.05	67.93	0.62	1.50	0.75	0.13	0.55	98.60
LCT84b	0.34	0.42	8.28	18.41	68.45	0.68	0.73	1.14	0.35	0.13	98.92
LIM83	0.07	0.28	8.31	19.74	66.36	0.87	1.06	0.86	0.40	0.25	98.19
179 BHS89	0.15	0.25	8.66	17.49	70.92	0.79	0.51	0.81	0.29	0.09	99.96
SWA81	0.21	0.22	1.06	25.11	67.96	0.48	1.49	1.60	0.07	1.46	99.66
SH74	0.20	0.17	2.48	26.35	61.70	0.48	2.86	1.04	0.10	2.73	98.12
Pom79	0.08	0.37	5.96	22.65	67.05	0.28	0.60	0.68	0.52	1.10	99.27
5315	0.17	0.34	9.21	19.27	68.30	0.78	0.37	0.82	0.35	0.04	99.66
5315a	0.15	0.28	8.33	18.67	70.05	0.56	0.32	0.73	0.39	0.08	99.56
5315b	0.19	0.30	8.32	17.45	70.60	0.51	0.36	0.69	0.31	0.05	98.78
4753	0.07	0.35	9.25	20.37	68.31	0.47	0.27	0.77	0.37	0.10	100.34
5655	0.18	0.32	8.73	18.55	69.36	0.80	0.41	0.67	0.33	0.06	99.41
5571	0.17	0.27	8.45	17.83	70.48	0.55	0.43	0.66	0.33	0.00	99.18
5571a	0.21	0.34	8.96	18.53	69.06	0.66	0.39	0.72	0.24	0.04	99.14
5571b	0.13	0.38	8.93	19.20	68.04	0.52	0.38	0.68	0.37	0.05	98.67
no number	0.17	0.33	8.52	18.48	69.93	0.73	0.59	0.72	0.36	0.05	99.87
202	0.21	0.30	8.76	18.32	70.17	0.78	0.31	0.67	0.42	0.06	99.98
13355	0.35	0.36	8.62	17.44	69.45	0.64	0.53	0.73	0.41	0.02	98.55
C 135/96	0.35	0.78	5.76	19.32	70.47	0.52	0.64	1.86	0.34	0.44	100.47
94-4736	0.36	0.72	5.80	19.55	68.77	0.48	0.79	1.93	0.32	0.44	99.17
no data	0.35	0.74	6.63	28.89	55.78	0.54	2.97	3.03	0.43	0.61	99.96
C 141/96	0.35	0.66	4.86	16.11	73.58	0.39	0.41	1.56	0.25	0.20	98.37
2553	0.38	0.57	6.16	20.49	68.71	0.10	0.91	0.53	1.98	0.33	100.17
93-573/1/29	0.29	0.65	5.18	18.30	70.88	0.18	0.52	0.39	2.31	0.34	99.05
93-1709a	0.19	0.56	6.43	28.41	61.61	0.22	1.05	0.48	1.33	0.46	100.74
93-1510	0.07	0.25	8.45	18.44	70.83	0.30	0.53	0.30	0.94	0.36	100.46
93-2060	0.38	0.40	5.61	20.60	71.20	0.12	0.37	0.41	1.02	0.37	100.48
93-4350	0.25	0.82	4.72	21.66	64.10	0.45	1.33	0.34	1.93	0.33	95.93
93-4741	0.34	0.86	7.23	25.81	61.20	0.24	0.80	0.36	2.71	0.31	99.87
93-3033	0.14	0.17	4.46	15.77	78.90	0.08	0.20	0.28	0.48	0.31	100.80
Nat.museum	0.41	0.97	7.31	23.93	63.28	0.83	0.72	1.83	0.40	0.10	99.76
S-1	0.26	0.30	8.71	17.59	69.47	0.54	0.48	0.78	0.31	0.02	98.46
S-2	0.18	0.36	8.52	17.79	71.06	0.46	0.37	0.68	0.39	0.04	99.85
S-3	0.13	0.39	5.60	20.94	70.16	0.57	0.31	0.75	0.42	0.09	99.35
S-4	0.08	0.45	6.47	24.14	65.18	0.76	0.42	1.12	0.44	0.00	99.05
S-5	0.11	0.37	8.88	17.14	71.04	0.54	0.39	0.89	0.34	0.00	99.69
S-6	0.34	0.63	5.61	18.01	71.14	0.53	0.73	1.56	0.33	0.17	99.04
S-7	0.34	0.94	7.19	23.00	63.89	0.67	0.71	2.32	0.41	0.12	99.58
Spoil	0.39	0.79	5.26	19.60	70.26	0.19	1.77	0.48	1.93	0.31	100.98
1850	0.46	0.87	5.84	22.42	65.90	0.12	1.05	0.65	1.80	0.38	99.49
1694	0.66	0.65	4.09	27.81	61.40	1.73	2.73	0.62	1.32	0.28	101.29
1797b	0.45	1.11	6.74	26.57	57.42	0.21	1.42	0.58	2.28	0.40	97.17
1770	0.62	1.20	8.11	29.93	55.90	0.22	1.35	0.93	2.39	0.43	101.09
2215	0.42	0.93	6.21	23.51	64.34	0.30	1.78	0.61	2.27	0.42	100.78
1970	0.52	0.92	5.99	24.33	62.70	0.55	1.30	0.74	2.11	0.35	99.51
1797	0.41	0.82	5.25	19.66	68.78	0.22	1.12	0.55	1.88	0.32	99.03
1007	0.71	0.95	5.92	22.64	62.96	0.87	3.59	0.72	1.98	0.32	100.67
1784	0.44	1.06	6.63	24.18	61.48	0.12	1.47	0.84	2.43	0.48	99.13
V59	0.34	0.24	3.29	27.88	59.87	0.68	3.52	1.19	0.14	2.57	99.73
V59b	0.26	0.29	2.79	29.12	59.86	0.61	3.33	3.18	0.13	0.06	99.61
V45	0.22	0.70	4.50	16.03	75.40	0.37	0.50	1.65	0.18	0.09	99.62
V45b	0.23	0.78	4.71	17.39	72.23	0.42	0.69	1.77	0.20	0.13	98.56
V27	0.35	0.35	0.51	30.47	62.20	0.36	2.00	0.50	0.07	2.40	99.21
V27b	0.48	0.48	3.99	27.94	60.83	0.64	2.00	1.89	0.28	0.07	98.62
V83	0.46	0.09	3.22	31.13	54.47	1.05	3.94	3.52	0.18	0.13	98.18
V83b	0.35	0.09	3.41	31.57	56.59	0.92	2.50	1.37	0.17	3.43	100.39
V46	0.37	0.56	3.86	15.67	76.38	0.40	0.39	1.50	0.20	0.06	99.39
V69	0.30	0.40	3.94	26.07	61.66	0.52	3.07	1.46	0.14	2.28	99.84
V69b	0.25	0.26	2.32	26.91	62.24	0.44	1.99	3.31	0.07	0.11	97.90

Table C.6: continued...

Sample	Na_2O	MgO	Al_2O_3	SiO_2	PbO	K_2O	CaO	Fe_2O_3	TiO_2	CuO	Total
Picon1	0.34	0.32	6.88	16.87	72.14	0.62	0.64	0.94	0.27	0.55	99.59
Picon2	0.17	0.23	6.55	13.22	77.38	0.42	0.55	0.80	0.44	0.13	99.89
Picon3	0.01	0.16	8.76	21.98	65.32	0.58	0.43	0.66	0.36	0.48	98.75
Picon4	0.30	0.48	3.34	29.69	57.02	0.81	3.12	3.35	0.18	0.30	98.58
Picon4b	0.42	0.60	3.05	29.36	56.18	0.78	3.64	1.49	0.15	2.71	98.39
V.24S.97-2256	0.43	0.24	4.13	33.03	55.02	0.88	2.19	0.95	0.09	1.61	98.57
V.2S.92	0.46	0.47	3.69	30.44	59.22	0.40	1.78	1.99	0.21	0.14	98.80
V.2S.92b	0.46	0.30	1.96	33.72	57.59	0.36	2.36	0.47	0.08	2.92	100.21
SA99RD37	0.34	0.99	5.30	23.65	64.57	0.55	0.90	2.34	0.31	0.06	99.01
SA2000RD7SAG	0.14	0.43	3.91	45.14	42.46	1.17	2.43	0.91	0.20	1.82	98.63
SA2000JP40A	0.05	0.23	2.98	27.48	67.07	0.18	0.33	0.42	0.11	0.34	99.18
SA2000JP40B	0.25	0.44	6.29	24.38	65.33	0.19	0.88	0.74	0.16	0.16	98.82
SA2000JP42	0.26	0.63	5.63	30.77	58.72	0.32	1.55	1.08	0.10	0.13	99.18
US55	0.22	0.94	4.58	31.55	58.55	0.90	1.97	1.96	0.26	0.08	101.02
US1040	0.30	0.73	5.81	19.55	70.48	0.35	0.99	2.19	0.32	0.01	100.73
US1489	0.19	1.00	5.84	26.37	61.22	0.52	1.82	2.59	0.41	0.08	100.02
Oberless	0.12	0.65	7.82	28.63	57.05	0.86	1.15	2.50	0.44	0.30	99.52
M.11	0.19	0.42	6.98	23.19	66.19	0.75	0.26	0.97	0.19	0.09	99.24
M.16	0.19	0.34	6.22	20.32	71.33	0.59	0.23	1.02	0.25	0.02	100.51
M.25	0.38	0.40	4.38	20.88	72.83	0.50	0.27	0.84	0.28	0.19	100.96
Campione1	0.11	0.29	1.12	28.44	63.51	0.25	1.75	2.53	0.16	0.12	98.29
Campione2	0.04	0.25	0.59	25.72	68.24	0.31	1.66	0.84	0.11	1.44	99.22
Campione3	0.10	0.09	0.36	26.94	68.56	0.15	0.86	1.48	0.04	0.17	98.76
RZ5574	0.19	0.27	1.01	26.11	68.12	0.29	2.20	0.63	0.05	1.23	100.10
RZ5636	0.34	0.53	5.23	28.26	59.54	0.64	2.34	1.73	0.24	0.04	98.90
RZ5636b	0.24	0.51	5.60	27.59	59.59	0.71	1.80	1.74	0.30	0.12	98.20
RZ5637	0.55	0.65	2.90	29.42	59.21	0.72	3.33	1.49	0.07	1.49	99.84
RZ5653	0.14	0.51	5.06	28.07	59.49	0.91	0.96	2.00	0.29	0.22	97.65
RZ5658a	0.29	0.38	5.03	24.12	67.06	0.42	0.57	1.58	0.22	0.19	99.84
RZ5658b	0.22	0.64	5.71	26.59	61.63	0.57	1.35	2.50	0.26	0.22	99.70
RZ5670 RZ5848	0.25	0.46	1.27	35.57	56.98	0.59	2.06	1.75	0.16	1.51	100.59
Carlino1	0.46	0.97	5.56	28.50	59.80	0.82	1.61	1.88	0.27	0.09	100.28
Carlino2	0.69	0.93	7.17	37.14	47.57	1.01	3.25	2.42	0.47	0.11	101.40
Carlino3	0.36	0.67	6.30	32.40	57.28	0.91	0.94	1.79	0.30	0.01	101.48
Carlino4	0.29	0.82	5.63	27.84	61.76	0.52	0.69	1.93	0.30	0.09	99.98
Carlino5	0.27	0.77	5.00	22.84	67.95	0.58	0.80	1.86	0.25	0.00	100.53
Carlino6	0.43	0.78	5.66	29.47	60.00	0.77	1.44	1.38	0.26	0.01	100.58
Carlino7A	0.33	0.84	5.78	24.81	58.29	0.74	6.39	2.35	0.30	0.05	100.21
Carlino7B	0.39	0.87	6.05	25.78	57.18	0.85	6.30	2.27	0.33	0.01	100.73
CR9550	0.11	0.27	6.39	19.13	66.36	0.15	0.29	0.65	0.51	4.58	98.44
CR9551	0.04	0.15	5.57	18.83	73.91	0.20	0.13	0.35	0.43	0.03	99.64
CR9548	0.11	0.32	1.40	25.52	65.28	0.52	2.53	0.88	0.10	2.23	98.88
CR9548b	1.07	0.55	2.20	34.56	55.04	2.72	2.74	0.29	0.16	0.76	100.08
CR9549	0.17	0.56	1.89	33.00	61.08	0.58	1.58	0.77	0.14	0.00	99.77
CR9560	0.84	0.08	0.74	26.99	64.98	0.18	0.62	4.33	0.08	0.22	99.06
CR9561	0.36	0.35	6.25	27.80	62.36	0.68	0.63	0.58	0.11	0.37	99.50
CR9559	0.56	0.26	1.05	28.71	62.92	0.32	1.48	3.36	0.03	0.54	99.22
CR9562	0.28	0.51	5.43	20.61	64.29	0.45	0.97	1.05	0.34	6.93	100.87
CR9564	0.01	0.06	0.77	26.13	72.04	0.14	0.39	0.17	0.07	0.02	99.80
CR9563	0.48	0.58	3.59	38.34	52.51	1.97	2.84	0.80	0.28	0.17	101.56
CR9567	0.20	0.30	0.79	30.39	67.37	0.22	1.43	0.28	0.07	0.26	101.30
Mango	9.27	0.50	2.96	41.58	30.85	0.79	3.48	9.89	0.11	0.38	99.80
Mangob	0.27	0.11	0.41	33.03	59.53	0.17	0.74	5.08	0.08	0.72	100.16
988.117.43 988.117.49	0.59	0.19	1.91	28.46	63.13	0.73	0.93	2.66	0.21	0.42	99.22
988.117.30 988.117.53	0.12	0.18	2.16	30.95	60.44	0.25	0.51	3.61	0.34	0.17	98.72
988.117.42 BA-525	0.30	0.35	2.02	28.72	64.80	0.33	1.16	0.81	0.30	2.54	101.32
BA-716	0.33	0.40	0.60	27.09	67.35	0.34	1.37	0.55	0.07	6.47	104.55
923.34.47	0.21	0.46	1.17	28.25	66.04	0.24	1.30	0.54	0.10	4.57	102.89
BA-952	1.30	0.48	1.60	30.51	56.93	1.65	2.57	0.88	0.29	6.07	102.28
909.43.42	0.15	0.23	2.93	34.46	59.40	0.22	0.60	2.43	0.24	0.50	101.16
909.43.43	0.17	0.31	3.12	34.28	60.11	0.25	0.77	0.85	0.26	0.48	100.60

Table C.6: continued...

Sample	Na_2O	MgO	Al_2O_3	SiO_2	PbO	K_2O	CaO	Fe_2O_3	TiO_2	CuO	Total
909.38.5	0.65	0.43	2.37	29.21	62.77	0.73	1.53	0.82	0.34	2.94	101.79
25968T	0.23	0.26	7.03	31.60	53.69	0.29	0.71	0.38	0.21	4.74	99.13
25968Tb	0.21	0.23	5.03	34.41	52.57	0.32	0.82	0.42	0.35	4.68	99.04
25969R	0.13	0.42	3.28	38.05	55.57	0.37	0.92	0.28	0.27	1.30	100.59
25969Rb	0.09	0.41	3.66	34.76	55.51	0.22	1.22	0.27	0.22	2.62	98.97
25971S	0.17	0.50	4.22	34.93	55.85	0.29	0.94	0.45	0.21	2.53	100.08
25970OU	0.63	0.47	5.60	31.48	56.10	1.11	2.28	0.13	0.28	0.04	98.11
Sherd C	0.35	0.56	9.07	44.03	42.20	0.83	0.85	0.40	0.32	0.90	99.53

Appendix D

Catalogue of Representative Cross Sections of Roman Sherds

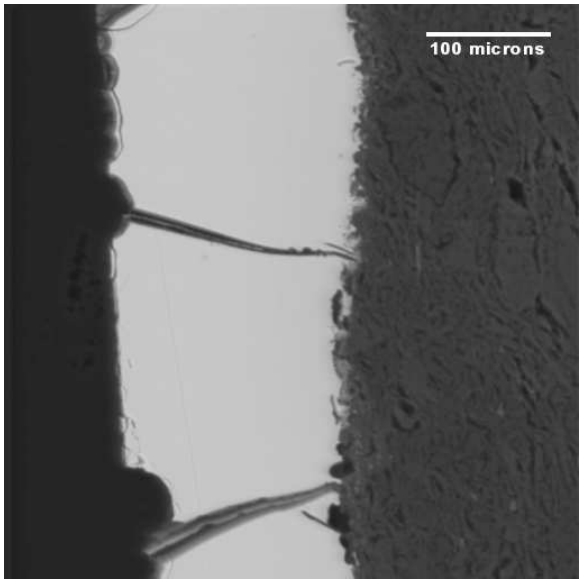

BGH95, 500x magnification, Group 1b

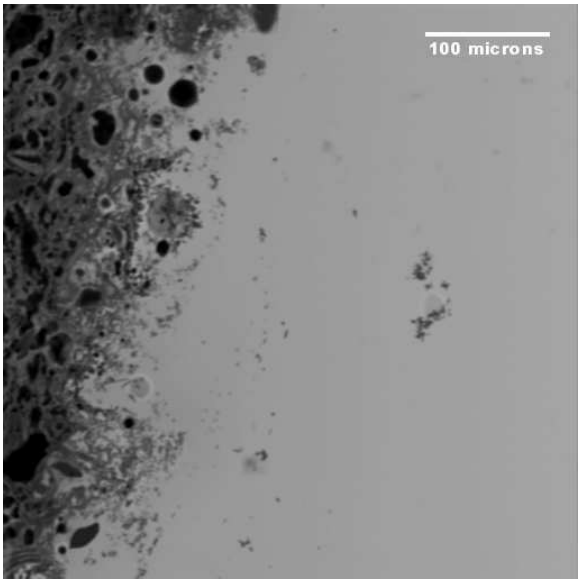

DGH86, 500x magnification, Group 3

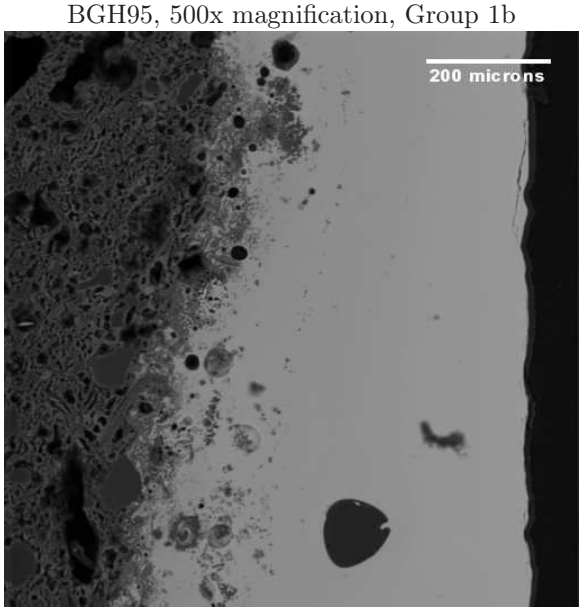

DGH86, 250x magnification, Group 3

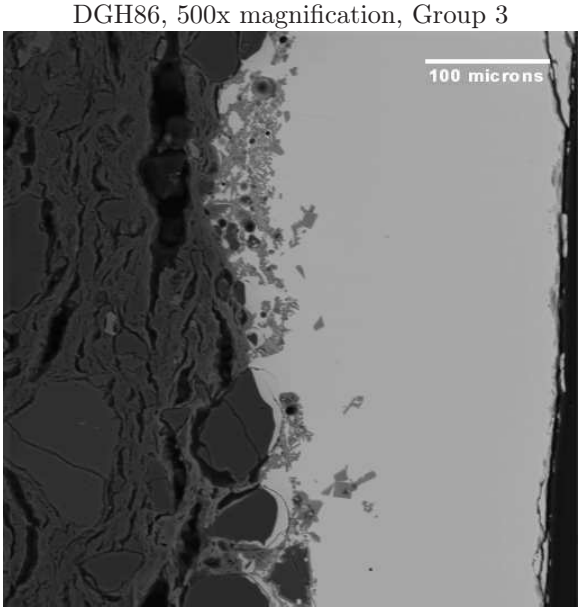

KWS94, 500x magnification, Group 2a

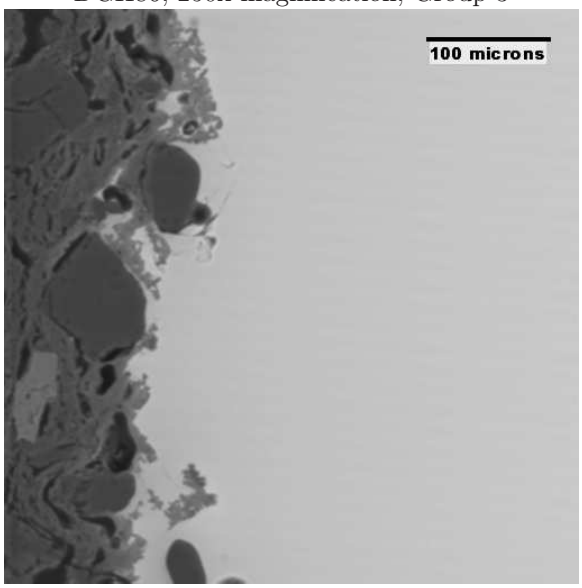

LB195, 500x magnification, Group 2a

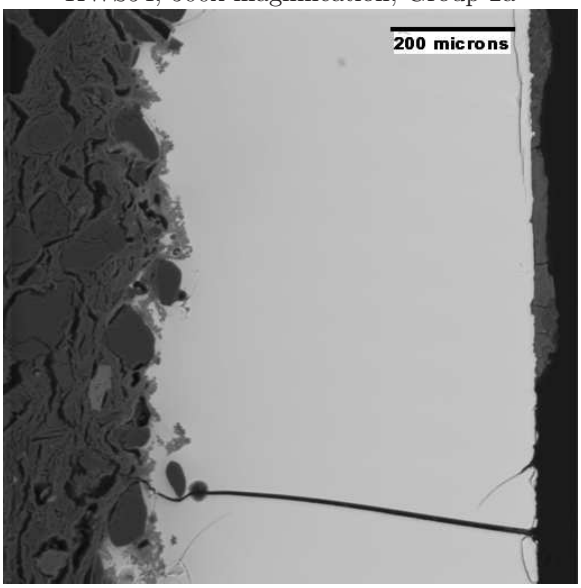

LB195, 250x magnification, Group 2a

Figure D.1: Glazes from the excavations of London, UK

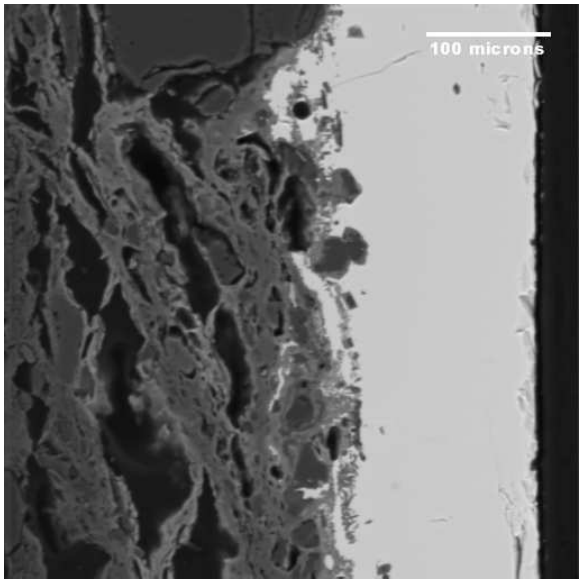

LCT84a, 500x magnification, Group 2a

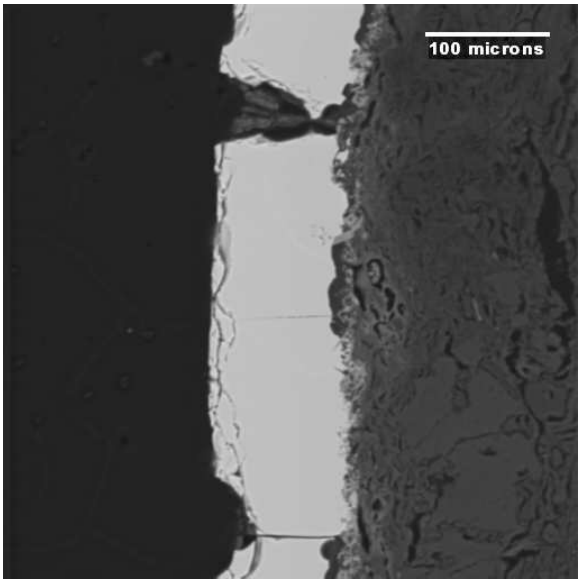

LCT84b, 500x magnification, Group 1b

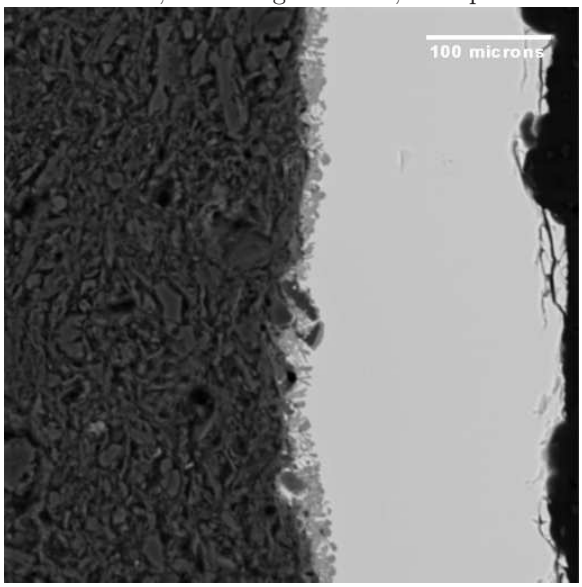

LIM83, 500x magnification, Group 1b

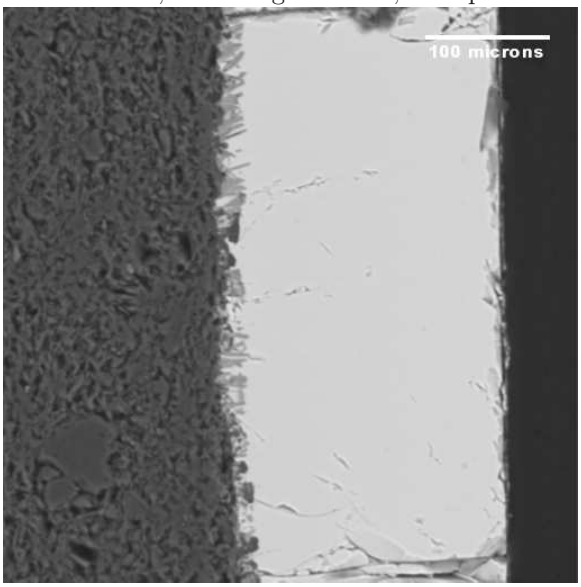

179BHS89, 500x magnification, Group 1b

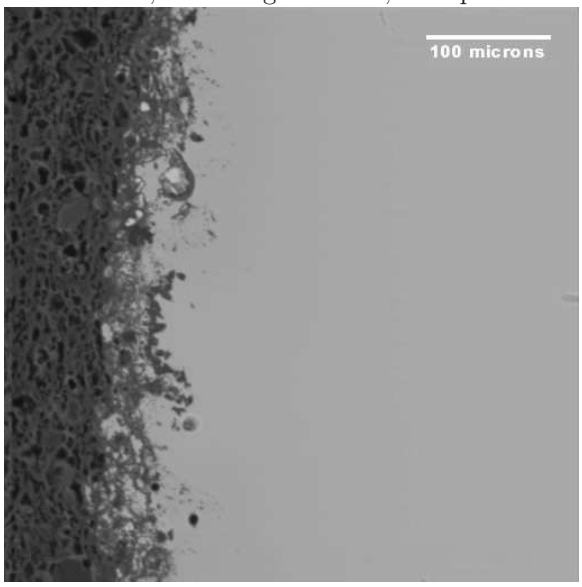

SWA81, 500x magnification, Group 3

SWA81, 250x magnification, Group 3

Figure D.1(continued)

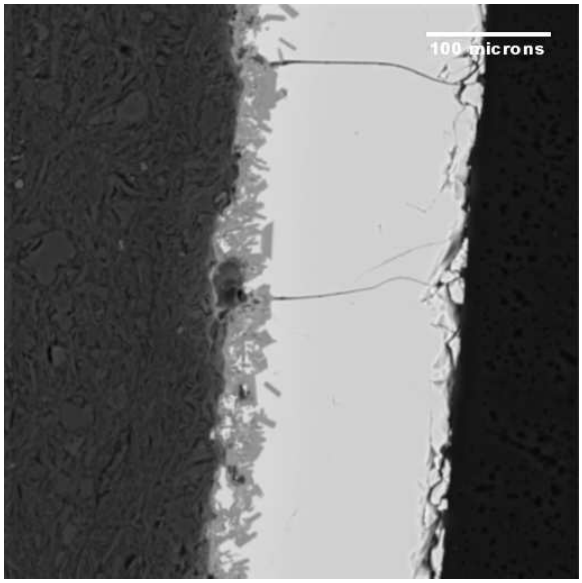

5315, 500x magnification, Group 1a

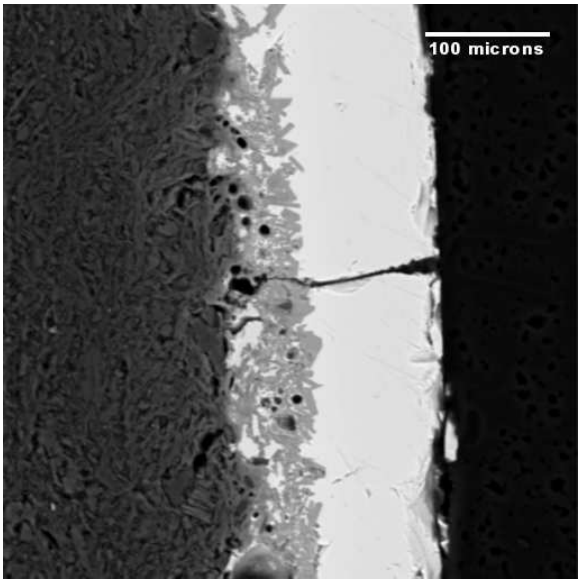

5315a, 500x magnification, Group 1a

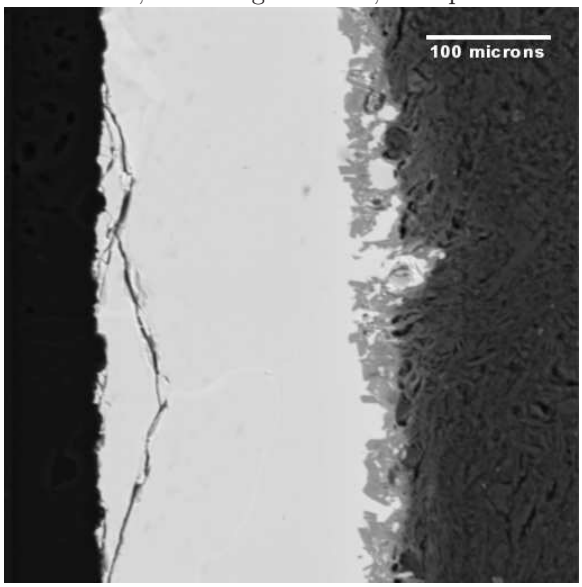

5315b, 500x magnification, Group 1a

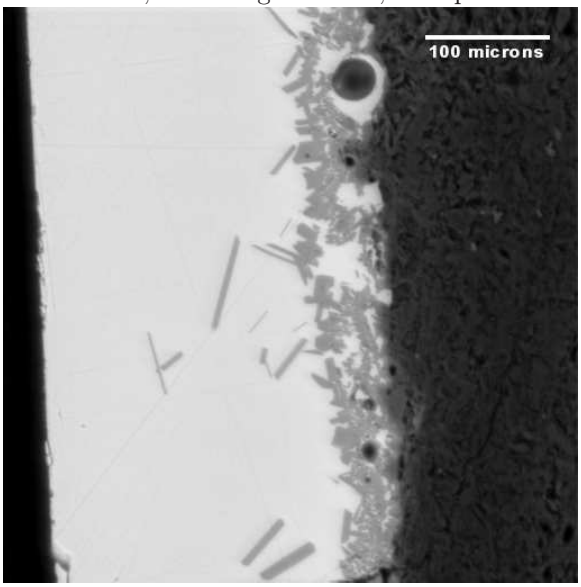

4753, 500x magnification, Group 1a

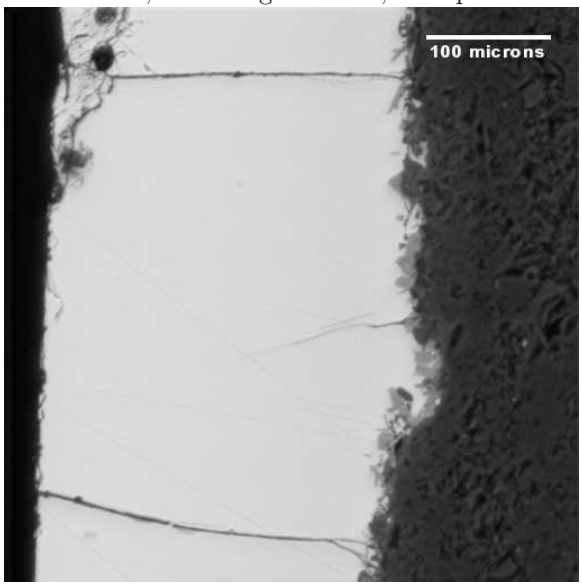

5655, 500x magnification, Group 1a

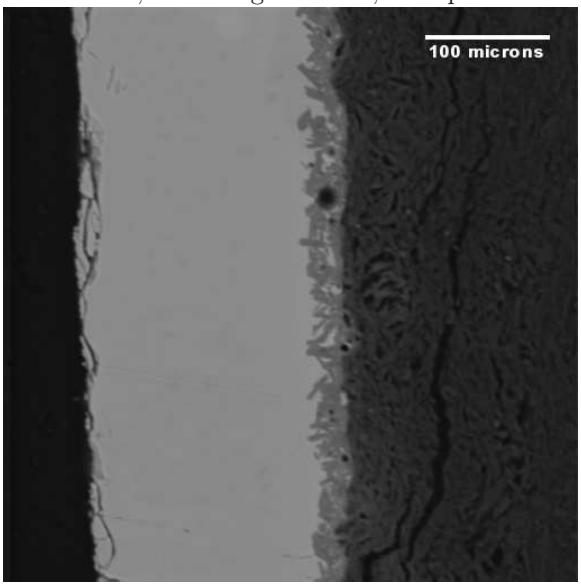

5571, 500x magnification, Group 1a

Figure D.2: Lead glazes excavated from Diana in Upper Moesia, present-day Serbia

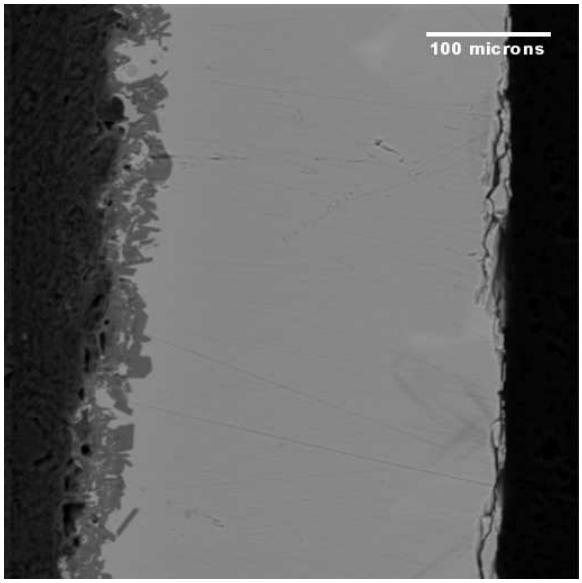

5571a, 500x magnification, Group 1a

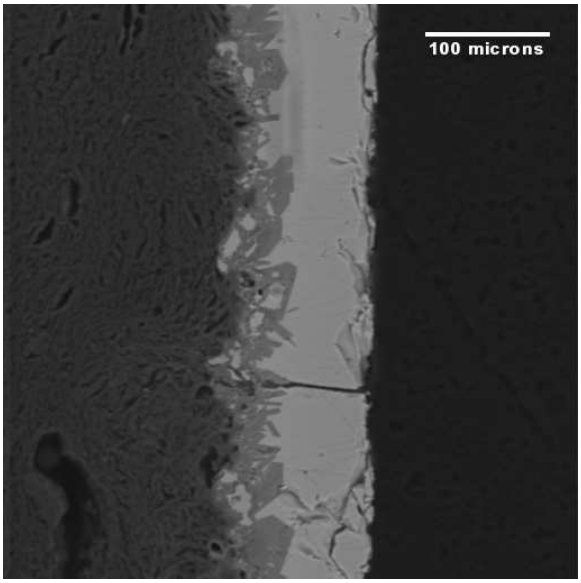

5571b, 500x magnification, Group 1a

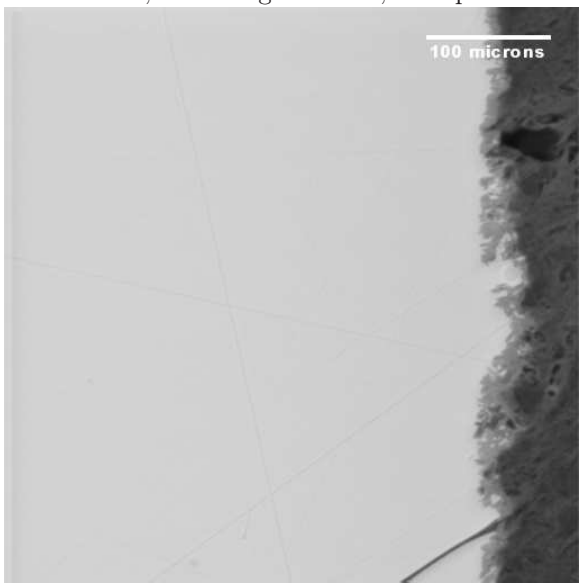

no number, 500x magnification, Group 1a

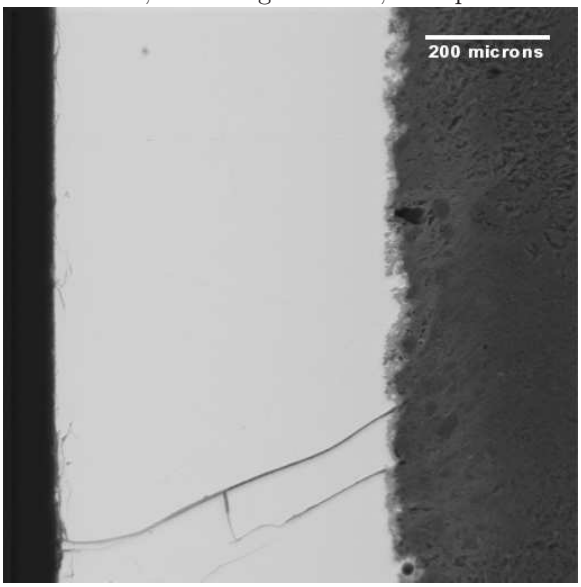

no number, 250x magnification, Group 1a

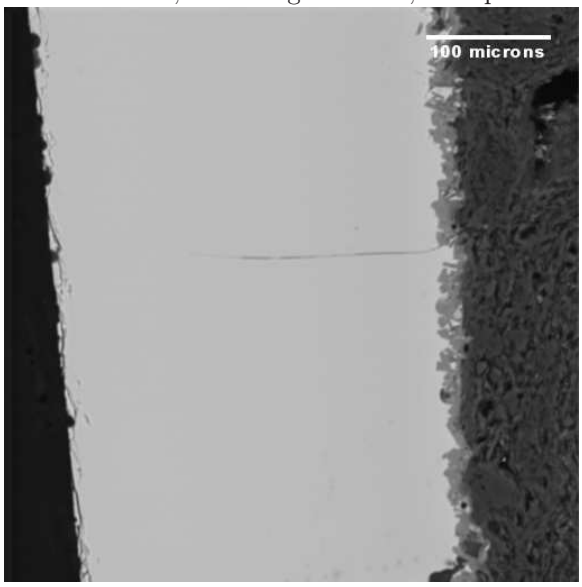

202, 500x magnification, Group 1a

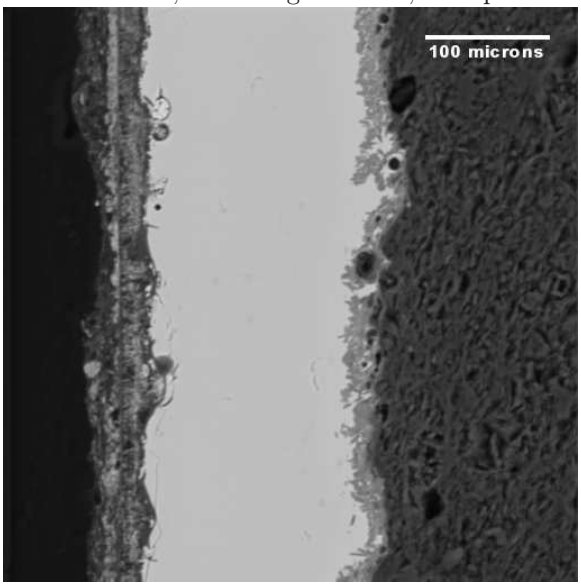

13355, 500x magnification, Group 1a

Figure D.2(continued)

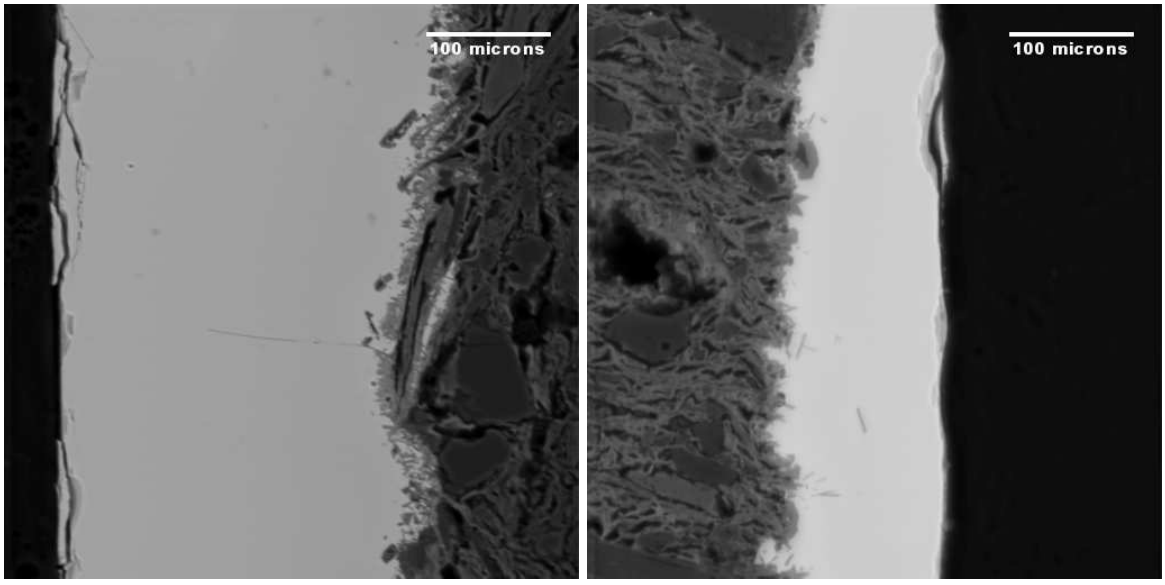

94-4736, 500x magnification, Group 2a National Museum, 500x magnification, Group 2a

Figure D.2(continued)

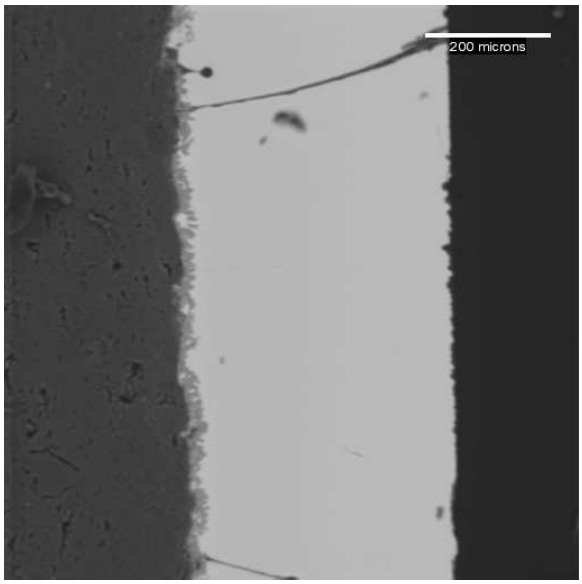

S1, 250x magnification, Group 1a

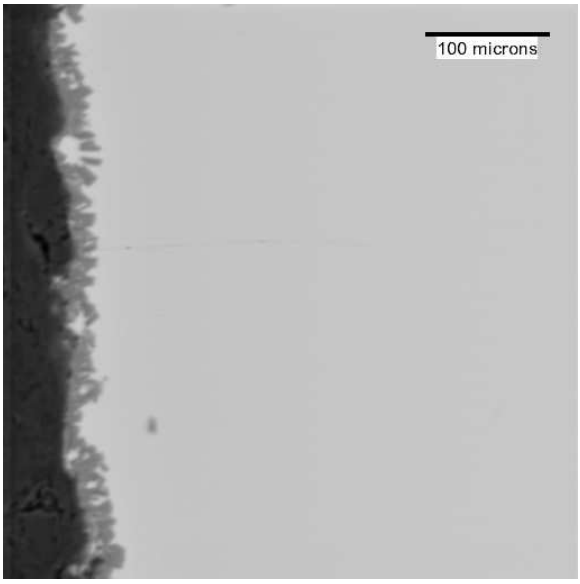

S1, 500x magnification, Group 1a

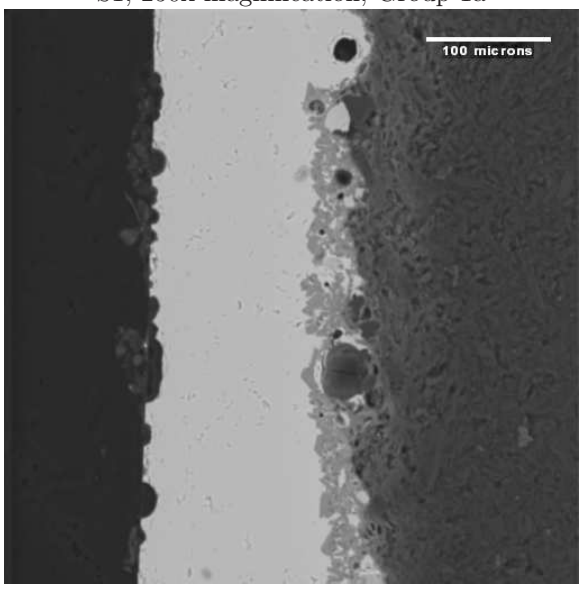

S2, 500x magnification, Group 1a

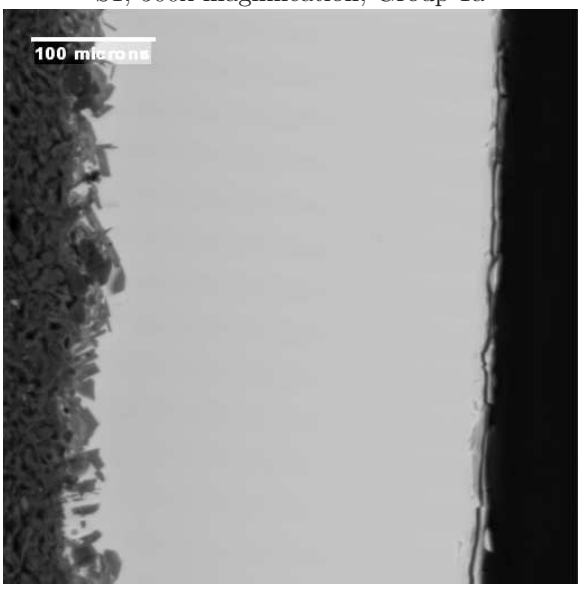

S3, 500x magnification, Group 2b

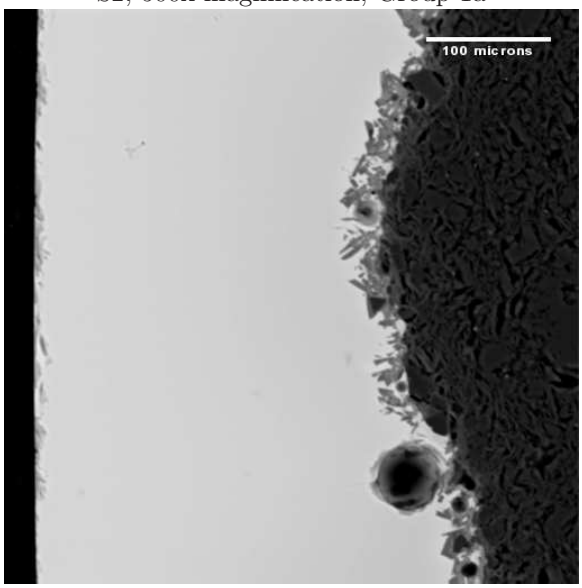

S4, 500x magnification, Group 2b

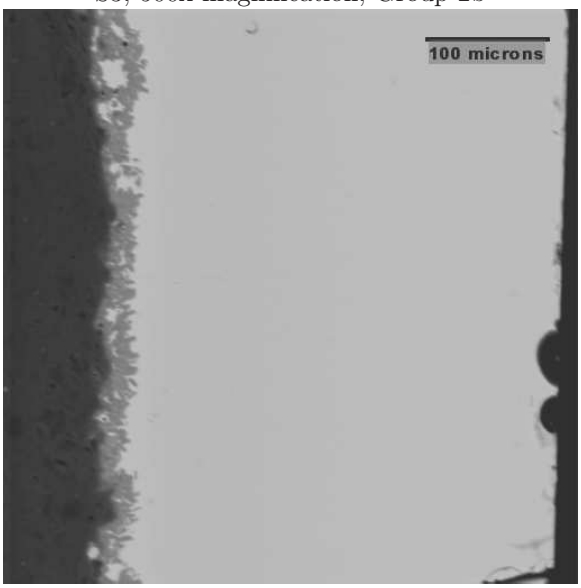

S5, 500x magnification, Group 1a

Figure D.3: Lead glazes excavated from Singidunum in Upper Moesia, present-day Serbia

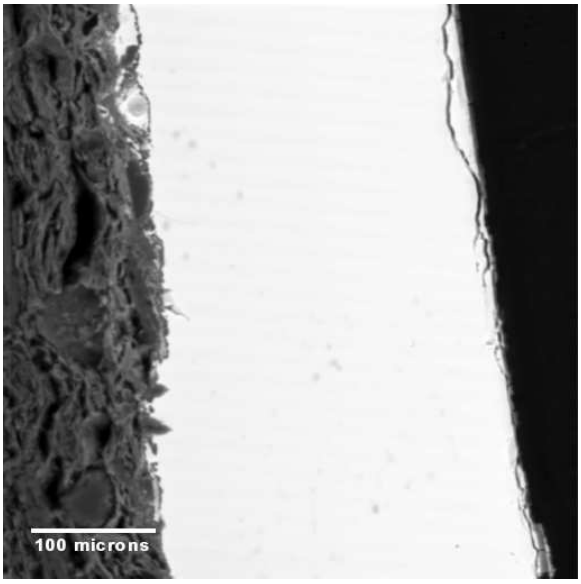

S6, 500x magnification, Group 2a

Figure D.3(continued)

Bibliography

Aitchison, J. (1986). *The Statistical Analysis of Compositional Data*. New York: Methuen.

Argyropoulos, V. (1995). Compositional variations of Roman Samian manufactured at Lezoux. *Archaeometry* **37**, 271–285.

Armstrong, P., H. Hatcher, and M. Tite (1997). Changes in Byzantine glazing technology from the ninth to thirteenth centuries. In G. d'Archimbaud (Ed.). *La Céramique Médiévale en Méditerranée, Actes du 6e Congrès de l'AICEM2. Aix-en-Provence*.

Arthur, P. (1978). The lead-glazed wares of Roman Britain. In P. Arthur and G. Marsh (Eds.). *Early Fine Wares in Roman Britain*. London: BAR.

Atik, N. (1995). *Die Keramik aus den südthermen von Perge*. Tübingen: Wasmuth.

Barag, D. (1962). Mesopotamian glass vessels of the second millennium BC. *Journal of Glass Studies*.

Barag, D. (1970). Mesopotamian core-formed glass vessels (1500-500 BC). In A. Oppenheim, R. Brill, D. Barag, and A. von Saldern (Eds.). *Glass and glass-making in ancient Mesopotamia*. New York: Corning Museum of Glass.

Bersani, M., B. Morten, M. Prudenziati, and A. Gualtieri (1997). Interactions between lead oxide and ceramic substrates for thick-film technology. *Journal of Material Research* **12(2)**, 501–508.

Bianchini, G., R. Laviano, S. Lovo, and C. Vaccaro (2002). Chemical-mineralogical characterization of clay sediments arround Ferrara (Italy): a tool for an environmental analysis. *Applied Clay Science* **21**, 165–176.

Bimson, M. and I. Freestone (Eds.) (1987). *Early Vitreous Materials*. Volume 56 of *British Museum Occasional Papers*.

Brill, R. (1999). *Chemical Analyses of Early Glasses*. The Corning Museum of Glass.

Brindley, G. and M. Nakahira (1959). The kaolinite-mullite reaction series: II, metakaolin. *Journal of the American Ceramic Society* **42(7)**, 314–318.

Brogiolo, G. and S. Gelichi (1997). Ceramiche, technologia ed organizzazione della produzione nell'Italia settentrionale tra VI e X secolo. In G. d'Archimbaud (Ed.). *La Céramique Médiévale en Méditerranée, Actes du 6e Congrès de l'AICEM2. Aix-en-Provence*.

Budd, P. and T. Taylor (1995). The faerie smith meets the bronze industry: magic versus science in the interpretation of prehistoric metal-making. *World Archaeology* **27(1)**, 133–43.

Caley, E. (1947). Results of a chemical examination of some specimens of Roman glaze from Tarsus. *American Journal of Archaeology* **51**, 389–393.

Casas i Genover, J. and J. Merino i Serra (1990). Troballes de ceràmica vidriada d'època romana a les comarques costaneres de Girona. *Cypsela* **8**, 139–155.

Chakraborty, A. and D. Ghosh (1978). Re-examination of the kaolinite-mullite reaction series. *Journal of the American Ceramic Society* **61(3-4)**, 170–173.

Chakraborty, S., D. Dingwell, and D. Rubie (1995a). Multicomponent diffusion in ternary silicate melts in the system K_2O–Al_2O_3–SiO_2: I. experimental measurements. *Geochimica et Cosmochemica Acta* **59(2)**, 255–264.

Chakraborty, S., D. Dingwell, and D. Rubie (1995b). Multicomponent diffusion in ternary silicate melts in the system K_2O–Al_2O_3–SiO_2: II mechanisms, systematics and geological applications. *Geochimica et Cosmochemica Acta* **59(2)**, 265–277.

Chen, S., B. Zhao, P. Hayes, and E. Jak (2001). Experimental study of phase equilibria in the PbO–Al_2O_3–SiO_2 system. *Metallurgical and Materials Transactions B* **32(b)**, 997–1005.

Cooper, A. and A. Varshneya (1968). Diffusion in the system K_2O–SrO–SiO_2. *Journal of the American Ceramic Society* **51(2)**, 103–106.

Crank, J. (1975). *The Mathematics of Diffusion*. Oxford: Oxford University Press.

Cvjetićanin, T. (1997). Late Roman glazed pottery as a military commodity. *Rei Cretariæ Romanæ Fautorum Acta* **35**, 17–26.

Cvjetićanin, T. (2000a). Eastern Mediterranean elements in technology and design of Upper Moesian pottery: the case of glazed pottery. *Rei Cretariæ Romanæ Fautorum Acta* **36**, 319–327.

Cvjetićanin, T. (2000b). *Glazed Pottery from Upper Moesia*. Belgrade: National Museum of Belgrade.

de Levie, R. (2001). *How to Use Excel in Analytical Chemistry and in General Scientific Data Analysis*. Cambridge: Cambridge University Press.

Deer, W., R. Howie, and J. Zussman (1993). *An Introduction to the Rock-Forming Minerals, 2nd Edition*. Harlow: Addison Wesley Longman Limited.

Desbat, A. (1985). Les productions précoces de céramiques à glaçure plombifère de la vallée du Rhône. *Rei Cretariæ Romanæ Fautorum Acta* **34**, 39–47.

Desbat, A. (1987). Cèramiques à glaçure plombifère des fouilles de Lyon. *Figlina* **7**, 105–123.

Duffy, J. (1993). A review of optical basicity and its application to oxidic systems. *Geochemica et Cosmochemica Acta* **57**, 3961–3970.

Duffy, J. and M. Ingram (1971). Establishment of an optical scale for Lewis basicity in inorganic oxyacids, molten salts, and glasses. *Journal of the American Chemical Society* **93(24)**, 6448–6454.

Duffy, J. and M. Ingram (1976). An interpretation of glass chemistry in terms of the optical basicity concept. *Journal of Non-Crystalline Solids* **21**, 373–410.

Eiland, M. (1995). *Parthian Ninevah*. D.Phil. thesis, University of Oxford.

Elsner, J. (1998). *Imperial Rome and Christian Triumph*. Oxford: Oxford University Press.

Eyring, H. (1936). Viscosity, plasticity, and diffusion as examples of absolute reaction rates. *Journal of Chemical Physics* **4**, 283–291.

Farmer, V. (1974). *The Infrared Spectra of Minerals*. London: Mineralogical Society.

Fayon, F., C. Landron, K. Skurai, C. Bessada, and D. Massicot (1999). Pb^{2+} environment in lead silicate glasses probed by Pb-L_{III} edge XAFS and ^{207}Pb NMR. *American Mineralogist* **83**, 685–699.

Freeman, I. (1964). Mineralogy of ten British brick clays. *Clay Mineralogy Bulletin* **5**, 474.

Freestone, I. (1991). Looking into glass. In S. Bowman (Ed.). *Science and the Past*. London: British Museum Press.

Freestone, I., Y. Garin-Rosen, and M. Hughes (2000). Primary glass from Israel and the production of glass in the late antique and early Islamic period. In M.-D. Nenna (Ed.), *La Route du Verre*. Lyon: Maison de l'Orient.

Freestone, I. and Y. Gorin-Rosen (1999). The great glass slab at Bet She'arim, Israel: an early Islamic glassmaking experiment? *Journal of Glass Studies* **41**, 105–116.

Freestone, I., K. Leslie, M. Thirwall, and Y. Gorin-Rosen (2003). Strontium isotopes in the investigation of early glass production Byzantine and early Islamic glass from the Near East. *Archaeometry* **45**, 19–32.

Geller, R. and E. Bunting (1943). Report on the systems lead oxide-alumina and lead oxide-silica. *Journal of Research of the National Bureau of Standards* **31**, 255–270.

Génin, D., A. Desbat, S. Elaigne, C. Laroche, and B. Dangreaux (1996). Les productions de l'atelier de La Muette. *Galli* **53**, 41–191.

Génin, D., J. Lasfargues, and A. Schmitt (1996). Les productions de l'atelier de Loyasse. *Galli* **53**, 19–38.

Goldman, H. (1950). *Excavations at Gözlü Kule, Tarsus. Volume 1: Hellenistic and Roman Periods*. Princenton: Princeton University Press.

Goldstein, J., D. Newbury, P. Echlin, D. Joy, A. Romig, C. Lyman, C. Fiori, and E. Lifshin (1992). *Scanning Electron Microscope and X-Ray Microanalysis*. New York: Plenum Press.

Green, K. (1979). Report on the excavations at Usk: 1965-1976. In K. Green (Ed.), *The Pre-Flavian Fine Wares*. Cardiff: University of Wales.

Gupta, P. and A. Cooper (1971). The [**D**] matrix for multicomponent diffusion. *Physica* **54**, 39–59.

Harris, D. (1998). Nonlinear least-squares curve fitting with Microsoft Excel Solver. *Journal of Chemical Education* **75**, 119–121.

Hatcher, H., R. Hedges, A. Pollard, and P. Kenrick (1980). Analyis of Hellenistic and Roman fine pottery from Benghazi. *Archaeometry* **22**, 131–151.

Hatcher, H., A. Kaczmarczyk, A. Scherer, and R. Symonds (1994). Chemical classification and provenance of some Roman glazed ceramics. *American Journal of Archaeology* **98**, 431–456.

Hayes, J. (1992). The pottery of Saraçhane. In R. Harrison (Ed.), *Excavations at Saraçhane 2*. Princeton: Princeton University Press.

Hayes, J. (1997). *Handbook of Mediterranean Roman Pottery*. London: British Museum Press.

Henderson, J. and M. Mango (1995). Glass at medieval Constantinople: Preliminary scientific evidence. In C. Mango, G. Dagron, and G. Greatrex (Eds.), *Constantinople and its Hinterland*. Aldershot: Variorum.

Hilger, J., D. Babel, N. Prioul, and A. Fissolo (1981). Corrosion of AZS and fireclay refractories in contact with lead glass. *Journal of the American Ceramic Society* **64**, 213–220.

Hochuli-Gysel, A. (1977). *Kleinasiatische glasierte Reliefkeramik (50 v. Chr. bis 50 n. Chr.) und ihre oberitalischen Nachahmungen*. Bern: Stämpfli.

Howard, E. and J. Cassidy (2000). Analysis of microelectrodes using Microsoft Excel Solver. *Journal of Chemical Education* **77**, 409–411.

Hurst, D. and I. Freestone (1996). Lead glazing technique from a medieval site of Hanely Swan, Warwickshire. *Medieval Ceramics* **20**, 13–19.

Iliffe, J. (1936). Hellenistic and sigillata wares in the Near East. *Journal of Hellenic Studies* **56(2)**, 234–235.

Isings, C. (1957). Roman glass from dated finds. *Archaeologica Traiectina* **2**.

Jones, F. (1945). Rhosica vasa. *American Journal of Archaeology* **49**, 45–51.

Kingery, W. (1958). *Ceramic Fabrication Processes*. New York: John Wiley & Sons.

Kingery, W., H. Bowen, and D. Uhlmann (1976). *Introduction to Ceramics*. New York: John Wiley & Sons.

Kress, V. and M. Ghioroso (1995). Multicomponent diffusion in basaltic melts. *Geochimica et Cosmochemica Acta* **59(2)**, 313–324.

Lane, A. (1948). *Early Islamic Pottery*. London: Faber and Faber.

Langanke, B. and H. Schmalzried (1979). Ionic transport in PbO-SiO_2 melts (1): Tracer diffusion and chemical interaction. *Berichte Bunsen-Gesellschaft Physical Chemistry* **83**, 59–64.

Lasaga, A. (1979). Multicomponent exchange and diffusion in silicates. *Geochimica et Cosmochemica Acta* **43**, 455–469.

Leaist, D. and R. Noulty (1985). An eigenvalue method for determination of multicomponent diffusion coefficients: Application to NaOH + NaCl + H_2O mixtures. *Canadian Journal of Chemistry* **63**, 476–482.

Lechtman, H. (1977). Style in technology: some early thoughts. In H. Lechtman and T. Merrill (Eds.). *Material culture: style, organization, and dynamics of technology*. St. Paul, MN: West Publishing Company.

Lee, S., Y. Kim, and H. Moon (1999). Phase transformation sequence from kaolinite to mullite investigate by an energy-filtering transmission electron microscope. *Journal of the American Ceramic Society* **82**, 2841–2848.

Legendre, C., M. Caroff, H. Leyrit, P. Nehlig, and D. Thièblemont (2001). Les premières phases d'édifcation du stratovolcan du Cantal (Massif Central, France) entre 9,5 et 8,0 ma: géologie et géochimie du secteur de l'Élancéze. *C.R. Acad. Sci. Paris, Sciences de la Terre et des planétes* **332**, 617–624.

Lemonnier, P. (1993). Introduction. In P. Lemonnier (Ed.). *Technological Choices: Transformation in Material Culture Since the Neolithic*. London: Routledge.

Lesher, C., R. Hervig, and D. Tinker (1996). Self diffusion of network formers (silicon and oxygen). *Geochemica et Cosmochemica* **60(3)**, 405–413.

Liang, Y. (1999). Diffusive dissolution in ternary systems: Analysis with applications to quartz quartzite dissolution in molten silicates. *Geochimica et Cosmochemica Acta* **63(23/24)**, 3983–3996.

Liang, Y. (2000). Dissolution in molten silicates: Effects of solid solution. *Geochimica et Cosmochemica Acta* **64(9)**, 1617–1627.

Liang, Y., F. Richter, and L. Chamberlin (1997). Diffusion in silicate melts: III empirical models for multicomponent diffusion. *Geochimica et Cosmochemica Acta* **61(24)**, 5295–5312.

Liang, Y., F. Richter, A. Davis, and E. Watson (1996). Diffusion in silicate melts: I multicomponent diffusion in CaO–Al_2O_3–SiO_2 at 1500 ℃ 1GPa. *Geochimica et Cosmochemica Acta* **60(22)**, 4353–4367.

Maccabruni, C. (1987). Ceramica romana con invetriatura al piombo. *Céramiques Hellénistiques et romaines II. Annales littéraires de l'Univ. de Besançon* **330**, 167–189.

Mannoni, T. (1992). Seminario di studi sulla ceramica a vetrina pesante in Italia: Bilancio di una esperienza. In L. Paroli (Ed.). *La Ceramique Invetriata Tardoantica E Altomedievale in Italia*. Firenze: Edizioni All'Insegna Del Giglio.

Marković, S., N. Kostić, and E. Oches (2004). Paleosols in the Ruma loess section (Vojvodina, Serbia). *Revista Mexicana de Ciencias Geológicas* **21**, 79–87.

Martin, A. (1992). La ceramica invetriata romana: la testimonianza dell'Area NE delle Terme del Nuotatore ad Ostia. In L. Paroli (Ed.). *La Ceramica Invetriata Tardoantica E Altomedievale in Italia*. Firenze: Edizioni All'Insegna Del Giglio.

Martin, A. (1995). Central Italian lead-glazed ware. *Rei Cretariæ Romanæ Fautorum Acta* **34**, 63–68.

Mason, R. (1994). *Islamic Glazed Pottery 700–1250*. D.Phil. thesis, University of Oxford.

Matousek, J. (1975). Transport of Pb ions at the interface between silicate glass and molten lead. *Journal of The American Ceramic Society* **58(11-12)**, 521–524.

McCarthy, B. (1996). *Microstructural and Compositional Studies of the Technology and Durability of Ceramic Glazes from Nippur: Iraq 250 BC–1450 AD*. Ph. D. thesis, The Johns Hopkins University.

Müller, G. and P. Stoffers (1974). Mineralogy and petrology of Black Sea basin sediments. In E. Degin and A. Ross (Eds.). *The Black Sea: Geology, Chemistry, and Biology*. Tulsa: American Association of Petroleum Geologists.

Molera, J. (1996). *Mineralogical Evolution and Interaction Between Calcareous Clays and Lead Glazes: Archaeometric Implications*. Ph. D. thesis, University of Barcelona.

Molera, J., T. Pradell, S. Martinez-Manent, and M. Vendrell-Saz (1993). The growth of sanidine crystals in the lead glaze of Hispano Moresque pottery. *Applied Clay Science* **7**, 483–491.

Molera, J., T. Pradell, N. Salvadó, and M. Vendrell-Saz (2001). Interactions bewteen clay bodies and lead glazes. *Journal of the American Ceramic Society* **84(5)**, 1120–1128.

Moorey, P. (1994). *Ancient Mesopotamian Materials and Industries*. Oxford: Oxford University Press.

Mungall, J., C. Romano, and D. Dingwell (1998). Multicomponent diffusion in the molten system K_2O–Na_2O–Al_2O_3–SiO_2–H_2O. *American Mineralogist* **83**, 685–699.

Mylyanych, A., M. Sheredka, and S. Melnyk (1999). Study of glass structures and crystalline phases in the PbO–Al_2O_3–SiO_2 system. *Journal of Analytical Atomic Spectrometry* **14**, 513–521.

Nesbitt, H. and G. Young (1982). Early Proterozoic climates and plate motions inferred from major element chemistry of lutites. *Nature* **299**, 715–717.

Nesbitt, H. and G. Young (1984). Prediction of some weathering trends of plutonic and volcanic rocks based on thermodynamic and kinetic considerations. *Geochimica et Cosmochimica Acta* **48**, 1523–1534.

Nishiyama, T. (1998). Uphill diffusion and a new nonlinear diffusion equation in ternary non-electrolyte systems. *Physics of the Earth and Planetary Interiors* **1-7**, 33–51.

Noda, I. (1986). Two-dimensional infrared spectroscopy of synthetic and biopolymers. *Bulletin of the American Physics Society* **31**, 520.

Onsager, L. (1945). Theories and problems of liquid diffusion. *Ann. N.Y. Acad. Sci.* **46**, 241–265.

Ouchi, Y. and E. Kato (1983). Viscosities of ternary lead-silicate melts and activities of Pbo in these melts. *Canadian Metallurgical Quarterly* **22**, 45–51.

Parlasca, K. (1990). Kleinasiatische terrakotten mit bleiglasur. *Istanbuler Mitteilungen* **40**, 195–206.

Paul, A. (1982). *Chemistry of Glasses*. London: Chapman and Hall.

Paynter, S. (2001). *The Development of Vitreous Materials in the Ancient Near East and Egypt*. D.Phil. thesis, University of Oxford.

Pérez-Arantegui, J., M. Uruñuela, and J. Castillo (1996). Roman glazed ceramics in the western Mediterranean: Chemical characterization by inductively coupled plasma atomic emission sepctrometry of ceramic bodies. *Journal of Archaeological Science* **23**, 903–914.

Pérez-Arantegui, J., M. Uruñuela, M. Lapuented, and J. Castillo (1995). Study of Roman lead glazing technology between 1^{st} and 2^{nd} centuries AD by scanning electron microscopy. In C. Palmonari (Ed.). *Proceedings of the 4^{th} European Ceramic Society Conference: Cultural Ceramic Heritage 3^{rd} European Meeting on Ancient Ceramics, Riccione Italy*.

Pernicka, E., T. Rehren, and S. Schmitt-Strecker (1998). Late Uruk silver production by cupellation at Habuba Kabira, Syria. In T. Rehren, T. Hauptmann, and J. Muhly (Eds.), *Metallurgica Antiqua, Der Anschinitt,* **8**. Deutsche Bergbau-Museum.

Peterson, S. (2004). *The Craft and Art of Clay*. New York: Prentice Hall.

Petusky, W. (1980). Electrochemical transport in molten lead silicates. *Canadian Metallurgical Quarterly* **20(2)**, 225–230.

Petusky, W. and H. Schmalzried (1980). Ionic transport in PbO-SiO_2. *Ber Bunsenges Chem* **83**, 64–69.

Picon, M. (1973). Introduction a l'étude technique des ceramique sigillés de Lezoux. *Centre de recherche sur les technique gallo-romaines* **2**.

Picon, M. and A. Desbat (1986). Note sur l'origine des ceramique à glacure plombifère, généralement bicolore, des IIème and IIIème siècles de Vienne et Saint-Romaine- en-gal. *Figlina* **7**, 125–127.

Picon, M. and M. Vichy (1974). Recherches sur la composition des ceramiques de Lyon. *Revue Archéologique de L'Est et du Centre-Est* **25**, 37–59.

Picon, M., M. Vichy, and E. Meille (1971). Composition of the Lezoux, Lyon, and Arezzo Samian ware. *Archaeometry* **13**, 191–208.

Pinkwart, D. (1972). Hellenistisch-römische Bleiglasurkeramik aus Pergamon. *Pergamenische Forschungen* **1**, 140–163.

Pollard, A., H. Hatcher, and R. Symonds (1980). Provenance studies of 'Rhenish' pottery by comparison with terra sigillata. *Revue d'Archéométrie, Actes du XX Symposium International d'Archéométrie* **2**, 177–185.

Pollard, A., H. Hatcher, and R. Symonds (1982). Provenance studies of 'Rhenish' wares. *Proceedings of the 22nd Symposium on Archaeometry, University of Bradford*, 343–354.

Porat, N. (1989). *Composition of Pottery– Application to the Study of the Interrelations between Cannan and Egypt during the 3rd millennium B.C.* Ph. D. thesis, Hebrew University of Jerusalem.

Pradell, T. (2003a). The high temperatures reactions of 40% SiO_2 and 60% PbO as determined by high temperature synchrotron radiation X-ray diffraction. unpublished data.

Pradell, T. (2003b). The role of cinnabar in luster production. unpublished data.

Rawson, J., M. Tite, and M. Hughes (1988). The export of Tang Sancai wares: some recent research. *Transactions of the Oriental Ceramic Society* **52**, 39–61.

Rice, P. (1987). *Pottery Analysis, A Source book*. Chicago: The University of Chicago Press.

Rita, R. (1976). *Effect of melt constitution on the growth of lead silicates*. Ph. D. thesis, University of Illinois.

Rollinson, H. (1993). *Using Geochemical Data: evaluation, presentation, interpretation*. London: Longman Group.

Rotroff, S. (1982). *Hellenistic Pottery: Athenian and Imported Moldmade Bowls*. Princeton: Princeton University Press.

Rybicki, J., A. Rybicka, A. Witkowska, G. Bergmanski, A. Di Cicco, M. Minicucci, and G. Mancini (2001). The structure of lead-silicate glasses: molecular dynamics and EXAFS studies. *Journal of Physics: Condensed Matter* **13**, 9781–9797.

Scheel, H. (1972). Lead feldspar. *Zeitscrift fur Kristallagraphie* **133**, 296–304.

Schmalzried, H., Y. Takada, and B. Langanke (1981). Tracer diffusion coefficients of Pb-, Si-, and O-ions in molten leadsilicates. *Zeitschrift fur Physikalische Chemie Neue Folge* **128**, 205–212.

Schneider, G. (1978). Anwendung quantitativer materialanalysen auf herkunftsbestimmungen antiker keramik. *Berliner Beitrage zur Archaeometrie* **17**, 63–122.

Schut, R. and A. Cooper (1982). A method for determination of [**D**] in ternary systems from a single experiment. *Acta Metallurgica* **30**, 1957–1959.

Scott, R., N. Wood, and R. Kerr (1995). The development of Chinese overglaze enamels: Part I. In P. Vincenzini (Ed.). *The Ceramics Cultural Heritage, volume 2*. Faenza: Techna Srl.

Segtnan, V., S. Sasic, T. Isaksson, and Y. Ozaki (2001). Studies on the structure of water using two-dimensional near infrared correlation spectroscopy and principal component analysis. *Analytical Chemistry* **73**, 3153–3161.

Shortland, A. (2000). *Vitreous Materials at Amarna: The production of glass and faience in 18th Dynasty Egypt*. Oxford: BAR International Series.

Sillar, B. and M. Tite (2000). The challenge of 'technological choices' for materials science approaches in archaeology. *Archaeometry* **42**, 2–20.

Stoch, L. (1999). Infrared spectroscopy in the investigation of oxide glasses structure. *Journal of Molecular Structure* **511/512**, 77–84.

Stos, Z. (2004). Comments on the lead isotope data for the 1^{st}–5^{th} century glazed pottery from Europe and the Islamic world. unpublished data.

Symonds, R. (2001). Personal communication.

Symonds, R. and H. Hatcher (1989). La céramique à glacure plombifère de l'époque romaine trouvée à Colchester at ailleurs: quelques analyses recentes. *Actes du Congrès de Lezoux, S.F.E.A.G.*, 85–92.

Tite, M. (2001). Materials study in archaeology. In D. Brothwell and A. Pollard (Eds.), *Handbook of Archaeological Sciences*. Chichester: John Wiley and Sons. Ltd.

Tite, M., I. Freestone, R. Mason, M. Vendrell-Saz, and N. Wood (1998). Lead glazes in antiquity – methods of production and reasons for use. *Archaeometry* **40(2)**, 163–172.

Trial, A. and F. Spera (1994). Measuring the multicomponent diffusion matrix: Experimental design and data analysis for silicate melts. *Geochimica et Cosmochemica Acta* **58(18)**, 3769–3783.

Tribaudino, M., P. Benna, and E. Bruno (1998). Structural variations induced by thermal-treatment in lead feldspar ($PbAl_2Si_2O_8$). *American Mineralogist* **83(1-2)**, 159–166.

Van Den Dreissche, J. and J. Brun (1991). The techtonic evolution of Montagne Noire, French Massif central: a model of extensional gneiss dome. *2nd Ed, Geodinamica Acta* **5(1-2)**, 85–99.

Vandiver, P. (1983). Egyptian faience technology. In A. Kaczmarczyk and R. Hedges (Eds.). *Ancient Egyptian Faience*. Warminster: Aris and Philips.

Velde, B. and I. Druc (1998). *Archaeological Ceramic Materials, Origin and Utilization*. Berlin: Springer-Verlag.

Vertet, H. (1986). Recherches sur les glaçures plombifères dans le centre de la Gaule. In L. Rivet (Ed.), *Actes du Congrès de Toulouse, 9-11 mai 1986*, Marseille. SFECAG.

Vickers, M. (1986). *Pots and Pans: Proceedings of the Colloquium on Precious Metal and Ceramics in the Muslim, Chinese, and Graeco-Roman Worlds*. Oxford Studies in Islamic Art 3. Oxford: Oxford University Press.

Vickers, M. (1995). Surface colour transfer from metal, ivory, and stone to ceramic and glass. In P. Vandiver, J. Druzik, J.L.G. Madrid, I. Freestone, and G. Wheeler (Eds.), *Materials Issues in Art and Archaeology IV*, Volume 352, Pittsburg: Materials Research Society.

Vickers, M., O. Impey, and J. Allan (1986). *From Silver to Ceramic*. Oxford: Ashmolean Museum.

Wang, P. and L. Zhang (1996). Structural role of lead in lead silicate glasses derived from XPS spectra. *Journal of Non-Crystalline Solids* **194**, 129–134.

Zachariasen, W. (1932). The atomic arrangement in glass. *Journal of the American Chemical Society* **54**, 3841–3851.

Zhang, Y., D. Walker, and C. Lesher (1989). Diffusive crystal dissolution. *Contributions to Mineral Petrology* **102**, 492–513.